

**CONDUCTING ORGANOGELEATORS: DESIGN, SYNTHESIS
AND SELF-ASSEMBLY OF OLIGO(THIENYLENEVINYLENE)
DERIVED MOLECULAR WIRES**

THESIS SUBMITTED TO
THE UNIVERSITY OF KERALA
FOR THE DEGREE OF
DOCTOR OF PHILOSOPHY
IN CHEMISTRY
UNDER THE FACULTY OF SCIENCE

By
SEELAM PRASANTHKUMAR

PHOTOSCIENCES AND PHOTONICS GROUP
CHEMICAL SCIENCES AND TECHNOLOGY DIVISION
NATIONAL INSTITUTE FOR INTERDISCIPLINARY SCIENCE AND TECHNOLOGY (NIIST)
CSIR, TRIVANDRUM – 695 019
KERALA, INDIA

JANUARY 2012

Dedicated to

My Beloved Parents and Sisters

DECLARATION

I hereby declare that the matter embodied in the thesis entitled: **“Conducting Organogelators: Design, Synthesis and Self-assembly of Oligo (thienylenevinylene) Derived Molecular Wires”** is the result of the investigations carried out by me at the Photosciences and Photonics Group, Chemical Sciences and Technology Division, National Institute for Interdisciplinary Science and Technology (NIIST), CSIR, Trivandrum, under the supervision of Dr. A. Ajayaghosh and the same has not been submitted elsewhere for any other degree.

In keeping with the general practice of reporting scientific observations, due acknowledgement has been made wherever the work described is based on the findings of other investigators.

Seelam Prasanthkumar

National Institute for Interdisciplinary Science and Technology (NIIST)



(Formerly Regional Research Laboratory)
Council of Scientific & Industrial Research (CSIR)
Industrial Estate P.O., Trivandrum-695 019
Kerala, INDIA



Dr. A. Ajayaghosh, F. A. Sc.
CSIR Outstanding Scientist (Director Level)
Dean Chemical Sciences (AcSIR)

Tel: 91-471-2515 306
Fax: +91-471-2491 712
E-mail: ajayaghosh62@gmail.com
ajayaghosh@niist.res.in

January 09, 2012

CERTIFICATE

This is to certify that the work embodied in the thesis entitled: **“Conducting Organogelators: Design, Synthesis and Self-assembly of Oligo (thienylenevinylene) Derived Molecular Wires”** has been carried out by Mr. Seelam Prasanthkumar under my supervision at the Photosciences and Photonics Group of the National Institute for Interdisciplinary Science and Technology (NIIST), CSIR, Trivandrum and the same has not been submitted elsewhere for a degree.

A. Ajayaghosh
(Thesis Supervisor)

ACKNOWLEDGEMENTS

It is with great pleasure that I extend my deep sense of gratitude to Dr. A. Ajayaghosh, my thesis supervisor, for suggesting the research problem, for his constant guidance, support and encouragement, leading to the successful completion of this work.

I would like to express my gratitude to Prof. M. V. George for his constant encouragement, inspiration and useful discussions during my stay at NIIST.

I thank Dr. Suresh Das, Director, NIIST, Trivandrum, for providing me the necessary facilities and infrastructure of the laboratory for carrying out this work.

I take this opportunity to thank the former Director of NIIST, Prof. T.K. Chandrasekhar for supporting my research activities at NIIST.

My Sincere thanks are also due to:

- *Dr. D. Ramaiah, Dr. K. R. Gopidas, Dr. K. George Thomas (presently at IISER, Trivandrum), Dr. A. Sreenivasan (presently at NISER, Bhubaneswar) scientists of the Photosciences and Photonics Section, for their help and valuable suggestions.*
- *I am grateful to Dr. J. D. Sudha for her help with technical support and also helping me in correcting the thesis.*
- *Prof. Shu Seki and Dr. Akinori Saeki, Osaka University, Japan for fruitful collaboration and also for their help and support during my visit under JENESYS programme at Osaka University.*
- *Dr. V. K. Praveen, Dr. Reji Varghese, Dr. C. Vijayakumar, Dr. P. Chithra, Dr. S. Mahesh, Dr. S. Sreejith, Dr. S. Santhosh Babu, Dr. S. Srinivasan, the former members of the Photosciences and Photonics Group for their help and advice.*
- *Ms. K. P. Divya, Mr. Anesh Gopal, Mr. Thirumalai Kumaran, Mr. Krishnan Kartha, Mr. P. Anees, Mr. A. Sandeep, Mr. Vedhanarayan, Mr. Sandeep, Mr. Rahul, Mr. Vishnu, Ms. Divya Susan, Mr. Samrat, Mr. Sudesh, Mr. Arindam Mal and other members of Photosciences and Photonics Section for their help and cooperation. I would also like to remember the help rendered by Ms. Sreedivya and Mr. Kiran.*
- *Mr. Robert Philip and Ms. Sarada Nair for their support.*
- *Ms. Saumini Mathew and Preethanuj for NMR spectra, Ms. S. Viji for HRMS, Ms. Priya A. Nair and Ms. Sreenakumari for GC-MS and IR spectra, Mr. P. Prabhakar Rao and Mr. M. R. Chandran for SEM, Dr. U. Shyamaprasad and Mr. P. Guruswamy for XRD, Dr. Prasad, Mr. Naren and Mr. Kiran for TEM measurements.*
- *All my friends at NIIST particularly Dr. Sreedhar Reddy, Mr. Fareed Basha, Mr. Hari Shankar, Mr. Ramesh, Mr. Ravi and Ms. Lalitha for their love and support.*
- *All my teachers for their encouragement at different stages of my academic career.*
- *All my family members for their love and support.*
- *CSIR, UGC, JENESYS (Japan) and DST for financial assistance.*

Seelam Prasanthkumar

CONTENTS

	Page
Declaration	i
Certificate	ii
Acknowledgements	iii
List of Tables	vii
List of Schemes	viii
List of Figures	ix
List of Abbreviations	xvii
Preface	xx
CHAPTER 1: Conducting Organogels – An Overview	01-41
1.1. Abstract	1
1.2. Introduction	1
1.3. Conducting Organogels	3
1.4. p-Type Semiconducting Organogels	4
1.4.1. Thiophene Derived Organogels	5
1.4.2. TTF Derived Organogels	11
1.4.3. Diacetylene Derived Organogels	17
1.4.4. Hexabenzocoronene Derived Organogels	20
1.4.5. Porphyrin Derived Organogels	24
1.5. n-Type Semiconducting Organogels	28
1.5.1. Perylene Bisimide Derived organogels	29
1.5.2. Naphthalene Diimide Organogels	34
1.5.3. Bisphenazine Derived Organogels	37
1.6. Origin, Objectives and Approach to the Thesis	39

CHAPTER 2: Thienylenevinylene Based Organogelators: Synthesis, Self-Assembly and Charge-Carrier Mobility Studies	42-74
2.1. Abstract	42
2.2. Introduction	43
2.3. Results and Discussion	49
2.3.1. Synthesis of TTV1-4	49
2.3.2. Electronic Absorption and Emission Properties	51
2.3.3. Gelation Properties	55
2.3.4. FT-IR Studies	57
2.3.5. Morphological Studies	57
2.3.6. X-ray Diffraction Measurements	60
2.3.7. Charge-Carrier Mobility Studies: FP-TRMC & TAS Analyses	61
2.4. Conclusions	64
2.5. Experimental Section	65
2.5.1. Synthesis and Characterization	65
2.5.2. Description of Experimental Techniques	72
CHAPTER 3: Epitaxial Self-Assembly and High Conductivity of Oligo(thienylenevinylene) Molecular Gelators	75-108
3.1. Abstract	75
3.2. Introduction	76
3.3. Results and Discussion	82
3.3.1. Synthesis of OTVs	82
3.3.2. UV-vis Absorption Studies	84
3.3.3. Gelation Studies	86
3.3.4. Morphological Studies	88
3.3.5. Conductivity Studies	92

3.4.	Conclusions	97
3.5.	Experimental Section	98
3.5.1.	Synthesis and Characterization	98
3.5.2.	Description of Experimental Techniques	106
CHAPTER 4: Interaction of p-Type Gelators with n-Type Semiconductors: Co-assembly, Morphology and Charge Carrier Properties		109-144
4.1.	Abstract	109
4.2.	Introduction	110
4.3.	Results and Discussion	116
4.3.1.	Synthesis of TV1-4 and PBI	116
4.3.2.	Photophysical Properties	117
4.3.3.	Gelation Studies	120
4.3.4.	Morphological Studies	121
4.3.5.	Kelvin Probe Force Microscopy Investigation	127
4.3.6.	X-ray Diffraction Measurements	133
4.3.7.	Mobility Studies	135
4.4.	Conclusions	140
4.5.	Experimental Section	140
4.5.1.	Synthesis and Characterization	140
4.5.2.	Description of Experimental Techniques	143
References		145-165
List of Publications		166
Posters Presented at Conferences		167

List of Tables

1)	Table 2.1. Critical gelator concentrations (mM) of TTV4 in different solvents	56
2)	Table 2.2. FP- TRMC and TAS values of TTV4 in chloroform and decane/chloroform	64
3)	Table 3.1. Gelation data of OTV1 , OTV2 and OTV3 in polar and non-polar solvents	87
4)	Table 3.2. Four-probe conductivity (S/cm) measurements of OTV1 , OTV2 and OTV3 xerogels before and after iodine doping	97
5)	Table 4.1. Gelation Studies of TV1-4 in polar and non-polar solvents	122
6)	Table 4.2. KPFM analysis of donor/acceptor (PBI) (1:1 M ratio) on freshly cleaved mica and Silicon wafer surfaces	134

List of Schemes

- 1) **Scheme 1.1.** Electronic band structures of metal, semiconductors and insulators. 3
- 2) **Scheme 2.1.** Synthesis of **TTV1**. Reagents and conditions: (a) Ni(dppp)Cl₂, RMgBr, Et₂O, 24 h, 40 °C, 65%; (b) POCl₃, DMF, 1,2-DCE, 2 h, 70 °C, 76%; (c) *n*-BuLi, TMEDA, DMF, Hexane, 2 h, -40 °C, 54%; (d) NaBH₄, DCM, MeOH, 1 h, 30 °C, 92%; (e) PBr₃, DCM, -5 °C, 4 h; (f) P(OEt₃), 120 °C, 65%; (g) *t*-BuOK, THF, 2 h, 30 °C, 72%. 50
- 3) **Scheme 2.2.** Synthesis of **TTV2**. Reagents and conditions: (a) POCl₃, DMF, 1,2 DCE, 2 h, 70 °C, 68%; (b) NaBH₄, DCM, MeOH, 2 h, 30 °C, 92%. 51
- 4) **Scheme 2.3.** Synthesis of **TTV3** and **TTV4**. Reagents and conditions: (a) *t*-BuOK, THF, 2 h, 30 °C, 94% ; (b) KOH, THF, MeOH, TFA, 4 h, 70 °C, 91%; (c) R- NH₂, HATU, DIPEA, CHCl₃, 12 h, 30 °C, 45%. 53
- 5) **Scheme 3.1.** Reagents and conditions: (a) POCl₃, DMF, 1,2 DCE, 2 h, 70 °C, 68%; (b) *t*-BuOK, THF, 2 h, 30 °C, 74%; (c) *t*-BuOK, THF, 2 h, 30 °C, 62%; (d) POCl₃, DMF, 1,2 DCE, 2 h, 70 °C, 68%. 83
- 6) **Scheme 3.2.** Synthesis of **OTV2** and **OTV3**. Reagents and conditions: (a) *t*-BuOK, THF, 2 h, 30 °C, 94%; (b) KOH, THF, MeOH, TFA, 4 h, 70 °C, 91%; (c) C₂H₅NH₂, HATU, DIPEA, CHCl₃, 12 h, 30 °C. **OTV2** (35%) and **OTV3** (28%). 84
- 7) **Scheme 4.1.** Chemical Structures of **3** (4Thio) and **4** (6Pery). 114
- 8) **Scheme 4.2.** Synthesis of **TV1-4**. Reagents and conditions: (a) R' NH₂, HATU, DIPEA, 20 h, 30 °C. 119
- 9) **Scheme 4.3.** Synthesis of **PBI**. Reagents and conditions: (b) C₁₂H₂₅NH₂, *t*-BuOH, 20 h, 120 °C, 82 %. 119

List of Figures

- 1) **Figure 1.1.** a) SEM images of a xerogel of **5**. b) Schematic view of an individual nanofibre transistor of **5** with bottom-contact geometry. 6
- 2) **Figure 1.2.** CP-AFM current images of the NWs formed by **6** on a SiO₂/Si substrate via drop-casting from a 0.1 wt% chloroform solution at different bias values; V_{bias} = (a) 3.0 V, and (b) 6.0 V. (c) Current profiles obtained from the solid lines in (a) and (b). 7
- 3) **Figure 1.3.** a) Hydrogen bonding of the *trans*-1, 2-diaminocyclohexyl groups. b) Self-assembly of molecule by hydrogen bonding of the head groups (in blue) and H aggregates of the sexithiophenes (in green) leading to nanofibres of width about the length of one arm. c) Transmission electron microscopic (TEM) image of the bundled fibres. 9
- 4) **Figure 1.4.** a) AFM height images of a film spin-coated from diluted gel solution of **12** in MCH (2×10^{-3} M) on to HOPG. Inset shows photograph of gel in cyclohexane at 1.5 mM concentration. b) Variation of dose-normalized conductivity transients ($\Delta\sigma/D$) with time for **12**. 10
- 5) **Figure 1.5.** a) Schematic of a fabricated device. b) SEM image of a typical device fabricated from **14** showing the gold pads and organic channel. Bundles of self-assembled nanofibres are present throughout the device as seen in the SEM image. c) Representative *I*-*V* curves of **13** (4TG) and **14** (5TG) devices. 11
- 6) **Figure 1.6.** Phase contrast microscopic picture of a gel of **15** 11
- 7) **Figure 1.7.** a) Temperature dependent organogelation of **16**. A 1 mm solution of **16** in CHCl₃/CH₃CN (6/4) at 333 K was slowly cooled to 298 K. Organogelation was accompanied by a color change from yellow (T = 333 K) to orange (T = 298 K). AFM image of b) nanodots of **16** and c) fibrous structure of **16** on HOPG for CP-AFM measurements. d) *I*-*V* characteristics at points I (HOPG), II (single nanodot in air), III (single nanodot), and IV (bundle of fibres). DC bias was applied from -0.2 to 0.2 V. 12
- 8) **Figure 1.8.** a) Photograph of the transparent gel prepared from **18** with hexane. TEM images of the hexane gel of **18**; the samples were prepared at b) 50 g dm⁻³ and c) at 100 g dm⁻³. 13
- 9) **Figure 1.9.** a) AFM image of fibrous aggregates of **19**. b) Current-voltage characteristics for fibrous aggregates of **19** before and after iodine-doping for 2 min: (i) before doping, (ii) immediately after doping, and (iii) 1 week after doping. 14
- 10) **Figure 1.10.** Stacking of TTF derivative having long alkylthio chains 15

- 11) **Figure 1.11.** FE-SEM images obtained from air-dried gels of **26** (a) and **27** (b) from toluene. c) *I-V* curves measured on xerogel **27** prepared from toluene before and after doping with I₂, respectively. The inset in Figure c is a schematic representation of a top-contact device. 17
- 12) **Figure 1.12.** Photopolymerization of diacetylenes to polydiacetylenes and the schematic representation of the concept of covalent fixation of diacetylenes derived self-assemblies. 18
- 13) **Figure 1.13.** Optical micrographs of the fibrous aggregates observed for the dodecylbenzene gel of **28** (8 mM): (a) aligned fibres formed under an AC electric field; (b) randomly entangled fibres without an electric field. 18
- 14) **Figure 1.14.** a, b) TEM images of **37** which forms tubes that can be placed between two electrodes. c) Tapping-mode AFM image of the nanotube of **37** on two-probe electrodes with a 180 nm gap (taken after the conductivity measurements). d) *I-V* profiles of unoxidized (blue circles) and oxidized (red circles) single nanotube at 285 K. 21
- 15) **Figure 1.15.** a) A polarized optical microscopy image of a macroscopic fibre consisting of bundled nanotubes of **38**. b) Temperature dependencies of its resistivities along (ρ_{\parallel}) and across (ρ_{\perp}) the fibre axis. 22
- 16) **Figure 1.16.** a) TEM micrograph of air-dried toluene suspension of the coassembled nanotubes with 25% of **39**. (b) Schematic representation of the formation of homotropic and coassembled nanotubes of **39** and **40** and the wall structure of the nanotube of **39** containing an electron transporting molecular layer of clustered C₆₀ (orange) and a hole transporting graphite-like layer of π -stacked HBC units (blue). 23
- 17) **Figure 1.17.** SEM pictures of the xerogels obtained from (a) **41** and (b) **41**/fullerene complex (1 : 2 molar ratio) in benzene. 25
- 18) **Figure 1.18.** Structure of tetra(thiafulvalene)-functionalized crown ether phthalocyanine **42**. a) TEM image of the tapes formed by **42**, showing an equal distribution of both M- and P-helical structures (bar represents 200 nm). b) Schematic representation of the aggregation mechanism of **42**, showing the dominating Pc-TTF and TTF-TTF interactions, which result in an initial bilayer structure that scrolls into helical tapes. 26
- 19) **Figure 1.19.** a) Aggregation mode of **44**. b) Side view of the energy minimized structure of (C₆₀)₃·(44)₆. c) SEM images showing the morphological changes of the benzene gels of **44** on adding fullerenes. 28
- 20) **Figure 1.20.** a) Absorption (—) and fluorescence (·····) spectra of the molecule **45** gel; [45] = 0.2 wt/vol% (1.5 mm), λ_{ex} = 457 nm. Inset shows photo of the gel of **45**. b) SEM image of the gel. 30

21)	Figure 1.21. a) Optical polarizing microscopic image of 46 . b) AFM height images of films spin-coated from diluted gel solutions of 46 in toluene (zoomed region image).	30
22)	Figure 1.22. Cryo-SEM images of the gel of 47 (8×10^{-3} M, water/THF mixture (80:20), Scale. 0.5 μm). Inset: vial inversion test.	31
23)	Figure 1.23. Schematic representation of organogel-polymer concept for realization of an interpenetrating organic bulk heterojunction. Route A: Formation of n-type xerogel with subsequent filling with p-type polymer. Route B: Concomitant embedding of the physical network by a blend approach.	33
24)	Figure 1.24. a) Schematic representation of the aggregation 53 with dCA in TCE. b) SEM image of nanofibres.	34
25)	Figure 1.25. a) Photograph depicting the spontaneous color changes of the organogel 54 upon addition of 55 . SEM images of the xerogel of b) 54 and c) the 54 + 55 complex prepared from the cyclohexane gel (4.0 mm); the scale bar denotes 1 mm.	35
26)	Figure 1.26. Structures of lysine-based bolaamphiphiles 56 ($R=O^-$) and 57 ($R=OMe$) and the assembly of 56 into rings, which stack to give tubes. The blue sections of 57 undergo hydrophobic π - π stacking interactions, and the red sections show electrostatic interactions.	36
27)	Figure 1.27. a) Pictures of organogel of compound 62 in decane (1.3 mM). SEM images of the xerogel of compound 62 : b) from decane gel (1.3 mM), scale bar: 1 mm (inset: 300 nm), c) from TCE gel (10 mM), scale bar: 1 mm (inset: 500 nm).	38
28)	Figure 1.28. Design features showing various non-covalent interactions for the self-assembly of linear π -conjugated oligomers.	40
29)	Figure 2.1. a,b) Electron micrographs of the lamellar fibers of 5 (A) and 6 (B). c) Possible arrangement of 6 in the lamella, and d) FP-TRMC kinetic profile of 5 and 6 .	46
30)	Figure 2.2. Scheme of the interconversion between nanorod and nanotape. Transient conductivities observed for films of a) 7 and b) 7 · BM12 under an excitation at $\lambda = 355$ nm by 1.8×10^{16} photons cm^{-2} pulse $^{-1}$.	47
31)	Figure 2.3. a) Absorption and emission spectra of (a,b) TTV1 , (c,d) TTV2 , and (e,f) TTV3 at 1.5×10^{-4} M in decane (blue) and chloroform (red). (Note: spectra of TTV3 was recorded in toluene due to insolubility in decane).	53
32)	Figure 2.4. a) Absorption spectra of TTV4 at 1.5×10^{-4} M in decane (blue) and chloroform (red). b) Fluorescence spectra of TTV4 at 1.5×10^{-4} M in decane (blue) and chloroform (red).	54

33)	Figure 2.5. a) Temperature dependent UV-vis absorption spectra of TTV4 at 1.5×10^{-4} M in decane. b) Plot of the fraction of aggregates (α) versus temperature obtained from the absorption changes monitored at 491 nm.	55
34)	Figure 2.6. a) Photograph of the reversible sol-gel transition of TTV4 in decane. b) Plot of gel melting temperature (T_{gel}) vs concentration of the gelator.	56
35)	Figure 2.7. FT-IR Spectra of TTV4 in dilute chloroform solution and gel in decane.	57
36)	Figure 2.8. TEM images of a) TTV1 and c) TTV2 . AFM images of b) TTV1 and d) TTV2 at 5×10^{-5} M concentration from decane.	58
37)	Figure 2.9. a) TEM and b) AFM images of TTV3 drop casted from decane solution ($c = 5 \times 10^{-5}$ M) at room temperature.	59
38)	Figure 2.10. a) TEM and b) AFM images of TTV4 drop casted from decane solution ($c = 5 \times 10^{-5}$ M) at room temperature.	59
39)	Figure 2.11. Models of the self-assembly of a) TTV3 and b) TTV4 .	60
40)	Figure 2.12. XRD pattern of TTV4 xerogel from decane (Inset: XRD pattern at small angle region).	61
41)	Figure 2.13. FP-TRMC profiles of TTV4 films prepared with PDI from a) chloroform and b) <i>n</i> -decane/chloroform (1:1 v/v) solutions. The color represents weight fraction of PDI relative to 100 wt% TTV4 .	62
42)	Figure 2.14. Transient absorption spectra ($\lambda_{ex} = 355$ nm) of TTV4 films prepared with PDI from a) chloroform and b) <i>n</i> -decane/chloroform solutions. The color represents weight fraction of PDI relative to 100 wt% TTV4 .	63
43)	Figure 3.1. a) General structure of the dendron-rod-coils. b) Photographs of 4 in toluene (left) and THF (right) under illumination with 365 nm light and c) AFM texture of 4 under electric field.	76
44)	Figure 3.2. TEM image of xerogels prepared from a) 7 (1.0 mM in 1,1,2,2-tetrachloroethane (TCE)), b) 8 (2.9 mM in TCE), and c) 9 (3.8 mM in TCE) .	77
45)	Figure 3.3. a) Current-sensing AFM image showing the current response of a doped and annealed xerogel of 10 on graphite. b) Representative <i>I-V</i> curves of different areas of the material which correspond to the numbered areas in image a.	78
46)	Figure 3.4. a) AFM ($30 \times 30 \mu\text{m}^2$) image of the nanowires on mica, formed by the horizontal lifting method deposited from 0.01 M KCl aqueous solution. b) AFM image of a Nanowire junction.	80

47)	Figure 3.5. AFM images (10 $\mu\text{m} \times 10 \mu\text{m}$) of organic thin-films. a) 13 (2 nm) grown on SiO_2 , b) 12 (3 nm) on 13 (2 nm), c) 13 (30 nm) on 12 (2 nm), and d) 13 (30 nm) on SiO_2 .	80
48)	Figure 3.6. Normalized absorption spectra of OTV1 , OTV2 and OTV3 in a) in chloroform and b) in decane.	85
49)	Figure 3.7. Temperature dependent absorption spectra of a) OTV2 and b) OTV3 in decane. c) Plots of the fraction of aggregate (α) versus temperature monitored at 491 nm for OTV1 , 539 nm for OTV2 and 561 nm for OTV3 . Concentration of the solutions are kept at 1.5×10^{-4} M in all cases.	86
50)	Figure 3.8. a) Photographs showing sol-gel transition of OTV1 , OTV2 and OTV3 in decane at millimolar (mM) concentrations. b) Plot of the gel melting temperature (T_{gel}) against the concentration of the gelators.	87
51)	Figure 3.9. TEM images of a) OTV1 , b) OTV2 and c) OTV3 from decane drop casted on carbon coated grid at room temperature ($c = 5 \times 10^{-5}$ M)	88
52)	Figure 3.10. SEM images of a) OTV1 , b) OTV2 and c) OTV3 from decane drop casted at room temperature ($c = 5 \times 10^{-5}$ M).	89
53)	Figure 3.11. AFM images of (a,b) OTV1 , (c,d) OTV2 and (e,f) OTV3 from decane dropcasted on freshly cleaved mica surface and corresponding section analysis as shown.	90
54)	Figure 3.12. AFM images of (a,d) OTV1 , (b,e) OTV2 and (c,f) OTV3 from decane dropcasted on highly ordered pyrolytic graphite (a-c) and silicon wafer (d-f) substrates at room temperature ($c = 1 \times 10^{-5}$ M). Z-scale: a, b, c) 100 nm and d, e, f) 80 nm.	91
55)	Figure 3.13. AFM images of OTVs from decane on freshly cleaved mica surface a) OTV1 , b) OTV2 and c) OTV3 at 5×10^{-5} M. d) OTV1 , e) OTV2 and f) OTV3 at 1×10^{-4} M. Z-scale: a) 40 nm, b) 70 nm, c) 60 nm, d) 40 nm, e)100 nm and f)100 nm.	92
56)	Figure 3.14. C-AFM measurements of OTV1-3 xerogels obtained from decane solution dropcasted on HOPG substrate ($c = 1 \times 10^{-4}$ M). <i>I-V</i> curves of undoped (a) and doped (b) xerogels of OTV1 (1), OTV2 (2) and OTV3 (3) .	93
57)	Figure 3.15. C-AFM measurements of OTV3 xerogels obtained from decane solution dropcasted on HOPG substrate ($c = 1 \times 10^{-4}$ M). Topography images before (a), and after iodine doping (b). The areas of measurements are marked on the inset and the corresponding <i>I-V</i> profiles are shown in (c and d).	94

58)	Figure 3.16. UV-vis-NIR spectra of a) OTV1 , b) OTV2 and c) OTV3 in xerogel upon exposure to iodine vapors.	95
59)	Figure 3.17. FT-IR spectra of OTV3 in xerogel state before (i) and after (ii) iodine doping.	96
60)	Figure 4.1. Illustration of mixed packing and segregated arrangements of electron-rich conjugated molecules (blue, hole conductor, donor) and electron-poor conjugated molecules (orange, electron conductor, acceptor). Although the illustration shows planar electron-poor compounds, the mixing also happens with nonplanar, fullerene-based compounds.	111
61)	Figure 4.2. a) UV-vis spectral data of 1 and 2 in MCH at room temperature of separate and mixed samples at concentrations of 1×10^{-5} M. b) Tapping mode AFM image of spin-coated films from MCH of a 1:1 mixture of 1 and 2 of a glass/ITO/PEDOT:PSS/ OPV:PB1 /Al device.	112
62)	Figure 4.3. Schematic representation of their self-sorting organogel formation yielding p-n heterojunction points and b) SEM images of 3 (a), 4 (b) and 3/4 (c) self-sorting gel.	113
63)	Figure 4.4. Schematic representation of the photoinduced electron transfer from 5 to C ₆₀ COOH. AFM images of a) 5 and b) 5 and C ₆₀ COOH (1:1 wt ratio).	114
64)	Figure 4.5. Schematic representation of the possible molecular assembly mechanism for 6 in the gel phases in the absence and presence of C ₆₀ .	115
65)	Figure 4.6. Absorption spectra of a) TV4 , b) PBI and c) TV4/PBI (1:1 M ratio) in decane ($c = 1 \times 10^{-4}$ M).	118
66)	Figure 4.7. Temperature dependent absorption studies of a) TV4 , b) PBI and c) TV4/PBI (1:1 M ratio) in decane in the range from 20 ° to 70 °C.	119
67)	Figure 4.8. Plot of fraction of aggregation (α) versus temperature monitored at 520 nm for TV4 and TV4/PBI (1:1 M).	119
68)	Figure 4.9. Plot of T_{gel} versus concentration for TV1-4 .	120
69)	Figure 4.10. AFM images of a) TV1 , b) TV2 , c) TV3 and d) TV4 from decane drop casted on freshly cleaved mica surface at room temperature ($c = 1 \times 10^{-5}$ M).	122
70)	Figure 4.11. AFM images of a) TV1 , b) TV2 , c) TV3 and d) TV4 from decane drop casted on freshly cleaved mica surface at room temperature ($c = 5 \times 10^{-5}$ M).	122
71)	Figure 4.12. AFM images of a) TV1 , b) TV2 , c) TV3 and d) TV4 from	123

	decane drop casted on silicon wafer surface at room temperature ($c = 5 \times 10^{-5} \text{ M}$).	124
72)	Figure 4.13. TEM images of a) TV1 , b) TV2 , c) TV3 and d) TV4 from decane drop casted on copper coated grid ($c = 5 \times 10^{-5} \text{ M}$).	124
73)	Figure 4.14. a) TEM image of PBI on copper coated grid. AFM images of PBI drop casted b) on freshly cleaved mica and c) on silicon wafer ($c = 1 \times 10^{-4} \text{ M}$).	125
74)	Figure 4.15. AFM images of a) TV1/PBI , b) TV2/PBI , c) TV3/PBI and d) TV4 /PBI (1:1 M) from decane drop casted on freshly cleaved mica ($c = 5 \times 10^{-5} \text{ M}$).	126
75)	Figure 4.16. AFM images of a) TV1/PBI , b) TV2/PBI , c) TV3/PBI and d) TV4 /PBI (1:1 M) from decane drop casted on silicon wafer ($c = 5 \times 10^{-5} \text{ M}$).	126
76)	Figure 4.17. TEM images of a) TV1/PBI , b) TV2/PBI , c) TV3/PBI and d) TV4 /PBI (1:1 M) from decane drop casted on freshly cleaved mica ($c = 5 \times 10^{-5} \text{ M}$).	127
77)	Figure 4.18. AFM/KPFM images of TV4 from toluene drop casted on mica at room temperature ($c = 1 \times 10^{-4} \text{ M}$). a) Topography and b) KPFM image. The corresponding section analyses are shown in c and d.	128
78)	Figure 4.19. AFM/KPFM images of PBI from toluene drop casted on mica at room temperature ($c = 1 \times 10^{-4} \text{ M}$). a) Topography and b) KPFM image. The corresponding section analyses are shown in c and d.	129
79)	Figure 4.20. a) AFM and b) KPFM images of TV4 /PBI (1:1 M) drop casted from decane on mica ($c = 5 \times 10^{-5} \text{ M}$) at room temperature. The corresponding section analyses are also shown.	130
80)	Figure 4.21. AFM/KPFM images of TV4 from decane drop casted on silicon wafer at room temperature ($c = 5 \times 10^{-5} \text{ M}$). a) Topography and b) KPFM image. The corresponding section analyses are shown in c and d.	131
81)	Figure 4.22. AFM/KPFM images of PBI from toluene drop casted on silicon wafer at room temperature ($c = 1 \times 10^{-4} \text{ M}$). a) Topography and b) KPFM image. The corresponding section analyses are shown in c and d.	131
82)	Figure 4.23. a) AFM and b) KPFM images of TV4 /PBI (1:1 M) drop casted on silicon wafer from decane ($c = 5 \times 10^{-5} \text{ M}$) at room temperature. The corresponding section analyses are also shown.	132
83)	Figure 4.24. X-ray diffraction of a) TV4 (p-type), b) PBI (n-type), and c) TTV/PBI (1:1 M ratio) xerogels on quartz substrate.	134

- 84) **Figure 4.25.** FP-TRMC profiles of **TV4** films prepared with **PBI** from a) chloroform and b) *n*-decane/chloroform (1:1 v/v) solutions. The color represents weight fraction of **PBI** relative to 100 wt% **TV4**. 136
- 85) **Figure 4.26.** a) Transient absorption spectra ($\lambda_{\text{ex}} = 355 \text{ nm}$) of **TV4** films prepared with **PBI** from chloroform solution. The color represents weight fraction of **PBI** relative to 100 wt% **TV4**. Kinetic decay profiles obtained at 670 nm (b) and 800 nm (c). 136
- 86) **Figure 4.27.** a) Transient absorption spectra ($\lambda_{\text{ex}} = 355 \text{ nm}$) of **TV4** films prepared with **PBI** from *n*-decane/chloroform (1:1 v/v) solutions. The color represents weight fraction of **PBI** relative to 100 wt% **TV4**. Kinetic decay profiles obtained at 670 nm (b) and 800 nm (c). 137
- 87) **Figure 4.28.** Transient profiles of **TV4/PBI** (1:1 M) observed for parallel ($\Delta\sigma_{\parallel}$) and perpendicular ($\Delta\sigma_{\perp}$) directions to the electric-field vector of the microwave in (a) chloroform and (b) decane-chloroform. 138
- 88) **Figure 4.29.** Bar diagram represents $\Sigma\mu$ values of a) **TV1-4/PBI** and b) **TV1-4/PDI** from decane-chloroform (1:1 v/v) and chloroform solutions. 138
- 89) **Figure 4.30.** a) Schematic representation of bilayer of thienylenevinylene and perylene bisimide films prepared from chloroform and decane. b) Plot of I_0 (photon density) versus $\phi\Sigma\mu$: Front and back exposure. Inset shows photograph of the **TVs/PBI** film. 139

List of Abbreviations

AFM	Atomic force microscopy
ATR	Attenuated total reflectance
BHJ	Bulk heterojunction device
CA	Cyanurate
CB	Conduction band
CD	Circular dichroism
CGC	Critical gelator concentration
CHCl ₃	Chloroform
CP-AFM	Conducting probe-atomic force microscopy
CV	Cyclic voltammetry
D-A	Donor-Acceptor
DCM	Dichloro methane
DMF	N,N-Dimethyl formamide
DMSO	Dimethyl sulfoxide
FP-TRMC	Flash photolysis-time resolved microwave conductivity
FT-IR	Fourier transform-infrared
HATU	2-(7-Azabenzotriazol-1-yl)-1,1,3,3-tetramethyluronium hexafluorophosphate
HBC	Hexa- <i>peri</i> -hexabenzocoronene
HOPG	Highly ordered pyrolytic graphite
I	Current
IPCE	Incident photon-to-current conversion efficiency
ITO	Indium tin oxide
KPFM	Kelvin probe force microscopy
LC	Liquid crystal
MALDI	Matrix-assisted laser desorption ionization
MCH	Methyl cyclohexane
MeOH	Methanol
Na ₂ SO ₄	Sodium sulphate

NaBH ₄	Sodium borohydride
NaHCO ₃	Sodium bicarbonate
<i>n</i> -BuLi	<i>n</i> -Butyl lithium
ND:YAG	Neodymium-doped yttrium aluminium garnet
NDI	Naphthalene tetracarboxylic diimide
Ni(dppp)Cl ₂	1,2-Bis(diphenylphosphino)ethane nickel(II) chloride
NMR	Nuclear magnetic resonance
NOBF ₄	Nitrosonium tetrafluoroborate
NW	Nanowire
OFET	Organic field effect transistor
OPV	Oligo(phenylenevinylene)
OTFT	Organic thin film transistor
OTV	Oligo(thienylenevinylene)
P(OEt) ₃	Triethyl phosphite
PAH	Polycyclic aromatic hydrocarbons
PBI	Perylene bisimide
PBr ₃	Potassium tribromide
Pc	Phthalocyanine
PCBM	[6,6]-phenyl-C ₆₁ -butyric acid methyl ester
POCl ₃	Phosphoryl chloride
PR	Pulse radiolysis
PTCDA	Perylene (3,4,9,10) tetracarboxylic dianhydride
SCLC	Space charge limited current
SEM	Scanning electron microscopy
SP	Surface potential
TAS	Transient absorption spectroscopy
<i>t</i> -BuOK	Potassium tertiary butoxide
TCE	1,1,2,2-tetrachloroethane
TCNQ	7,7,8,8-tetracyanoquinodimethane
TCSPC	Time correlated single photon counting
TEM	Transmission electron microscopy

TOF	Time-of-flight
T_{gel}	Gel melting temperature
THF	Tetrahydrofuran
TMEDA	Tetramethylethylenediamine
TTF	Tetrathiafulvalene
TTV	Trithienylenevinylene
UV-vis-NIR	Ultra violet-visible-near infrared
V	Voltage
VB	Valence band
XRD	X-ray diffraction
$\phi\Sigma\mu$	Photoconductivity
ϕ	Quantum efficiency of charge carrier generation
$\Sigma\mu$	Charge-carrier mobility
σ	Conductivity
S	Siemen
V_{OC}	Open-circuit voltage
J_{SC}	Short-circuit current
ρ	Resistivity
μ_{e}	Electron mobility
μ_{h}	Hole mobility
nm	Nanometer
μm	Micrometer
mM	Millimolar
mV	Millivolt
I_2	Iodine
nA	Nanoampere

PREFACE

Study of the self-assembly of π -conjugated oligomers into nanosized architectures, promoted by non-covalent interactions is a topic of considerable importance. Substantial advancement have been achieved in the formation of self-assembled supramolecular structures from potentially electroactive subunits of conjugated linear π -systems. In particular, self-organization of thiophene derived molecules have attracted considerable interest among researchers, since they are widely used as molecular wires in organic electronic devices. The intermolecular interactions between π -conjugated molecules play an important role on the electronic properties when put into electronic devices. For example, the size and shape of the self-assembled structures and their interaction with a given substrate are of great significance. In this context, organogelators based on π -systems are excellent candidates to the preparation of self-assembled architectures that can be transferred on to various substrates. Organogelators based on molecules having good electronic conductivity and high charge carrier mobility are required for a variety of electronic applications. In the first chapter, an overview of the recent reports on conducting gels based on p- and n-type semiconducting molecules, their property and application are presented. At the end of the first chapter, the aim and the outline of the thesis are also presented.

The second chapter of the thesis describes the synthesis, self-assembly and charge-carrier mobility studies of a few thienylenevinylene derivatives (**TTV1-4**), having various end functional groups such as $-H$, $-OH$, $-CO_2H$ and $-CONHR$. It has been found that among **TTV1-4**, only **TTV4** with amide end functional groups facilitated gelation of nonpolar hydrocarbon solvents. For example, a solution of **TTV4** in chloroform showed the π - π^* absorption maximum at 501 nm. However, in decane, λ_{max} is blue-shifted to 464 nm with a shoulder band at 550 nm. This observation indicates that **TTV4** exist as H-type aggregates in decane. The gelation properties and the morphology of the gels are established from the FT-IR, XRD, SEM, TEM, and AFM analyses. Microscopic analysis revealed that **TTV4** forms entangled micrometer sized fibres of size ranging from 50-200 nm in width. XRD

analysis revealed a lamellar type packing of the molecules in the gel state. FP-TRMC and TAS studies suggested that films of **TTV4** prepared from decane-chloroform gels exhibited high charge carrier mobility when compared to films obtained from chloroform solutions, highlighting the role of self-assembly and gelation on the electronic properties.

In the third chapter, effect of conjugation length of oligo(thienylenevinylene)s (**OTVs**) on the gelation and conducting properties are described. **OTV1-3**, having molecular lengths of ca. 2.7-4.9 nm were synthesized and characterized. These molecules form amide hydrogen bond assisted 1D self-assembly leading to supramolecular gels. Detailed photophysical and gelation properties of **OTVs** revealed that **OTV3** aggregates have more stability when compared to that of **OTV1** and **OTV2**. TEM analysis of the self-assemblies revealed the formation of elongated fibrous structures. Interestingly, AFM studies revealed that these gels exhibit the unique property of solution phase epitaxy leading to the alignment of fibres on mica surface. However, entangled micrometer sized fibres are formed on silicon wafer and HOPG substrates with diameter ranging from 50-200 nm in width and several micrometer in length. The electrical conductivities of these fibres were measured using conducting probe atomic force microscopy (CP-AFM) and four-Probe dc resistance method. These data revealed that **OTV3** xerogel behaves like metallic wires after doping with iodine which indicates that an extended conjugation length and strong gelation in **OTV3** have resulted in efficient charge carrier generation upon doping with iodine. Detailed UV-vis-NIR studies of **OTVs** revealed strong polaron/bipolaron bands in the range 800-2500 nm indicating mixed valence states responsible for the metallic conductivity. This new class of conducting gels are useful in organic electronics and photonics applications.

The last chapter describes the results of co-assembly experiments of **TV1-4** with **PBI** on different substrates. Detailed studies on the gelation, morphology, substrate interaction, and charge-carrier mobilities of these n-type and p-type molecules have been carried out. Atomic force microscopy investigation of the co-assembly on mica and silicon wafer surfaces have shown that the co-assembly leads to different morphologies when compared to the individual self-assemblies.

TEM analysis of the co-assemblies revealed the formation of elongated fibres which is in agreement with the AFM analysis. X-ray studies on films indicated the occurrence of individual self-assembly (self-sorting) of the n-type and p-type molecules on the nanometer scale. Charge generation of the co-assemblies was measured using Kelvin probe force microscopy (KPFM) and FP-TRMC & TAS. KPFM analysis revealed that the surface potential exhibits more negative values for the self-assembled nanowires on silicon wafer when compared to those formed on mica surface. Mobility data showed the enhancement of uni-directional charge carrier transport in self-assembled films when compared to those obtained from isotropic solution.

In summary, we have carried out a systematic investigation on the synthesis and self-assembly property of oligo(thienylenevinylenes) (OTVs) a class of novel π -systems with interesting electronic properties. Our studies have revealed that the self-assembly and gelation of OTVs strongly influence on their electronic properties. It is also observed that the self-assembly of OTVs are controlled by mica surface leading to epitaxial organization. We have also shown that increasing the conjugation length of OTVs improve the gelation ability and conductivities. This is the first extensive investigation on the gelation behavior of OTVs and the consequent changes in the optical, morphological and electronic properties. The self-assembled structures of OTVs with high charge carrier mobility and conductivity are useful in the design of bulk heterojunction photovoltaic devices.

References

1. Prasanthkumar, S.; Saeki, A.; Seki, S.; Ajayaghosh, A. *J. Am. Chem. Soc.* **2010**, *132*, 8866.
2. Prasanthkumar, S.; Gopal, A.; Ajayaghosh, A. *J. Am. Chem. Soc.* **2010**, *132*, 13206.

Conducting Organogels – An Overview

1.1. Abstract

Self-assembly of π -conjugated oligomers leading to nanosized architectures, using weak non-covalent interactions is a topic of considerable importance. Among different π -conjugated systems, thiophene derivatives are widely used in organic electronic devices due to their electronic properties. The intermolecular interactions between π -conjugated molecules play an important role on the electronic properties when put into devices. Therefore, insight on the self-assembly of these molecules to different architectures of controlled size and shape are important. In this context, organogelation approach to the preparation of 1D fibres of thiophene derivatives have attracted the attention of chemists. These 1D structures are expected to have good electronic conductivity and high charge-carrier mobility, required for a variety of electronic applications. In this chapter, an overview of the recent developments on conducting gel based on p- and n-type semiconducting molecules, their properties and applications are described. Finally, the aim and the outline of the present thesis are given.

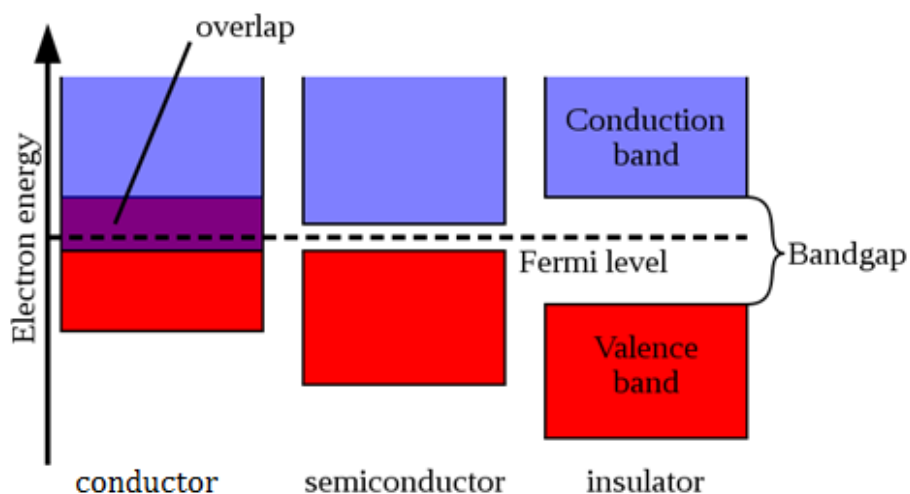
1.2. Introduction

The electronic properties of π -conjugated systems have acquired a growing importance in many areas of modern chemistry and physics of condensed matter. At the

molecular level, conjugated systems represent the simplest models of molecular wires, which together with their complementary functions such as molecular switches or logical gates have contributed to the emergence of the concepts of molecular electronics [Lehn *et al.* 1988; Aviram *et al.* 1988]. The unique properties of conjugated systems originate from their π -electrons which are delocalized over a large number of repeating monomer units. The origin of the band gap in conjugated systems lies in the alternation of single and double bonds. The characteristics of the π -bonds are the source of the semiconducting properties. First, the π -bonds are delocalized over the entire molecule; and then, the quantum mechanical overlap of p_z orbitals actually produces two orbitals, a bonding (π) orbital and an antibonding (π^*) orbital. The lower energy π -orbitals produce the valence band, and the higher energy π^* -orbitals form the conduction band. The difference in energy between the two levels produces the band gap that determines the electronic properties of the material. According to the band theory, electron transfer takes place from the valence band (VB) to the conduction band (CB) resulting in the flow of current. If VB and CB overlap each other, electrons can flow easily to the CB, resulting in conductors. If the gap between VB and CB is large then the promotion of electrons to the CB is practically not possible leading to insulators. If the band gap is moderate, limited conduction occurs, resulting in semiconductors (Scheme 1.1).

π -Conjugated oligomers and polymers are semiconductors. The conductivity of these systems can be improved by doping with suitable dopants. Polyanilines, polypyrroles and polythiophenes are examples. However, the electronic properties of short π -systems can be improved to the level of semiconductors and conductors upon strong intermolecular interaction. Therefore, molecular self-assembly of π -systems is an alternative approach to manipulate the electronic properties. This is possible with the help of non-covalent forces such as hydrogen bonding, π -stacking, van der Waals or

dipole interactions. In many of the cases, cooperative interactions of these forces allow molecules to form supramolecular assemblies leading to soft materials.



Scheme 1.1. Electronic band structures of conductors, semiconductors and insulators

1.3. Conducting Organogels

Gels are viscoelastic solid-like materials comprised of an elastic, cross-linked network and a solvent in which the latter is the major component. Most of these gels are composed of covalently crosslinked polymers having high molecular weights [Saiani *et al.* 1997; Suzuki *et al.* 2006]. More recently there has been an enormous increase of interest in the design of low molecular weight gelators, which immobilize various organic fluids or water as a result of three-dimensional supramolecular network formation [Terech *et al.* 1997; Shimizu *et al.* 2005; George *et al.* 2006]. Gels derived from low molecular mass compounds are also known as “supramolecular gels”. This novel class of supramolecular materials exhibit striking properties with respect to self-assembly phenomena leading to diverse architectures. The diversity of nanostructures provided by supramolecular gels makes them promising candidates for several potential applications. Low molecular weight organogel network is held together solely by non-covalent interactions such as hydrogen bonding, π -stacking, solvophobic, electrostatic

and donor-acceptor interactions rendering the gelation process thermally or mechanically reversible. The directional nature of intermolecular interactions allows gelator molecules to self-organize in one-dimensional (1D) arrays producing elongated fibrous nanostructures. Entanglement of these fibres produces three-dimensional networks capable of trapping solvent molecules thereby yielding a gel. In recent years, a variety of organogels based on chromophore assemblies have been reported (Sangeetha *et al.* 2005; Ajayaghosh *et al.* 2007]. Conducting gels are one such class of soft functional materials.

The preparation of conducting gels based on the self-assembly of functional π -conjugated molecules is important since, a variety of supramolecular structures of different length scale and properties are possible by which the electronic properties can be significantly altered. Even though conducting supramolecular wires offer many advantages, controlling the size and shape of the self-assembly is a challenging task. In particular, transfer and deposition of self-assembled structures on to surfaces is difficult to control, and in many cases, different morphologies and size distributions are common. Gelation of molecules offers an interesting way to form fibres in a homogeneous medium, which can then be physically deposited on a required surface. Many supramolecular gels based on π -systems are reported to form conducting nanowires.

1.4. p-Type Semiconducting Organogels

Electron rich molecules such as oligo/polythiophenes, tetrathiafulvalenes, hexabenzocoronenes, diacetylene etc are p-type organic semiconductors. Incorporation of electron donating groups such as alkoxy and alkylamino groups improves the p-type character of the molecules. They serve as electron donors in many of the organic electronic devices. Proper functionalization of these molecules with hydrogen bonding

groups allow the self-assembly resulting in gelation of organic solvents. A few representative examples are described below.

1.4.1. Thiophene Derived Organogels

Thiophenes are widely used for the preparation of oligo/polythiophenes since they are amenable to a variety of reactions allowing the preparation of a number of materials useful for device fabrication. In addition to the tunable electronic properties, thiophenes have good chemical and physical stabilities. They are typically stable in various oxidation states and can be readily characterized by many methods. The high polarizability of sulfur atoms in thiophene rings leads to a stabilization of the conjugated chain and to excellent charge transport properties, which are crucial for applications in organic and molecular electronics. Therefore, self-assembly of thiophene derivatives have attracted considerable attention of scientists.

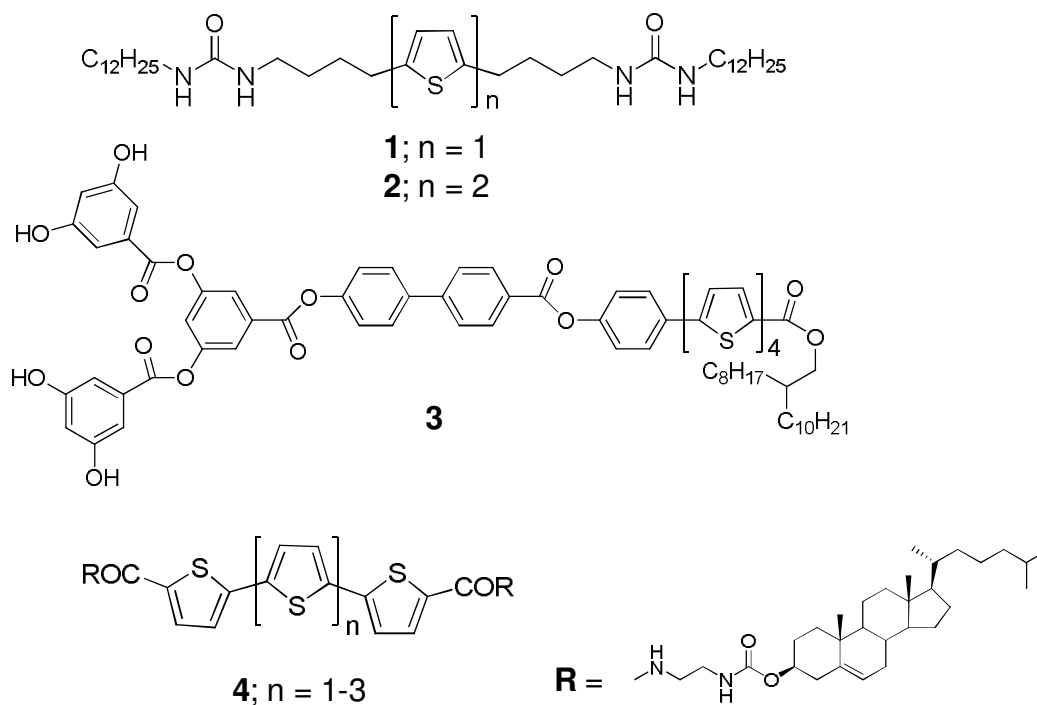


Chart 1.1

One of the early reports on thiophene based gels pertains to the urea appended thiophenes **1-2** (Chart 1.1) [Schoonbeek *et al.* 1999]. The xerogels of **2** exhibits high charge-carrier mobility. The directional self-assembly of the urea moiety and the lamellar packing of the molecules facilitate the intermolecular interaction of the bithiophene moieties resulting in high charge-carrier mobility. Later, Shinkai and co-workers reported that the dendron rod coil molecule (**3**) and the oligo(thiophene) (**4**) gelators show high conductivity [Messmore *et al.* 2004].

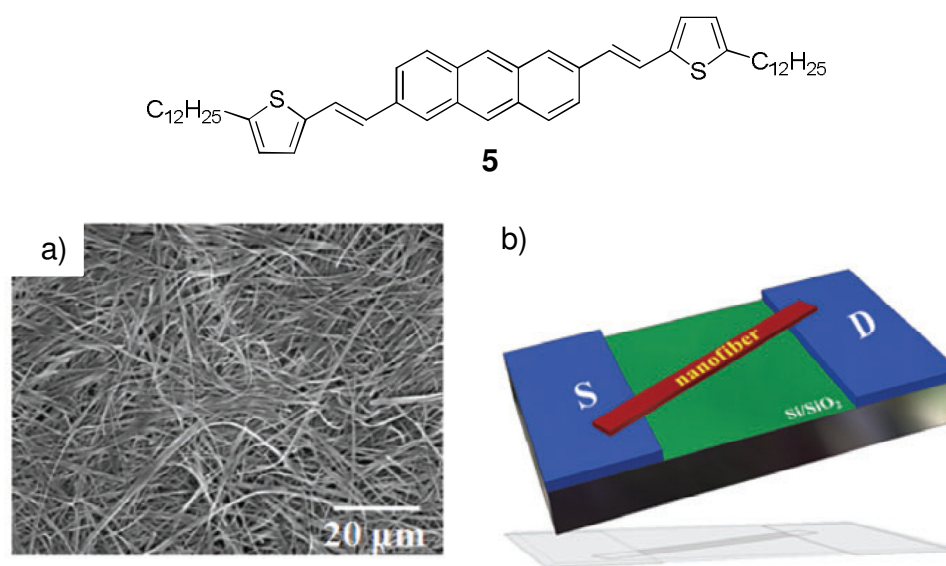


Figure 1.1. a) SEM image of a xerogel of **5**. b) Schematic view of an individual nanofiber transistor of **5** with bottom-contact geometry.

Hong *et al.* have developed high performance organic single nanofiber transistors from the organogelators [Hong *et al.* 2008]. The unique gelation capability of **5** comes from strong π - π stacking interactions between the thienylvinylene anthracene backbones and van der Waals interactions between the long alkyl chains (Figure 1.1). Scanning electron microscopic (SEM) analysis of the xerogel showed three dimensional fibre network structure (Figure 1.1a). Organic thin film transistors (OTFTs) prepared from **5** exhibited p-type characteristics with an estimated hole

mobility of $0.02\text{--}0.05\text{ cm}^2\text{ V}^{-1}\text{ s}^{-1}$ in the saturation region. However, organic single-nanofibre transistors showed field effect mobility of $0.48\text{ cm}^2\text{ V}^{-1}\text{ s}^{-1}$ (Figure 1.1b). These results suggest that 1D single nanofibre of **5** produced through a gelation process has a highly ordered structure and thus provides efficient transport path when compared to a film type transistor. Park and co-workers have reported the semiconducting one-dimensional nanowires (1D NWs) from the fused thiophene derivative **6** (Figure 1.2) [Chung *et al.* 2009]. Detailed UV-vis, AFM and XRD analyses revealed the strong self-assembling capability that leads to the formation of 1D NWs exhibiting a drastic fluorescence emission enhancement upon the formation of NW aggregates. Conducting probe-atomic force microscopy (CP-AFM) and space charge limited current (SCLC) measurements revealed that well-ordered 1D NWs exhibit good current flow along the crystals with effective carrier mobility of up to $3.1\text{ cm}^2\text{ V}^{-1}\text{ s}^{-1}$.

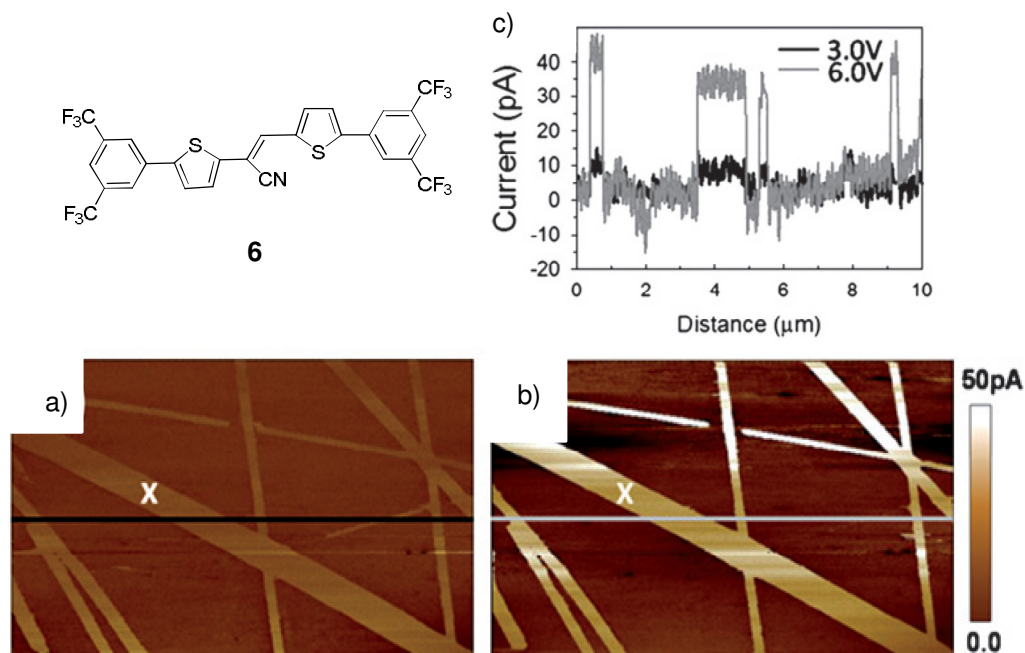


Figure 1.2. CP-AFM current images of the NWs formed by **6** on a SiO_2/Si substrate via drop-casting from a 0.1 wt% chloroform solution at different bias values; $V_{\text{bias}} =$ (a) 3.0 V, and (b) 6.0 V. (c) Current profiles corresponding to the solid lines in (a) and (b).

Recently, Diegelmann *et al.* have reported the compound **7** (Chart 1.2), consisting of a peptide-sequence in which a bithiophene moiety was incorporated by solid phase-supported peptide synthesis approach [Diegelmann *et al.* 2008]. The peptide sequence based on amyloid fibres help the bithiophene moiety to self-assemble into 1D nanostructures under aqueous conditions. However, bithiophene is typically nonconducting without doping. The two other examples of oligothiophene peptide hybrids (**8** and **9**) were introduced by Stupp and co-workers [Stone *et al.* 2009]. These hybrid molecules found to form self-supporting gels in water at low concentrations. Oligothiophene derivatives with four or more repeating units exhibit semiconducting nature without external doping. The organic field effect transistors (OFET) of α -helical polypeptide functionalised thiophene gelator **10** and [6,6]-phenyl-C₆₁-butyric acid methyl ester (PCBM) (1:2) revealed enhanced hole mobility of $1.9 \times 10^{-7} \text{ cm}^2 \text{ V}^{-1} \text{ s}^{-1}$ when compared to that of the corresponding nongelators [Kumar *et al.* 2011].

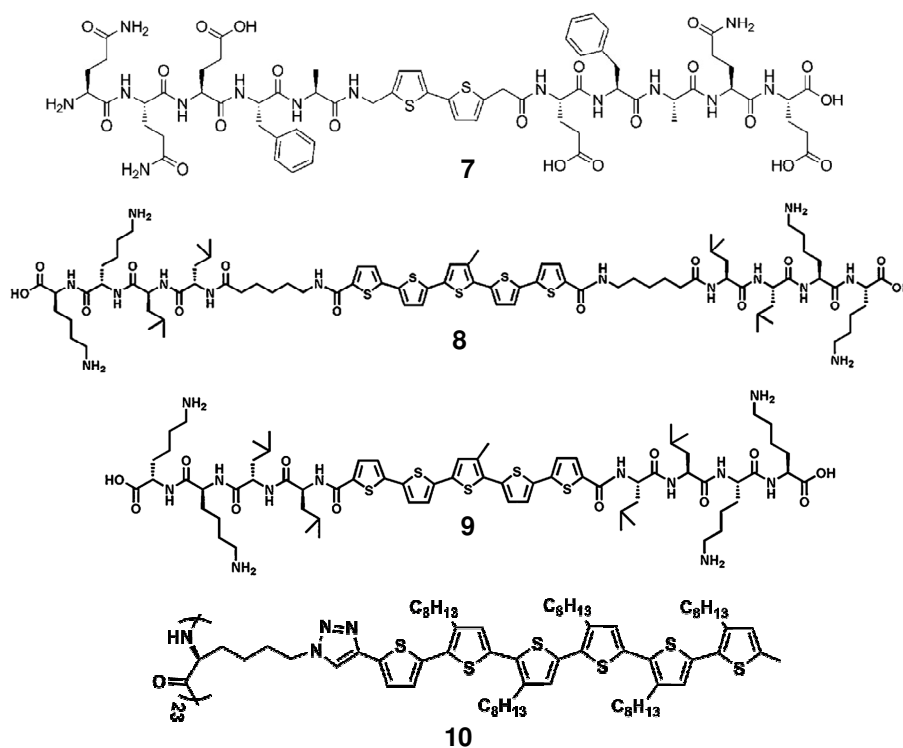


Chart 1.2

Recently, 1, 2-diaminocyclohexane moiety has been used for the self-assembly of sexithiophenes [Tsai *et al.* 2010]. The hairpin-shaped molecule **11** (Figure 1.3) forms organogels in several nonpolar organic solvents. The gels are composed of nanofibres with uniform diameters of 3.0 (\pm 0.3) nm (Figure 1.3c). NMR and spectroscopic studies suggest that the self-assembly is driven by π - π interactions of the sexithiophene moieties and the hydrogen bonding of the amide groups at the head of the hairpin. Field effect transistors (FETs) built with this molecule revealed p-type semiconducting behaviour and higher hole mobilities when films were cast from solvents that promote self-assembly.

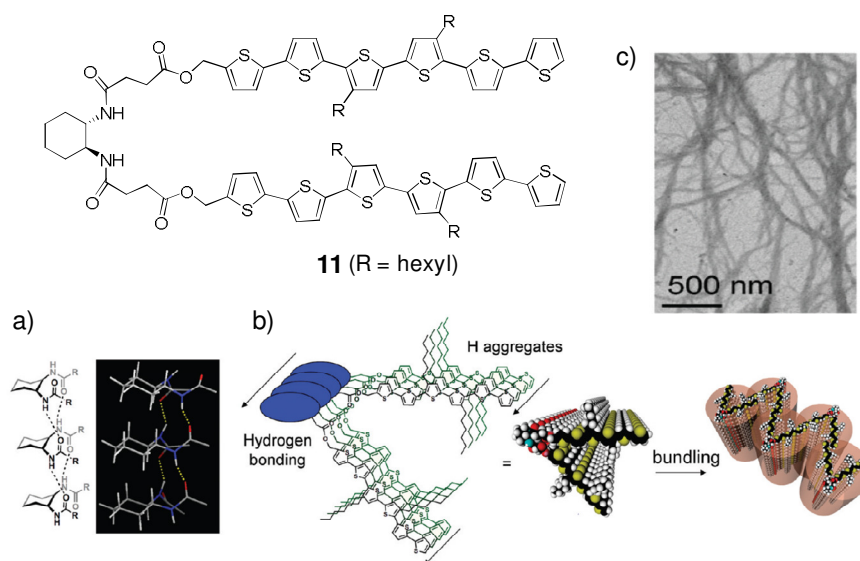


Figure 1.3. a) Hydrogen bonding of the *trans*-1, 2-diaminocyclohexyl groups. b) Self-assembly of molecule by hydrogen bonding of the head groups (in blue) and H aggregates of the sexithiophenes (in green) leading to nanofibres of width about the length of one arm. c) Transmission electron microscopic (TEM) image of the bundled fibres.

Symmetric oligothiophene derivatives containing hydrogen bond forming segments result in conducting organogels consisting of self-assembled 1D nanostructures at low concentrations. Würthner and co-workers have reported the charge transport properties of a trialkoxybenzamide-functionalized quarterthiophene π -

gelator (**12**) (Figure 1.4) [Pratihari *et al.* 2010]. Atomic force microscopic (AFM) analysis showed entangled fibres that are formed with an H-type molecular arrangement due to synergistic effect of hydrogen bonding and π -stacking (Figure 1.4a). The self-assembled fibres were found to gelate numerous organic solvents of diverse polarity. The charge transport ability of such elongated fibres of **12** was studied by the pulse radiolysis-time resolved microwave conductivity (PR-TRMC) technique. The mobility value was found to be $2.9 \times 10^{-3} \text{ cm}^2 \text{ V}^{-1} \text{ s}^{-1}$ at a temperature of 20°C .

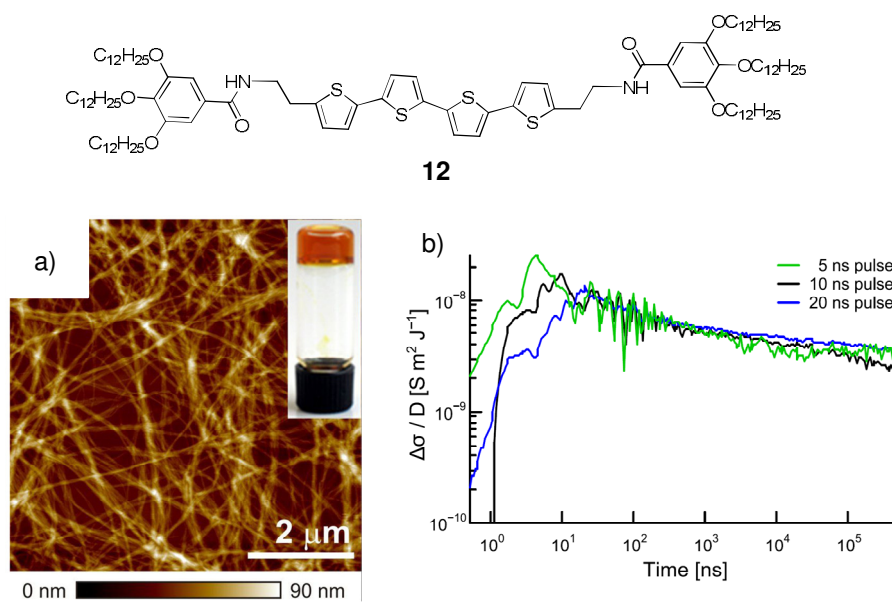


Figure 1.4. a) AFM height images of a film spin-coated from diluted gel solution of **12** in MCH ($2 \times 10^{-3} \text{ M}$) on to HOPG. Inset shows photograph of gel in cyclohexane at 1.5 mM concentration. b) Variation of dose-normalized conductivity transients ($\Delta\sigma/D$) with time for **12**.

Recently, Stupp and co-workers have reported the self-assembly of quarter- and quinquethiophene derivatives (**13** and **14**) into 1D nanostructures in organic solvents (Figure 1.5) [Stone *et al.* 2011]. Both **13** and **14** formed self-supporting gels in several organic solvents. SEM analysis revealed bundled networks consisting of 1D nanostructures extending to several microns in length (Figure 1.5b). The average conductivity value of **14** was found to be $9.9 \pm 1.7 \times 10^{-6} \text{ S/cm}$. In contrast, **13** did not reveal any detectable conductivity (Figure 1.5c).

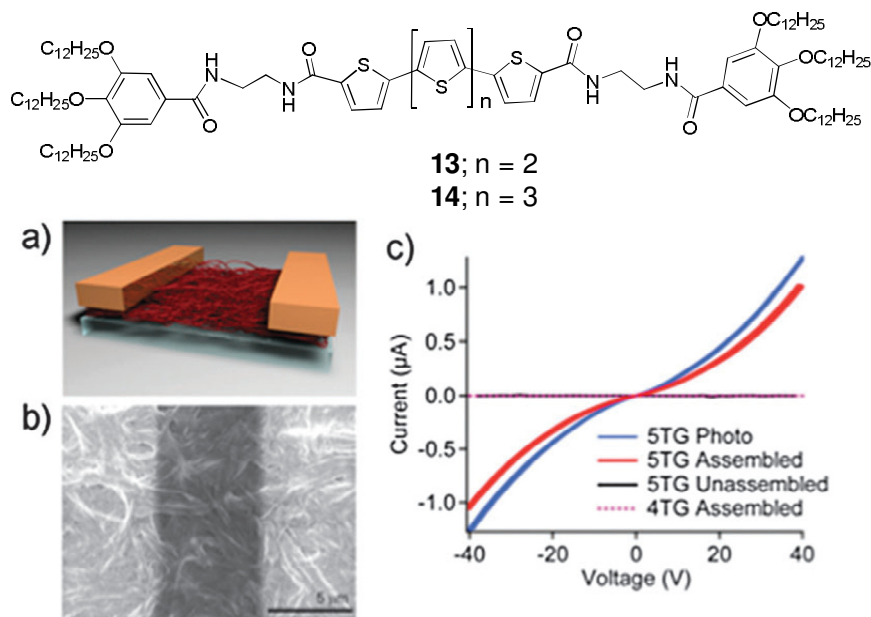


Figure 1.5. a) Schematic of a fabricated device. b) SEM image of a typical device fabricated from **14** showing the gold pads and organic channel. Bundles of self-assembled nanofibres are present throughout the device as seen in the SEM image. c) Representative I - V curves of **13** (4TG) and **14** (5TG) devices.

1.4.2. TTF Derived Organogels

Tetrathiafulvalene (TTF) is known as an organic conductive material whose high electron conductivity is enhanced by π -stacked columnar structures. The first attempt to design self-assembling molecular wires using TTF was reported by Jørgensen and Bechgaard, in which TTF molecules were attached to bis-arborols (**15**), which was found to be an efficient organogelator (Figure 1.6) [Jørgensen *et al.* 1994].

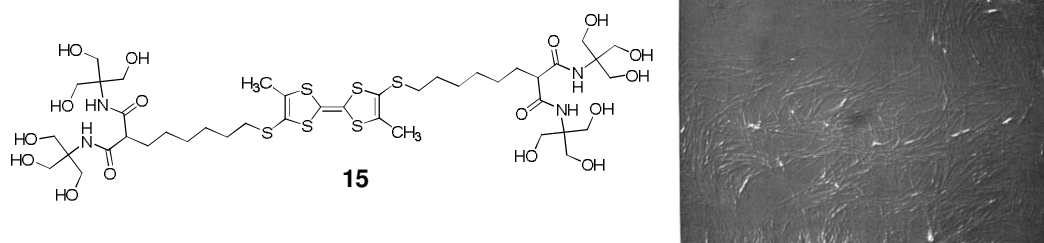


Figure 1.6. Phase contrast microscopic picture of a gel of **15**

Amphiphilic bis-TTF annulated macrocycle derivatives (**16** and **17**) reported by Nakamura and co-workers [Akutagawa *et al.* 2005] form redox active organogels and electrically active nanostructures (Figure 1.7). Detailed AFM analysis showed that organogelator produced nanodot-array structures in Langmuir–Blodgett films, whereas chemically oxidized organogelator formed size-controllable isolated nanodot structures, which were simply fabricated by the spin-coating technique (Figure 1.7b). CP-AFM study revealed the conductance of a single nanodot with an open-shell electronic structure which was four to five orders of magnitude higher than that of fibres of **16** with a closed-shell electronic structure (Figure 1.7d).

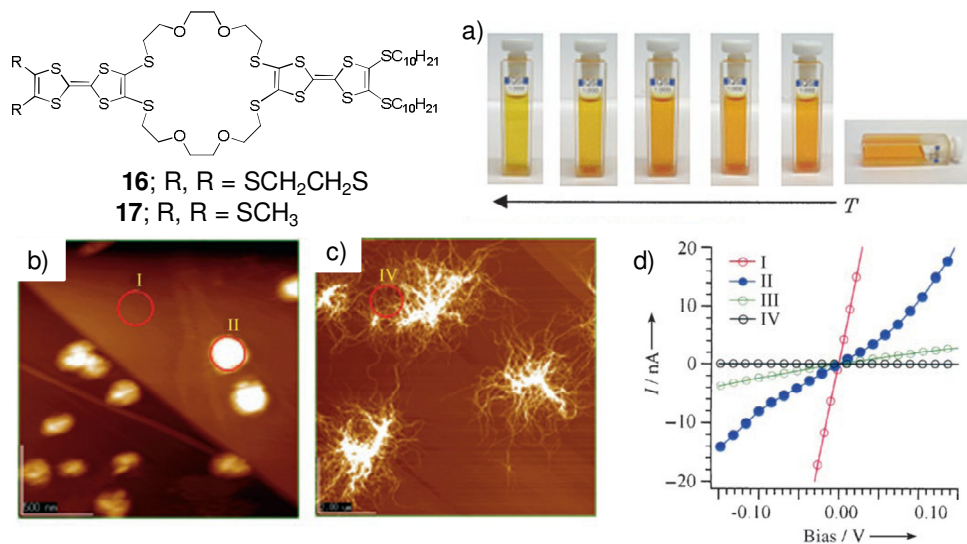


Figure 1.7. a) Temperature dependent organogelation of **16**. A 1 mm solution of **16** in $\text{CHCl}_3/\text{CH}_3\text{CN}$ (6/4) at 333 K was slowly cooled to 298 K. Organogelation was accompanied by a color change from yellow ($T = 333\text{ K}$) to orange ($T = 298\text{ K}$). AFM image of b) nanodots of **16** and c) fibrous structure of **16** on HOPG for CP-AFM measurements. d) I - V characteristics at points I (HOPG), II (single nanodot in air), III (single nanodot), and IV (bundle of fibres). DC bias was applied from -0.2 to 0.2 V.

Since hydrogen bonding is highly effective for self-assembly, the introduction of an amide group into a TTF unit is an efficient means of constructing conducting nanofibres. Kitahara *et al.* have demonstrated the formation of one-dimensional

columnar structure of a low molecular-weight gel system (**18**), which is useful as a potential strategy for the construction of TTF nanowires (Figure 1.8) [Kitahara *et al.* 2005]. TEM images showed the formation of one dimensional wire-like superstructures at low concentration (Figure 1.8b). On the other hand, the self-assembled TTF fibres are aligned on the surface at high concentration (Figure 1.8c). UV-vis-NIR absorption spectral analysis revealed characteristic absorption bands at 850 and 1750 nm upon iodine doping.

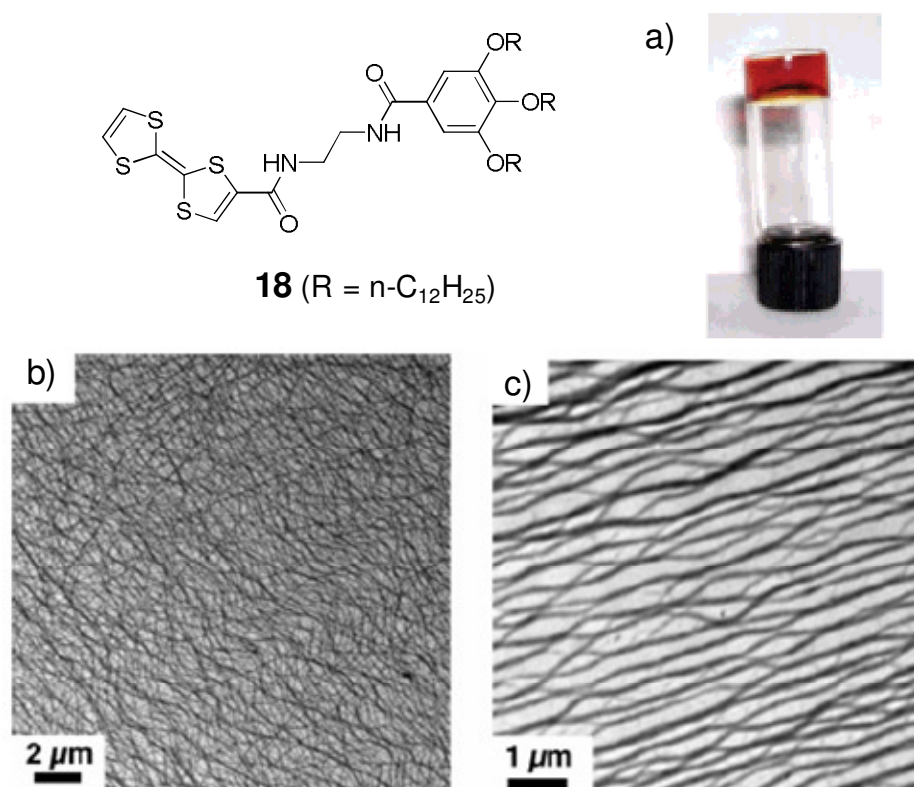


Figure 1.8. a) Photograph of the transparent gel prepared from **18** with hexane. TEM images of the hexane gel of **18**; the samples were prepared at b) 50 g dm⁻³ and c) at 100 g dm⁻³.

Kato and co-workers have reported the amino acid derivative **19** which forms fibrous aggregates through hydrogen bonding in liquid crystals (Figure 1.9) [Kitamura *et al.* 2005]. The homogeneously oriented smectic A phase facilitates the alignment of

fibres. The doping of fibres of **19** with iodine immediately increased the conductivity from 3×10^{-10} S/cm to 3.0×10^{-7} S/cm without the destruction of the fibre morphology.

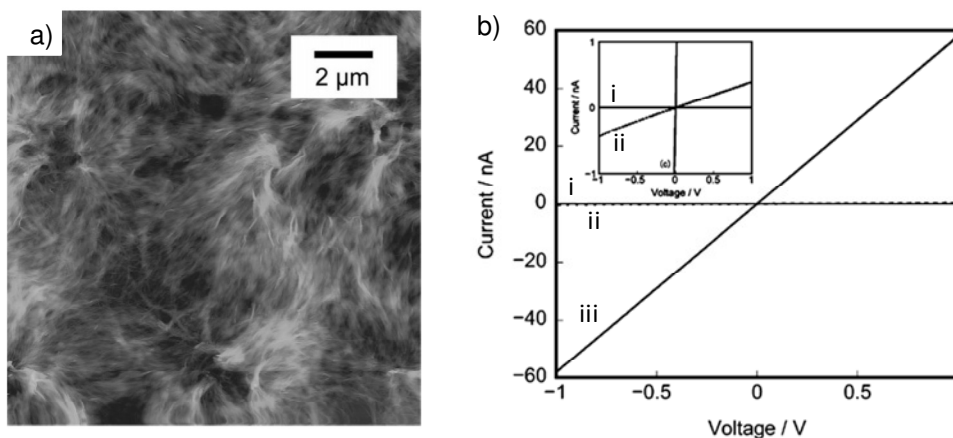
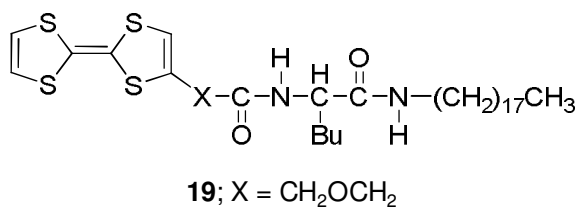


Figure 1.9. a) AFM image of fibrous aggregates of **19**. b) Current-voltage characteristics for fibrous aggregates of **19** before and after iodine-doping for 2 min: (i) before doping, (ii) immediately after doping, and (iii) 1 week after doping.

Simple TTF derivatives with a long alkyl chain self-aggregate into a 1D columnar structure owing to π - π and van der Waals interactions. Thus, the amphiphilic diesters **20** and **21** form gels from hexane, cyclohexane, decaline and diethyl ether solutions [Honna *et al.* 2010]. A scheme for the stacking and the assembly of TTF derivatives are shown in Figure 1.10. The stacked molecule upon oxidation gives a mixed valence state leading to conducting nanostructures. The compressed pellet of **20** showed an electrical conductivity of $\sigma = 2 \times 10^{-5}$ S/cm with iodine doping. When iodine vapor is removed by standing in the air, the doped pellet becomes an insulator. This on-off switching procedure can be repeated several times.

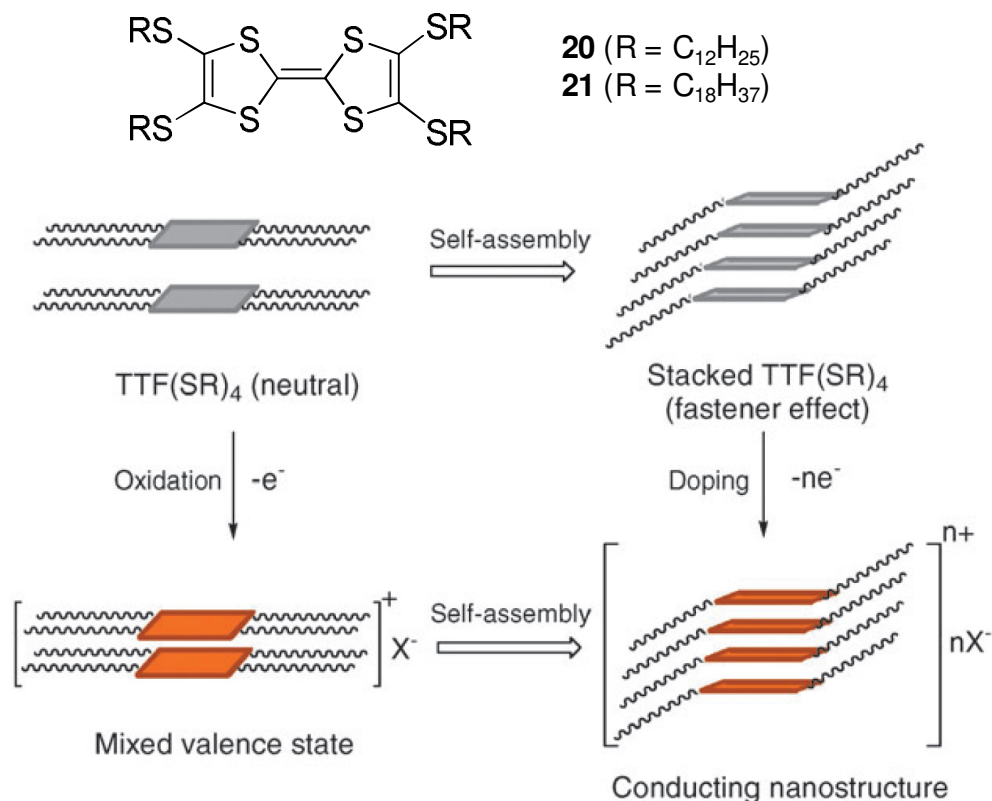


Figure 1.10. Stacking of TTF derivative having long alkylthio chains

Superstructures composed of nanofibres and nanoparticles have also been fabricated from a hybrid gel of **22** with 1 wt% TTF-capped gold nanoparticles (**23** and **24**) (Chart 1.3) [Puigmartí-Luis *et al.* 2008]. Exposure of the xerogel to iodine vapour resulted in conducting nanofibres. **23** and **24** showed a fairly high electric conductivity of 10 S/cm, as determined by CP-AFM. On the other hand, the doped hybrid gel of **22** and **24** revealed an inhomogeneous surface, as determined by CP-AFM, that showed different conductivities. Thus, the addition of only 1 wt% Au-nanoparticles induced the formation of a metallic phase, which has been observed after annealing the xerogel of **23**. Formation of supramolecular electroactive organogel from a C₃-symmetric tris-TTF derivative (**25**) was demonstrated by Amabilino and co-workers (Chart 1.3) [Danila *et al.* 2009]. Detailed gelation studies revealed that the thioalkyl substituents on the TTF units form a moderate organogel in chlorinated solvents, but stable gel in ortho-

dichlorobenzene. Xerogel showed complex network of small as well as thick straight fibres. Doping of the xerogel induced a charge transfer, without any change in the gel morphology, or in its supramolecular organization. CP- AFM studies revealed that the doped xerogel exhibited semiconducting behavior, with the large fibres being more conductive than the finer ones.

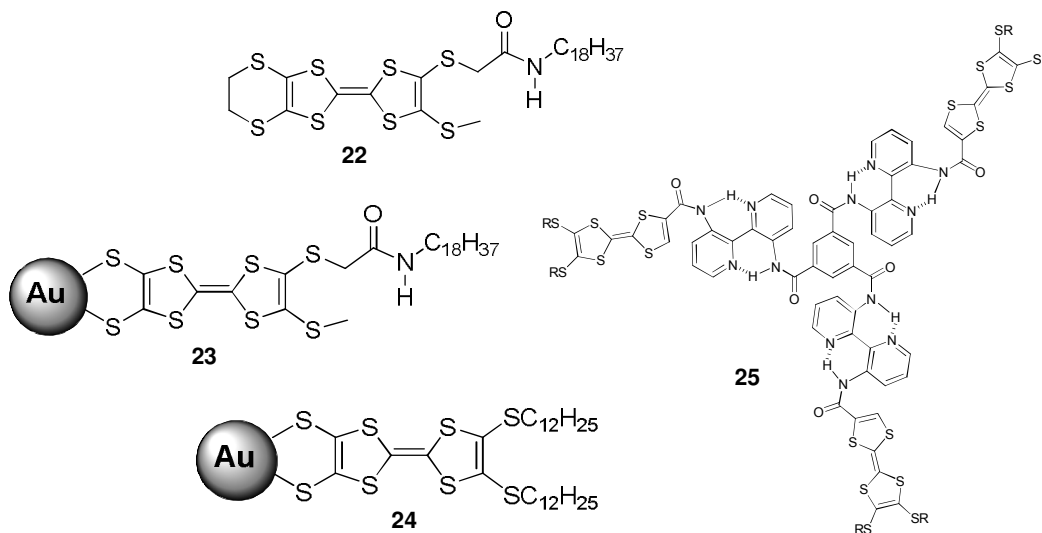


Chart 1.3

The organogelators **26** and **27** having one and two electroactive TTF residues respectively (Figure 1.11), reported by Wang *et al.* can gelate a variety of organic solvents [Wang *et al.* 2011]. Compounds **27** with two TTF subunits exhibited higher gel stability when compared to the gelator **26**. Detailed FE-SEM studies showed fibrillar aggregates with entangled three dimensional network structures (Figure 1.11a and 1.11b). Upon oxidization by iodine, these xerogels showed semiconductive behaviour. The columnar TTF cores stacked as fibres could provide an efficient pathway for the electron conduction as evidenced by the polaron absorption at around 2000 nm. Additionally, the electrical conductivity of the doped-xerogel of **27** was found one order of magnitude higher than that of **26** under identical conditions (Figure 1.11c).

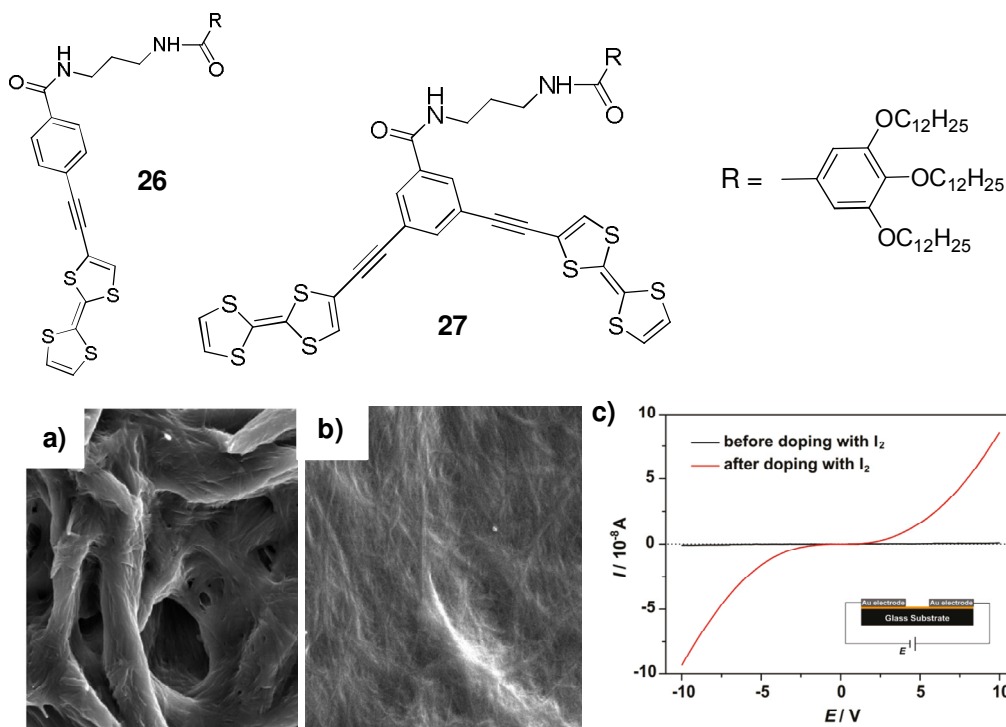


Figure 1.11. FE-SEM images obtained from air-dried gels of **26** (a) and **27** (b) from toluene. c) *I*-*V* curves measured on xerogel **27** prepared from toluene before and after doping with I_2 , respectively. The inset in Figure c is a schematic representation of a top-contact device.

1.4.3. Diacetylene Derived Organogels

In recent years there has been considerable interest in the self-assembly of diacetylene derivatives as they allow the covalent fixation of supramolecular assemblies through photopolymerization reactions to give polydiacetylenes (Figure 1.12), which are attractive candidates as conducting nanowires. Gel forming diacetylenes are particularly interesting because the gel network which is stabilized by the non-covalent interactions can be permanently supported by strong covalent bonds under photolytic conditions, thereby retaining the morphological characteristics with increased thermal stability.

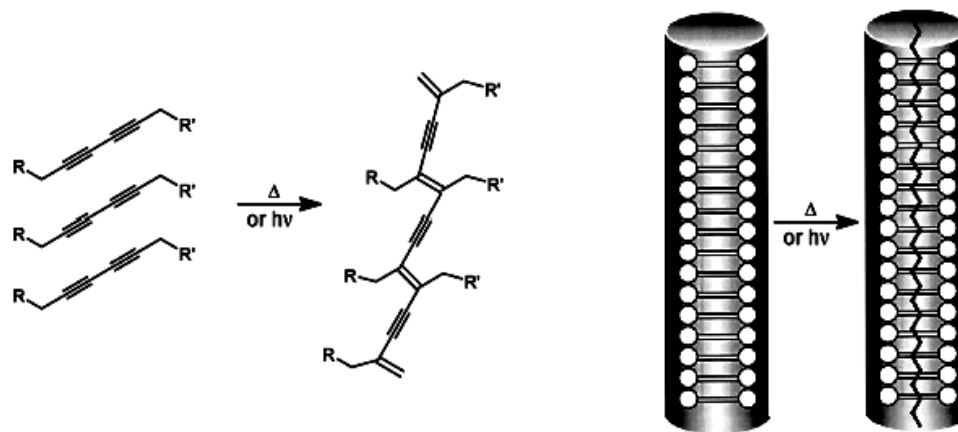


Figure 1.12. Photopolymerization of diacetylenes to polydiacetylenes and the schematic representation of the concept of covalent fixation of diacetylenes derived self-assemblies.

Hydrogen bonded fibre forming molecules bearing rod-shaped fluorinated mesogens are known (Figure 1.13) [Yoshio *et al.* 2009]. The compound (**28**) having laterally fluorinated aromatic mesogens connected through amides exhibits well aligned fibrous aggregates under alternating current electric field (1.0 V/ μm , 1 kHz) in dodecylbenzene (Figure 1.13a). In contrast, randomly entangled fibres were formed in the solvent without electric field (Figure 1.13b).

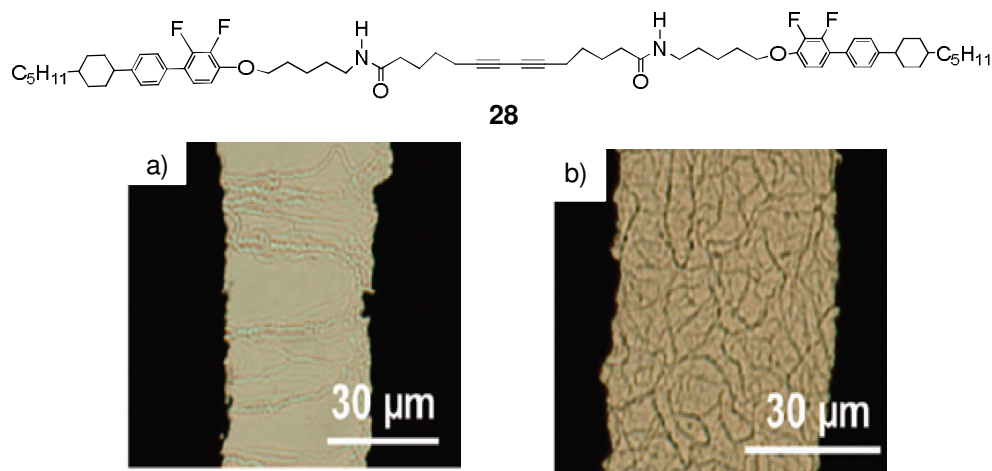


Figure 1.13. Optical micrographs of the fibrous aggregates observed for the dodecylbenzene gel of **28** (8 mM): (a) aligned fibres formed under an AC electric field; (b) randomly entangled fibres without an electric field.

Tamaoki *et al.* have reported the diacetylene-1-glucosamide bolaamphiphiles (Chart 1.4) (**29** and **30**), which self-assemble to form nanofibres leading to the gelation of organic solvents [Tamaoki *et al.* 2000]. The diacetylene dicholesteryl ester derivative (**31**) having urethane linkages has been polymerized in the organogel state to form nanowires. Photopolymerization of 10,12-pentacosadiynoic acid derived organogelators **32** with conjugated diyene units has been reported by Weiss and co-workers [George *et al.* 2003]. 1,2-Aminocyclohexyl derivative (**33**) has also been polymerized in the gel network, by incorporating diacetylene linkages to the alkyl side chains [De Loos *et al.* 1997]. Shinkai and co-workers have reported polydiacetylene based conducting nanofibres from a low molecular weight gelator (**34**) [Fujita *et al.* 2007]. The gelator consists of two trialkoxybenzoic acid connected to a diacetylene group on both ends through a flexible alkyl chain containing two amide groups.

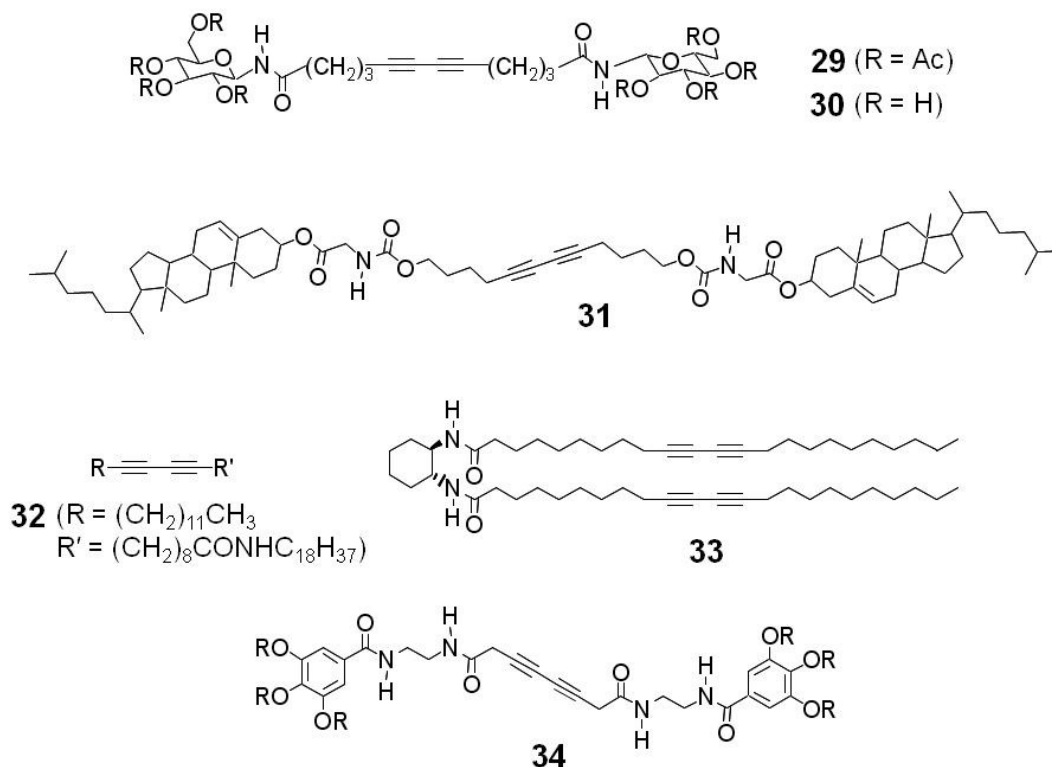


Chart 1.4

1.4.4. Hexabenzocoronene Derived Organogels

Polycyclic aromatic hydrocarbons (PAHs) are considered as one of the promising components for molecular electronics because of their strong tendency to form one-dimensional columnar structures via π -stacking interactions. Unidirectionally assembled PAHs have been shown to exhibit anisotropic charge and energy transport activities. A representative example of PAHs includes hexa-*peri*-hexabenzocoronene (HBC), which consists of thirteen fused benzene rings. Self-assembly and gelation of HBCs result in ordered nanostructures with one-dimensional charge transport properties.

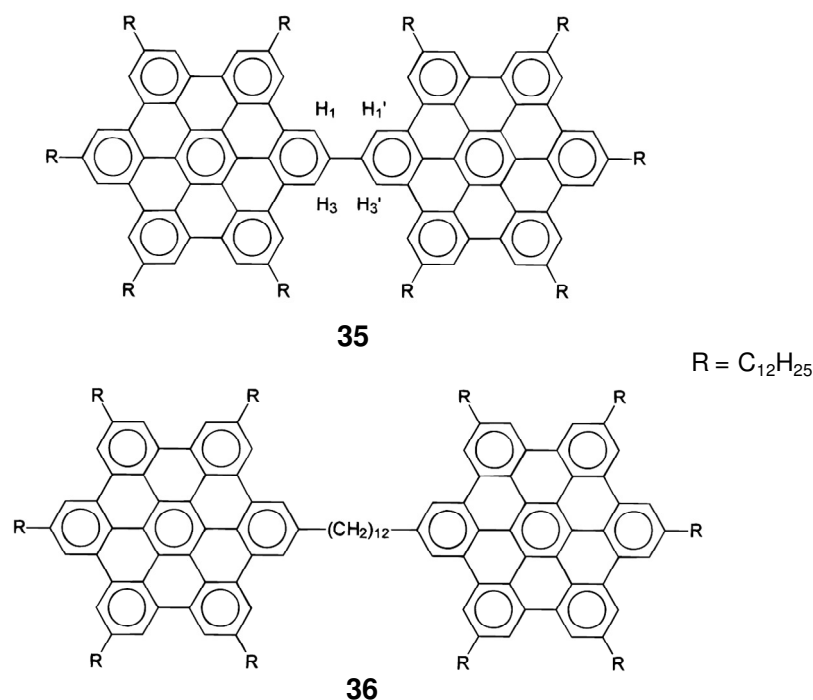


Chart 1.5

First report of the gelation of alkyl substituted bis HBC derivatives (**35** and **36**) was from Müllen's group (Chart 1.5) [Ito *et al.* 2000]. Both **35** and **36** form liquid crystalline phases. Interestingly, in the case of **36**, a highly ordered columnar structure with a hexagonal superstructure could be observed. Optical studies revealed a strong

intermolecular interaction of the aromatic cores of **35**, in contrast to **36**, where only weak intermolecular interactions could be observed. These materials exhibited redox properties by doping with alkali metal ions.

Aida and co-workers have also made significant contribution to the self-assembly of HBC derivatives. For example, they have reported the formation of nanotubes of an amphiphilic derivative (**37**) from THF solution. These nanotubes showed an aspect ratio greater than 1000 and are 14 nm wide (Figure 1.14) [Hill *et al.* 2004]. The walls of the tubes consist of helical arrays of π -stacked coronenes covered by hydrophilic glycol chains. Interestingly, an individual nanotube could be positioned across Pt nanogap electrodes (180 nm) on a SiO_2 substrate. The tube was essentially insulating, however, after oxidation with nitrosonium tetrafluoroborate (NOBF_4) it showed an I - V profile with an ohmic behaviour having a resistance of 2.5 megaohm ($\text{M}\Omega$) at 285 K. This value is comparable to inorganic semiconductor nanotubes.

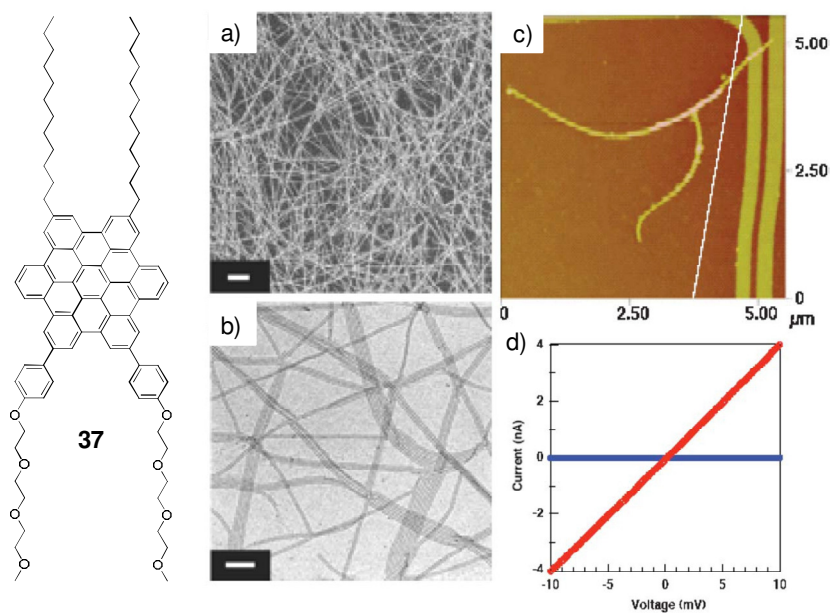


Figure 1.14. a,b) TEM images of **37** which forms tubes that can be placed between two electrodes. c) Tapping-mode AFM image of the nanotube of **37** on two-probe electrodes with a 180 nm gap (taken after the conductivity measurements). d) I - V profiles of unoxidized (blue circles) and oxidized (red circles) single nanotube at 285 K.

Graphitic nanotubes and gels composed of the chiral HBC amphiphile (**38**) can be readily obtained by self-assembly, where majority of the nanotubes are aligned unidirectionally along the fibre axis (Figure 1.15) [Yamamoto *et al.* 2006]. Although these nanotubes were essentially insulating, they showed semiconducting behavior upon treatment with NOBF_4 in acetonitrile, with a resistivity of $2.5 \text{ M}\Omega$ at 285 K . The resistivities of a bundled fibre along (ρ_{\parallel}) and across (ρ_{\perp}) were quite different upon exposure to I_2 vapor ($\rho_{\parallel} = 20 \text{ }\Omega\text{cm}$ and $\rho_{\perp} = 280 \text{ }\Omega\text{cm}$, 300 K) owing to a long-range intermolecular electronic communication through the graphite-like molecular arrays. Anisotropic conduction in the fibre was also confirmed by FP-TRMC measurements (Figure 1.15b).

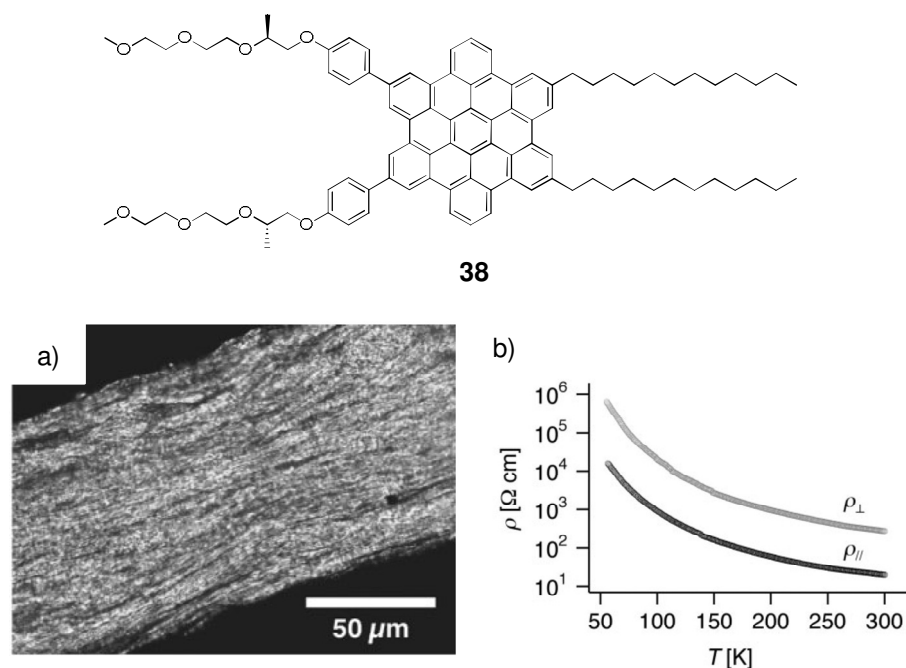


Figure 1.15. a) A polarized optical microscopy image of a macroscopic fibre consisting of bundled nanotubes of **38**. b) Temperature dependencies of its resistivities along (ρ_{\parallel}) and across (ρ_{\perp}) the fibre axis.

Recently, Aida and co-workers have reported the self-assembly and photovoltaic properties of C_{60} -appended amphiphilic HBC, which forms coaxial nanotubes with a π -stacked HBC array covered by a molecular layer of C_{60} (Figure 1.16) [Yamamoto *et al.*

2009]. The FE charge-carrier mobility measurements of the nanotube formed by **39** containing long, paraffinic side chains at one end and triethylene glycol containing C₆₀ at the other end revealed an ambipolar hole mobility (μ_h) of $9.7 \times 10^{-7} \text{ cm}^2 \text{ V}^{-1} \text{ s}^{-1}$ and electron mobility (μ_e) of $1.1 \times 10^{-5} \text{ cm}^2 \text{ V}^{-1} \text{ s}^{-1}$. The nanotubes resulting from the co-assembly with HBC derivative **40** without C₆₀ showed a nonlinear relation in the values of μ_e and μ_h with the nanotube composition. The advantage of the co-assembly is the possibility to optimize the p-n heterojunction and ambipolar carrier transport properties, thereby enhancing the open-circuit voltage in the photovoltaic output.

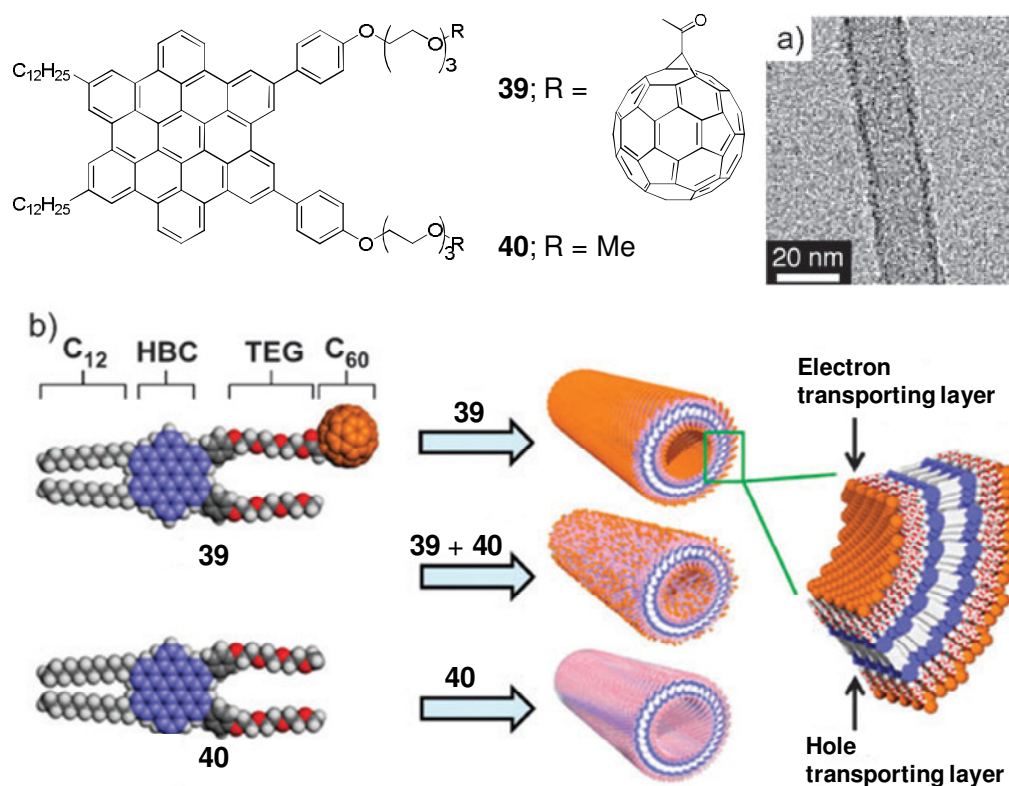


Figure 1.16. a) TEM micrograph of air-dried toluene suspension of the coassembled nanotubes with 25% of **39**. (b) Schematic representation of the formation of homotropic and co-assembled nanotubes of **39** and **40** and the wall structure of the nanotube of **39** containing an electron transporting molecular layer of clustered C₆₀ (orange) and a hole transporting graphite-like layer of π -stacked HBC units (blue).

The co-assembled nanotube with 10 M% of **39** showed an intra-tubular hole mobility of $2.0 \text{ cm}^2 \text{ V}^{-1} \text{ s}^{-1}$, closer to the inter-sheet mobility in graphite measured by FP-TRMC. The photovoltaic studies also indicated the importance of a small content of **39** in achieving the largest short-circuit current (I_{sc}), open-circuit voltage (V_{oc}) and largest incident photon-to-current conversion efficiency (IPCE, 2%) in the co-assembled nanotube. This study reveals that the co-assembly approach of the two amphiphiles **39** and **40** can control the performance of the system by balancing the hole and electron transporting molecular components.

1.4.5. Porphyrin Derived Organogels

Shinkai and co-workers have reported that the gelation ability of Zn(II) porphyrin–appended cholesterol derivatives could be enhanced by fullerene interaction [Ishi-i *et al.* 2000]. UV-vis and gelation studies have revealed that the gelation of **41** ($2.55 \times 10^{-2} \text{ mol dm}^{-3}$) occurs at 20 °C in toluene only in the presence of C_{60} . The sorbet absorption band was shifted bathochromically. This observation indicates that an intermolecular electronic interaction does exist between the Zn(II) porphyrin and the fullerene chromophores in the gel phase. However, **41** was not gelled even in the presence of C_{60} at low concentration. This observation implies that the Zn(II) porphyrin–fullerene interaction is very weak in the solution phase. SEM picture of the xerogel, which was obtained from **41** in benzene showed fibrous structures (Figure 1.17).

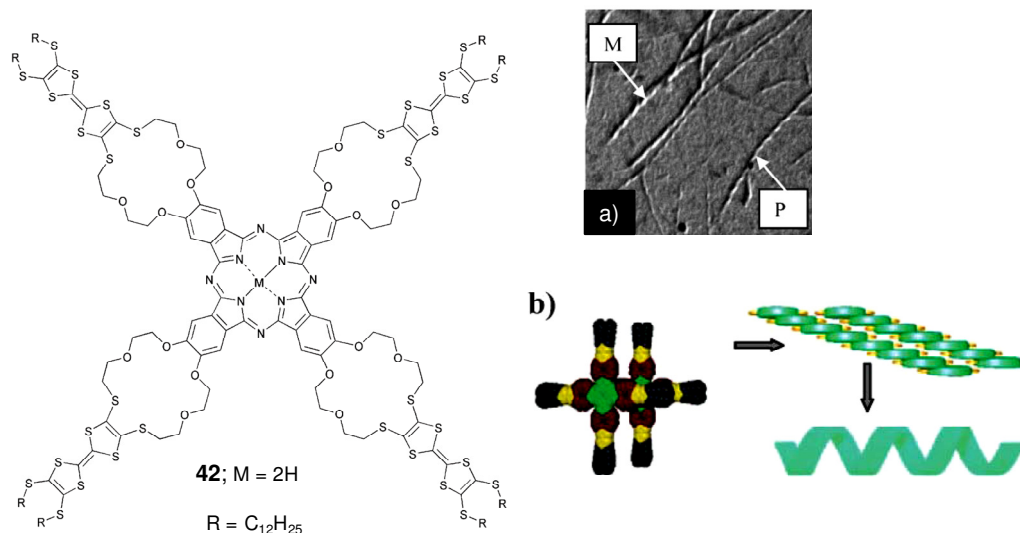


Figure 1.18. Structure of tetra(thiafulvalene)-functionalized crown ether phthalocyanine **42**. a) TEM image of the tapes formed by **42**, showing an equal distribution of both M- and P-helical structures (bar represents 200 nm). b) Schematic representation of the aggregation mechanism of **42**, showing the dominating Pc–TTF and TTF–TTF interactions, which result in an initial bilayer structure that scrolls into helical tapes.

Shinkai and co-workers have synthesized the amide-appended porphyrin organogelators **43** and **44** which showed competition between H vs J aggregation mode of the porphyrin in the gel assemblies (Chart 1.6) [Shirakawa *et al.* 2003]. Appropriate positioning of the peripheral H-bonding motifs could facilitate the formation of one of the aggregates preferentially. The gelators **43** and **44** are substituted with amide groups at the 4-position and 3,5-positions of the meso-phenyl groups, respectively. X-ray analysis of the single crystals established that the porphyrins in **43** adopt the H-aggregation mode of **43** resulting in columnar stacks, whereas the molecule **44** adopt the J-aggregation mode resulting in two-dimensional planar assemblies. UV-vis absorption, XRD and SEM measurements established that the organization modes of the porphyrin in the gel state of **43** and **44** are similar to the respective single crystals. SEM analysis of the cyclohexane gels of **43** and **44** revealed one-dimensional fibrillar and two dimensional sheet like structures, indicating that the difference in the microscopic hydrogen bonded

organization of the porphyrin chromophores are expressed even at the macroscopic morphology.

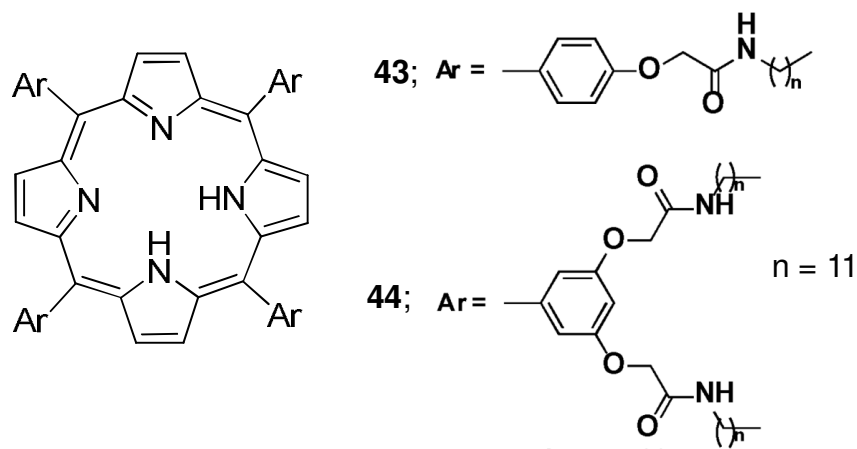


Chart 1.6

The porphyrin derivative **44** can self-assemble to one-dimensional multicapsular structures in the presence of C_{60} due to the cooperative effect of the strong C_{60} -porphyrin interactions and inter- and intra capsular H-bonding interaction between the amide groups, which is entirely different from that of the two dimensional J-type aggregates in the absence of C_{60} . Detailed UV-vis absorption, elemental analysis, XRD, ATR-IR and computer modelling studies have shown that four amide groups from two adjacent porphyrins form a circular H-bonding array, which can encapsulate a C_{60} molecule to give a 1:2 complex. These ‘capsules’ will further grow into a one-dimensional assembly through intercapsular H-bonding interaction between amide groups on the other side of the complex. SEM and TEM analysis showed a gradual change from the sheet like morphology to a fibrous network on increasing the concentration of C_{60} from 0-0.5 equivalents, which clearly support the one-dimensional aggregation mode (Figure 1.19). The complete quenching of fluorescence of one-dimensional multicapsular structure indicated electron transfer between the porphyrin ‘walls’ and the encapsulated C_{60} .

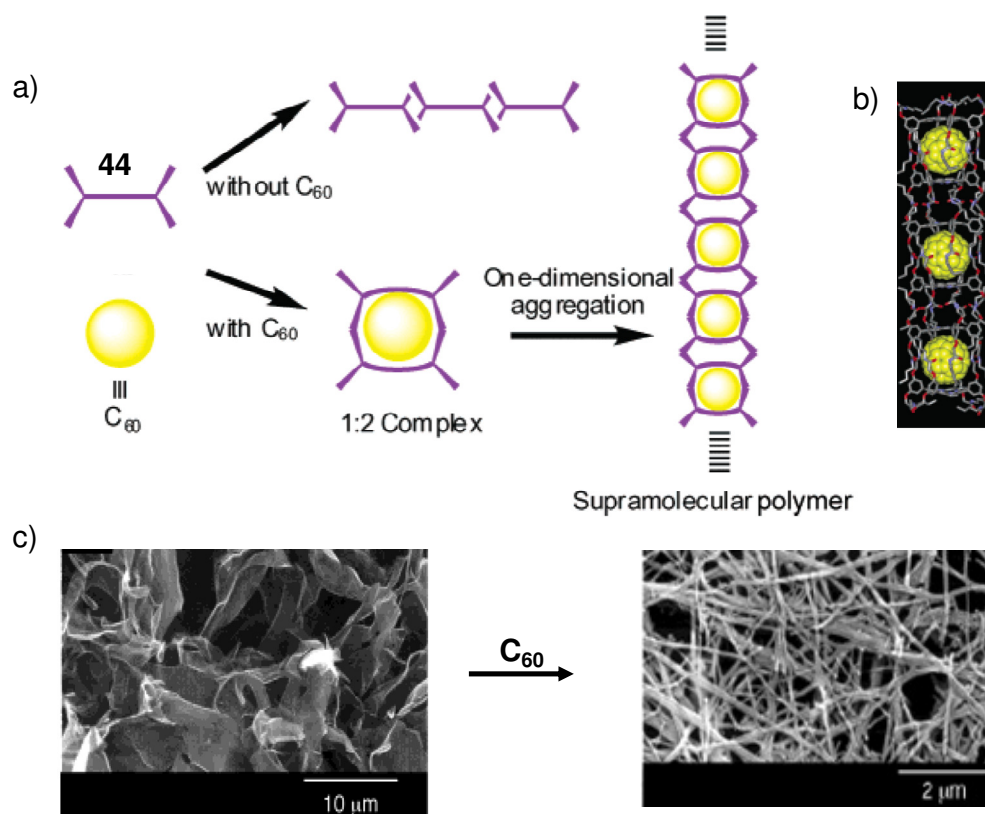


Figure 1.19. a) Aggregation mode of **44**. b) Side view of the energy minimized structure of $(C_{60})_3(44)_6$. c) SEM images showing the morphological changes of the benzene gels of **44** on adding fullerenes.

1.5. n-Type Semiconducting Organogels

A common strategy in the design of n-type organic semiconductors is the substitution of the molecule with electron deficient moieties such as fluorine, cyano groups, carbonyls and imine nitrogens. Among these moieties, aromatic molecules containing imine nitrogens are of increasing interest in the development of n-type semiconductors. Incorporation of imine nitrogens into ladder-type conjugated oligomers can result in: (i) an increase in electron affinity, (ii) enhancement in the propensity of π -stacking, (iii) ability to tune the electronic and optoelectronic properties by protonation or metal ion complexation and (iv) a substantial improvement in photo-oxidative stability of the molecules. Experimental and theoretical studies have shown that

heteroaromatic rings containing imine nitrogens have higher reduction potential when compared to similar hydrocarbons. Theoretical studies have shown that linear expansion of size in such imine nitrogen-containing polycyclic molecules is beneficial towards increasing the reduction potential and reducing the intrinsic energy barriers and trapping centers that cause low carrier mobility. Examples of such an extension of the size of π -conjugated polycyclic molecules and incorporation of imine nitrogens to increase the reduction potentials include core-expanded perylene bisimides, naphthalene bisimides and bisphenazine derivatives.

1.5.1. Perylene Bisimide Derived Organogels

Perylene bisimides are one of the well studied classes of dyes for optoelectronic applications because of their promising optical properties such as the strong absorption in the visible range, high fluorescence quantum yields (almost 100%) as well as its high stability towards photooxidation. In addition, perylene bisimides feature a relatively low reduction potential, which enables them to act as an electron acceptor in photoinduced charge transfer reactions.

Shinkai and co-workers have reported the first cholesterol functionalized perylene bisimide organogelator (**45**) (Figure 1.20) which exhibits cascade energy transfer and electron transfer processes [Sugiyasu *et al.* 2004; Sugiyasu *et al.* 2008]. SEM studies have suggested the formation of well-defined fibrous aggregates through π - π stacking and intermolecular hydrogen bonding between the constituent PBI molecules (Figure 1.20b). These gels showed broad UV-vis absorption and inferior emission properties when compared to solutions of the monomeric dyes. The gelator also showed efficient electron transfer in organic solar cells upon mixing with p-type organic semiconductors.

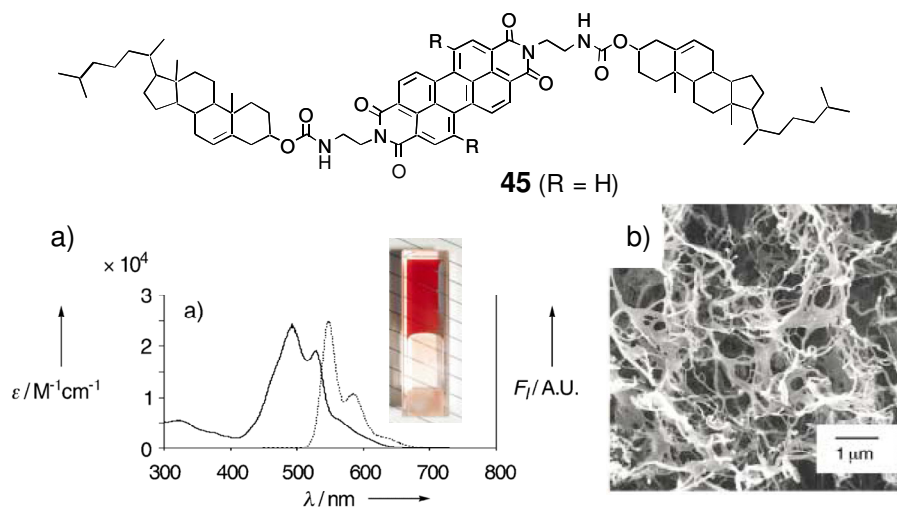


Figure 1.20. a) Absorption (—) and fluorescence (.....) spectra of the molecule **45** gel; [**45**] = 0.2 wt/vol% (1.5 mm), $\lambda_{\text{ex}} = 457$ nm. Inset shows photo of the gel of **45**. b) SEM image of the gel.

The n-type semiconducting perylene bisimide dye **46** synthesized by Würthner and co-workers forms gels in a broad variety of organic solvents to afford well-defined nano- and mesoscopic helical fibres and bundles (Figure 1.21) [Li *et al.* 2006]. PR-TRMC of **46** in the solid state revealed that the sum of the electron and hole mobility is $\Sigma_{\mu\text{TRMC}} = 0.052 \text{ cm}^2 \text{ V}^{-1} \text{ s}^{-1}$. This value is significantly higher than the values measured with similar type of compounds.

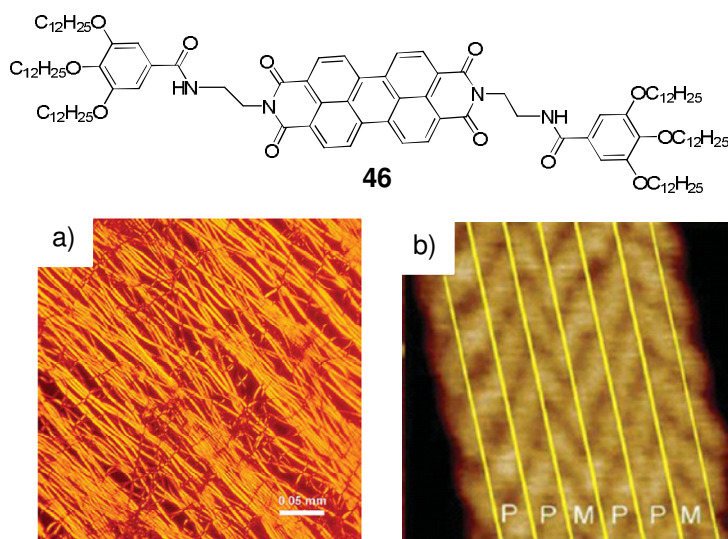


Figure 1.21. a) Optical polarizing microscopic image of **46**. b) AFM height images of films spin-coated from diluted gel solutions of **46** in toluene (zoomed region image).

Recently, Krieg *et al.* have reported the synthesis of the supramolecular gel for **47** based on a perylene diimide dye (Figure 1.22) [Krieg *et al.* 2009]. This molecule self-assembles in aqueous media into extended supramolecular fibres that form a robust three-dimensional network resulting in gelation. The self-assembled systems were characterized by cryo-TEM, cryo-SEM, and rheological measurements. This supramolecular gel shows robustness and multiple stimuli-responsiveness. Detailed studies have revealed that the molecule undergoes reduction in water with sodium dithionite to produce an aromatic dianion. The dianion is stable for months in deoxygenated aqueous solutions, in contrast to other known aromatic dianions which readily react with water. Such stability is due to extensive electron delocalization and the aromatic character of the dianion. The dianion reacts with oxygen to restore the parent neutral compound, which can be reduced again in an inert atmosphere with sodium dithionite to give the dianion. Such reversible charging renders PDIs useful for controlled electron storage and release in aqueous media. Simple preparation of the dianion, reversible charging, high photoredox power, and stability in water can lead to development of new photofunctional and electron transfer systems in the aqueous phase.

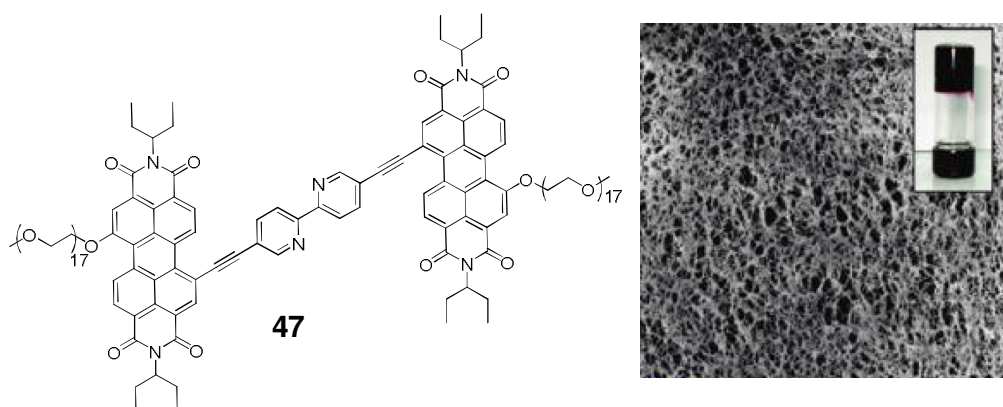


Figure 1.22. Cryo-SEM images of the gel of **47** (8×10^{-3} M, water/THF mixture (80:20), scale. 0.5 μm). Inset: vial inversion test.

Kelly and co-workers have reported the nematic liquid crystal (LC) gels useful for the design of organic solar cells. The compound **48** is a reactive mesogen, which forms a nematic phase at room temperature on cooling (Chart 1.7) [Carrasco-Orozco *et al.* 2006]. The non-polymerizable LC, **49**, has the same aromatic core as **48** and retains a metastable nematic phase in a thin film for extended periods at room temperature, although the T_g is lower. Gel was formed by mixing the LCs **49** and **50** in the ratio 1:2 by weight. LC gel forms a surface with nanometer-sized grooves with a large interface area by AFM images. Photoinduced absorption shows large signals from hole and electron polarons in the blends (**48/50**), confirming the charge separation. A photovoltaic cell constructed based on this system exhibited a monochromatic power conversion efficiency of 0.6% at an incident intensity of 45 mWcm^{-2} .

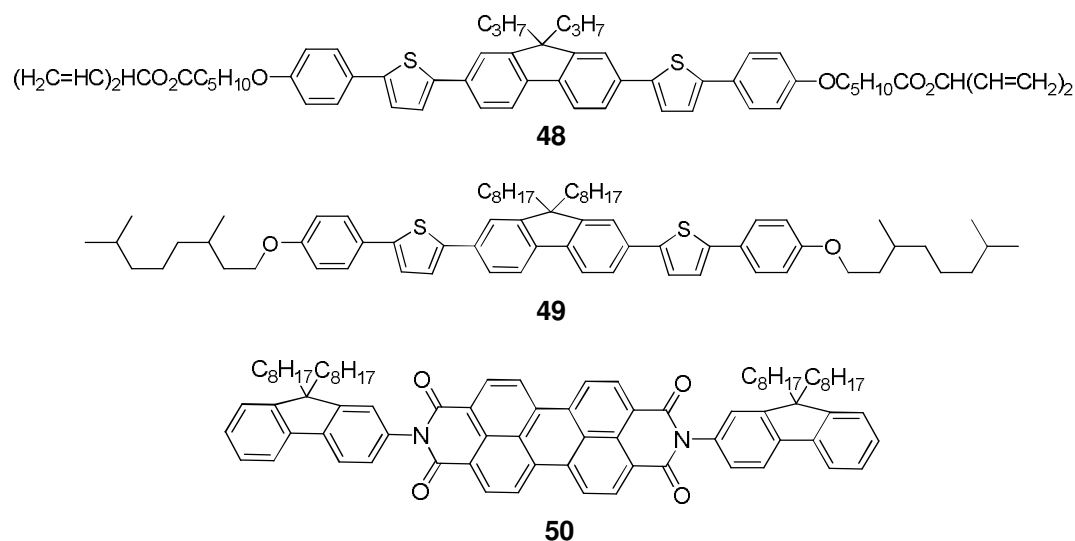


Chart 1.7

Creation of D-A nanostructures facilitate charge generation and transport. Wicklein *et al.* found that an electron-conducting perylene bisimide organogelator **52** forms nanowires in appropriate solvents [Wicklein *et al.* 2009]. This phenomenon was utilized for PBI self-assembly in an amorphous hole-conducting polymer matrix **51** to

bisimide (**53**) and the cyanurates (dCA) (Figure 1.24) [Yagai *et al.* 2010]. The resulting nanofibres could gelate aliphatic solvents (1,1,2,2-tetrachloroethane (TCE)) under low concentrations. The resulted gels were optically transparent. Various microscopic and XRD studies suggest that a hydrogen bonded polymer complex is formed along the long axis of the nanofibres by the 1:2 complexation of the two components (Figure 1.24b). Photoinduced carrier generation in the nanofibres was investigated by time-of-flight (TOF) experiments under electric and magnetic fields, revealing the efficient recombination of the geminate electron-hole pairs. FP-TRMC measurements revealed intrinsic 1D electron mobilities upto $0.6 \text{ cm}^2 \text{ V}^{-1} \text{ s}^{-1}$ within the nanofibres.

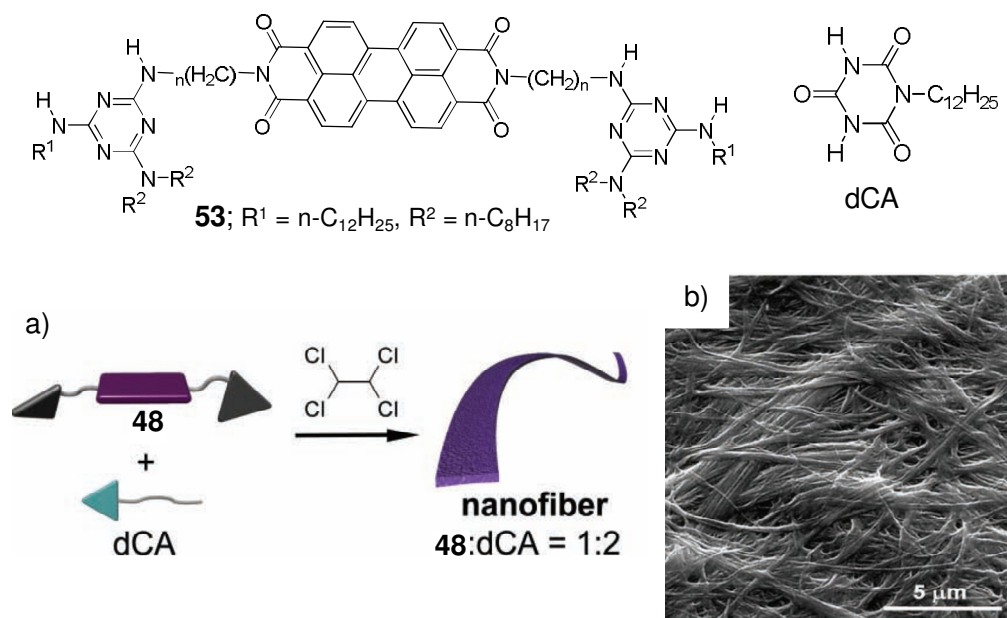


Figure 1.24. a) Schematic representation of the aggregation **53** with dCA in TCE. b) SEM image of nanofibres.

1.5.2. Naphthalene Diimide Derived Organogels

Shinkai and co-workers have reported the gelation of naphthalene diimide (**54**) (Figure 1.25). The UV-vis absorption spectrum exhibits charge-transfer band at 600 nm upon adding increasing amounts of the dihydroxynaphthalene (**55**) in the gel

matrix of **54** [Mukhopadhyay *et al.* 2006]. SEM analysis showed the presence of long 1D fibrous network for **54** which transformed into a 2D sheet like structure in the presence of **55** (Figure 1.25b and c). It has been found that the gel superstructure is extremely sensitive even to the upper limit of the added donor molecules, since the addition of more than 1.2 equivalents can readily transform the gel matrix into a sol phase.

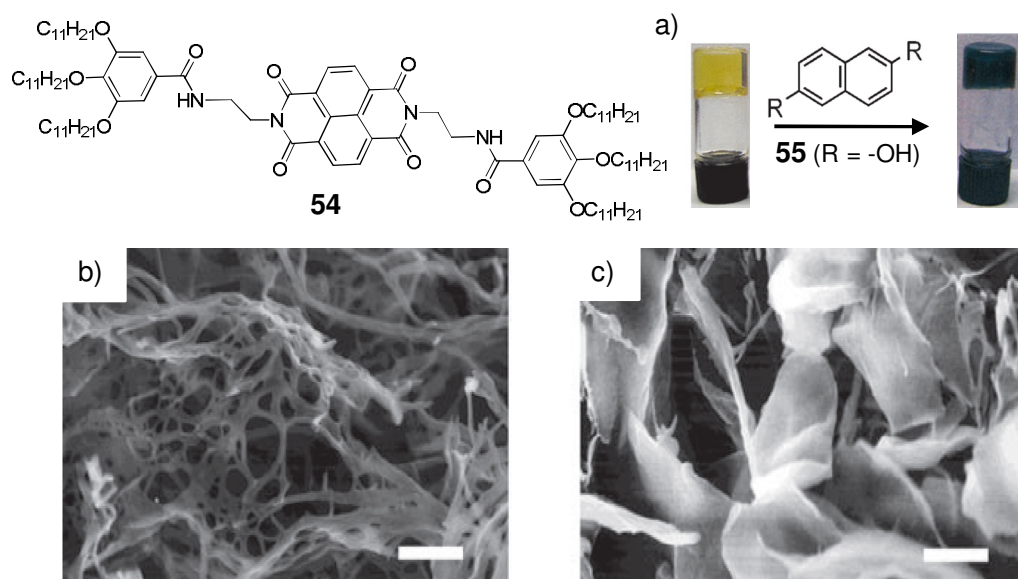


Figure 1.25. a) Photograph depicting the spontaneous color changes of the organogel **54** upon addition of **55**. SEM images of the xerogel of b) **54** and c) the **54** + **55** complex prepared from the cyclohexane gel (4.0 mm); the scale bar denotes 1 mm.

Recently, Parquette and co-workers have reported the formation of 1D n-type nanotube formed from 1,4,5,8-naphthalene tetracarboxylic diimide (NDI) (**56**) with l-lysine head groups [Shao *et al.* 2010]. These bolaamphiphiles formed transparent gels in water at concentrations as low as 1% (w/w), and was stable in the gel state for several months. TEM images revealed the formation of micrometer-long nanotubes with uniform diameters of (12 ± 1) nm. The thickness of the wall was approximately (2.5 ± 0.5) nm. A few nanorings, could also be observed in the TEM images. These observations suggest that the nanotube assembles via a monolayer nanoring that further

stacks into the nanotube structure (Figure 1.26). Time correlated single photon counting (TCSPC) suggested that the nature of the intermolecular organization and packing within the nanostructures significantly impacts the excited state properties of the material.

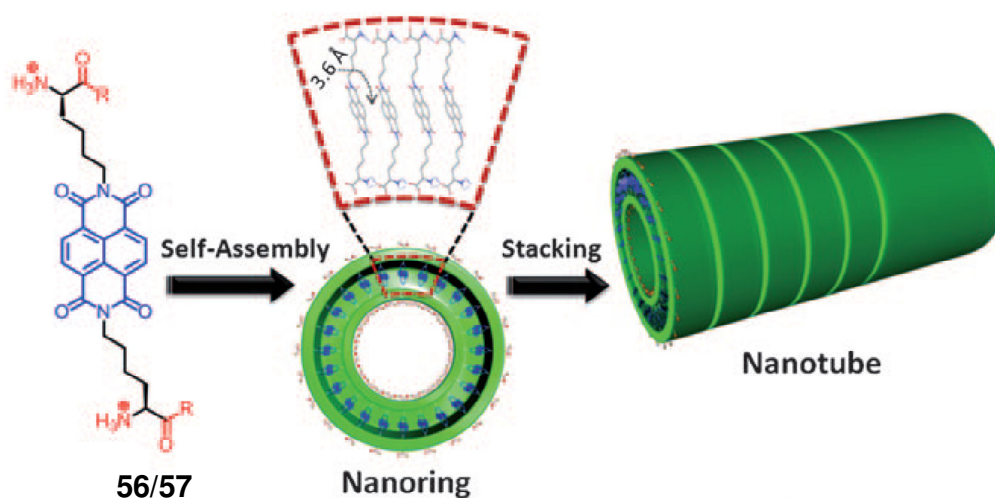


Figure 1.26. Structures of lysine-based bolaamphiphiles **56** ($R=O^-$) and **57** ($R=OMe$) and the assembly of **56** into rings, which stack to give tubes. The blue sections of **57** undergo hydrophobic π - π stacking interactions, and the red sections show electrostatic interactions.

Supramolecular assembly and electrochemical properties of a series of bis-(trialkoxybenzamide)-functionalized NDI chromophores (**58-61**) are known in the literature (Chart 1.8) [Molla *et al.* 2011]. The number of methylene units (0-4) in between the NDI chromophore and the amide functionalities have been systematically varied to understand the effect of this simple structural variations on the self-assembly. UV-visible spectroscopic studies revealed facile self-assembly in nonpolar medium by synergistic effect of π -stacking, hydrogen bonding, and hydrophobic interactions. AFM studies revealed unique morphology for the self-assembled structure in each case such as nanostructure with short-range order (**58**), elongated nanowires (**59**), relatively flat nanoribbons (**60**), and discontinuous nanofibres (**61**). Effect of such diverse

morphologies was found to be highly relevant in correlating the macroscopic properties such as gelation of the individual chromophore. The viscoelastic properties of the gels were studied by rheological measurements which revealed remarkable dependence on the morphology of the self-assembled structure. Redox properties of these chromophores were studied and the results corroborate well with the literature to indicate the n-type semiconducting nature of the NDI chromophore.

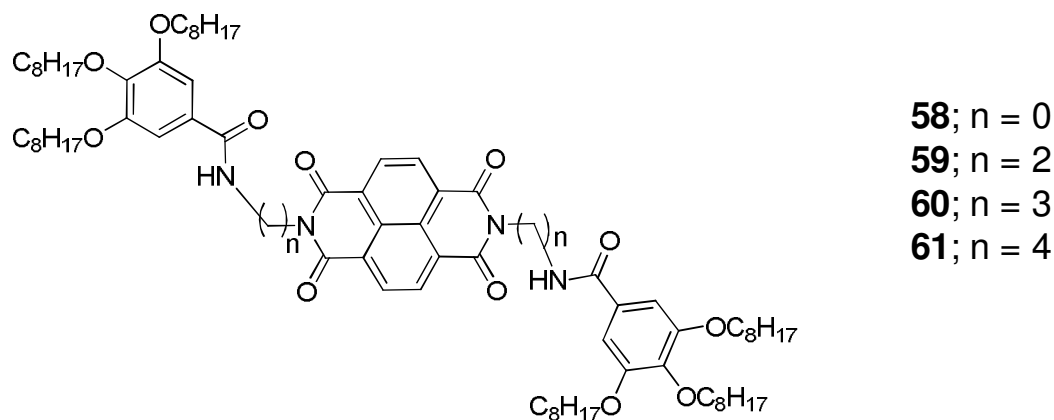


Chart 1.8

1.5.3. Bisphenazine Derived Organogels

Jang *et al.* have reported the formation of an organogel of an asymmetric bisphenazine (**62**) through the growth of one-dimensional nanofibres (Figure 1.27) [Jang *et al.* 2008]. Detailed gelation studies revealed that the critical gelator concentration (CGC) was the highest in TCE (10 mM), while gelation in decane and hexadecane were observed at significantly lower concentrations. SEM analysis revealed that effective gelation is possible only through the harmonious interplay of π - π interaction, hydrogen bonding and van der Waals interaction producing unusual belt like fibres (Figure 1.27b and c). The cyclic voltammetry (CV) results of **62** implies that these compounds are potentially applicable for optoelectronics for n-channel functions.

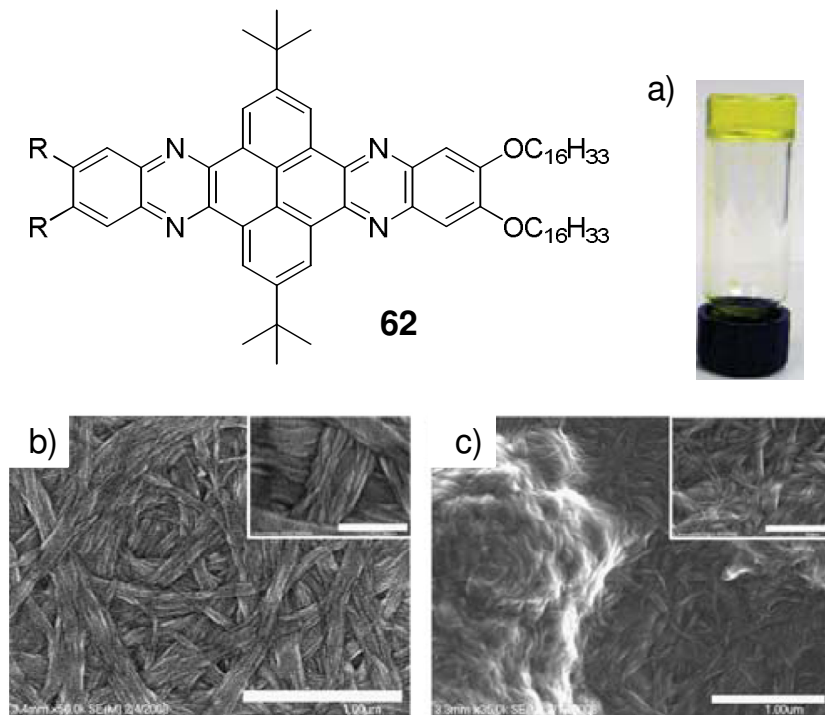


Figure 1.27. a) Pictures of organogel of compound **62** in decane (1.3 mM). SEM images of the xerogel of compound **62**: b) from decane gel (1.3 mM), scale bar: 1 mm (inset: 300 nm), c) from TCE gel (10 mM), scale bar: 1 mm (inset: 500 nm).

There are other reports on the electronic and organogelation properties of novel T-shaped bisphenazines (**63-68**) functionalized with alkyl side groups and small peripheral cyano (CN) or aldehyde (CHO) substituents (Chart 1.9) [McGrath *et al.* 2009; Lee *et al.* 2008]. Detailed UV-vis spectroscopy and CV studies revealed the effect of the position, type, and number of the peripheral substituents on the electronic properties. This design approach illustrates a reasonable method for tailoring electronic and self-assembly properties of bisphenazine, a system that exhibits excellent potential for optoelectronic applications.

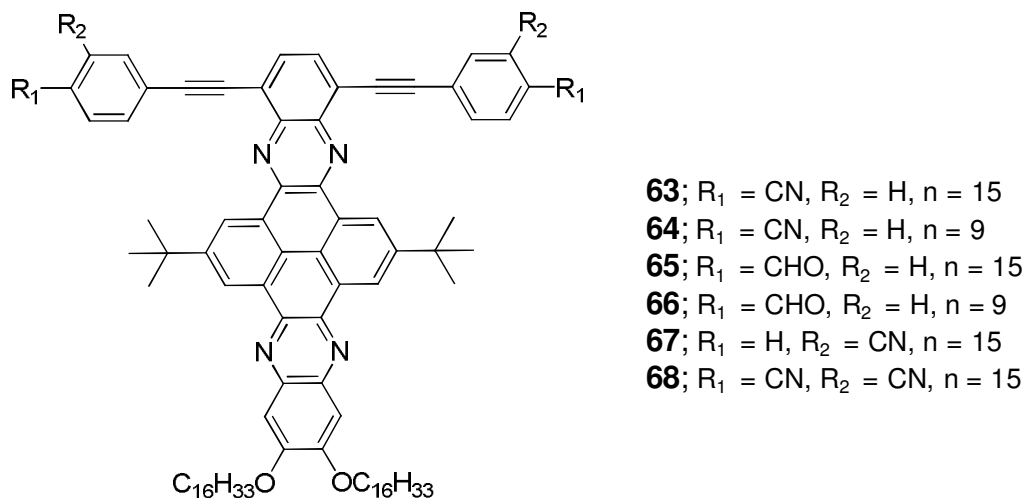


Chart 1.9

1.6. Origin, Objectives and Approach to the Thesis

In recent years several reports have been appeared in the literature pertaining to the self-assembly and gelation of thiophenes, tetrathiafulvalenes, perylene bisimides etc. However, so far, no breakthroughs occurred with respect to the application of these materials in electronic devices such as OFETs and solar cells. Therefore, preparation and study of self-assembled soft materials based on n-type and p-type organic semiconductors with improved electronic properties that are useful for device applications are important. The main challenges in the preparation of self-assembled π -systems are controlling the size to a few nanometers in length scale with high charge transport properties, charge separation and stability. Therefore, intense research is required in this area to achieve the preparation of new materials with optimum properties and device performance. The main objective of the present thesis is to have a detailed investigation on the design, self-assembly and electronic properties of new π -systems. For this purpose, we have chosen oligo(thienylenevinylene)s (OTVs), a class of molecules which have received considerable attention due to their unique optical and electronic properties. Though a few reports are available in the literature on the optical

and electrochemical properties of OTVs, none of them pertain to the design of nanostructures through organogel approach. In view of this, we aimed at the creation of functional chromophoric assemblies of π -conjugated OTVs through the formation of organogels, with the objective of crafting nanoscopic assemblies of different size and shape, thereby modulating their optical and electronic properties.

In order to fulfill the above objectives, the design and synthesis of a variety of OTVs with appropriate structural variations were planned. The design principle involves the derivatization of OTVs with hydrogen bonding end groups and with long aliphatic hydrocarbon side chains (Figure 1.28). The non-covalent interactions in these molecules were expected to lead the formation of supramolecular assembly and gels in hydrocarbon solvents. As a result of the strong intermolecular interaction during self-assembly, the electronic properties such as conductivity and charge carrier mobilities are expected to be strongly perturbed. Therefore, detailed study on the gelation induced optical and electronic properties and morphological characteristics were planned.

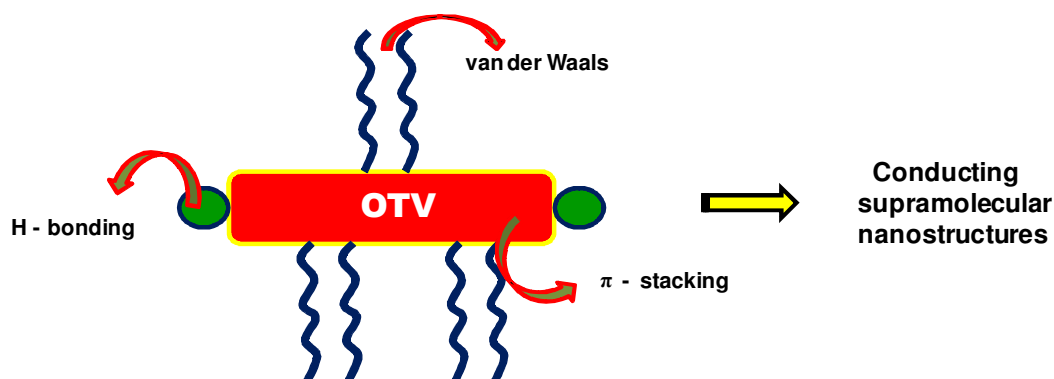


Figure 1.28. Design features showing various non-covalent interactions for the self-assembly of linear π -conjugated oligomers.

It is also important to study the effect of conjugation length on the self-assembly, gelation and electronic properties. Therefore, synthesis of OTV derivatives with different conjugation length was planned. The final question that we wanted to

address was the controlled assembly of donor and acceptor systems to achieve nanoscale phase separation and efficient charge generation in p-n type organogels. The present thesis is a detailed and systematic approach to the realization of the above objectives which are presented in different chapters.

Thienylenevinylene Based Organogelators: Synthesis, Self-Assembly and Charge-Carrier Mobility Studies

2.1. Abstract

Self-assembled architectures of thiophene derived oligomers and polymers are important in the field of organic electronics. Herein, we present the synthesis, self-assembly and charge-carrier mobility studies of a few thienylenevinylene derivatives (TTVI-4), having various end groups such as –OH, –CO₂H, and –CONHR. It has been found that among TTVI-4, only TTV4 with amide end functional groups facilitated gelation of nonpolar hydrocarbon solvents. The gelation properties and the morphology of the gels are established through FT-IR, XRD, SEM, TEM, and AFM analyses. Microscopic analysis revealed that TTV4 forms entangled micrometer sized fibres having width ranging from 50-200 nm. XRD data suggested a lamellar type packing of the molecules in the gel state. Flash photolysis time resolved microwave conductivity and transient absorption spectroscopy (TAS) studies suggested that films of TTV4 prepared from decane-chloroform gels exhibit high charge-carrier mobility when compared to films obtained from chloroform solutions, highlighting the role of self-assembly and gelation on the electronic properties.

2.2. Introduction

Advances in the performance of organic devices, over the past few years have attracted a great deal of interest not only from the academia but also from the technology domain [Forrest *et al.* 2004; Grimsdale *et al.* 2005; Hoeben *et al.* 2005; Schenning *et al.* 2005; Ariga *et al.* 2008; Zang *et al.* 2008; Tsao *et al.* 2010]. In organic electronic devices, the efficiency of charge carrier transport through the organic layer plays a key role in the final device performance [Tang *et al.* 1986]. In the case of organic field effect transistors, it is necessary to develop new materials displaying high electron and hole mobilities to improve the performance of complex organic circuits [Allard *et al.* 2008]. In the case of organic photovoltaic cells, the charges created upon photoexcitation of the active components have to be transported efficiently to get collected at the metallic electrodes with minimal charge recombination at the organic donor/acceptor interfaces [Blom *et al.* 2007]. Along these lines, organic chemists have been pursuing various π -conjugated systems as active materials for electronic devices [Arias *et al.* 2010]. The charge-carrier transport properties critically rely not only on the intrinsic electronic properties of the materials but also on the microscopic and macroscopic order of the molecules in the solid state. In this regard, the control of molecular organization with long-range ordering on surface through chemical design and physical processing constitute the key aspects in electronic devices [Ariga *et al.* 2008]. Organogelation is an effective way of organizing chromophores through non-covalent interactions [Lehn *et al.* 1995; Terech *et al.* 1997; Sangeetha *et al.* 2005; Ishi-i *et al.* 2005; Ajayaghosh *et al.* 2007].

In recent years, organogelators based on functional π -systems and dyes having good electronic conductivity and high charge-carrier mobility have been reported for a variety of electronic applications [Jørgensen *et al.* 1994; van Esch *et al.* 2000]. For example, Aida and

co-workers have reported the nanotube of **1** (Chart 2.1) which exhibits a p-type FET property, with a hole mobility of $1.0 \times 10^{-4} \text{ cm}^2 \text{ V}^{-1} \text{ s}^{-1}$ [Hill *et al.* 2004]. Later, Würthner and co-workers have reported n-type semiconducting perylene bisimide (**2**) dye with the isotropic electron and hole mobility of $\Sigma\mu_{\text{TRMC}} = 0.052 \text{ cm}^2 \text{ V}^{-1} \text{ s}^{-1}$ [Li *et al.* 2006]. Diring *et al.* have reported that gel fibres of pyrene substituted 4-ethynylphenylaminoacyl derivative **3** exhibits good electron and hole transport properties from source to drain electrodes [Diring *et al.* 2009]. Recently, Yagai *et al.* have reported that the nematic gel forming supramolecular complex of **4** and the complementary hydrogen bonding unit comprised of ribbon like aggregates exhibits a higher $\Phi\Sigma\mu$ value of $5.2 \times 10^{-6} \text{ cm}^2 \text{ V}^{-1} \text{ s}^{-1}$ than the vesicular aggregates of **4** ($4.4 \times 10^{-6} \text{ cm}^2 \text{ V}^{-1} \text{ s}^{-1}$) stressing the role of the morphology on electronic properties [Yagai *et al.* 2010].

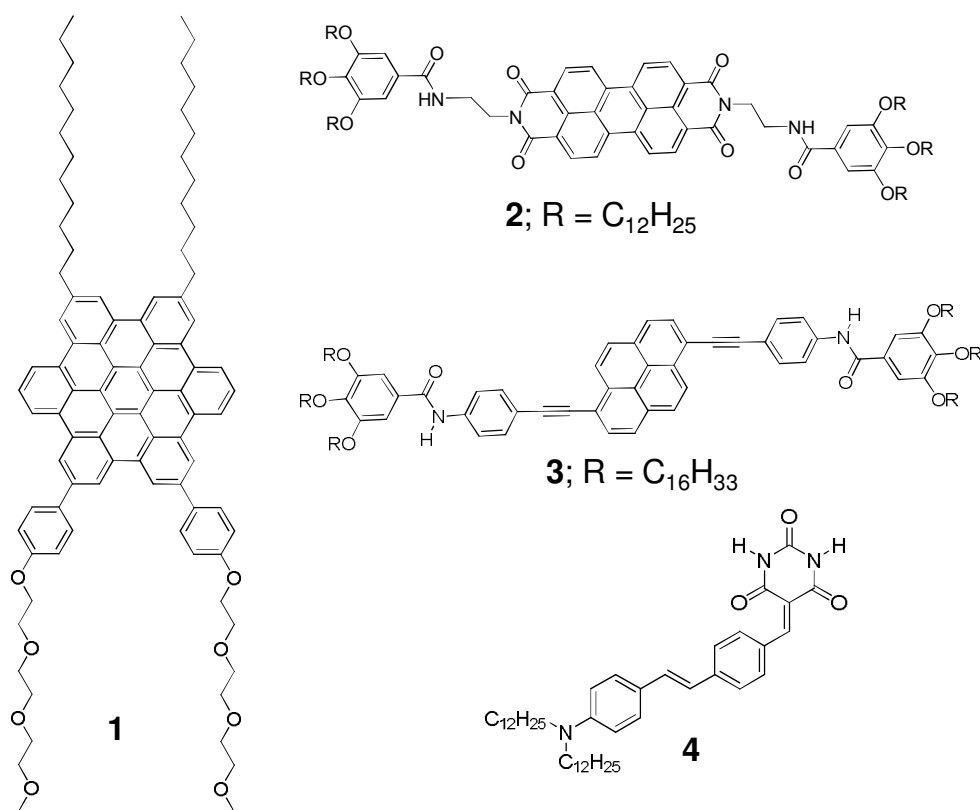


Chart 2.1

Among various widely investigated conjugated molecules, sulfur containing π -conjugated systems are the prominent building blocks for the construction of conducting nanostructures, useful for organic electronic applications [Roncali *et al.* 1997; Kitamura *et al.* 2005; Kitahara *et al.* 2005; Wang *et al.* 2005; Akutagawa *et al.* 2005; Puigmartí-Luis *et al.* 2007]. In particular, thiophene containing hetero aromatic molecules have attracted great scientific research interest because thiophenes provide the desired continuous pathway for better transport of the charge carriers [Gronowitz *et al.* 1985; Otsubo *et al.* 2002; Mishra *et al.* 2009]. Therefore, thiophene containing π -conjugated molecules are extensively used in various devices such as field effect transistors and photovoltaic cells [Katz *et al.* 2001; Kiriy *et al.* 2004; Xin *et al.* 2008; Peet *et al.* 2009].

The electronic properties of organic molecules are strongly dependent upon the molecular self-assembly. Organogelators are known to form self-assemblies leading to the formation of 1D fibres and hence are good candidate for the design of organic electronic devices. Feringa and co-workers have reported that the bisurea appended oligo(thiophene)s (**5** and **6**) (Figure 2.1) self-assemble into elongated fibres resulting in the formation of organogels in solvents such as tetralin and 1,2-dichloroethane. Electron microscopy and X-ray diffraction studies have revealed that the fibres have a lamellar structure, in which the molecules are arranged as one-dimensional ribbons with their long molecular axis parallel to each other (Figure 2.1a-c). Moreover, it was shown by FP-TRMC experiments that the good electronic overlap between the thiophene rings due to the H-bond assisted π -stacking of adjacent oligomers results in high charge-carrier mobility of $0.001 \text{ cm}^2 \text{ V}^{-1} \text{ s}^{-1}$ for **5** and $0.005 \text{ cm}^2 \text{ V}^{-1} \text{ s}^{-1}$ for **6** (Figure 2.1d). These values are relatively high when compared to that of simple thiophene oligomers [Schoonbeek *et al.* 1999].

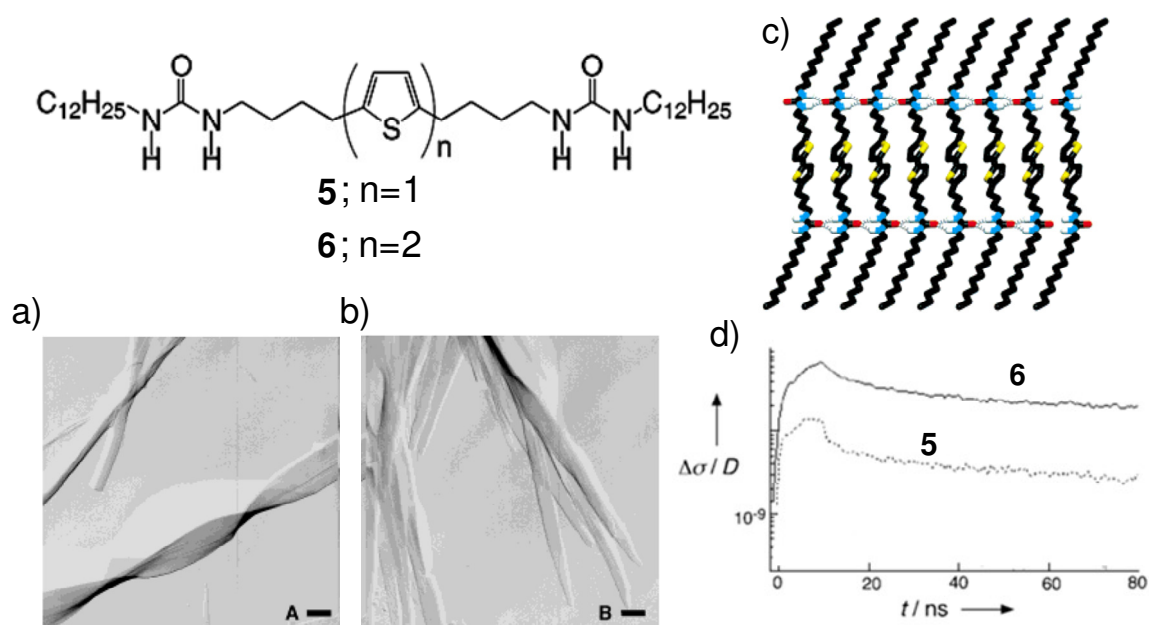


Figure 2.1. a,b) Electron micrographs of the lamellar fibres of **5** (A) and **6** (B). c) Possible arrangement of **6** in the lamella, and d) FP-TRMC kinetic profile of **5** and **6**.

Recently, Yagai *et al.* have reported the thermally interconvertible semiconductive nanorods and nanotapes comprising of π -conjugated oligothiophenes, displaying high charge-carrier mobilities in their condensed states (Figure 2.2) [Yagai *et al.* 2009]. AFM of the H-aggregates of **7** exhibited uniform rod like nanostructures with hundreds of nanometers in length, which are arranged in monolayered fashion. On the other hand, **7·BM12** showed flat, tape like nanostructures with an average thickness of 1.7 nm and the width of ~ 5.5 nm. FP-TRMC study revealed that the hole mobility (μ^+) of **7·BM12** is $0.57 \text{ cm}^2 \text{ V}^{-1} \text{ s}^{-1}$, whereas for **7** alone is $1.3 \text{ cm}^2 \text{ V}^{-1} \text{ s}^{-1}$. While a large number of thiophene derivatives have been studied from the view of self-assembly and electronic properties, thienylenevinylene have not been exploited for the purpose of studying self-assembly or gelation.

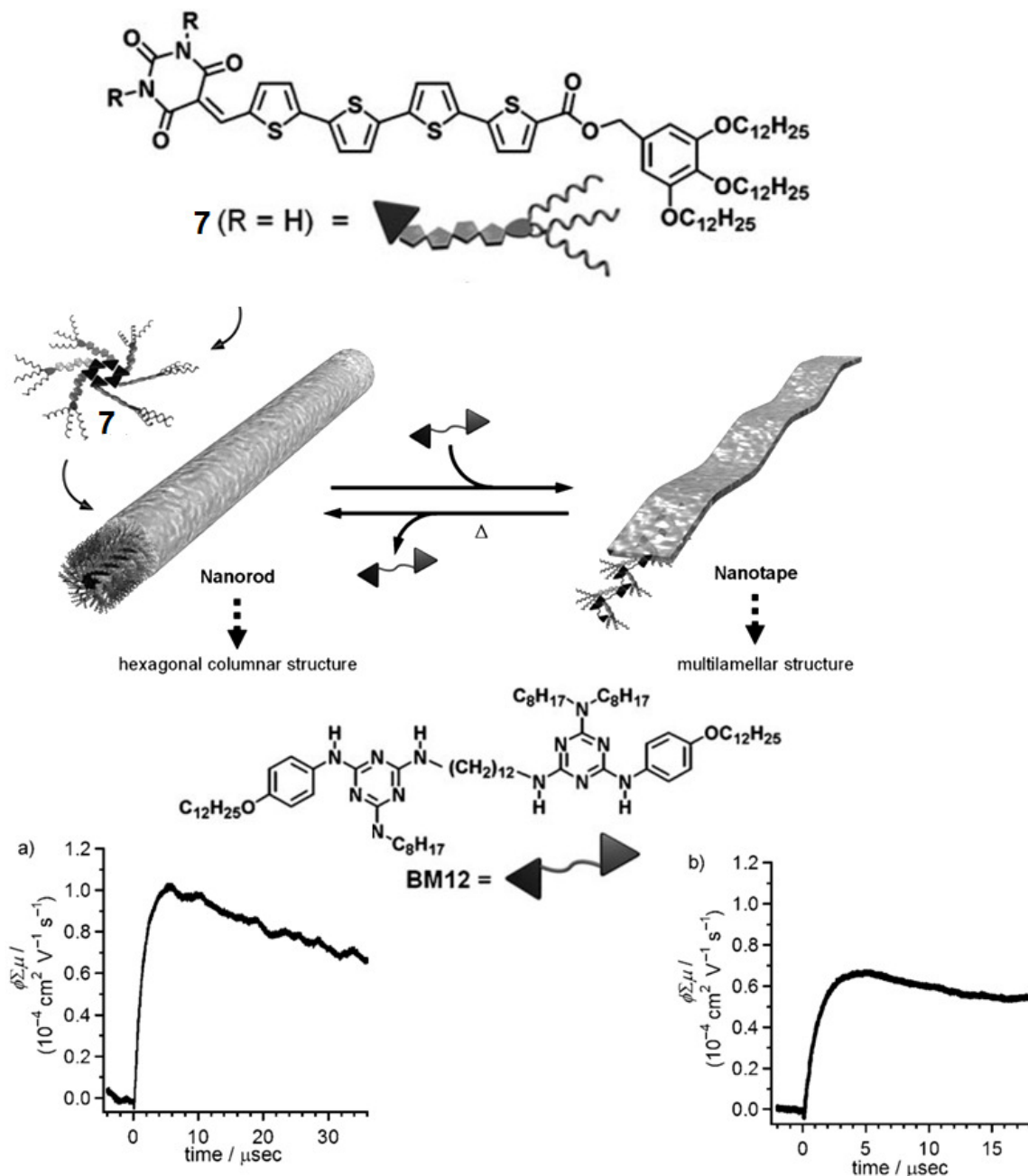


Figure 2.2. Scheme of the interconversion between nanorod and nanotape. Transient conductivities observed for films of a) **7** and b) **7·BM12** under an excitation at $\lambda = 355 \text{ nm}$ by $1.8 \times 10^{16} \text{ photons cm}^{-2} \text{ pulse}^{-1}$.

Roncali and co-workers have reported the electrochemical and electronic properties of thienylenevinylene oligomers (*n*TVs) (**8a-d**) with multinanometer dimensions (Chart 2.2) [Jestín *et al.* 1998]. Cyclic voltammetry data revealed that chain lengthening induces a

negative shift of the first redox potential, an increase of the number of accessible redox states, and a decrease in the coulombic repulsion in multicationic species. Thus, a 16-mer can be charged up to the hexacationic state within a 0.60 V potential window. UV-vis spectra of the n TVs suggest the bathochromic shift of λ_{\max} and the decrease of the HOMO-LUMO gap with the extension of conjugation length. Therefore, n TVs with extended conjugation are good candidates for the fabrication of FET devices.

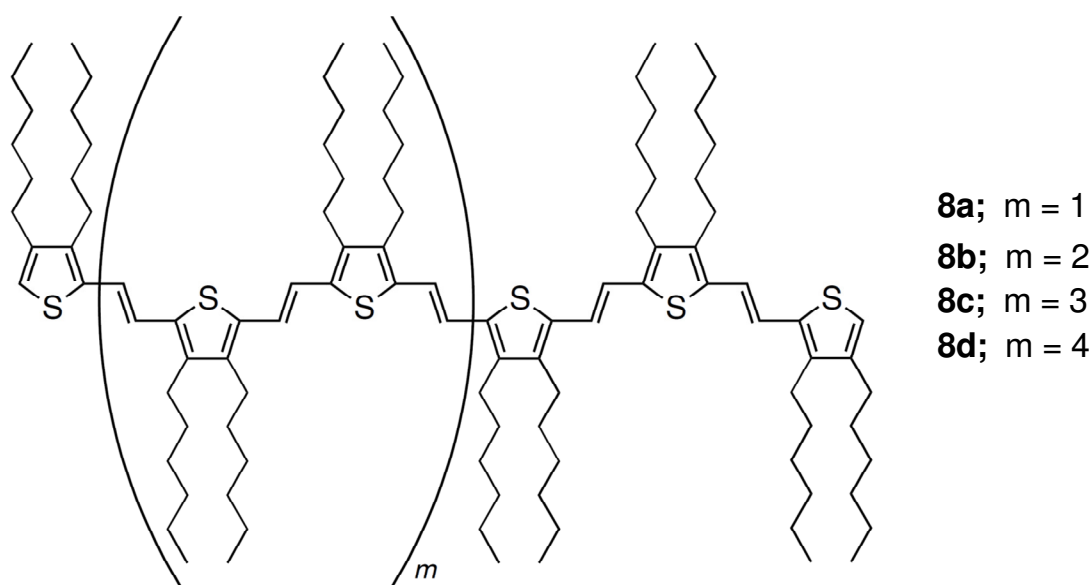


Chart 2.2

The main objective of the present investigation was to synthesize OTVs with different end functional groups to study their self-assembly and electronic properties. Herein, we present the synthesis, gelation, morphology and charge-carrier mobility of a few thienylenevinylene derivatives (**TTV 1-4**) (Chart 2.3).

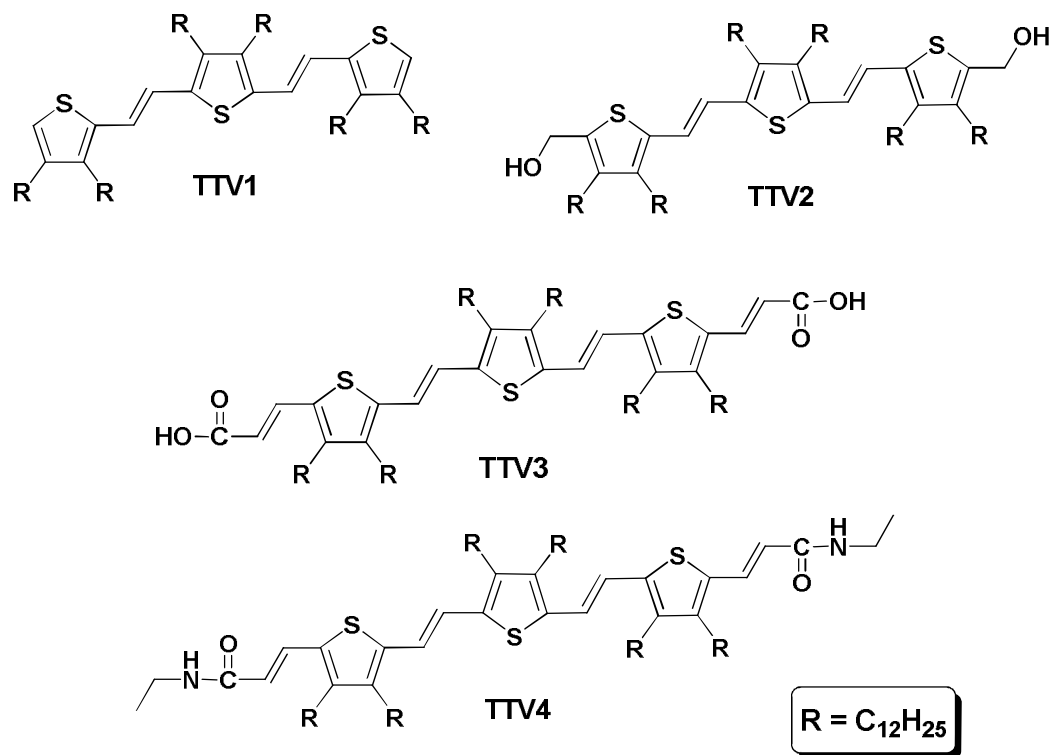


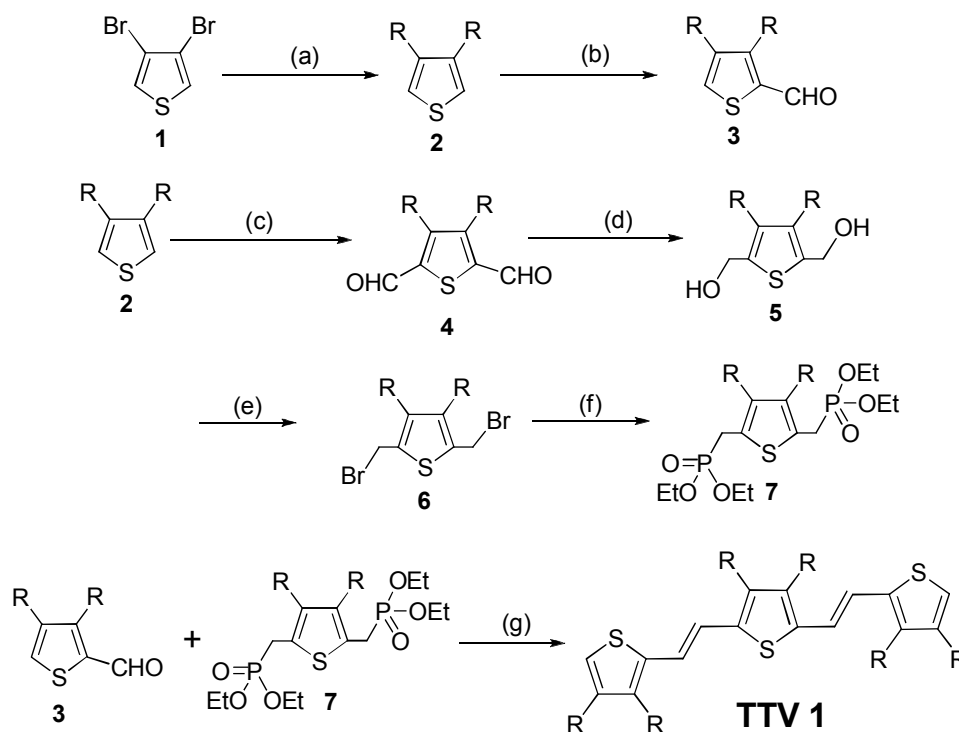
Chart 2.3

2.3. Results and Discussion

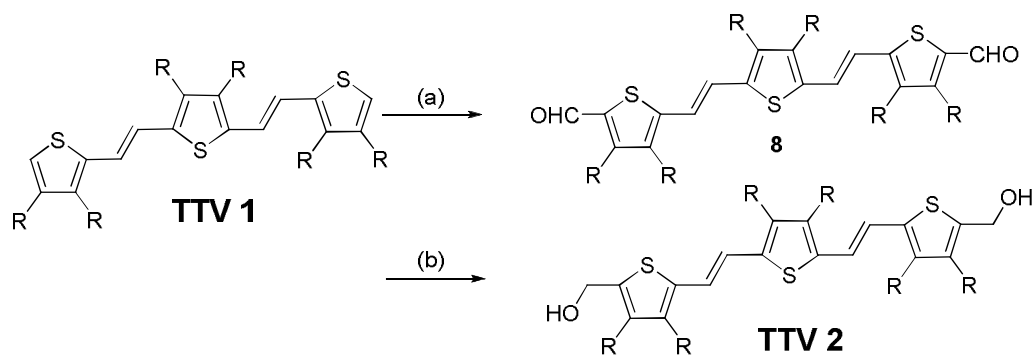
2.3.1. Synthesis of TTV1-4

The synthetic strategy adopted for the preparation of **TTV1** is illustrated in Scheme 2.1 [Jestín *et al.* 1998]. 3,4-Dibromothiophene was treated with Grignard reagent of dodecylbromide followed by the Kumada coupling to give the 3,4-didodecylthiophene (**2**), which was converted to 3,4-didodecylthiophene-2-carbaldehyde (**3**) using Vilsmeier formylation reaction. Compound **4** was synthesized from **2** by treating with *n*-BuLi/TMEDA in hexane followed by reduction to the corresponding alcohol **5** with NaBH₄. The compound **5** was converted into the corresponding bromo derivative **6** by treatment with PBr₃ in dichloromethane followed by reaction with triethyl phosphite to give the **7** in 65% yield. **TTV1** was prepared by using Wittig-Horner olefination with compounds **3** and **7** as shown in Scheme 2.1 in 72% yield after purification by column chromatography.

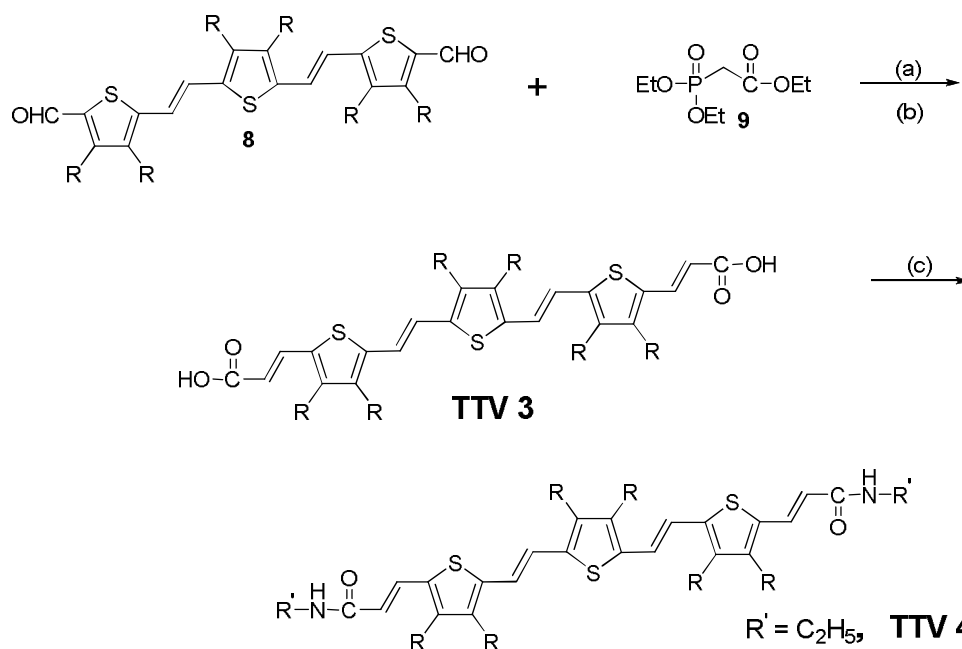
TTV1 was converted to **8** by Vilsmeier formylation at appropriate conditions and reduced to the corresponding alcohol **TTV2** with NaBH_4 as shown in Scheme 2.2. Reaction of **8** with the phosphonate ester **9** followed by hydrolysis in basic medium gave **TTV3** in 91% yield. **TTV4** was prepared from **TTV3** by treating with ethylamine in the presence of 2-(1H-7-azabenzotriazol-1-yl)-1,1,3,3-tetramethyluroniumhexafluorophosphate methanaminium (HATU, a peptide coupling reagent) as shown in Scheme 2.3. These thienylenevinylene derivatives were characterized by ^1H NMR, ^{13}C NMR, FAB-MS and FT-IR spectral analyses. The presence of *trans* double bonds in **TTV1-4** was confirmed by the vinylic protons appeared in the range of $\delta = 6.95\text{-}6.89$ ppm ($J \sim 16$ Hz), in the ^1H NMR spectra.



Scheme 2.1. Synthesis of **TTV1**. Reagents and conditions: (a) $\text{Ni}(\text{dppp})\text{Cl}_2$, RMgBr , Et_2O , 24 h, 40°C , 65%; (b) POCl_3 , DMF, 1,2-DCE, 2 h, 70°C , 76%; (c) $n\text{-BuLi}$, TMEDA, DMF, Hexane, 2 h, -40°C , 54%; (d) NaBH_4 , DCM, MeOH, 1 h, 30°C , 92%; (e) PBr_3 , DCM, -5°C , 4 h; (f) $\text{P}(\text{OEt})_3$, 120°C , 65%; (g) $t\text{-BuOK}$, THF, 2 h, 30°C , 72% .



Scheme 2.2. Synthesis of **TTV2**. Reagents and conditions: (a) POCl_3 , DMF, 1,2 DCE, 2 h, 70 °C, 68%; (b) NaBH_4 , DCM, MeOH, 2 h, 30 °C, 92%.



Scheme 2.3. Synthesis of **TTV3** and **TTV4**. Reagents and conditions: (a) *t*-BuOK, THF, 2 h, 30 °C, 94%; (b) KOH, THF, MeOH, TFA, 4 h, 70 °C, 91%; (c) $\text{R}'\text{-NH}_2$, HATU, DIPEA, CHCl_3 , 12 h, 30 °C, 45%.

2.3.2. Electronic Absorption and Emission Properties

The absorption and emission properties of **TTV1-4** were investigated in CHCl_3 and decane. **TTV1** in chloroform (1.5×10^{-4} M) showed an absorption maximum at 436 nm. In decane, the absorption maximum was blue shifted to 432 nm and there was no considerable change in the nature of the spectrum. Subsequently, emission studies of **TTV1**

in chloroform and decane were carried out and the emission spectrum was found to be weak. No significant changes were noted upon changing the solvent from chloroform to decane (Figure 2.3b). The weak absorption and emission spectral shifts in chloroform and decane, indicate weak intermolecular excitonic interaction due to weak aggregation of the molecules. More insights about the effect of functional group on the self-assembly of thienylenevinylenes could be obtained from UV-vis absorption and emission spectral measurements of **TTV2**, **TTV3** and **TTV4** having **-OH**, **-CO₂H** and **-CONHR** respectively in polar and non-polar solvents.

The absorption spectrum of **TTV2** in chloroform ($c = 1.5 \times 10^{-4}$ M) showed a peak maximum at 444 nm. In decane, the absorption maximum was blue shifted to 441 nm, indicating that **TTV2** exists as molecularly dissolved species in chloroform and decane as observed in the case of **TTV1** (Figure 2.3c and 2.3d). The emission spectrum did not show any considerable change in chloroform and decane. **TTV3** in chloroform exhibited an absorption maximum at 506 nm. Since the molecule was not soluble in decane, the absorption spectrum was recorded in toluene for comparison. In toluene the absorption maximum was observed at 504 nm. In this case, the carboxyl group assisted linear hydrogen bonded polymerization is possible. The absorption spectrum did not show considerable shift indicating that intermolecular interaction is weak. In contrast to **TTV1** and **TTV2**, emission spectrum of **TTV3** showed weak but broad fluorescence in chloroform and toluene. Interestingly, **TTV4** having **-CONHR** as the end functional group exhibited considerable change in the absorption spectrum when recorded in chloroform and decane (Figure 2.4a). In chloroform (1.5×10^{-4} M), the absorption maximum of **TTV4** was observed at 501 nm and in decane, the absorption maximum was blue shifted to 464 nm with the appearance of a shoulder band at 550 nm. This large blue shift in the λ_{\max} ($\Delta\lambda_{\max} = 27$ nm) points to a large

oscillator strength and strong exciton coupling due to the 1D arrangement of the molecules. Such an arrangement is possible through hydrogen bonded face-to-face assembly of molecules as in the case of H-type aggregation. The emission studies of **TTV4** revealed weak emission in chloroform whereas in decane, enhanced fluorescence could be noticed (Figure 2.4b).

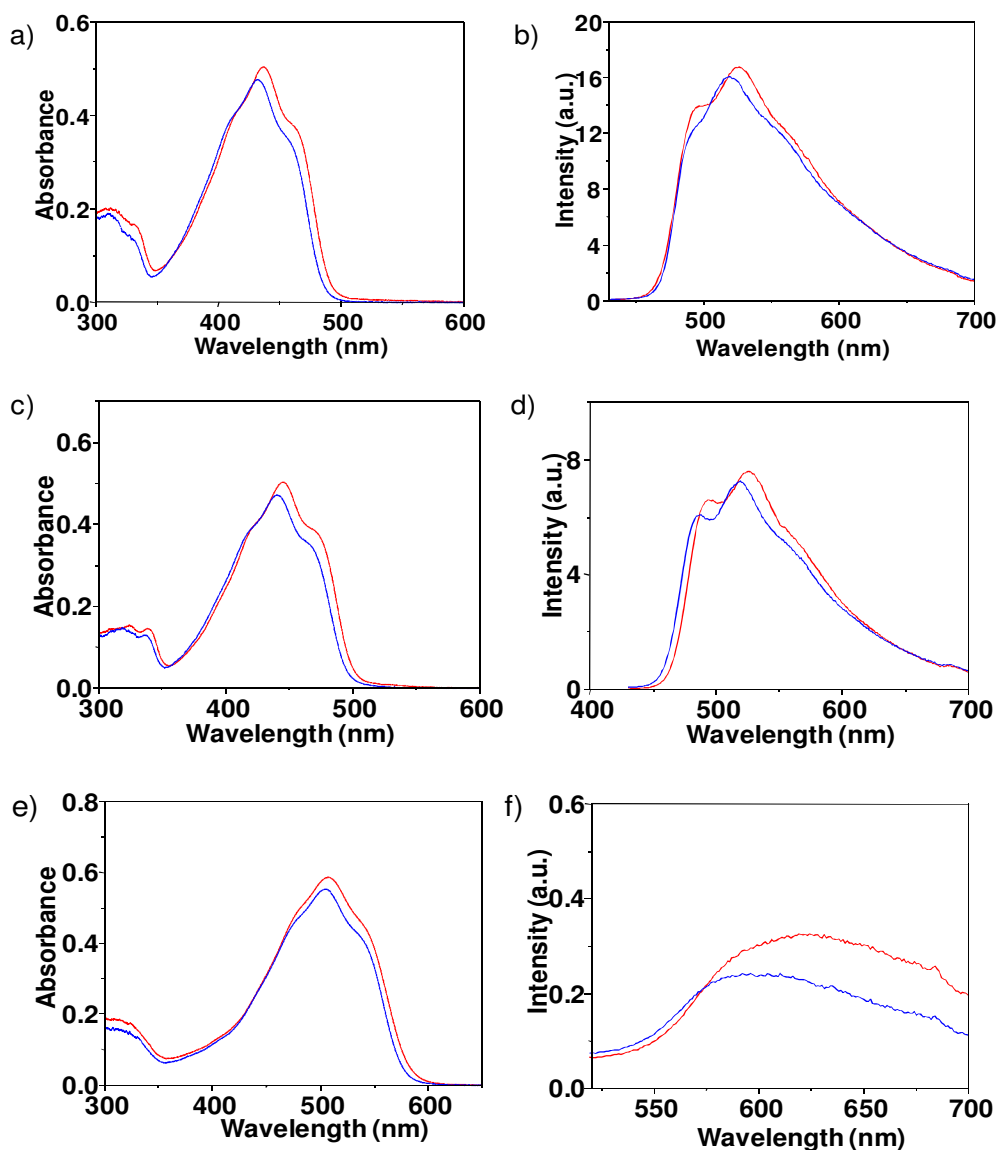


Figure 2.3. a) Absorption and emission spectra of (a,b) **TTV1**, (c,d) **TTV2**, and (e,f) **TTV3** at 1.5×10^{-4} M in decane (blue) and chloroform (red). (Note: spectra of **TTV3** was recorded in toluene due to insolubility in decane).

Further details of the **TTV4** self-assembly were obtained by variable temperature dependent absorption studies. The initial absorption spectrum of **TTV4** in decane at 1.5×10^{-4} M at 20 °C exhibited a shoulder band at 550 nm in addition to the strong π - π^* transition band at 464 nm. Upon increasing the temperature to 70 °C, the absorption maximum was red shifted to 491 nm with a concomitant decrease in the intensity of the shoulder band at 550 nm through an isosbestic point at 550 nm (Figure 2.5a). This observation indicated the breakage of the H-type aggregates at higher temperature. Further proof for the existence of the aggregated and molecularly dissolved phases of **TTV4** is obtained from the plot of the fraction of aggregates (α) versus the temperature, as obtained from the temperature dependent absorption spectral changes. In this case, the melting transition curve (Figure 2.5b) showed a sigmoidal nature indicating a co-operative transition of the self-assembled species to molecularly dissolved species with increase in temperature.

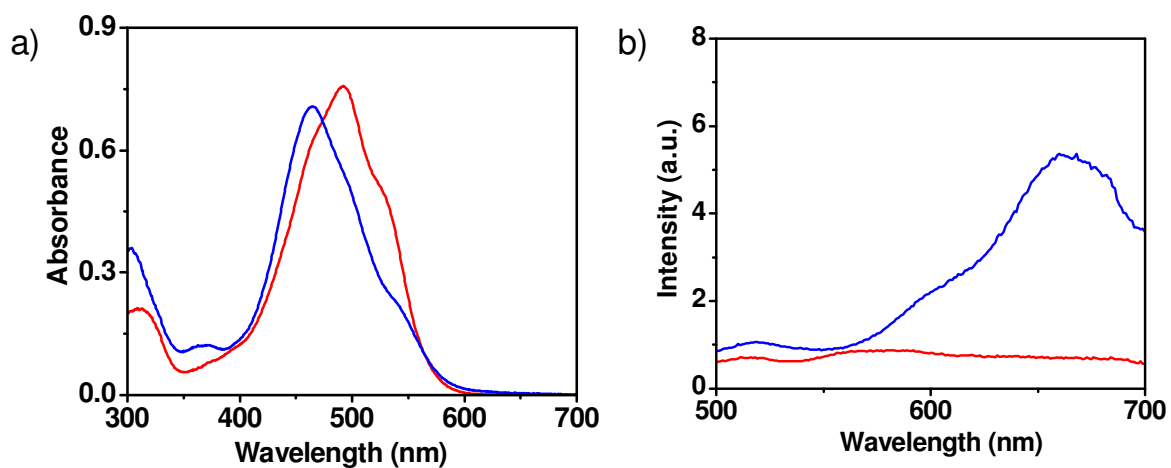


Figure 2.4. a) Absorption spectra of **TTV4** at 1.5×10^{-4} M in decane (blue) and chloroform (red). b) Fluorescence spectra of **TTV4** at 1.5×10^{-4} M in decane (blue) and chloroform (red).

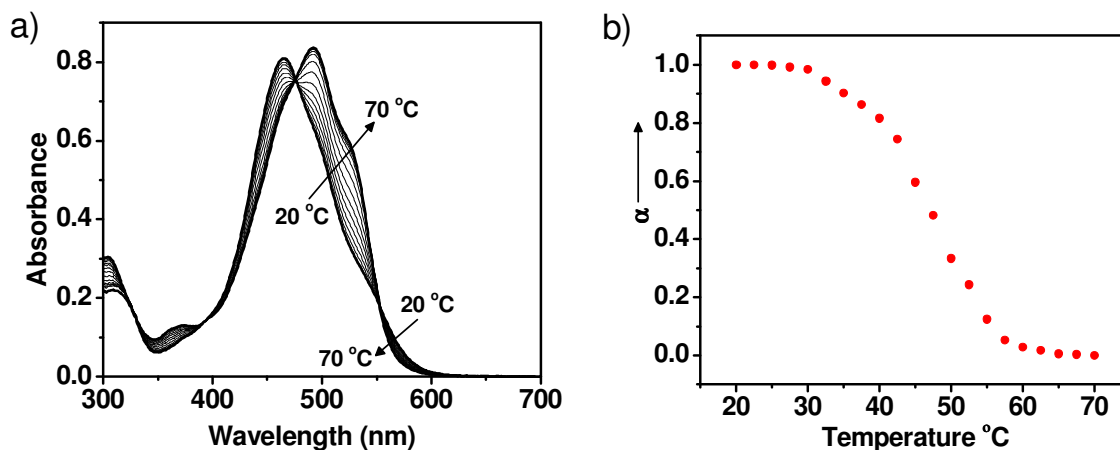


Figure 2.5. a) Temperature dependent UV-vis absorption spectra of **TTV4** at 1.5×10^{-4} M in decane. b) Plot of the fraction of aggregates (α) versus temperature obtained from the absorption changes monitored at 491 nm.

2.3.3. Gelation Properties

The gelation ability of **TTV4** was studied in different organic solvents. For this purpose, a specific amount of **TTV4** was added to 1 mL of a particular solvent and heated until dissolution. After cooling the sample to ambient temperature, the vessel was turned upside down to verify the gel formation. The soft solid mass obtained was self-standing as shown in Figure 2.6a. No gels were formed in polar solvents such as chloroform and methanol. This property could be due to the lack of hydrogen bonding and π -stacking interaction in polar solvents suggesting the crucial role of self-complementary hydrogen bonding in the gelation process of **TTV4**. Results of the gelation studies of **TTV4** in various solvents are summarized in Table 2.1.

Effect of temperature on the gelation of **TTV4** in decane was studied using the dropping ball method [Murata *et al.* 1994]. Phase diagram of the gel of **TTV4** in decane was obtained by plotting the gel melting temperature (T_{gel}) at different concentrations (Figure 2.6b). The phase above the curve represents the solution, whereas the phase below is a gel.

Table 2.1. Critical gelator concentrations (mM) of **TTV4** in different solvents

SI. No.	Solvent	Nature of gel	CGC (mM)
1.	Decane	G	0.98
2.	Cyclohexane	G	1.22
3.	Hexane	G	1.61
4.	Benzene	G	4.63
5.	Toluene	G	5.29
6.	Chloroform	S	-
7.	Methanol	NS	-

CGC = Critical gelator concentration, which is the minimum concentration required for the formation of a stable gel at room temperature. In parenthesis, G = gel, S = Soluble and NS = Not soluble.

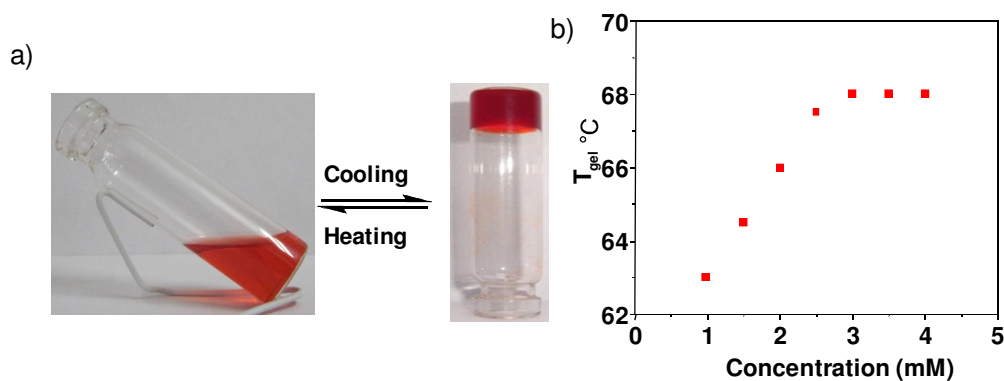


Figure 2.6. a) Photograph of the reversible sol-gel transition of **TTV4** in decane. b) Plot of gel melting temperature (T_{gel}) vs concentration of the gelator.

In the case of **TTV4**, a regular increase in the gel melting temperature with increasing the concentration of the gelator molecules was observed. The maximum stability of the gel was at 68 °C at a concentration of 3 mM of the gelator. Further increase of

concentration of the gelator did not show any considerable improvement in the gel melting temperature.

2.3.4. FT-IR Studies

The FT-IR spectrum of the decane gel of **TTV4** (Figure 2.7) exhibited a band at 3291 cm^{-1} that can be assigned to the hydrogen-bonded N-H stretching vibrations. In chloroform, the stretching frequency was shifted to 3440 cm^{-1} characteristic of the free NH (For a reference, the NH stretching vibration of free NH group of secondary amides in dilute solution occurs around $3500\text{-}3400\text{ cm}^{-1}$. In the solid-state the NH band shifts to the lower frequency, typically $3350\text{-}3100\text{ cm}^{-1}$) [Silverstein *et al.* 1981]. In addition, the amide I band at 1638 cm^{-1} and amide II band at 1544 cm^{-1} indicate the H-bonded amide groups in the gel state.

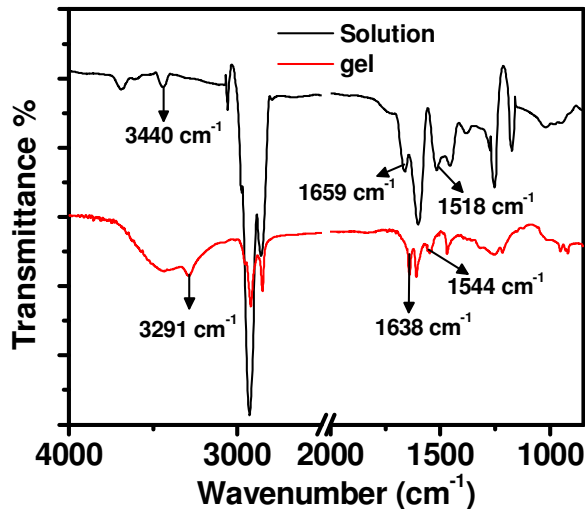


Figure 2.7. FT-IR Spectra of **TTV4** in dilute chloroform solution and gel in decane.

2.3.5. Morphological Studies

Self-assembly behavior of **TTV1-4** was examined using TEM and AFM techniques. For this purpose, samples were drop casted from decane solution at $5 \times 10^{-5}\text{ M}$

concentration on the required substrate. TEM images of **TTV1-2** showed randomly clustered aggregates without any specific shape (Figure 2.8a and 2.8c). AFM image of **TTV1** did not show any clear morphology whereas **TTV2** showed particles of 0.5-1.0 μm in size.

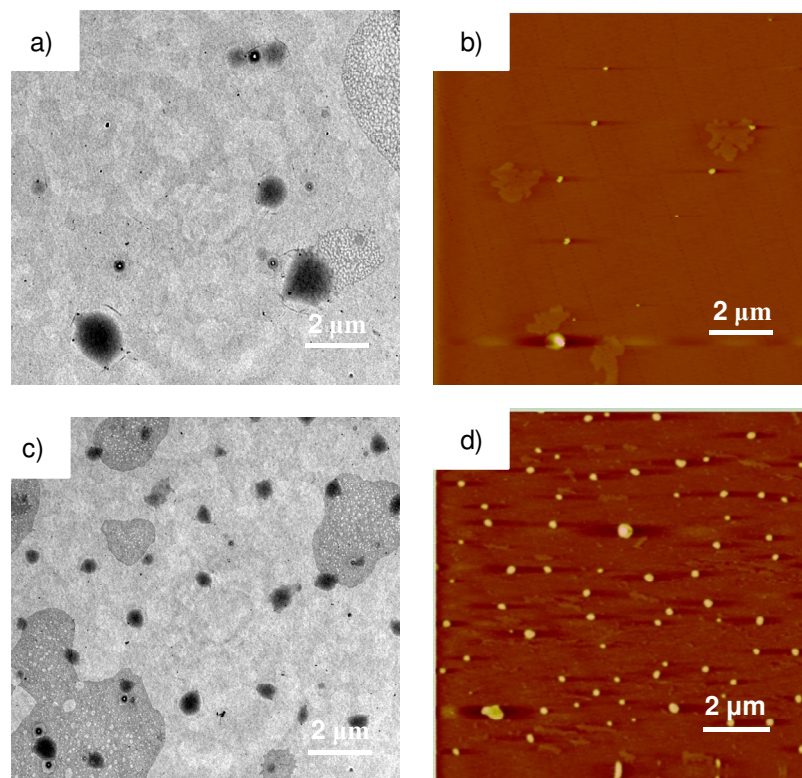


Figure 2.8. TEM images of a) **TTV1** and c) **TTV2**. AFM images of b) **TTV1** and d) **TTV2** at 5×10^{-5} M concentration from decane.

Interestingly, TEM and AFM images of **TTV3** showed fibrous aggregates when drop casted from decane, the morphology of which is different from those of **TTV1-2** (Figure 2.9). This observation indicates the possible H-bond formation between the terminal carboxylic acid groups which facilitate one dimensional supramolecular polymerization leading to elongated fibres. Despite the formation of fibrous structures, it was surprising that **TTV3** did not form gels. This observation implies that the fiber formation does not occur in the solution state as confirmed by the weak absorption spectral change (Figure 2.3e). Thus, in this case, the fibres might have formed on the substrate upon evaporation. However,

TTV4 showed thin, flexible, intertwined, and entangled network fibrous structures with diameter ranging from 50-200 nm and several micrometers in length as observed under TEM (Figure 2.10a). AFM images of **TTV4** showed thin fibre formation with average height of 20-60 nm and width of 50-200 nm and several micrometers in length (Figure 2.10b). The morphological analysis by TEM and AFM of **TTV1-4** revealed that **TTV4** with amide functional group forms supramolecular nanowires in solution leading to gelation. Figure 2.11 represents the models of the self-assembly of **TTV3** and **TTV4**.

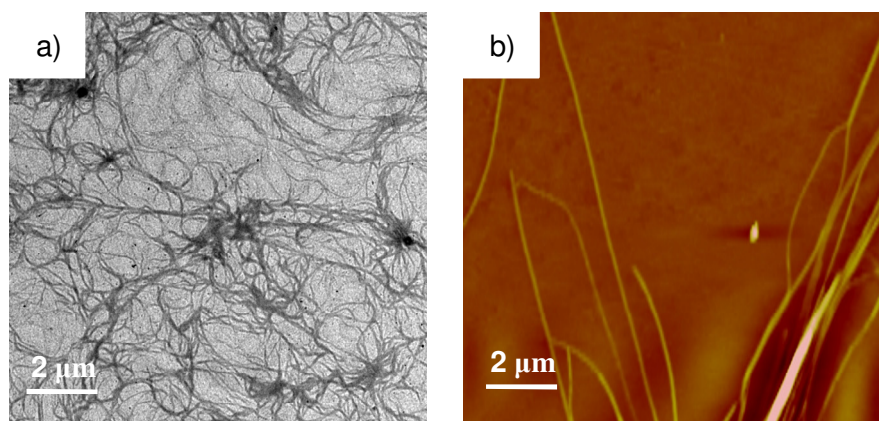


Figure 2.9. a) TEM and b) AFM images of **TTV3** drop casted from decane solution ($c = 5 \times 10^{-5} \text{ M}$) at room temperature.

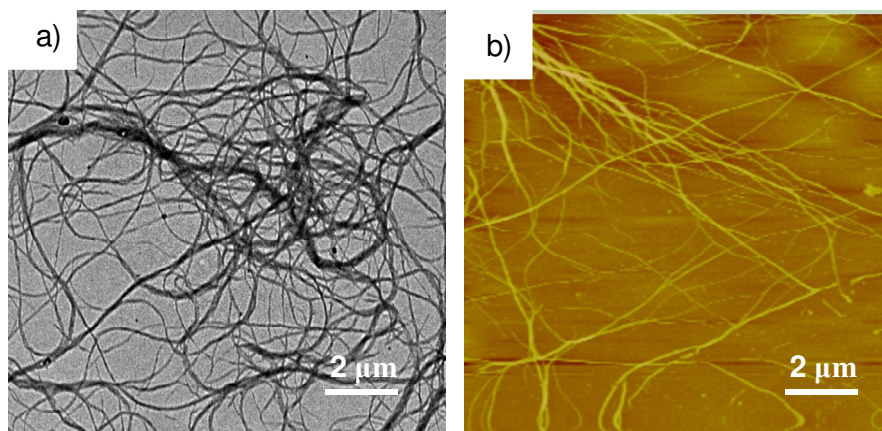


Figure 2.10. a) TEM and b) AFM images of **TTV4** drop casted from decane solution ($c = 5 \times 10^{-5} \text{ M}$) at room temperature.

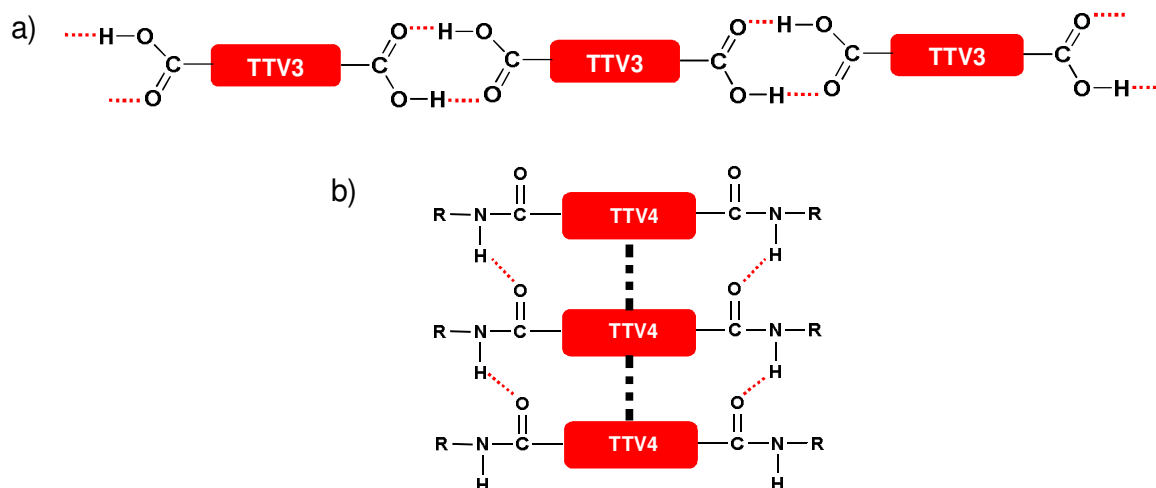


Figure 2.11. Models of the self-assembly of a) **TTV3** and b) **TTV4**.

2.3.6. X-ray Diffraction Measurements

X-ray diffraction (XRD) patterns of the xerogel obtained from **TTV4** showed diffraction peaks with d-spacing of 34.5, 31.2, 20.3, 4.2 and 3.3 Å (Figure 2.12). The strong diffraction peak at 34.5 Å in the small angle region is close to the calculated molecular width (34.8 Å) in which the alkyl chains are almost in fully extended conformation. Another strong peak in the small angle region is at 31.2 Å which is very close to the calculated length (27.0 Å) of the molecule. The broad signals with a d-spacing of 3.3 and 4.2 Å at the wide angle region may correspond to the π - π stacking distance and the alkyl chain packing distance of the **TTV4** molecule in the xerogel state. From these diffraction peaks in the XRD, it can be concluded that **TTV4** self-assembles in the xerogel in a lamellar fashion. In the lamellar phase, **TTV4** adopts a planar structure in which aryl rings are almost coplanar and the alkyl chains are laterally extended with a complete stretching of side chains. In the case of **TTV4**, the lack of higher order diffraction peaks in the wide angle region points towards a low

degree of ordering in these systems which prevent the crystallization of these molecules from the solvents, instead leading to the gelation.

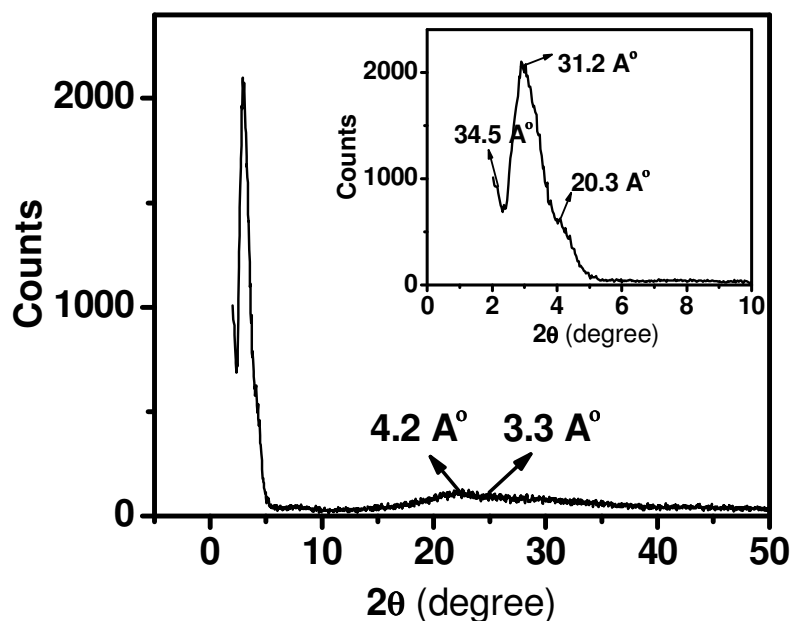


Figure 2.12. XRD pattern of TTV4 xerogel from decane (Inset: XRD pattern at small angle region).

2.3.7. Charge-Carrier Mobility Studies: FP-TRMC and TAS Analyses

Insight into the charge carrier transport property of the gelator, TTV4 on smaller spatial scales, could be obtained from electrode-less flash-photolysis time-resolved microwave conductivity studies [Saeki *et al.* 2008]. Charge carriers were generated photolytically by adding *N,N'*-bis(2,5-di-*tert*-butylphenyl)-3,4,9,10-perylenedicarboximide (PDI) as an electron acceptor [Gosztola *et al.* 2000]. For these studies, 1 mM CHCl₃ solution of PDI was mixed with TTV4 solution. The volume of PDI solution was changed so that 2, 5, and 20 wt% PDI relative to 100 wt% TTV4 was incorporated in the mixed solution. The solutions were drop casted on quartz substrate and dried in vacuum oven. The conductivity was measured using TRMC and the results are shown in Figure 2.13a. It was found that

$\phi\Sigma\mu$ values were progressively increased by addition of small amount of PDI, as a result of efficient electron transfer from **TTV4** to PDI [Terao *et al.* 2009]. For a comparison of the mobility between amorphous and self-assembled films, the **TTV4**/PDI films were dissolved again in decane- CHCl_3 mixed solvent and measured the conductivity. The data are shown in Figure 2.13b, which reveal that the $\phi\Sigma\mu$ values are higher when compared to the values of the film obtained from CHCl_3 . The minimum charge-carrier mobilities ($\Sigma\mu_{\min}$) of **TTV4** films drop casted on quartz plates were determined by dividing $\phi\Sigma\mu$ of TRMC by ϕ , where ϕ (quantum efficiency of charge carrier generation) was estimated from the transient absorption spectra (TAS) of PDI radical anion. The ϕ at the peak of each PDI fraction was estimated by TAS from the absorption of PDI radical anion using its reported extinction coefficient, according to the reported procedure [Gosztola *et al.* 2000]. In the present case, the observed transient absorption of **TTV** radical cation and PDI radical anion are relatively weak. The mobility was estimated indirectly, and it is described by the $\Sigma\mu_{\min}$.

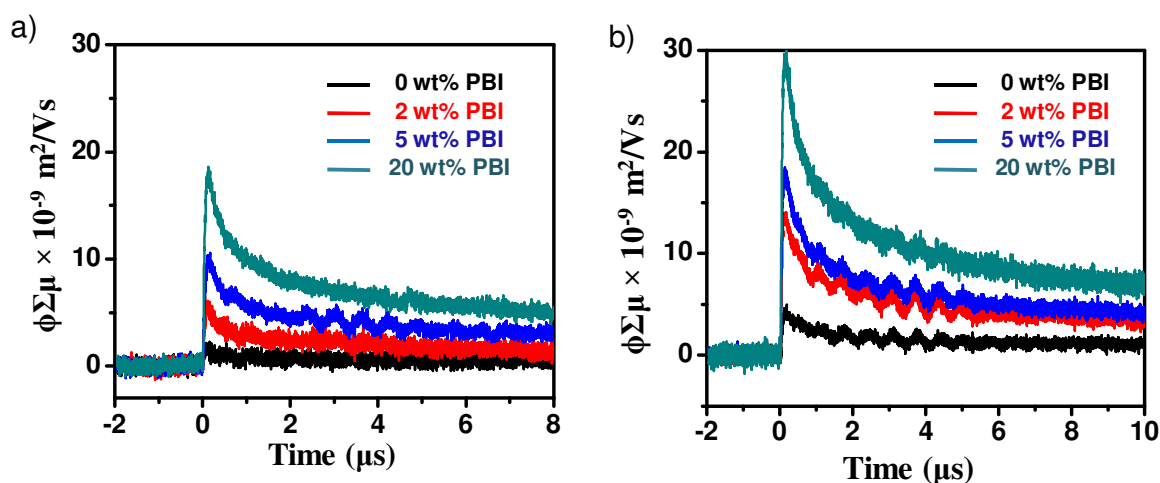


Figure 2.13. FP-TRMC profiles of **TTV4** films prepared with PDI from a) chloroform and b) *n*-decane/chloroform (1:1 v/v) solutions. The color represents weight fraction of PDI relative to 100 wt% **TTV4**.

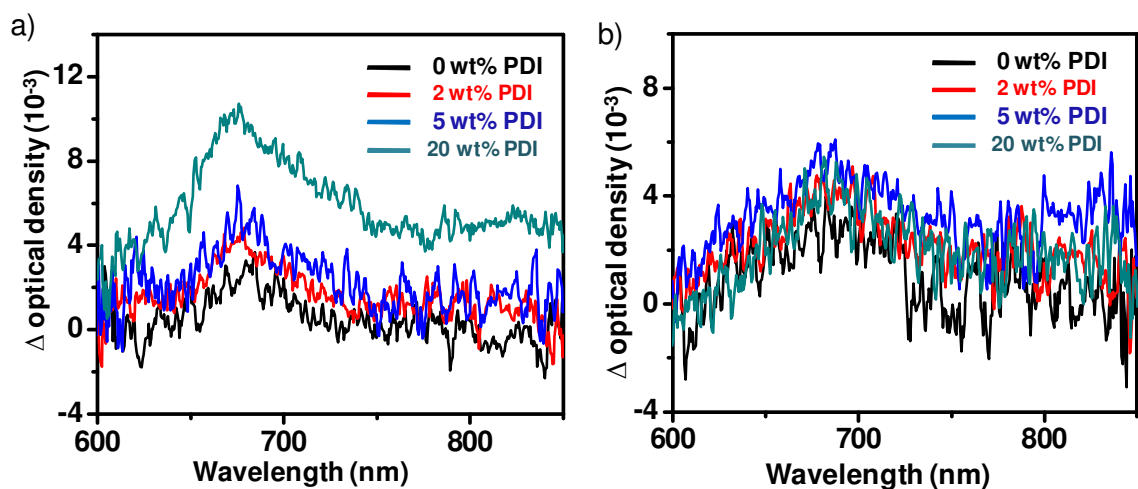


Figure 2.14. Transient absorption spectra ($\lambda_{\text{ex}} = 355 \text{ nm}$) of **TTV4** films prepared with PDI from a) chloroform and b) *n*-decane/chloroform solutions. The color represents weight fraction of PDI relative to 100 wt% **TTV4**.

As seen in Figure 2.14b, the transient absorption intensities of **TTV4** with PDI were decreased in *n*-decane/ CHCl_3 xerogel films. This observation indicates that the quantum efficiency of charge carrier generation (ϕ) is decreased because PDI may be entrapped in **TTV4** assemblies. However, the TRMC transients ($\phi\Sigma\mu$) shown in Figure 2.13b is rather increased in spite of the decrease of ϕ indicating enhanced charge-carrier mobility in the mixed solvent. The absolute value of charge-carrier mobility is not determined in this study, due to the overlap of **TTV4** radical cation and PDI radical anion and weak intensity of their TA spectra. We therefore mention only the “minimum” mobility. This minimum mobility was obtained by averaging the values over 2, 5, and 20 wt% of PDI (Table 2.2). The fluctuation of the value was ca. 15 %. For **TTV4** films prepared by drop-casting of chloroform solutions, the $\Sigma\mu_{\text{min}}$ was $\sim 1.5 \times 10^{-2} \text{ cm}^2 \text{ V}^{-1} \text{ s}^{-1}$. Once the films were prepared from *n*-decane/chloroform (1:1 v/v), the $\Sigma\mu_{\text{min}}$ increased to $6.0 \times 10^{-2} \text{ cm}^2 \text{ V}^{-1} \text{ s}^{-1}$ due to the formation of hydrogen bonded 1D assemblies.

Table 2.2. FP- TRMC and TAS values of **TTV4** in chloroform and *n*-decane/chloroform

PDI wt%	TTV4 in Chloroform			TTV4 in decane/chloroform		
	$\phi \Sigma \mu$ (m ² /Vs)	ϕ	$\Sigma \mu_{\min}$ (cm ² /Vs)	$\phi \Sigma \mu$ (m ² /Vs)	ϕ	$\Sigma \mu_{\min}$ (cm ² /Vs)
2	5.3×10^{-9}	3.9×10^{-3}	1.4×10^{-2}	1.4×10^{-8}	2.2×10^{-3}	5.6×10^{-2}
5	1.1×10^{-8}	6.7×10^{-3}	1.6×10^{-2}	2.1×10^{-8}	2.7×10^{-3}	6.7×10^{-2}
20	1.8×10^{-8}	9.9×10^{-3}	1.8×10^{-2}	3.0×10^{-8}	3.1×10^{-3}	8.9×10^{-2}

In parenthesis, $\phi \Sigma \mu$ is the transient conductivity obtained from TRMC profile. Here, ϕ is the quantum efficiency of charge carrier generation and $\Sigma \mu$ is the sum of charge carrier mobilities. The minimum $\Sigma \mu$ was obtained by dividing $\phi \Sigma \mu$ of TRMC by ϕ . The $\Sigma \mu_{\min}$ was averaged over the PDI concentrations from 2, 5, and 20 wt%.

2.4. Conclusions

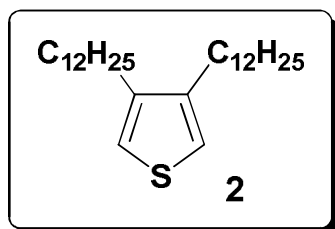
In conclusion, a few thienylenevinylene derivatives (**TTV1-4**) have been synthesized and characterized. Among these derivatives, **TTV3** with carboxylic end groups forms 1D supramolecular polymers whereas **TTV4** having amide functional group self-assembles to supramolecular gels. UV-vis absorption spectral studies revealed that **TTV4** forms hydrogen bonded H-type self-assembly. Interestingly **TTV2** with hydroxyl end groups and **TTV3** with carboxylic acid groups did not form gels in any of the solvents tested indicating that weak hydrogen bonds as in the case of **TTV2** or 1D linear hydrogen bonds as in the case of **TTV3** do not favor gelation. From these observations it is inferred that a network type assembly formed by hydrogen bonding and π -stacking of **TTV4** is responsible for gelation. The FP-TRMC and TAS studies revealed that self-assembly and gelation play important roles in the charge-carrier mobility of **TTV4**. This study highlights the importance of having strong hydrogen bonded and π -stacked molecular assemblies in improving the electronic properties of π -systems.

2.5. Experimental Section

2.5.1. Synthesis and Characterization

Unless otherwise stated, all starting materials and reagents were purchased from commercial suppliers and used without further purification. The solvents and the reagents were purified and dried by standard methods prior to use. Melting points were determined with MEL-Temp-II melting point apparatus. ^1H and ^{13}C NMR spectra were measured on a 300 MHz and 500 MHz Bruker Avance DPX spectrometer using TMS as an internal standard. FT-IR spectra were recorded on a Nicolet Impact 400D infrared spectrometer. Matrix-assisted laser desorption ionization time-of-flight (MALDI-TOF) mass spectra were obtained on a AXIMA-CFR PLUS (SHIMADZU) MALDI-TOF mass spectrometer. High-resolution mass spectra were recorded on a JEOL JM AX 505 HA mass spectrometer. UV-vis spectra were recorded on a Shimadzu UV-3101 PC NIR scanning spectrophotometer.

Synthesis of 3,4-didodecylthiophene (2) : To a suspension of magnesium turnings (0.5 g,

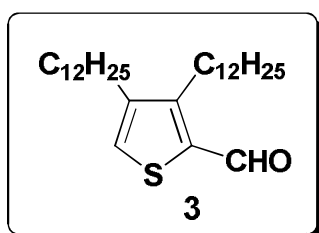


20.8 mmol) in dry ether (20 mL), 1-bromododecane (8 mL, 31.3 mmol) was added drop wise, keeping in an ice bath. The reaction mixture was then allowed to attain room temperature and stirred until the disappearance of magnesium. 3,4-

Dibromothiophene (1 mL, 8.93 mmol) was added followed by the addition of [1,3-bis(diphenylphosphino) propane]-nickel(II)chloride (0.1 g, 0.18 mmol) in ether (50 mL) in drop wise to the reaction mixture. After refluxing for 24 h, the reaction mixture was poured into dilute hydrochloric acid (10%). The aqueous layer was extracted with ether and dried over anhydrous sodium sulphate. The solvent was removed under reduced pressure. The residue was purified by column chromatography (silica gel, hexane) to give a colorless liquid.

(Yield = 65%). ^1H NMR (CDCl_3 , 300 MHz) δ (ppm) = 6.87 (s, 2H), 2.54 (t, 4H,), 1.64-1.57 (m, 4H), 1.39-1.31 (m, 36H), 0.92-0.88 (m, 6H); ^{13}C NMR (CDCl_3 , 75 MHz) δ (ppm) = 142.14, 141.93, 125.06, 123.79, 32.12, 31.96, 31.87, 29.93, 29.68, 29.40, 29.31, 27.26, 22.62, 14.06; GCMS (m/z) = 420.

3,4-Didodecylthiophene-2-carbaldehyde (3): Compound (3) was prepared by Vilsmeier

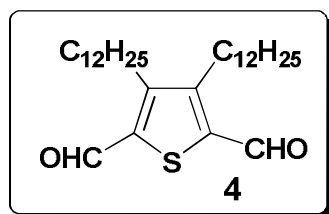


formylation of **2** (5 g, 11.9 mmol), using DMF (5.5 mL, 71.4 mmol) and POCl_3 (4.3 mL, 47.6 mmol) in dry 1,2 dichloroethane (40 mL). After refluxing for 2 h, the reaction mixture was cooled followed by the addition of 1 M sodium acetate. The mixture

was then stirred for 1 h and the solution was extracted with DCM. The organic layer was separated out and dried over Na_2SO_4 . The solvent was removed and the crude product was purified by column chromatography (yellow liquid).

(Yield = 76%). ^1H NMR (CDCl_3 , 300 MHz) δ (ppm) = 10.01 (s, 1H), 7.34 (s, 1H), 2.88 (t, 2H), 2.54 (t, 2H), 1.64 -1.57 (m, 4H), 1.39-1.31 (m, 36H), 0.92-0.88 (m, 6H); ^{13}C NMR (CDCl_3 , 75 MHz) δ (ppm) = 183.59, 151.62, 143.16, 141.93, 32.12, 31.84, 29.56, 29.43, 29.27, 29.24, 26.56, 22.62, 14.04; FAB-MS (m/z) = 450; FT-IR (KBr) = 701, 828, 921, 1000, 1091, 1166, 1352, 1662, 2849 cm^{-1} .

3,4-Didodecylthiophene-2,5-dicarbaldehyde (4): To a solution of compound (2) (4.0 g,



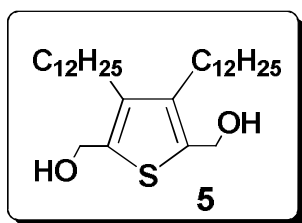
9.52 mmol) and tetramethylethylenediamine (TMEDA) (3.2 mL, 28.6 mmol) in 10 mL of hexane, was added 18 mL of *n*-BuLi (1.6 M in hexane) under an inert atmosphere, and the mixture was refluxed for 30 min. After cooling to room

temperature, THF (50 mL) was added and then the mixture was cooled to $-40\text{ }^\circ\text{C}$, followed

by the drop wise addition of DMF (2.8 mL, 38.1 mmol). The solution was allowed to attain room temperature. It was then poured into 300 mL of 0.5 M aqueous HCl, and vigorously stirred for 15 min. After neutralization with 0.5 M NaHCO₃, the aqueous phase was extracted with diethyl ether, the organic phase was washed with water and dried using anhydrous Na₂SO₄, and the solvent was evaporated. The residue was purified by column chromatography (silica gel, hexane/chloroform).

(Yield: 45%). mp = 44-46 °C. ¹H NMR (CDCl₃, 300 MHz) δ (ppm) = 10.11 (s, 2H), 2.88 (t, 4H), 1.64-1.57 (m, 15H), 1.39-1.31 (m, 40H), 0.92-0.88 (m, 6H); ¹³C NMR (CDCl₃, 75 MHz) δ (ppm) = 183.59, 151.62, 143.16, 141.93, 32.12, 31.84, 29.56, 29.43, 29.27, 29.24, 26.56, 22.62, 14.04; FAB-MS (m/z) : 477.59; FT-IR (KBr) = 690, 772, 801, 921, 1000, 1091, 1166, 1352, 1468, 1664, 2891 cm⁻¹.

3,4-Didodecylthiophene-2,5-diyl)dimethanol (5): **4** (1 g, 2.16 mmol) was dissolved in 30

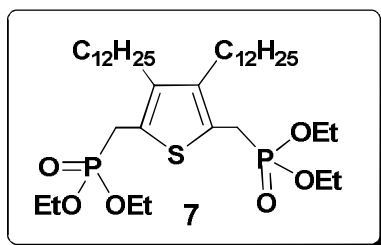


mL of 1:1 CH₂Cl₂/MeOH. NaBH₄ (0.2 g, 6.2 mmol) was added in portions to the reaction mixture and stirred for 30 min. After removal of the solvent, the residue obtained was dissolved in chloroform and washed with water. The organic layer was

separated out and dried over anhydrous Na₂SO₄. The solvent was removed under vacuum resulting in pure product.

(Yield: 92%). mp = 105-107 °C. ¹H NMR (CDCl₃, 300 MHz) δ (ppm) = 4.72 (s, 4H), 2.53 (t, 4H), 1.64-1.57 (m, 15H), 1.39-1.31 (m, 40H), 0.92-0.88 (m, 6H); ¹³C NMR (CDCl₃, 75 MHz) δ (ppm) = 141.93, 140.09, 136.24, 136.15, 58.16, 31.96, 31.87, 29.93, 29.68, 29.40, 29.31, 27.26, 22.62, 14.06; FAB-MS (m/z) = 480.64; FT-IR (KBr) = 698, 784, 801, 921, 1048, 1166, 1352, 2911, 3600 cm⁻¹.

Tetraethyl-3,4-didodecylthiophene-2,5-diyl-diphosphonate (7): To a solution of (3,4-

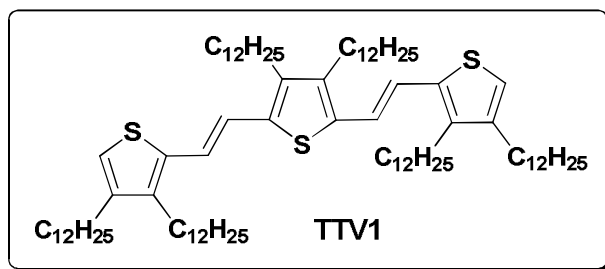


didodecylthiophene-2,5-diyl)dimethanol (1 g, 2.08 mmol), in dichloromethane, PBr_3 (80 μL) was added drop wise keeping the reaction mixture under an ice bath (-5°C) for 4 h in an inert atmosphere. After removal of the solvent,

1equivalent of $\text{P}(\text{OEt}_3)$ was added to the residue and then refluxed at 120°C for 12 h. The crude product was purified by column chromatography (Silica gel/methanol) to give a viscous yellow liquid. (Yield : 65%)

^1H NMR (CDCl_3 , 300 MHz) δ (ppm) = 4.12 (t, 4H), 3.27 (d, 4H), 2.55 (t, 4H), 1.64-1.57 (m, 4H), 1.39-1.31 (m, 40H), 0.92-0.88 (m, 6H); ^{13}C NMR (CDCl_3 , 75 MHz) δ (ppm) = 143.91, 140.18, 136.24, 136.15, 65.16, 63.75, 63.50, 62.02, 58.25, 31.85, 30.53, 29.88, 29.62, 29.39, 29.29, 27.17, 22.61, 17.94, 16.19, 15.98, 14.06; FAB-MS (m/z) = 722.34.

2,2'-(1E,1'E)-2,2'-(3,4-didodecylthiophene-2,5-diyl)bis(ethene-2,1-diyl)bis(3,4-didodecylthiophene) (TTV1): To a mixture of **3** (0.63 g, 1.38 mmol) and **7** (0.5 g, 0.69 mmol) in 30

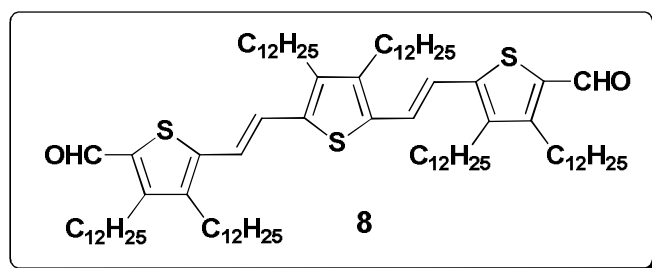


mL of dry THF, *t*-BuOK (0.5 g, 4.14 mmol) was added in portions under nitrogen atmosphere. The reaction mixture was then stirred for 3 h. After removal of

the solvent under reduced pressure, the residue was dissolved in CH_2Cl_2 and washed with water. After extraction, the organic layer was separated out, dried over anhydrous Na_2SO_4 . The solvent was removed under reduced pressure. The crude product was purified by column chromatography (silica gel/hexane). Yield 72%. mp. $118-120^\circ\text{C}$. ^1H NMR (CDCl_3 , 300 MHz, TMS) δ (ppm) = 6.97 (s, 4H), 6.75 (s, 2H), 2.61-2.45 (t, 12H), 1.59 (q, 12H) 1.39-1.31 (m, 120H) , 0.89 (t, 18H); ^{13}C NMR (CDCl_3 , 75 MHz) δ (ppm) = 142.38,

141.10, 140.27, 138.39, 136.08, 133.71, 118.84, 118.29, 30.92, 28.73, 28.69, 28.67, 28.65, 28.60, 28.54, 28.47, 28.41, 28.37, 28.35, 21.68, 13.10; IR (KBr) ν_{\max} = 720, 801, 861, 921, 1026, 1083, 1261, 1377, 1466, 2851, 2922 cm^{-1} ; FAB-MS (m/z) = 1309.7; MALDI-TOF (m/z) = 1309.7 (calculated mass = 1310.38).

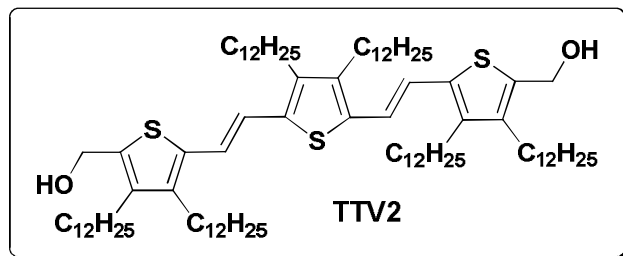
5,5'-(1E,1'E)-2,2'-(3,4-didodecylthiophene-2,5-diyl)bis(ethene-2,1-diyl)bis(3,4-didodecylthiophene-2-carbaldehyde) (8): Compound (8) was prepared by Vilsmeier formylation of



TTV1 (0.4 g, 0.3 mmol), using DMF (0.14 g, 1.8 mmol) and POCl₃ (0.14 g, 1.8 mmol) in dry 1,2 dichloromethane (40 mL). The reaction mixture was

refluxed for 2 h. After cooling the reaction mixture, 1M sodium acetate was added for neutralization. The mixture was further stirred for 1h. Then, the solution was extracted with dichloromethane. The organic layer was separated out and dried over Na₂SO₄. The solvent was removed under reduced pressure and the product was purified by column chromatography using basic alumina (hexane/chloroform 8:2). Yield = 72%, mp. 119-121 °C, ¹H NMR (CDCl₃, 300 MHz) δ (ppm) = 9.97 (m, 2H), 7.22-7.17 (J = 16 Hz, d, 2H), 6.94-6.88 (J = 12 Hz, d, 2H), 2.61-2.45 (t, 12H), 1.59 (q, 12H) 1.39-1.31 (m, 120H), 0.89 (t, 18H); ¹³C NMR (CDCl₃, 75 MHz) δ (ppm) = 181.65, 152.65, 146.75, 143.96, 141.81, 135.72, 122.46, 32.17, 31.47, 31.42, 31.27, 29.24, 27.25, 26.56, 22.66, 14.01; FT-IR (KBr) = 711, 780, 811, 921, 1000, 1091, 1166, 1352, 1468, 1652, 2849, 2918, cm^{-1} ; FAB-MS (m/z) = 1364.37 (calculated mass = 1365.13).

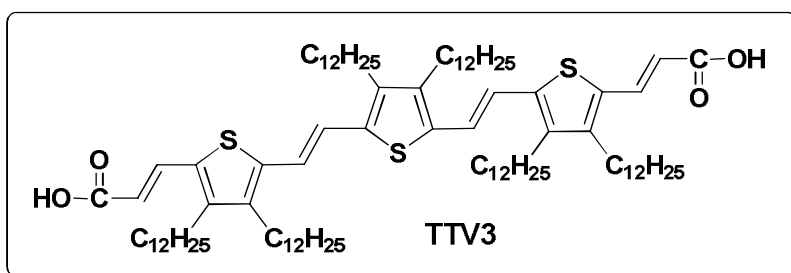
(5,5'-(1E,1'E)-2,2'-(3,4-didodecylthiophene-2,5-diyl)bis(ethene-2,1-diyl)bis(3,4-didodecylthiophene-5,2-diyl))dimethanol (TTV2): Compound (**8**) (0.1 g, 0.07 mmol) was dissolved



in 30 mL of 1:1 CH₂Cl₂/MeOH and then NaBH₄ (0.01 g, 0.21 mmol) was added portion wise to the reaction mixture with stirring for 30 min. After the solvent was

removed under reduced pressure, the residue was dissolved in chloroform and washed with water. The organic layer was separated out, dried over Na₂SO₄ and the solvent was removed under vacuum. The product was precipitated by using CH₂Cl₂/MeOH. Yield 92%. mp. 122-123 °C, ¹H NMR (CDCl₃, 300 MHz) δ (ppm) = 6.88 (s, 4H), 4.68 (s, 4H), 2.49 (t, 12H), 1.59 (s, 12H), 1.39-1.31 (m, 120H), 0.89 (t, 18H); ¹³C NMR (CDCl₃, 75 MHz) δ (ppm) = 141.53, 140.68, 140.61, 136.29, 135.22, 134.96, 119.74, 118.96, 58.46, 31.94, 31.42, 31.27, 29.24, 29.68, 29.49, 29.36, 27.25, 26.56, 22.66, 14.01; IR (KBr) ν_{max} = 716, 772, 798, 921, 1000, 1091, 1166, 1352, 1468, 2849, 2918, 3400 cm⁻¹; FAB-MS (m/z) = 1369.25; MALDI-TOF (m/z) = 1371.8 (calculated mass = 1370.43).

(E)-3-(5-((E)-2-(5-((E)-2-(3,4-didodecyl-5-((E)-3-hydroxybuta-1,3-dienyl)thiophen-2-yl)vinyl)-3,4-didodecylthiophen-2-yl)vinyl)-3,4-didodecylthiophen-2-yl)acrylic acid(TTV3):

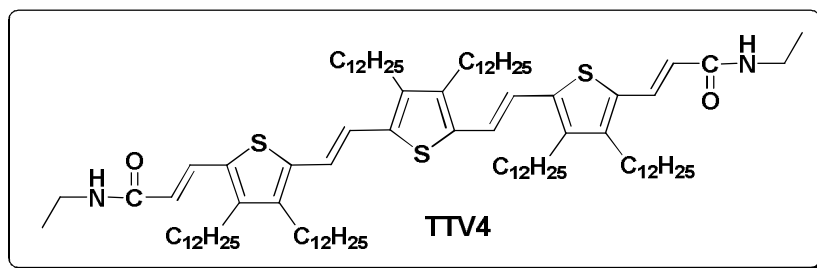


To a mixture of **8** (0.15 g, 0.108 mmol) and 2 equivalents of **9** in 30 mL of dry THF, potassium *tert*-

butoxide was added in portions under nitrogen atmosphere. The reaction mixture was then stirred for 3 h. After removal of the solvent under reduced pressure, the residue was dissolved in CH₂Cl₂ and washed with water. After extraction, the organic layer was separated

out, dried over anhydrous Na_2SO_4 and the solvent was removed under reduced pressure. The crude product was converted to the corresponding acid by hydrolysis using KOH in Methanol/THF mixture. Yield 90%, mp. 133-135 °C, ^1H NMR (CDCl_3 , 300 MHz) δ (ppm) = 7.93-7.88 (J = 15.5 Hz, d, 2H), 7.11-7.05 (J = 15.3 Hz, d, 2H), 6.99-6.94 (J = 15.5 Hz, d, 2H), 6.17-6.12 (J = 15.0 Hz, d, 2H), 2.61-2.45 (t, 12H), 1.59 (q, 12H) 1.39-1.31 (m, 120H) , 0.89 (t, 18H); ^{13}C NMR (CDCl_3 , 75 MHz) δ (ppm) = 171.65, 152.65, 148.20, 143.03, 141.70, 140.52, 137.52, 135.72, 131.60, 122.06, 119.37, 116.96, 114.31, 108.23, 107.69, 32.17, 31.47, 31.42, 31.27, 29.24, 27.25, 26.56, 22.66, 14.01; IR (KBr) ν_{max} = 718, 801, 861, 921, 1026, 1083, 1262, 1377, 1466, 1673, 1731, 2849, 2922, 3435 cm^{-1} ; FAB-MS (m/z) = 1449.92; MALDI-TOF (m/z) = 1449.92 (calculated mass = 1450.47).

(E)-3-(5-((E)-2-(5-((E)-2-(3,4-didodecyl-5-((E)-3-(ethylamino)buta-1,3-dienyl)thiophen-2-yl)vinyl)-3,4-didodecylthiophen-2-yl)vinyl)-3,4-didodecylthiophen-2-yl)-N-ethylacryl amide (TTV4): To an ice cooled solution of TTV3 (0.15 g, 0.103 mmol), in dry chloroform



(30 mL), ethylamine (0.011 g, 0.25 mmol) and HATU (0.08 g, 0.192 mmol) were added. Then,

diisopropylethylamine (0.056 g, 0.4 mmol) was added drop wise to the reaction mixture and stirred at room temperature for 12 h. After removal of the solvent, the residue was dissolved in chloroform and washed with water. After extraction with chloroform, the organic layer was separated and dried over Na_2SO_4 . The solvent was evaporated under vacuum. The crude product was purified by column chromatography (basic alumina, (hexane/ethyl acetate 8:2) resulting in the pure product as a red solid compound. Yield 47 %, mp. 138-140 °C, ^1H NMR (CDCl_3 , 300 MHz) δ (ppm) = 7.82-7.77 (J = 14.9 Hz, d, 2H), 7.01 (d, 2H), 6.95-6.89

(J = 15.9 Hz, d, 2H), 6.12-6.07 (J = 14.9 Hz, d, 2H), 5.58 (t, 2H), 3.44 (t, 4H), 2.61-2.45 (t, 12H), 1.59 (q, 12H) 1.39-1.31 (m, 120H) , 0.89 (t, 18H); ^{13}C NMR (CDCl_3 , 75 MHz) δ (ppm) = 165.84, 146.60, 142.19, 141.60, 138.01, 135.31, 132.06, 131.93, 120.76, 119.23, 118.19, 34.59, 31.90, 31.69, 31.27, 29.24, 27.25, 26.56, 22.66, 14.01; FT-IR (KBr) ν_{max} = 720, 816, 930, 1019, 1257, 1479, 1544, 1638, 2849, 2920, 3291 cm^{-1} ; FAB-MS (m/z) = 1504.50; MALDI-TOF (m/z) = 1504.97 (calculated mass =1504.61).

2.5.2. Description of Experimental Techniques

Optical Measurements: Electronic absorption spectra of **TTV1-4** were recorded on a Shimadzu UV-3101 PC NIR scanning spectrophotometer. Temperature dependent absorption studies were carried out either in a 0.1 cm or 1 cm quartz cuvette with a thermistor directly attached to the wall of the cuvette holder at a heating and cooling rate of 2 $^{\circ}\text{C}/\text{min}$.

General procedure for gelation: The gelation studies were carried out as per reported procedures [George *et al.* 2005]. A definite amount of **TTV4** was added to 1 mL of a required solvent in a glass vial and heated to dissolve the gelator. After cooling to ambient temperature, the vessel was turned upside down to verify the gel formation. The reversibility of the gelation was confirmed by repeated heating, and cooling. The critical gelator concentration of **TTV4** was determined from the minimum amount of gelator required for the formation of gel at room temperature. The xerogels were prepared by removing the solvents under reduced pressure at room temperature.

Gel Melting Temperature (T_{gel}) Determination: The T_{gel} values were determined by the dropping ball method [Murata *et al.* 1994]. In a dropping ball method, a steel ball was placed on the top of a 1mL volume of the gel in a glass vial of diameter (0.5 cm) and the vial was

sealed. Then the gel was slowly heated (2 °C/min) and the temperature at which the ball reaches the bottom of vial was taken as the gel-sol transition temperature (T_{gel}).

Transmission Electron Microscopy (TEM): TEM studies were carried out using a FEI (TECNAI G² 30 S-TWIN) with an accelerating voltage of 100 kV. Samples were prepared by drop casting of decane solutions of **TTV1-4** on to carbon coated copper grids at the required concentrations at ambient conditions. The solvent was removed under vacuum. TEM images were obtained without staining.

Atomic Force Microscopy (AFM): Atomic Force Microscopy images were recorded under ambient conditions using a NTEGRA (NT-MDT) microscope operating with a tapping mode regime. Micro-fabricated TiN cantilever tips (NSG10) with a resonance frequency of 299 kHz and a spring constant of 20-80 Nm⁻¹ were used. AFM section analysis was done offline. Samples for the imaging were prepared by drop casting the **TTV1-4** solution on silicon wafer at the required concentrations at ambient conditions.

Flash-Photolysis Time Resolved Microwave Conductivity (FP-TRMC): Third harmonic generation (355 nm) of a Nd:YAG laser (5-8 ns pulse duration, Spectra Physics GCR-130, incident photon density to a sample was set to $9.5 \times 10^{15} \text{ cm}^{-2}$) was used as an excitation source for TRMC and transient absorption spectroscopy. The transient photoconductivity ($\Delta\sigma$) was measured by TRMC using 3 mW X-band (~9.1 GHz) microwave. The obtained transient conductivity ($\Delta\sigma$ in S m⁻¹) was converted to the product of the quantum yield: ϕ and the sum of charge carrier mobilities: ($\Sigma\mu = \mu_+ + \mu_-$), by $\phi\Sigma\mu = \Delta\sigma (eI_0F_{\text{light}})^{-1}$, where e , I_0 , and F_{Light} are the unit charge of a single electron, incident photon density of excitation laser (in m⁻²), a correction (or filling) factor (in m⁻¹), respectively. The F_{Light} was calculated by taking into consideration the geometry and optical properties of the sample such as the size, laser cross-section, and absorption of the excitation laser. A white light continuum from a Xe

lamp was used as a probe light for TAS. The probe light was guided into a wide-dynamic-range streak camera (Hamamatsu C7700) which collects two-dimensional image of the spectrum and time profiles of light intensity. The details of the system were reported previously. All the experiments were carried out at room temperature. PDI was used as an acceptor. The chloroform solutions of **TTV4** and PDI were mixed according to the fraction of each weight, giving the mixed solutions of 0-20 wt% PDI relative to 100 wt% **TTV4**. The solutions were drop-casted on a quartz plate and dried in vacuum at 40 °C. After the TRMC and TAS measurements, the films were treated by *n*-decane/chloroform mixed solvent (1:1 v/v) and dried in vacuum at 100 °C. TRMC and TAS of these films were performed again. The TAS showed the absorption of PDI radical anion and **TTV4** radical cation at visible to near-infrared (ca. 600-850 nm).

Epitaxial Self-Assembly and High Conductivity of Oligo(thienylenevinylene) Molecular Gelators

3.1. Abstract

Effect of conjugation length on the self-assembly, gelation and conducting properties of the oligo(thienylenevinylene) derivatives OTV1-3 are described. These molecules form hydrogen bond assisted 1D self-assembly leading to supramolecular gels. OTV3 with extended conjugation formed a strong gel when compared to the less conjugated OTV2 and OTV1. TEM analysis of the self-assemblies revealed the formation of elongated fibrous structures. Interestingly, AFM studies revealed that these gels exhibit the unique property of solution phase epitaxy leading to the alignment of fibres on mica surface. However, entangled micrometer sized fibres are formed on silicon wafer and HOPG substrates with diameter ranging from 50-200 nm in width and several micrometer in length. The electrical conductivity data revealed high conductivity for OTV3 after doping with iodine which indicates that the extended conjugation length and strong gelation in OTV3 have resulted in efficient charge carrier transport upon doping with iodine.

3.2. Introduction

Self-assembled organic nanostructures of semiconducting molecules which resemble the electronic properties of inorganic semiconductors are important in the field

of organic electronics [Forrest *et al.* 2004; Hoeben *et al.* 2005; Schenning *et al.* 2005; Ariga *et al.* 2008]. Supramolecular self-assembly is one of the promising approaches for the bottom-up fabrication of molecular materials [Service *et al.* 2002; Lehn *et al.* 2002; Kato *et al.* 2002; Sawamura *et al.* 2002; Ikkala *et al.* 2004; Ajayaghosh *et al.* 2005]. For example, molecular self-assembly from solution state often leads to the formation of one-dimensional (1D) fibres [Shinkai *et al.* 1998; Würthner *et al.* 2004; Weiss *et al.* 2005]. This process has attracted attention because 1D fibrous solids, ranging from the submicrometer to nanometer scale are easily obtained by simple self-assembly through noncovalent interactions such as hydrogen bonding, van der Waals interactions, and π - π stacking in a variety of solvents. The network formation of the fibres in the solvents leads to the formation of physical gels [Abdallah *et al.* 2000]. Gels formed by electroactive groups are excellent candidates for the preparation of conducting supramolecular nanowires [Puigmartí-Luis *et al.* 2007].

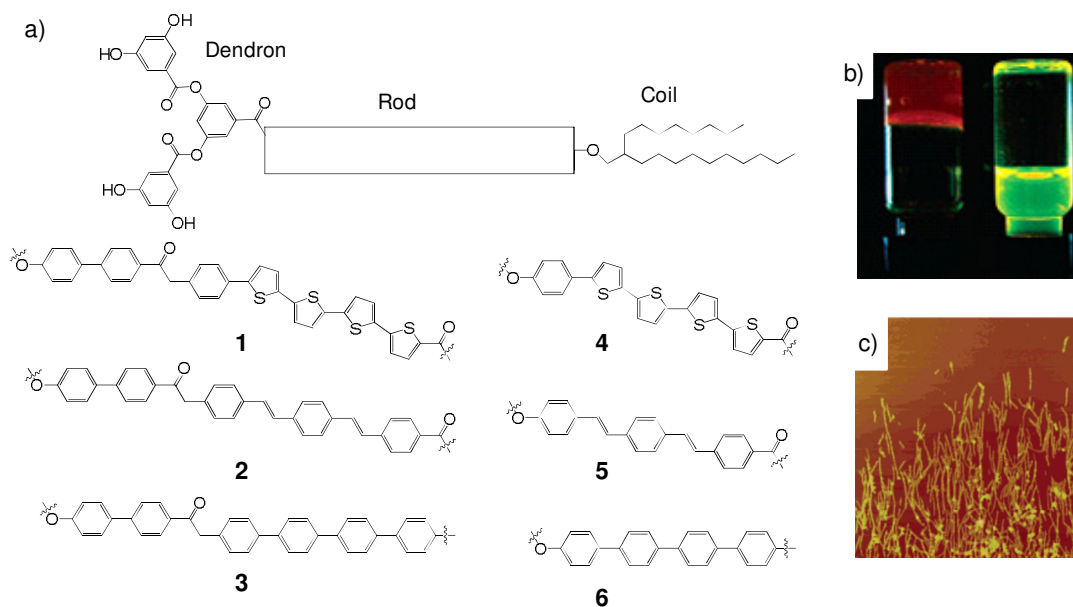


Figure 3.1. a) General structure of the dendron-rod-coils. b) Photographs of **4** in toluene (left) and THF (right) under illumination with 365 nm light and c) AFM texture of **4** under electric field.

Stupp and co-workers have demonstrated the self-assembly of a series of linear π -conjugated molecules with dendron rod-coil architecture of oligo(thiophene), oligo(phenylenevinylene) and oligo(phenylene) (**1-6**) (Figure 3.1a) [Messmore *et al.* 2004]. Morphological studies revealed that these molecules self-assemble into high aspect ratio ribbon-like nanostructures which induce gelation in nonpolar solvents at higher concentrations (Figure 3.1b). Self-assembly leads to three orders of magnitude increase in the conductivity of iodine-doped films of **1** and **4**. Electric field alignment of these assemblies creates arrays of self-assembled nanowires on suitable substrates which is useful for the fabrication of electronic devices (Figure 3.1c).

Kawano *et al.* have reported redox responsive organogels based on oligothiophenes (**7-9**) bearing cholesteryl groups at both ends [Kawano *et al.* 2005]. These molecules have shown unique thermochromic properties during sol-gel transition in nonpolar solvents. The TEM images have displayed well-developed network structures composed of fibrous aggregates (Figure 3.2a-c). Moreover, the AFM images offered important evidence of unimolecular helical aggregates of **9**.

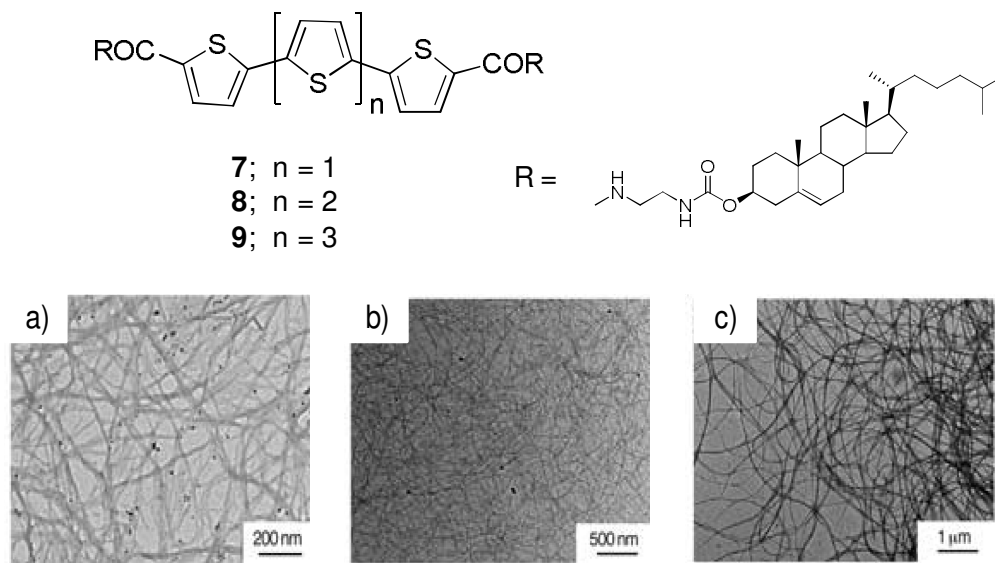


Figure 3.2. TEM image of xerogels prepared from a) **7** (1.0 mM in 1,1,2,2-tetrachloroethane (TCE)), b) **8** (2.9 mM in TCE), and c) **9** (3.8 mM in TCE).

Amabilino and co-workers have made significant contributions in the field of conducting gels based on tetrathiafulvalenes (TTF) [Puigmurrtí-Luis *et al.* 2007]. For example, the amide-functionalized TTF derivative **10** forms stable gels with high conductivity in decane or hexane. TEM images of the xerogel showed the presence of a complex network of fibres. Four-probe dc resistivity measurements have revealed an average conductivity (σ) of 3.5×10^{-3} S/cm at room temperature for the as-prepared doped xerogels. The I - V responses with semiconductor-like character are probably associated with a network of nanocontacts between these metallic wires (Figure 3.3b). These results showed the power of non-covalent bonds in the self-assembly processes that can lead to electrically conducting nanoscale supramolecular wires. The ease of the processing method makes it very appealing for applications in molecular electronics.

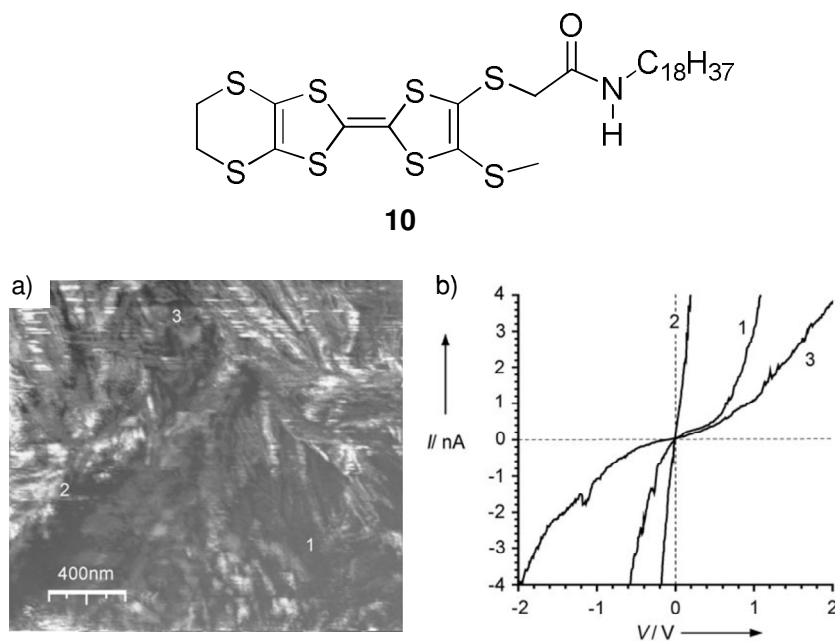


Figure 3.3. a) Current-sensing AFM image showing the current response of a doped and annealed xerogel of **10** on graphite. b) Representative I - V curves of different areas of the material which correspond to the numbered areas in image a.

In order to improve the electrical conductivity in self-assembled films, controlled orientation of organic semiconducting molecules is necessary [Liu *et al.*

2009]. To achieve the alignment of semiconducting molecules on surface, epitaxy approach is one of the best strategy [Yanagi *et al.* 2003; Koller *et al.* 2004; Cicoira *et al.* 2006; Dienel *et al.* 2008]. When dealing with organic thin films, the term epitaxy refers to the growth of a crystalline film on the surface of a crystal substrate, if one of these two requirements are met: (1) the existence of a commensurate relationship between the crystal lattice of the molecular layer and that of the substrate; (2) in the case where the substrate and the film are incommensurate, the existence of a well-defined orientational relationship between the film and the substrate unit cell [Forrest *et al.* 1997; Sassella *et al.* 2007]. The molecular film order and the growth mode depend on many parameters (nature of the substrate, substrate temperature, deposition rate) and are determined by the balance between molecule-molecule and molecule-substrate interactions. It is well known that organic thin films grow epitaxially on alkali halide substrates by various deposition techniques such as molecular beam epitaxy and chemical vapor deposition process [Borghesi *et al.* 2001; Resel *et al.* 2003; Sassella *et al.* 2007]. Nakamura and co-workers have reported the epitaxial growth of bis-tetrathiafulvalene substituted macrocycle and tetrafluorotetracyanoquinodimethane (**11**) (Figure 3.4) complex on mica substrate [Akutagawa *et al.* 2002]. AFM analysis showed nanowires, oriented to specific directions from a dilute aqueous potassium chloride subphase, corresponding to the directions of the potassium-ion array on the mica surface having a six fold symmetry (Figure 3.4a and b). The conductivity of the nanowires was estimated to be of the order of 10^{-3} Scm^{-1} . The films showed a semiconducting behavior in the measurement of temperature-dependent conductivity. Wang *et al.* have developed weak epitaxial growth (WEG) approach, which allows the molecules to stand up on the substrate by reducing the interaction between organic molecules and inorganic substrates [Wang *et al.* 2007]. In this approach, a thin layer of the rod-like oligomer **13** (Figure 3.5) is first deposited on a substrate to form large monodomains (Figure 3.5a). Then a disk-like molecule, such as

zinc phthalocyanine (**12**), was deposited on top of **13**. It was observed that oriented domains of **12** can be obtained in this way (Figure 3.5b and c). When compared with ZnPc films on SiO₂ (Figure 3.5d), the grain size of single-crystalline domains of **12** on

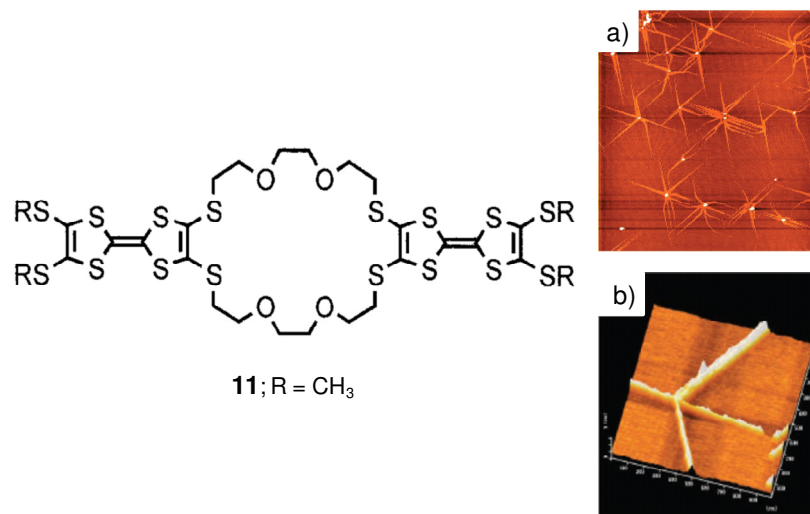


Figure 3.4. a) AFM (30 × 30 μm²) image of the nanowires on mica, formed by the horizontal lifting method deposited from 0.01 M KCl aqueous solution. b) AFM image of a nanowire junction.

the surface of the molecule **13** is much larger. The results from electron diffraction study indicate incommensurate growth of **12** on **13**. The **12** (30 nm)/**13** (2 nm) OFETs exhibited mobilities as high as 0.32 cm² V⁻¹ s⁻¹, which is of the same level as single-crystal transistors with metal-phthalocyanine materials [Zeis *et al.* 2005; De Boer *et al.* 2005].

In many cases, hierarchical self-assembly of 1D structures of organic molecules may lead to gelation of solvents, which allow the direct transfer of the self-assembled structures on to various substrates [Zhang *et al.* 2008; Palmer *et al.* 2008]. Using this approach organogels of semiconducting molecules comprising of electronically active nanowire networks with high electrical conductivity can be prepared for potential applications [Kitamura *et al.* 2005; Kitahara *et al.* 2005; Wang *et al.* 2005; Akutagawa *et al.* 2005; Würthner *et al.* 2005; Würthner *et al.* 2008; Puigmartí-Luis *et al.* 2008; Puigmartí-Luis *et al.* 2010]. Organogelators based on thiophene derivatives are relatively

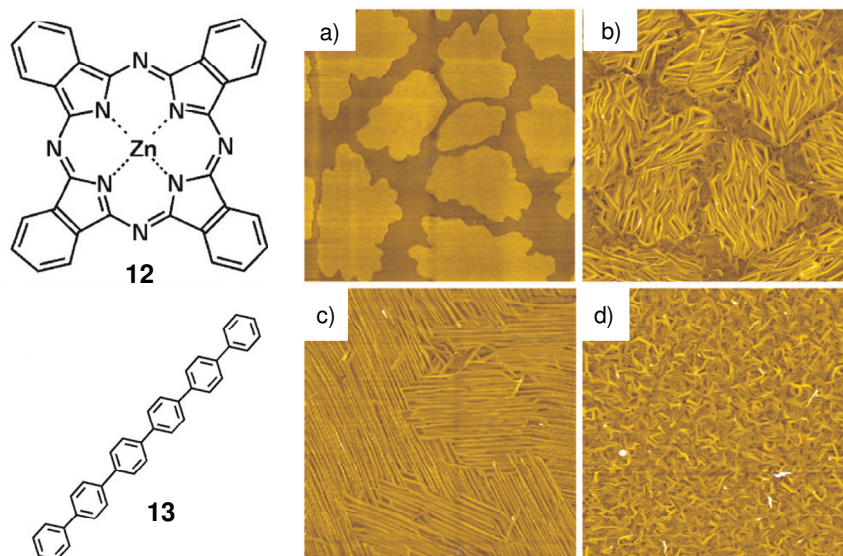


Figure 3.5. AFM images ($10\ \mu\text{m} \times 10\ \mu\text{m}$) of organic thin-films. a) **13** (2 nm) grown on SiO₂, b) **12** (3 nm) on **13** (2 nm), c) **13** (30 nm) on **12** (2 nm), and d) **13** (30 nm) on SiO₂.

very few despite the wide ranging application of this class of molecules in organic electronic devices [van Esch *et al.* 2000; Messmore *et al.* 2004]. In this context, oligo(thienylenevinylene) derivatives (OTVs) reported by Roncali *et al.* are appropriate to the design of conducting gels due to their favorable electronic and redox properties [Jestín *et al.* 2008]. **OTV1** based conducting gel that forms hydrogen bonded networks with high charge carrier mobility is already described in Chapter 2 of this thesis. This study has prompted us to explore the possibility of thienylenevinylenes with different conjugation length, in search of organogelators with metallic conductivity which may be useful for electronic devices such as bulk heterojunction organic solar cells. Herein we present the synthesis, self-assembly, gelation and electrical conducting properties of a few molecular wires, **OTV1-3**, having molecular lengths of ca. 2.7-4.9 nm, which form amide hydrogen bond assisted 1D self-assembly leading to supramolecular gels with semiconducting to metallic conductivity (Chart 3.1). **OTV1-3** having different conjugation length were synthesized from the corresponding thiophene derivative by

multi step procedures. These derivatives were characterized by ^1H NMR, ^{13}C NMR, MALDI-TOF and FT-IR spectroscopic techniques.

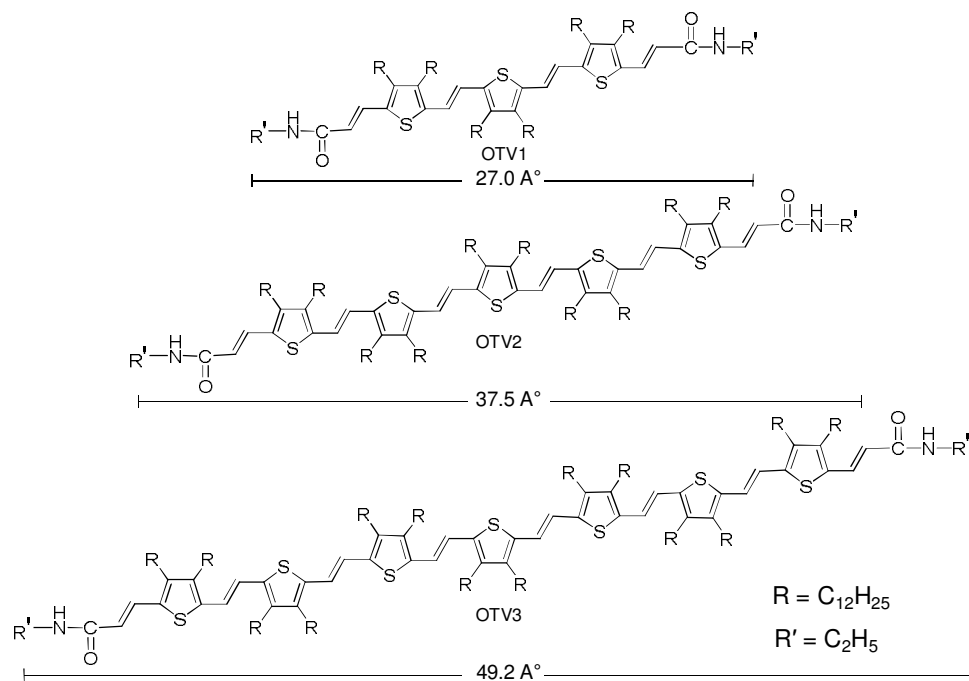


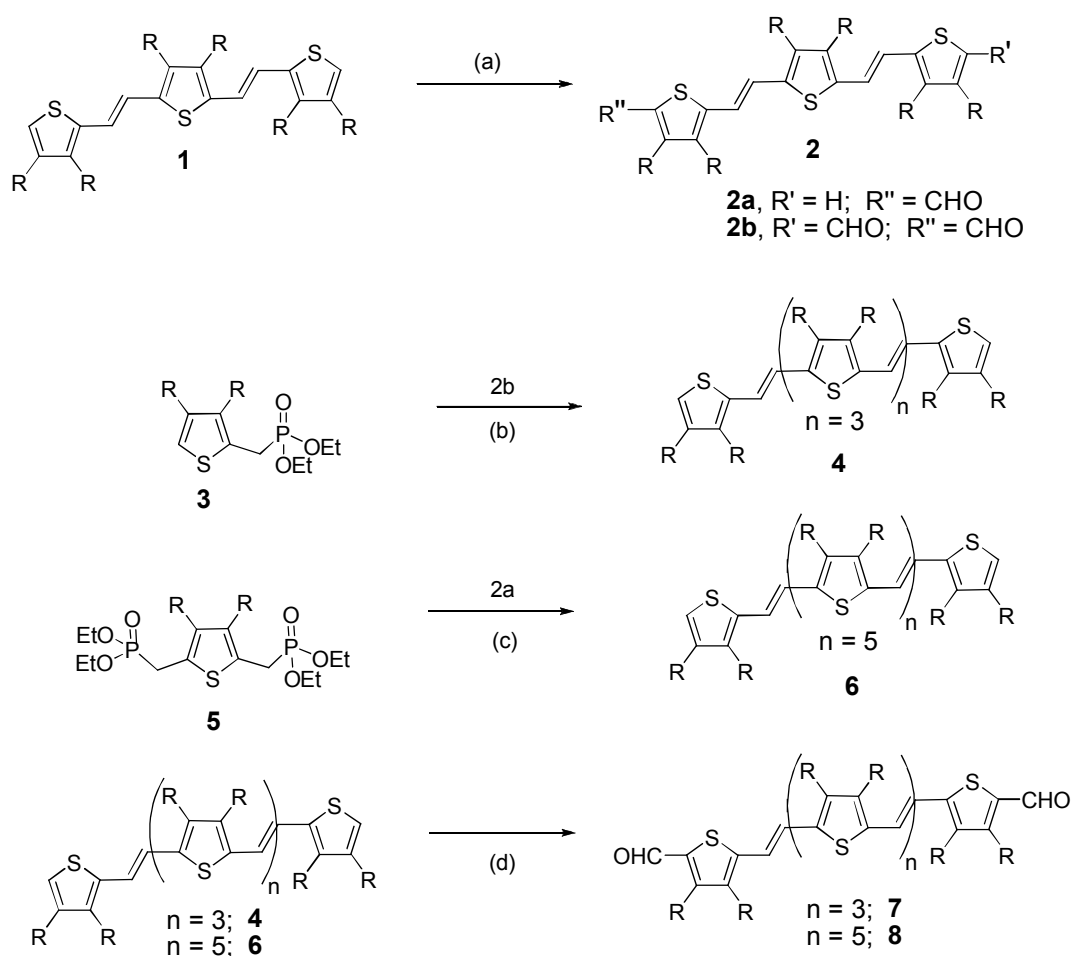
Chart 3.1

3.3. Results and Discussions

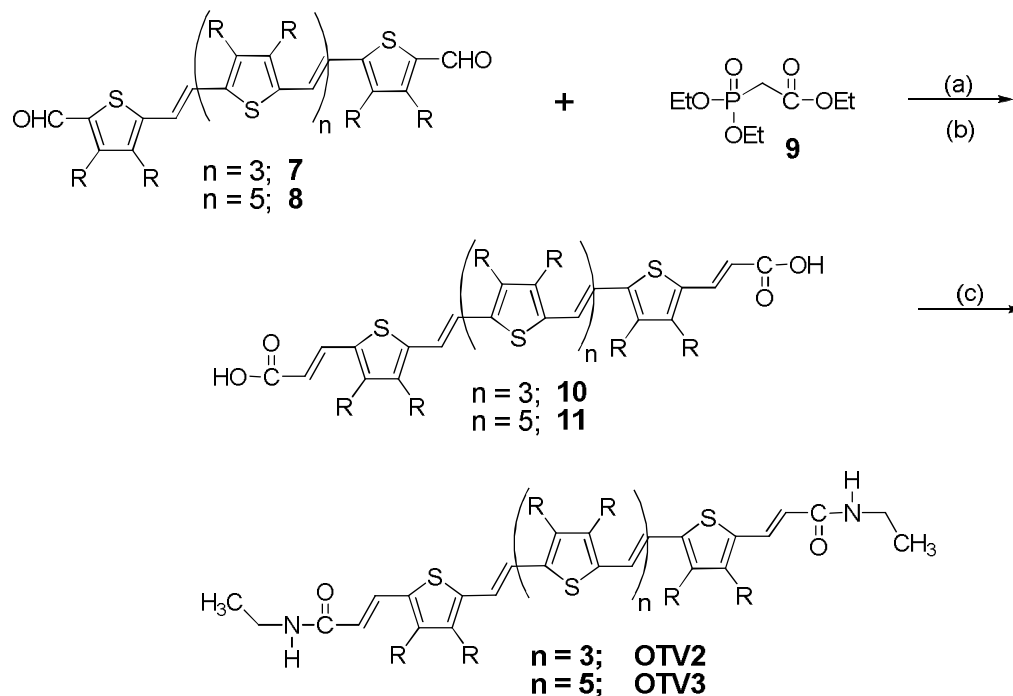
3.3.1. Synthesis of OTVs

Synthesis and characterization of **OTV1** is reported in Chapter 2. **OTV2** and **OTV3** were prepared by a known synthetic strategy (Scheme 3.1 and 3.2). Compound **1** was converted to 5-((E)-2-(5-((E)-2-(3,4-didodecylthiophen-2-yl)vinyl)-3,4-didodecylthiophen-2-yl)vinyl)-3,4-didodecylthiophene-2-carbaldehyde (**2a**) and 5,5'-(1E,1'E)-2,2'-(3,4-didodecylthiophene-2,5-diyl)bis(ethane-2,1-diyl)bis(3,4-didodecylthiophene-2-carbaldehyde) (**2b**) by using Vilsmeier formylation reaction. Compounds **4** and **6**, were synthesized from **2a** and **2b** respectively by treating with phosphonate esters **3** and **5** followed by Wittig-Horner olefination and then converting into bisaldehydes **7** and **8** using Vilsmeier formylation as shown in Scheme 3.1. Reaction of the **7** and **8** with the

phosphonate ester **9** followed by hydrolysis in basic media gave the corresponding carboxylic acid derivatives **10** and **11**. **OTV2** and **OTV3** were obtained by the reaction of **10** and **11** with ethylamine using HATU as the coupling agent in 35% and 28% yields respectively. These thienylenevinylene derivatives **OTV2** and **OTV3** were characterized by ^1H NMR, ^{13}C NMR, FAB-MS, MALDI-TOF-MS and FT-IR spectral analysis. In the ^1H NMR spectra of **OTV2**, the vinylic protons appeared in the range of $\delta = 6.95\text{-}6.91$ ppm ($J \sim 12$ Hz), whereas in the case of **OTV3**, the vinylic protons appeared at $\delta = 6.98\text{-}6.92$ ppm ($J \sim 18$ Hz), indicating the presence of *trans* double bonds.



Scheme 3.1. Reagents and conditions: (a) POCl_3 , DMF, 1,2 DCE, 2 h, 70°C , 68%; (b) *t*-BuOK, THF, 2 h, 30°C , 74%; (c) *t*-BuOK, THF, 2 h, 30°C , 62%; (d) POCl_3 , DMF, 1,2 DCE, 2 h, 70°C , 68%. (R = $\text{C}_{12}\text{H}_{25}$).



Scheme 3.2. Synthesis of **OTV2** and **OTV3**. Reagents and conditions: (a) *t*-BuOK, THF, 2 h, 30 °C, 94% ; (b) KOH, THF, MeOH, TFA, 4 h, 70 °C, 91% ; (c) C₂H₅NH₂, HATU, DIPEA, CHCl₃, 12 h, 30 °C. **OTV2** (35%) and **OTV3** (28%). (R = C₁₂H₂₅).

3.3.2. UV-vis Absorption Spectral Studies

UV-vis absorption spectra of **OTV1-3** were measured in chloroform and decane which are shown in Figure 3.6a and 3.6b respectively. In chloroform, **OTV1-3** (1.5×10^{-4} M) exhibited the π - π^* transition bands at 501, 544 and 561 nm, respectively (Figure 3.6a). The gradual red-shift in the absorption maximum ($\Delta\lambda_{\text{max}} = 60$ nm) is the result of the increasing conjugation length that allows delocalization of the π -electrons along the molecule. The absorption spectrum in chloroform did not show any considerable change with variation in concentration or temperature indicating that the molecules exist in the isotropic state. However, in decane (1.5×10^{-4} M), it showed blue-shifted absorption maxima with red-shifted shoulder bands indicating aggregation of the molecules (Figure 3.6b). For example, the absorption maximum of **OTV1** is blue shifted to 464 nm from 501 nm ($\Delta\lambda = 37$ nm) with the appearance of a shoulder band at 550 nm

when compared to the molecularly dissolved species in chloroform. **OTV2** exhibited a blue shifted absorption maximum at 521 nm ($\Delta\lambda = 23$ nm) with a shoulder band at 626 nm whereas **OTV3** showed an absorption maximum at 549 nm ($\Delta\lambda = 12$ nm) with the shoulder band shifting to a higher wavelength region at 661 nm. These observations indicate H-type excitonic interaction in **OTVs** through the head-to-head 1D amide hydrogen bonding in decane. The aggregation of **OTV1-3** is confirmed by temperature dependent UV-vis spectral studies in decane. For example, **OTV2** showed a red shift in the absorption maximum at 521 nm and the disappearance of the shoulder band at 626 nm through an isosbestic point at 600 nm upon increasing the temperature from 20-70 °C (Figure 3.7a). A similar thermal transition of **OTV3** absorption spectrum is shown in Figure 3.7b. The thermal stability of the self-assemblies of **OTV1-3** is determined from the plots of the fraction of aggregates, as obtained from the temperature dependent absorption spectral changes. Figure 3.7c represents the melting transition curves for **OTV1-3** with increase in temperature. The melting temperature of **OTV1-3** were obtained at 48 °C, 55 °C and 60 °C respectively, which indicates that **OTV3** aggregates have more stability when compared to that of **OTV1** and **OTV2**.

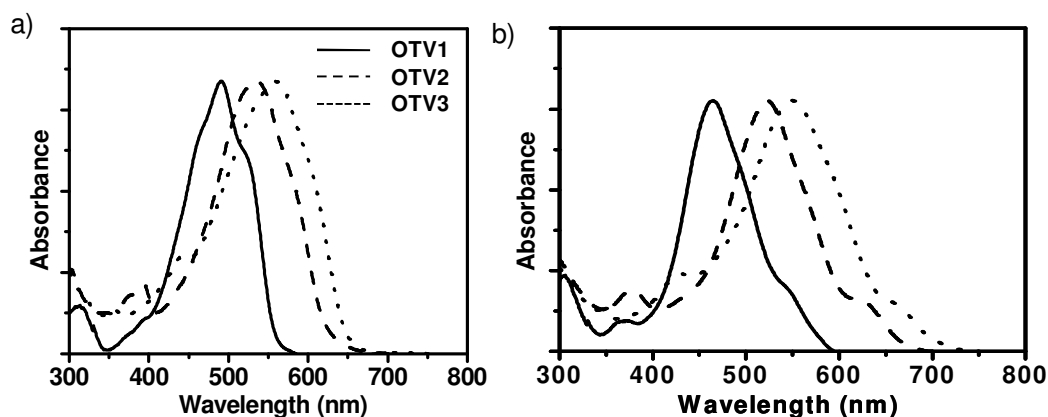


Figure 3.6. Normalized absorption spectra of **OTV1**, **OTV2**, and **OTV3** a) in chloroform and b) in decane.

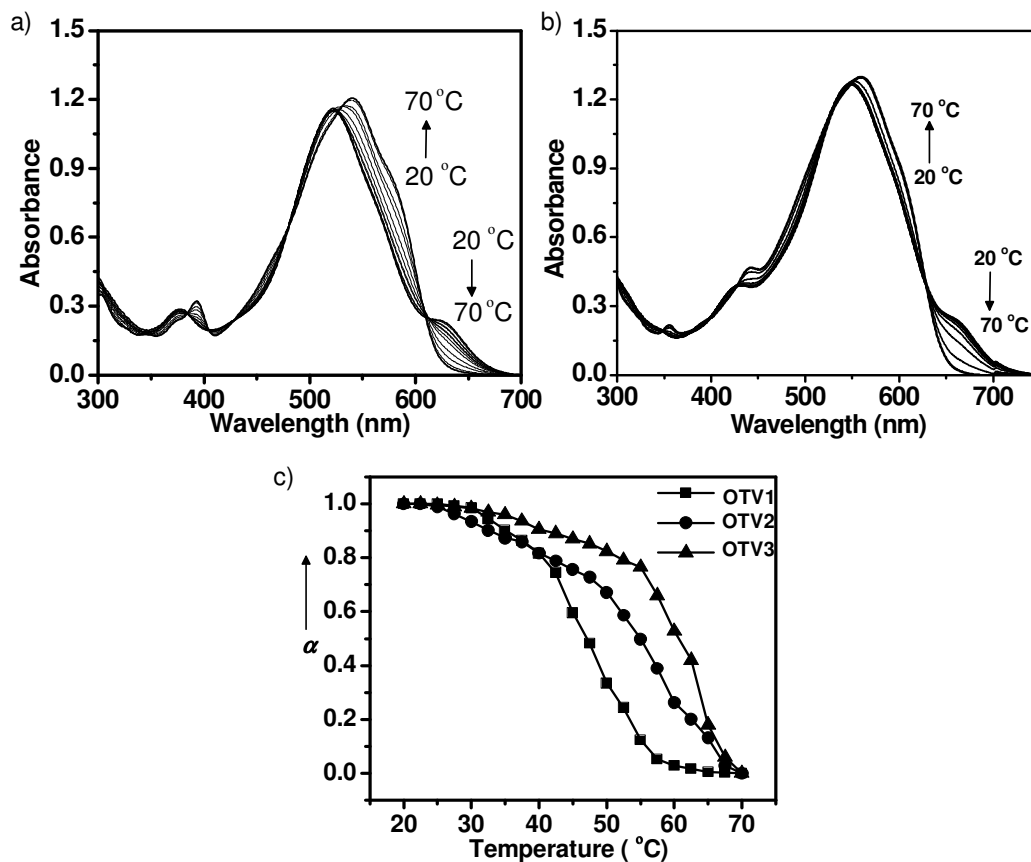


Figure 3.7. Temperature dependent absorption spectra of a) **OTV2** and b) **OTV3** in decane. c) Plots of the fraction of aggregate (α) versus temperature monitored at 491 nm for **OTV1**, 539 nm for **OTV2** and 561 nm for **OTV3**. Concentration of the solutions are kept at 1.5×10^{-4} M in all cases.

3.3.3. Gelation Studies

The gelation properties of **OTV1** is described in Chapter 2. **OTV2** and **OTV3** exhibited similar gelation behavior in a variety of nonpolar solvents at concentrations above 0.4 mM. The color of the gels varies from red for **OTV1** to purple for **OTV2** and deep blue-black for **OTV3** respectively (Figure 3.8a). The critical gelator concentration (CGC) to form a stable gel of **OTV1** in decane is 0.98 mM whereas that of **OTV2** and **OTV3** is 0.66 and 0.44 mM, respectively and hence **OTV3** belongs to the class of super gelators. A comparison of the gelation properties of **OTV1-3** is presented in Table 3.1.

Table 3.1. Gelation data of **OTV1**, **OTV2** and **OTV3** in polar and non-polar solvents

SI. No.	Solvent	Nature of gel	CGC		
			OTV1 (mM)	OTV2 (mM)	OTV3 (mM)
1.	Decane	G	0.98	0.66	0.44
2.	Cyclohexane	G	1.22	0.84	0.56
3.	Benzene	G	4.61	2.92	2.13
4.	Toluene	G	5.29	3.34	2.43
5.	Chloroform	S	-	-	-
6.	Methanol	NS	-	-	-
7.	DMSO	NS	-	-	-

In parenthesis, G = gel, S = soluble and NS = not soluble at room temperature.

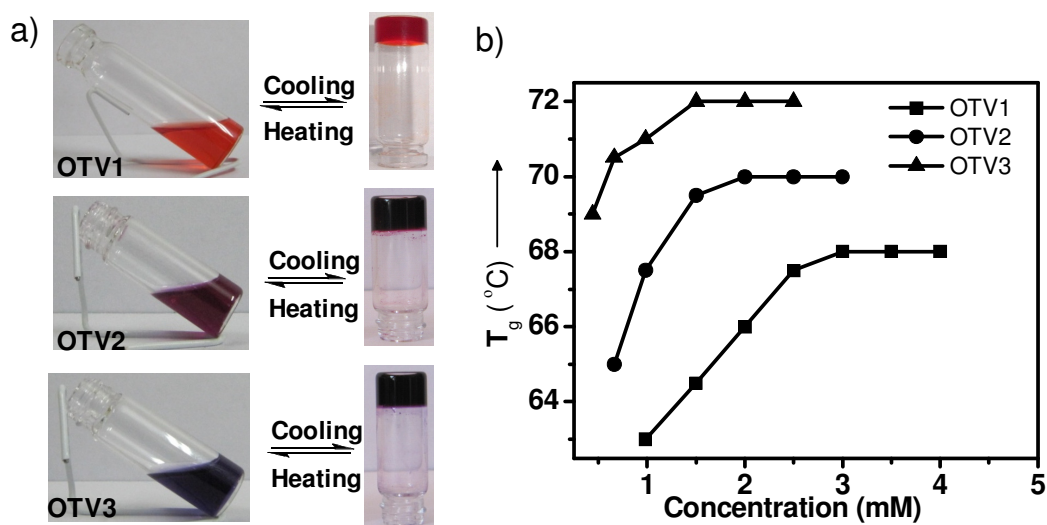


Figure 3.8. a) Photographs showing sol-gel transition of **OTV1**, **OTV2** and **OTV3** in decane at millimolar concentrations. b) Plot of the gel melting temperature (T_{gel}) against the concentration of the gelators.

The gel stabilities were determined from the plots of the gel melting temperature at different concentration of the gelator (Figure 3.8b). From these studies, T_{gel} of **OTV1-3** were found as 68, 70 and 72 °C respectively, indicating a gradual increase in the thermal stability of the gels. From Figure 3.8b it is clear that the T_{gel} for

OTV3 attain stability at a much lower concentration of 1.5 mM whereas for **OTV1**, a concentration of 3 mM was required. These results indicate that the higher conjugation length of **OTV3** facilitates stronger π -stacking of the molecules resulting in more stable gels when compared to **OTV1** and **OTV2**.

3.3.4. Morphological Studies

Transmission electron microscopy images of **OTV1-3** (5×10^{-5} M) self-assemblies from decane solution, placed on carbon coated grids are shown in Figure 3.9a-c. In these cases, entangled fibrous network structures with dimensions ranging from several nanometers in width to several micrometers in length are observed. This type of morphology is characteristics of 1D arrays of molecules leading to gels comprising of entangled fibres. These fibres have a width of 50-200 nm and several of them are bundled to form large structures. As evident from these images, the self-assembled fibres of **OTV1** appear to be more flexible whereas the fibres of **OTV3** are more straight. The rigidity of the nanofilaments of **OTV3** implies strong longitudinal π -interaction of the lengthy conjugated gelator molecules and strong inter fibre interaction between the elementary 1D filaments. This type of self-assembled structures of molecular wires are expected to show high electrical conductivity due to efficient inter-filament hopping of the charge carriers.

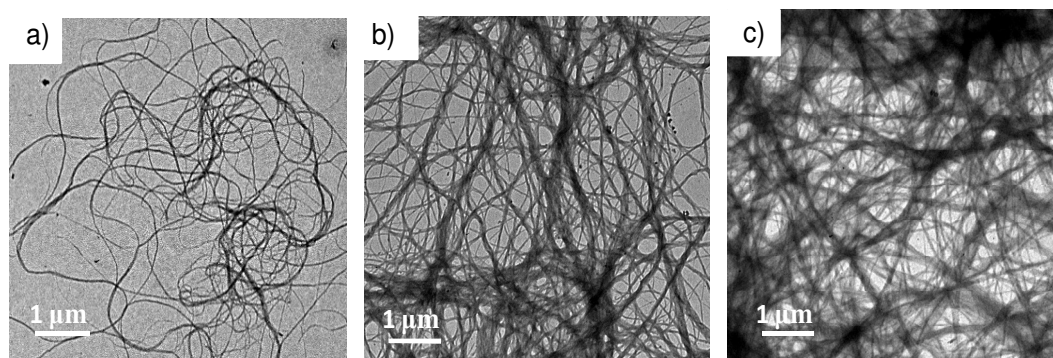


Figure 3.9. TEM images of a) **OTV1**, b) **OTV2** and c) **OTV3** from decane drop casted on carbon coated grid at room temperature ($c = 5 \times 10^{-5}$ M).

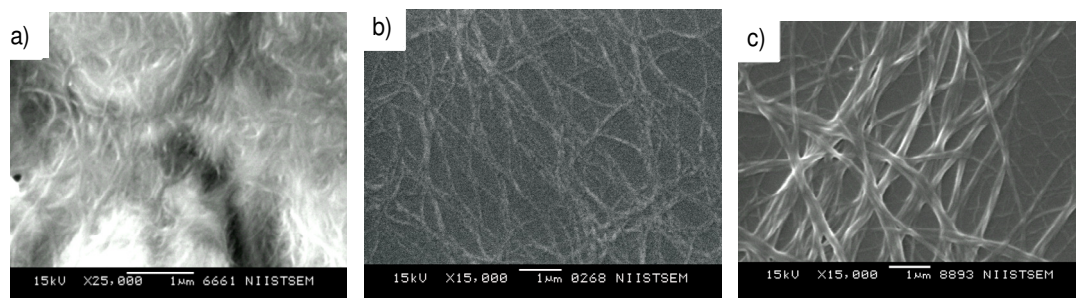


Figure 3.10. SEM images of a) **OTV1**, b) **OTV2** and c) **OTV3** from decane drop casted at room temperature ($c = 5 \times 10^{-5}$ M).

SEM analysis of **OTV1-3** (5×10^{-5} M) showed a fibrous morphology with dimensions ranging from 50-200 nm in width and several micrometers in length as shown in Figure 3.10a-c. AFM images of **OTV1-3** drop casted from decane solutions ($c = 1 \times 10^{-5}$ M) on freshly cleaved mica surface revealed interesting morphological features for the self-assembled fibres (Figure 3.11a-f). In the case of **OTV1**, longitudinally aligned fibres are obtained whereas **OTV3** exhibited short interconnected rod-like structures, several of which were aligned in parallel with trigonal shapes leading to several junction zones. The corresponding height profiles are shown in Figure 3.11b,d,f. **OTV2** also showed interconnected rod like structures. These types of structures are very rarely seen in the AFM images of organic molecules. These images indicate a rare case of a solution phase epitaxial self-assembly which is otherwise achieved by vapor phase deposition or by molecular beam epitaxy. In the case of **OTV2**, the epitaxial assembly could be seen on the bottom surface, on which large unoriented fibres could also be seen. Cross-sectional analysis of these fibres showed an average height of 20-60 nm after deducting the tip broadening effect. The width of the fibres varies between 50-200 nm. Interestingly, the self-assembly of **OTV1-3** on surface is found to have strong influence by the nature of substrate. For example, the AFM images on HOPG and silicon wafer surfaces exhibited entangled fibres as shown in Figure 3.12.

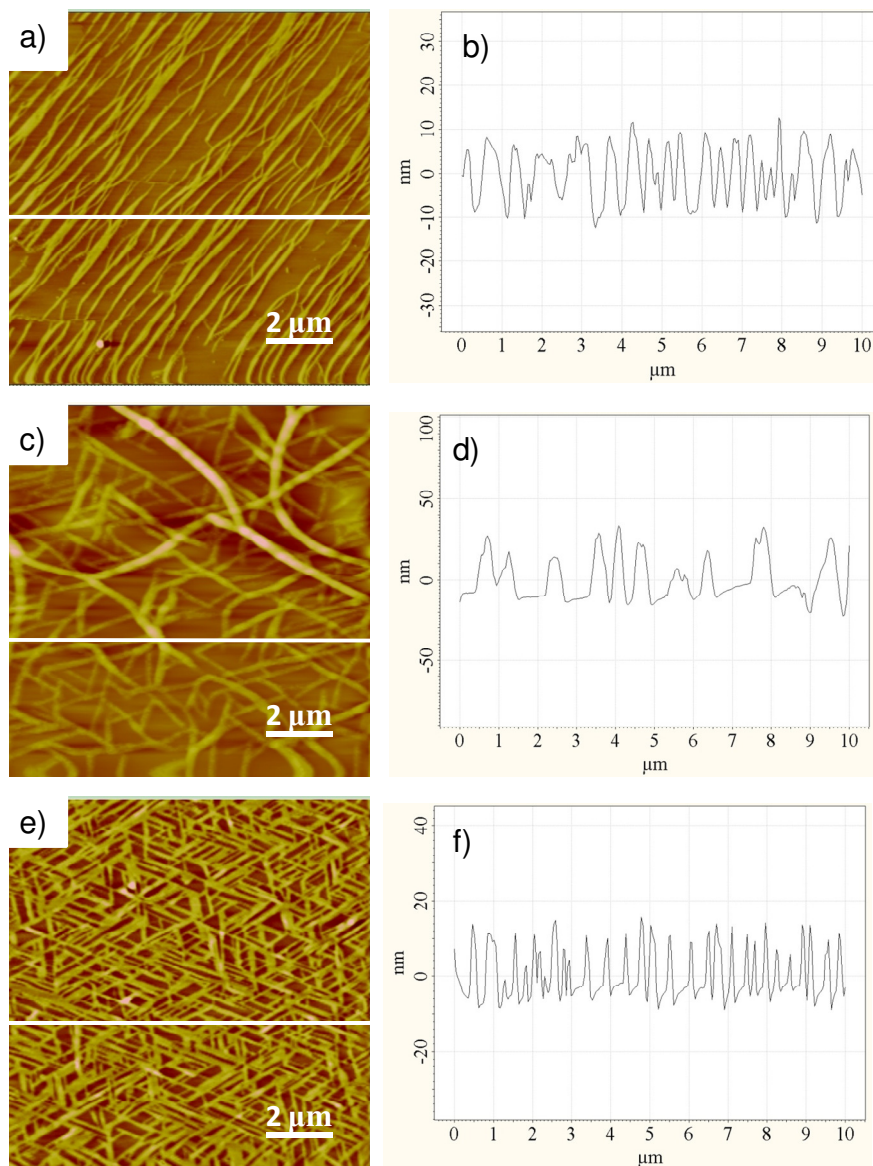


Figure 3.11. AFM images of (a,b) **OTV1**, (c,d) **OTV2** and (e,f) **OTV3** from decane dropcasted on freshly cleaved mica surface and corresponding section analysis as shown.

From these observations, it is clear that the mica surface has significant influence on the morphology of the self-assembled fibres [Samorí *et al.* 1999; Leclère *et al.* 2004]. This phenomenon is ascribed to the exposed K^+ ions having a C_6 symmetry on freshly cleaved mica [Akutagawa *et al.* 2002]. The self-assembled p-type **OTVs** may strongly interact with the electron deficient K^+ ions and align themselves to the directions of the cation array [Lau *et al.* 2009]. Epitaxial growth of organic molecules has been of great

importance in the design of electronic devices [Forrest *et al.* 1997]. There are reports pertaining to the epitaxial growth of thiophene derivatives on different substrates [Borghesi *et al.* 2001; Lau *et al.* 2006; Sassella *et al.* 2007]. In this context, the simple solution phase epitaxial self-assembly of **OTVs** observed here is of great significance. Moreover, the epitaxial self-assembly of **OTV1-3** is found to be strongly dependent upon the concentration of the molecule. For example, upon increasing the concentration of the solution from 1×10^{-5} M to 1×10^{-4} M, **OTV1** changes the morphology from one dimensionally aligned fibres to cross aligned network structures on mica surface whereas **OTV3** exhibited random self-assembly into micrometer sized fibres (Figure 3.13). In addition, it is clear that the conjugation length of the molecule also play a significant role in the epitaxial self-assembly. This may be due to the fact that as the conjugation length increases the p-type character also increases which facilitates a strong interaction with the mica surface as noticed for **OTV3**.

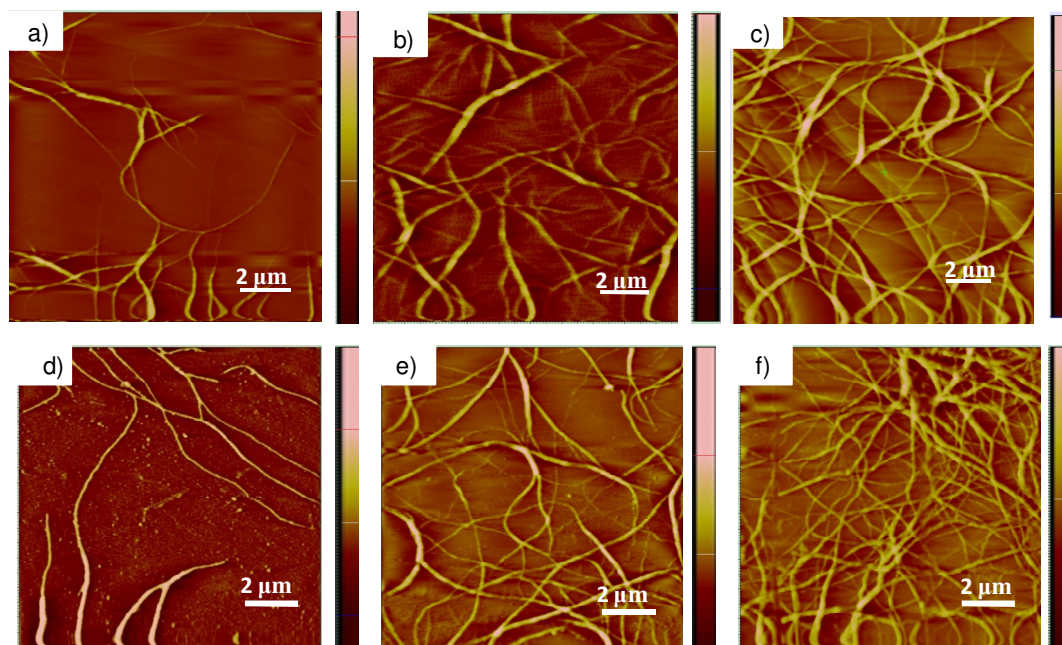


Figure 3.12. AFM images of (a,d) **OTV1**, (b,e) **OTV2** and (c,f) **OTV3** from decane dropcasted on highly ordered pyrolytic graphite (a-c) and silicon wafer (d-f) substrates at room temperature ($c = 1 \times 10^{-5}$ M). Z-scale: a, b, c) 100 nm and d, e, f) 80 nm.

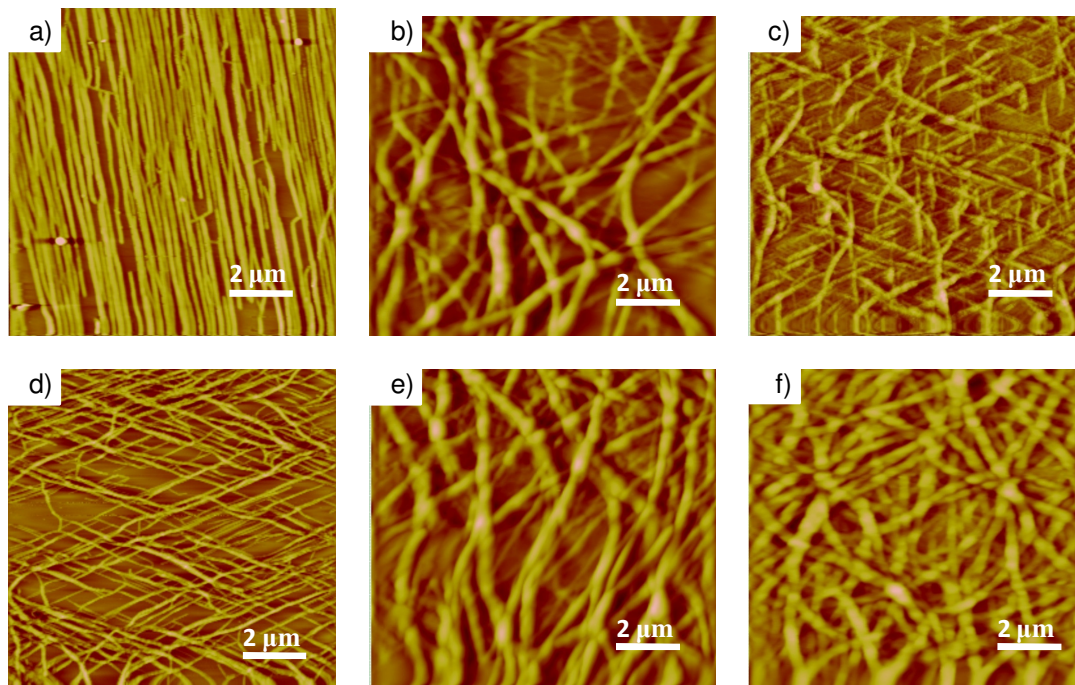


Figure 3.13. AFM images of **OTVs** from decane on freshly cleaved mica surface a) **OTV1**, b) **OTV2** and c) **OTV3** at 5×10^{-5} M. d) **OTV1**, e) **OTV2** and f) **OTV3** at 1×10^{-4} M. Z-scale: a) 40 nm, b) 70 nm, c) 60 nm, d) 40 nm, e) 100 nm and f) 100 nm.

3.3.5. Conductivity Studies

The electrical transport characteristics of these fibres were measured using the conducting probe atomic force microscopy (C-AFM) [Loiacono *et al.* 1998; Kelley *et al.* 1999]. For this purpose, a metal coated cantilever–tip assembly was used as the scanning electrical contact and the force sensor to probe the topological and electrical signals. We have used the tapping mode to image the **OTV** fibres and employed an operator-activated external circuit to switch to the contact mode for point contact electrical characterization of the preselected fibres. The *I-V* responses at different positions of the images were recorded and the representative *I-V* curves of **OTV1-3** are shown in Figure 3.14a and b. The as prepared **OTV1** fibres behave almost like an insulator whereas **OTV2** and **OTV3** fibres exhibited conductivity in the range of semiconductors with wide gaps. The highest conductance of the fibre bundles of the undoped **OTV3** having 40 nm

height was about 0.93 nS. In order to achieve high conductivity, it is necessary to create mixed valence state in the self-assembled fibres which will enhance the charge transport. Since the p-type **OTV**s are easily oxidisable upon doping with iodine vapors, the *I-V* responses were measured after doping which showed significant increase in the conductivity of the fibres (Figure 3.14b). From the AFM analysis, we have confirmed that the fibrous morphology of the xerogels is retained after doping (Figure 3.15a-d). The C-AFM analysis of the iodine doped fibres of **OTV1** and **OTV2** showed enhanced semiconductivity whereas **OTV3** fibres became close to metallic conductivity with a narrow gap after exposure for 5 minutes. The highest conductance obtained for **OTV3** gel fibre bundles, after doping, was about 7.1 nS which corresponds to the conductivity of 5.6 S/cm for a fibre height of 50-60 nm and tip contact radius of 70 nm. The high conductance of the charge transfer complex of **OTV3** reflects the high concentration of the charge carriers upon iodine doping. The UV-vis-NIR spectra were recorded for each sample before and after doping for different intervals. To avoid the instrument error, spectra were recorded for the glass slides without sample. The UV-vis-NIR spectra of the **OTV1-3** xerogel upon exposure to iodine vapor are shown in Figure 3.16a-c.

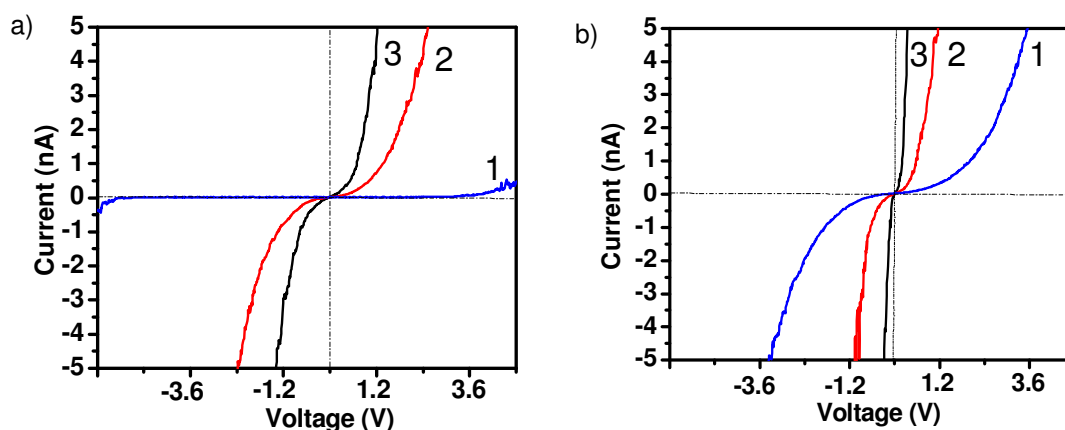


Figure 3.14. C-AFM measurements of **OTV1-3** xerogels obtained from decane solution dropcasted on HOPG substrate ($c = 1 \times 10^{-4}$ M). *I-V* curves of undoped (a) and doped (b) xerogels of **OTV1** (1), **OTV2** (2) and **OTV3** (3).

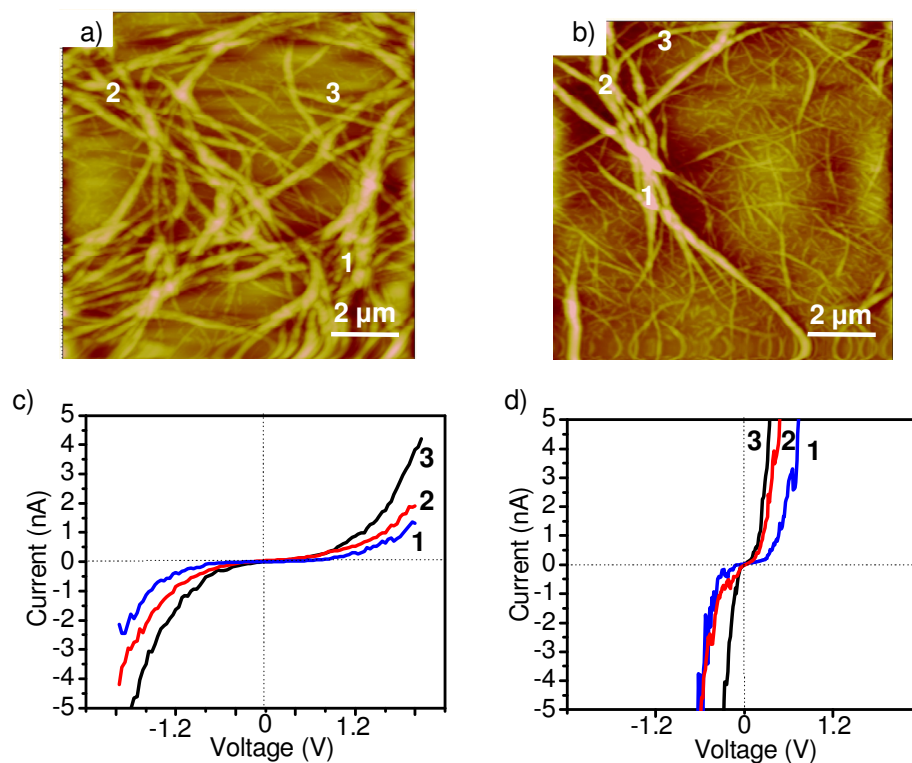


Figure 3.15. C-AFM measurements of **OTV3** xerogels obtained from decane solution dropcasted on HOPG substrate ($c = 1 \times 10^{-4}$ M). Topography images before (a), and after iodine doping (b). The areas of measurements are marked on the inset and the corresponding I - V profiles are shown in (c and d).

The absorption spectra exhibited significant changes in presence of iodine vapors which are predominant in the case of **OTV2** and **OTV3**. In the case of **OTV3** strong polaron/bipolaron bands at 850 nm, 1100 nm and 2300 nm could be observed (Figure 3.16c). The intensity of the polaron bands increases with the iodine exposure time and get saturated within 1h of exposure. The intensity and the absorption wavelength of the polaron bands were found to increase with increase in the conjugation length. Further analysis from FT-IR studies of **OTV1-3** revealed a broad CT band around 1000 and 4000 cm^{-1} when the xerogel was exposed to iodine vapor in a sealed container for 5 min, which indicates mixed valence state of **OTVs** in neutral and cationic radical states.

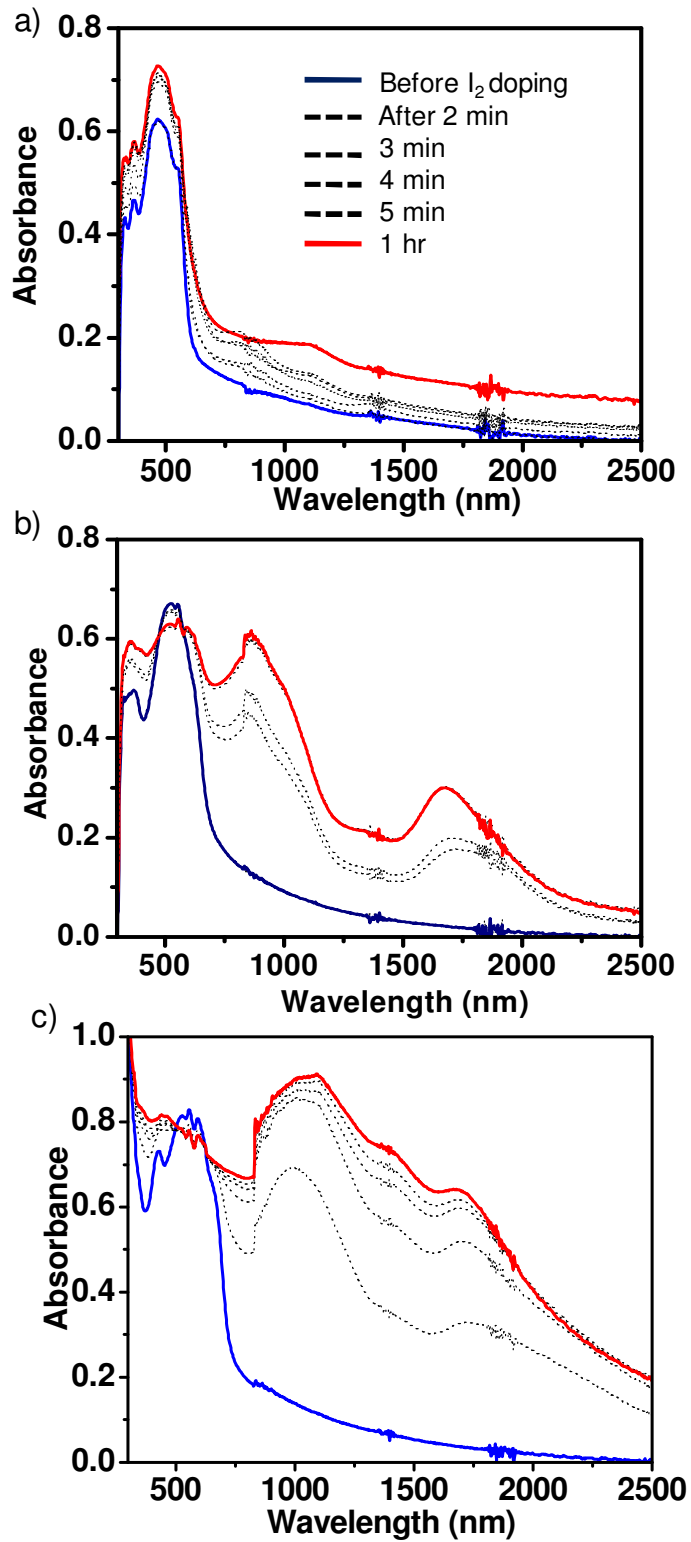


Figure 3.16. UV-vis-NIR spectra of a) OTV1, b) OTV2 and c) OTV3 in xerogel upon exposure to iodine vapors.

This result suggests that electronic conduction may occur along the aligned fibres of **OTVs**. The steady state is reached in an hour after doping. No significant change was observed for a few days. The N-H and C=O stretching bands of the amide groups do not shift with iodine-doping, which shows that the doping does not change the hydrogen-bonded structure (Figure 3.17). This observation indicates that before and after iodine doping of the xerogels, molecularly assembled structures (topography) are not disturbed. These studies suggest that **OTV3** has better electronic conduction in the fibres than those of **OTV1** and **OTV2**.

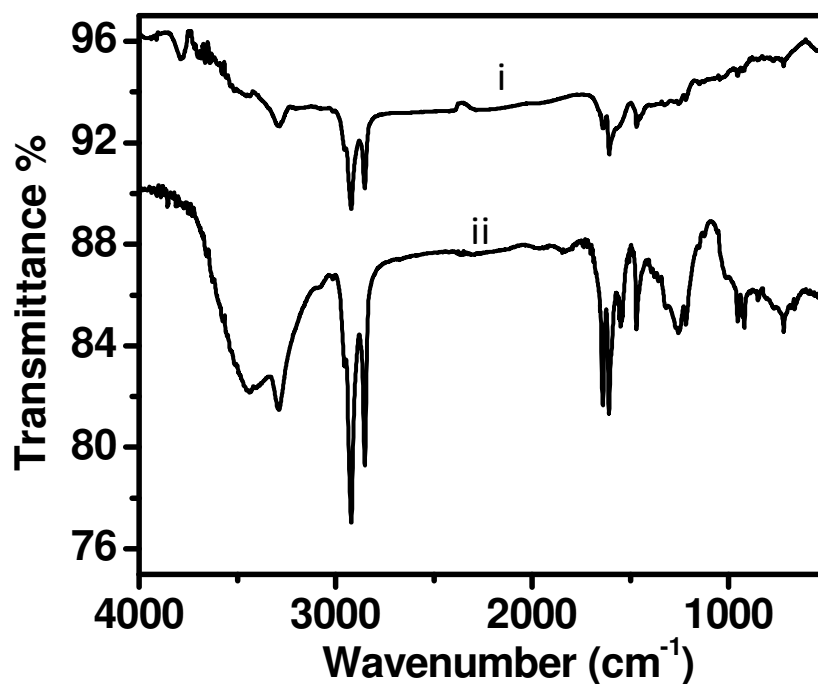


Figure 3.17. FT-IR spectrum of **OTV3** in xerogel state before (i) and after (ii) iodine doping.

The bulk electrical conductivities of **OTV1-3** xerogels on glass substrate before and after doping with iodine vapors were measured by four-probe dc resistivity method (Table 3.2). The room temperature conductivity (σ) of the as prepared **OTV1-3** films are 4.8×10^{-6} , 6.4×10^{-4} and 4.83×10^{-2} S/cm, respectively. The conductivity has been significantly enhanced (an order of two magnitude increase) to the range of 6×10^{-4} , 1.02

$\times 10^{-2}$ and 4.8 S/cm for **OTV1-3**, respectively after doping. These data revealed that **OTV3** xerogel fibres behave like metallic wires in conductivity after doping which indicates that extended conjugation length and strong gelation in **OTV3** have resulted in the efficient charge carrier generation upon doping.

Table 3.2. Four-probe (electrical) conductivity (S/cm) measurements of **OTV1**, **OTV2** and **OTV3** xerogels before and after doping ^a

Gelator	Before doping (σ)	After doping (σ)
OTV1	4.8×10^{-6}	6.03×10^{-4}
OTV2	6.45×10^{-4}	1.02×10^{-2}
OTV3	4.83×10^{-2}	4.83

^a The values are average of three independent measurements. The thickness of the films varied between 18-27 μm .

3.4. Conclusions

In summary, we have demonstrated the synthesis, gelation and electronic properties of thienylenevinylene derived molecular wires with different conjugation length. Increase in conjugation length has remarkable influence on the self-assembly, morphology and the conducting properties of these gelators. Microscopic analysis revealed that these gels exhibit the unique property of solution phase epitaxy leading to the alignment of fibres on mica surface. Electrical conductivity of these new p-type semiconducting gels could be improved to metallic range by increasing the conjugation length and by doping. The bulk electrical conductivity of 4.8 S/cm observed for the doped **OTV3** xerogel which is one of the highest values reported so far for a molecular gelator. This new class of metallic gels comprising of 1D nanowires are expected to

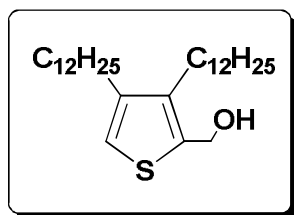
generate interests among scientists working in the field of organic materials for electronics and photonics applications.

3.5. Experimental Section

3.5.1. Synthesis and Characterization

Unless otherwise stated, all starting materials and reagents were purchased from commercial suppliers and used without further purification. The solvents and the reagents were purified and dried by standard methods prior to use. Details of the instrumental techniques used for characterization of molecules are described in the experimental section (section of 2.5.1.) of Chapter 2. Preparation, yield, melting point, and spectral details of each product are given below.

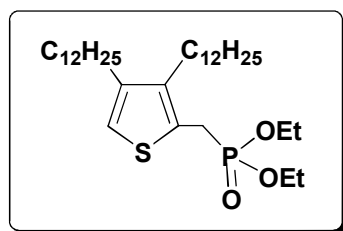
Synthesis of (3,4-didodecylthiophen-2-yl)methanol: 3,4-Didodecylthiophene-2-



carbaldehyde (1 g, 2.16 mmol) was dissolved in 30 mL of 1:1 $\text{CH}_2\text{Cl}_2/\text{MeOH}$. NaBH_4 (0.2 g, 6.2 mmol) was added in portions to the reaction mixture and stirred for 30 min. After removal of the solvent, the residue was dissolved in

chloroform and washed with water. The organic layer was separated out and dried over anhydrous Na_2SO_4 . The solvent was removed under vacuum resulting in an yellow liquid (Yield = 92%). ^1H NMR (CDCl_3 , 300 MHz) δ (ppm) = 6.84 (m, 1H), 4.72 (s, 2H), 2.55-2.45 (t, 4H), 1.64-1.57 (m, 15H), 1.39-1.31 (m, 40H), 0.92-0.88 (m, 6H); ^{13}C NMR (CDCl_3 , 75 MHz) δ (ppm) = 141.93, 140.09, 136.24, 136.15, 58.16, 31.96, 31.87, 29.93, 29.68, 29.40, 29.31, 27.26, 22.62, 14.06; FAB-MS (m/z) = 431.64.

Diethyl(3,4-didodecylthiophen-2-yl)methylphosphonate: To a solution of (3,4-didodecylthiophen-2-yl)methanol (1 g, 2.08 mmol), in dichloromethane, under an ice bath (-5°C) PBr_3 (0.08 mL) was added drop wise for 4 h in inert atmosphere. After removal of the solvent, 1 equivalent of $\text{P}(\text{OEt})_3$ was added to the residue and then

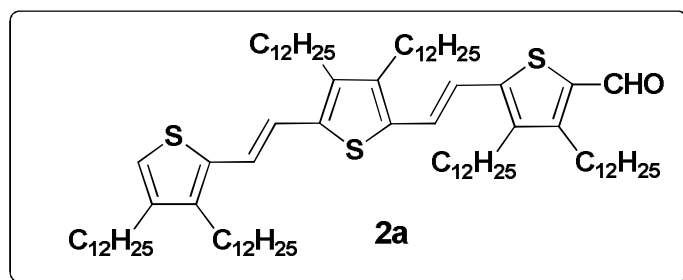


refluxed at 120 °C for 12 h. The crude product was purified by column chromatography (silica gel/methanol).

(Yield : 65%)

^1H NMR (CDCl_3 , 300 MHz) δ (ppm) = 6.73 (m, 1H), 4.12-4.09 (t, 4H), 3.27 (d, 2H), 2.46 (t, 4H), 1.64-1.57 (m, 4H), 1.39-1.31 (m, 40H), 0.92-0.88 (m, 6H); ^{13}C NMR (CDCl_3 , 75 MHz) δ (ppm) = 143.91, 140.18, 136.24, 136.15, 65.16, 63.75, 63.50, 62.02, 58.25, 31.85, 30.53, 29.88, 29.62, 29.39, 29.29, 27.17, 22.61, 17.94, 16.19, 15.98, 14.06; FAB-MS (m/z) = 588.09.

Synthesis of 2a: Compounds **2a** was prepared by Vilsmeier formylation of **1** (0.4 g, 0.3

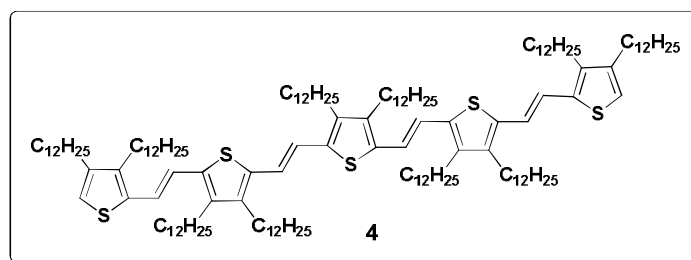


mmol), using DMF (0.13 mL, 1.8 mmol) and POCl_3 (0.12 mL, 1.2 mmol) in dry 1,2-dichloroethane (40 mL).

The reaction mixture was

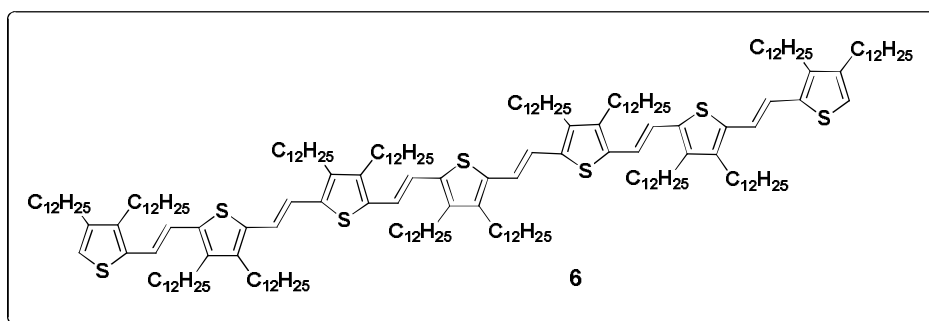
refluxed for 2 h. After cooling the reaction mixture, 1 M sodium acetate was added for neutralization. The mixture was further stirred for 1 h. Then the solution was extracted with dichloromethane. The organic layer was separated out and dried over Na_2SO_4 . The solvent was removed to get the crude products **2a** which was purified by column chromatography using basic alumina (hexane/chloroform 9:1 for compound **2a**). Yield = 68%, mp. 118-120 °C, ^1H -NMR (CDCl_3 , 300 MHz) δ (ppm) = 9.97 (m, 1H), 7.01-6.95 (J=15 Hz, d, 2H), 6.77-6.72 (J = 15 Hz, d, 2H), 6.48 (m, 1H), 2.61 (t, 12H), 1.57 (q, 12H), 1.26 (m, 120H), 0.88 (t, 18H); ^{13}C NMR (CDCl_3 , 75 MHz) δ (ppm) = 182.55, 146.55, 142.93, 141.86, 135.56, 127.91, 123.70, 31.93, 31.33, 31.42, 29.74, 29.38, 26.99, 22.70, 14.14; FT-IR (KBr) ν_{max} = 720, 801, 861, 921, 1026, 1083, 1261, 1377, 1466, 1652, 2851, 2922 cm^{-1} ; FAB-MS (m/z) : 1337.21 (Found), 1337.13 (Calcd).

Synthesis of 4: Compound **4** was synthesized by the Wittig-Horner olefination of compound **2b** with diethyl (3,4-didodecylthiophen-2-yl)methylphosphonate. To a mixture of **2b** (0.17 g, 0.13 mmol) and diethyl (3,4-didodecylthiophen-2-yl)methylphosphonate (0.15 g, 0.25 mmol) in 30 mL of dry THF, *t*-BuOK (0.09 g, 0.99 mmol) was added in portions under nitrogen atmosphere. The reaction mixture was then stirred for 3 h. After removal of the solvent under reduced pressure, the residue was dissolved in CH₂Cl₂ and washed with water. After extraction, the organic layer was separated out and dried over anhydrous Na₂SO₄ and the solvent was removed under reduced pressure. The crude product was purified by column chromatography (silica gel/hexane). Yield 72%, mp. 122-125 °C, ¹H NMR (CDCl₃, 300 MHz, TMS) δ (ppm) = 6.97 (s, 8H), 6.75 (s, 2H), 2.59-2.48 (t, 20H), 1.59 (q, 28H), 1.26 (m, 180H), 0.89 (t, 40H); ¹³C NMR (CDCl₃, 75 MHz) δ (ppm) = 142.38, 141.10, 140.27, 138.39, 136.08, 133.71, 118.84, 118.29, 99.97, 95.60, 92.76, 30.92, 28.73, 28.69, 28.67, 28.65, 28.60, 28.54, 28.47, 28.41, 28.37, 28.35, 21.68, 13.10; FT-IR (KBr) ν_{max} = 719, 801, 861, 921, 1026, 1083, 1261, 1377, 1465, 2851, 2918 cm⁻¹; MALDI-TOF (m/z) = 2198.14 (calculated mass = 2198.90).



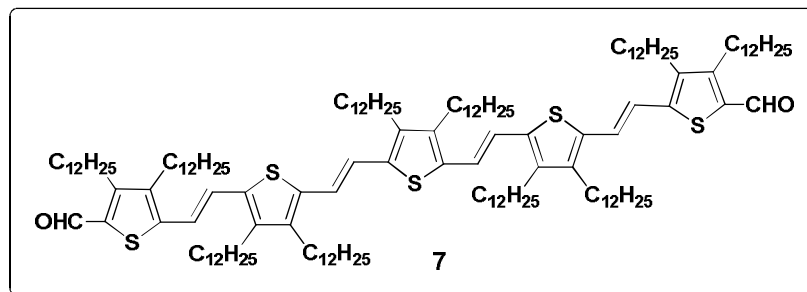
Synthesis of compound 6: To a solution of **2a** (0.2 g, 0.27 mmol) and diethyl (3,4-didodecylthiophen-2-yl)methyldiphosphonate (0.05 g, 0.14 mmol) in 30 mL of dry THF, *t*-BuOK (0.06 g, 2.97 mmol) was added in portions under nitrogen atmosphere. The reaction mixture was then stirred for 3 h. After removal of the solvent under reduced pressure, the residue was dissolved in CH₂Cl₂ and washed with water. After extraction,

the organic layer was separated out and dried over anhydrous Na_2SO_4 . The solvent was removed under reduced pressure. The crude product was purified by column chromatography (Silica gel/hexane). Yield = 52%. mp. 130-132 °C. ^1H NMR (CDCl_3 , 500 MHz, TMS) δ (ppm) = 6.97 (s, 12H), 6.75 (s, 2H), 2.59-2.45 (t, 28H), 1.56 (q, 40H), 1.26-1.18 (m, 285H), 0.89 (t, 49H); ^{13}C NMR (CDCl_3 , 125 MHz) δ (ppm) = 146.62, 142.36, 141.85, 141.67, 138.23, 136.02, 135.53, 135.19, 134.70, 132.13, 121.05, 119.92, 119.50, 118.94, 118.14, 117.04, 99.97, 95.60, 92.76, 34.59, 31.93, 31.70, 31.28, 29.74, 29.68, 29.48, 29.38, 27.12, 22.68, 14.95, 14.08; FT-IR (KBr) ν_{max} = 720, 801, 861, 921, 1026, 1083, 1261, 1377, 1466, 2851, 2922 cm^{-1} ; MALDI-TOF (m/z) = 3089.14 (calculated mass = 3089.57).



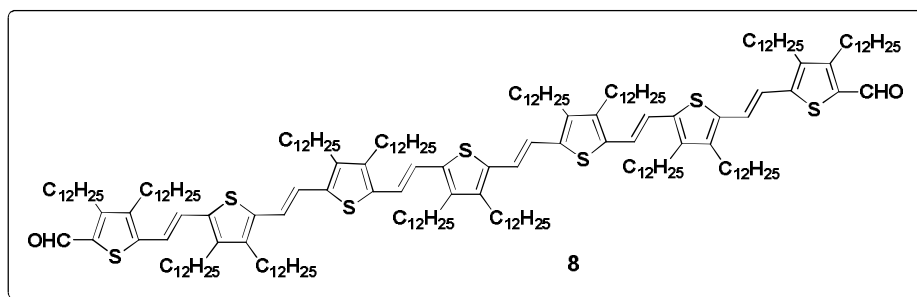
Synthesis of 7: Compound 7 was prepared by Vilsmeier formylation of 4 (0.2 g, 0.09 mmol), using DMF (0.03 mL, 0.4 mmol) and POCl_3 (0.02 mL, 0.6 mmol) in dry 1,2-dichloroethane (40 mL). The reaction mixture was refluxed for 2 h. After cooling the reaction mixture, 1 M sodium acetate was added for neutralization. The mixture was further stirred for 1 h. The organic layer was extracted with dichloromethane and dried over Na_2SO_4 . The solvent was removed to get the crude product which was purified by column chromatography using basic alumina (hexane/chloroform 9:1 for compound 7). Yield = 68%, mp. 127-129 °C, ^1H NMR (CDCl_3 , 500 MHz) δ = 9.97 (m, 2H), 7.00-6.97 (J = 9 Hz, d, 4H), 6.92-6.79 (J = 15 Hz, d, 4H), 2.87-2.61 (t, 20H), 1.57 (q, 17H), 1.26 (m, 122H), 0.85 (t, 39H); ^{13}C -NMR (CDCl_3 , 125 MHz) δ (ppm) = 182.55, 146.62,

142.36, 141.85, 141.67, 138.23, 136.02, 135.53, 135.19, 134.70, 132.13, 121.05, 119.92, 119.50, 118.94, 118.14, 117.04, 99.97, 95.60, 92.76, 34.59, 31.93, 31.70, 31.28, 29.74, 29.68, 29.48, 29.38, 27.12, 22.68, 14.95, 14.08; FT-IR (KBr) ν_{\max} = 720, 801, 861, 921, 1026, 1083, 1261, 1377, 1466, 1652, 2851, 2922 cm^{-1} ; MALDI-TOF-MS (m/z) = 2257.25 (Found), 2255.59 (Calcd).

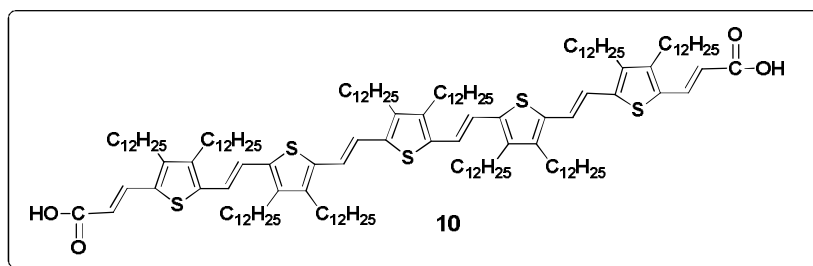


Synthesis of 8: Compound **8** was prepared by Vilsmeier formylation of **6** (0.15 g, 0.05 mmol), using DMF (0.02 mL, 0.3 mmol) and POCl_3 (0.02 mL, 0.2 mmol) in dry 1,2-dichloroethane (40 mL) as described in the synthesis of compound **7**.

Yield = 68%, mp. 128-131 °C, ^1H NMR (CDCl_3 , 500 MHz) δ (ppm) = 9.97 (m, 2H), 7.01-6.98 (J = 9 Hz, d, 10H), 6.96-6.91 (J = 15 Hz, d, 2H), 2.84-2.60 (t, 28H), 1.59 (q, 37H), 1.26 (m, 300H), 0.865 (t, 50H); ^{13}C NMR (CDCl_3 , 125 MHz) δ (ppm) = 183.15, 146.62, 142.36, 141.85, 141.67, 138.23, 136.02, 135.53, 135.19, 134.70, 132.13, 121.05, 119.92, 119.50, 118.94, 118.14, 117.04, 99.97, 95.60, 92.76, 34.59, 31.93, 31.70, 31.28, 29.74, 29.68, 29.48, 29.38, 27.12, 22.68, 14.95, 14.08; FT-IR (KBr) ν_{\max} = 720, 801, 861, 921, 1026, 1083, 1261, 1377, 1466, 1652, 2851, 2922 cm^{-1} ; MALDI-TOF-MS (m/z) = 3143.45 (Found) (calculated mass = 3144.65).

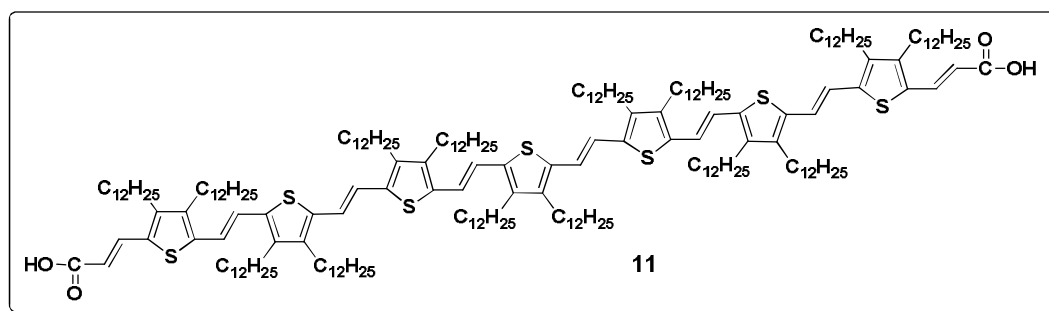


Synthesis of Compound 10: To a mixture of **7** (0.15 g, 0.058 mmol) and **9** (0.02 g, 0.16 mmol) in 30 mL of dry THF, *t*-BuOK (0.05 g, 0.24 mmol) was added in portions under nitrogen atmosphere. The reaction mixture was then stirred for 3 h. After removal of the solvent under reduced pressure, the residue was dissolved in CH₂Cl₂ and washed with water. After extraction, the organic layer was dried over anhydrous Na₂SO₄ and the solvent was removed under reduced pressure. The crude product was directly converted to the corresponding acid by hydrolysis using KOH in Methanol/THF mixture. Yield 90%. mp. 133-135 °C, ¹H NMR (CDCl₃, 500 MHz, TMS) δ (ppm) = 7.94-7.89 (J = 15.5 Hz, d, 2H), 7.11-7.05 (J = 15.3 Hz, d, 6H), 6.99-6.94 (J = 15.5 Hz, d, 2H), 6.17-6.12 (J = 15.0 Hz, d, 2H), 2.86-2.61 (t, 20H), 1.59 (q, 28H), 1.39-1.31 (m, 190H), 0.89 (t, 39H); ¹³C NMR (CDCl₃, 125 MHz) δ (ppm) = 171.82, 145.61, 141.35, 140.76, 140.51, 137.17, 134.96, 134.83, 134.36, 133.89, 131.12, 130.85, 119.99, 118.73, 118.43, 118.05, 117.17, 33.59, 30.92, 30.69, 30.33, 30.25, 30.19, 28.74, 28.67, 28.47, 28.37, 26.26, 26.09, 21.68, 14.95, 14.08; IR (KBr) ν_{max} = 718, 801, 861, 921, 1026, 1083, 1262, 1377, 1466, 1673, 1731, 2849, 2922, 3435 cm⁻¹; MALDI-TOF-MS (m/z) = 2338.34 (Found) (calculated mass = 2340.07).



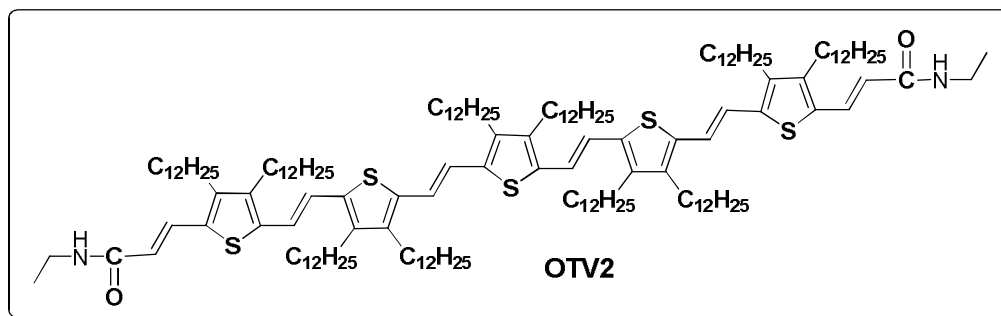
Synthesis of compound 11: The same experimental procedure as in the case of compound **10** was followed for the synthesis of compound **11**. Yield 90%. mp. 137-139 °C, ¹H NMR (CDCl₃, 500 MHz, TMS) δ (ppm) = 7.93-7.88 (J = 15.5 Hz, d, 2H), 7.05-6.99 (J = 15.3 Hz, d, 10H), 6.99-6.94 (J = 15.5 Hz, d, 2H), 6.17-6.12 (J = 15.0 Hz, d, 2H), 2.65-2.45 (t, 28H), 1.59 (q, 37H), 1.39-1.31 (m, 280H), 0.89 (t, 48H); ¹³C NMR

(CDCl₃, 125 MHz) δ (ppm)= 170.83, 146.62, 142.36, 141.85, 141.67, 138.23, 136.02, 135.53, 135.19, 134.70, 132.13, 121.05, 119.92, 119.50, 118.94, 118.14, 117.04, 99.97, 95.60, 92.76, 34.59, 31.93, 31.70, 31.28, 29.74, 29.68, 29.48, 29.38, 27.12, 22.68, 14.95, 14.08; IR (KBr) ν_{\max} = 718, 801, 861, 921, 1026, 1083, 1262, 1377, 1466, 1673, 1731, 2849, 2922, 3435 cm⁻¹; MALDI-TOF-MS (m/z) = 3227.46 (Found) (calculated mass = 3229.60).

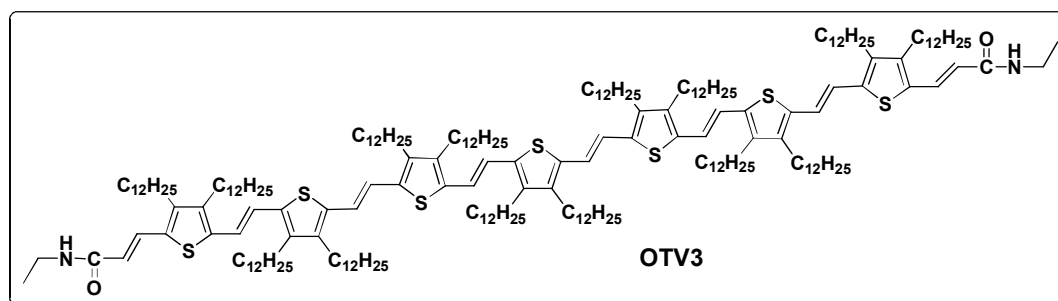


Synthesis of OTV2: To an ice cooled solution of **11** (0.15 g, 0.047 mmol), in dry chloroform (30 mL), ethylamine (0.01 mL, 0.141 mmol) and HATU (0.06 g, 0.141 mmol) were added. Then diisopropylethylamine (0.02 mL, 0.188 mmol) was added drop wise to the mixture and stirred at room temperature for 12 h. After removal of the solvent, the residue was dissolved in chloroform and washed with water. The organic layer was separated and dried over Na₂SO₄. Solvent was evaporated under vacuum. The crude product was purified by column chromatography (Basic Alumina, hexane/ethyl acetate 8:2) to give the pure black solid compound (**OTV2**). Yield = 35%, mp. 141-143 °C, ¹H NMR (CDCl₃, 500 MHz) δ (ppm)= 7.82-7.77 (J = 15 Hz, d, 2H), 7.04-6.97 (J = 18 Hz, d, 6H), 6.95-6.91 (J = 12 Hz, d, 2H), 6.11-6.06 (J = 15 Hz, d, 2H), 5.35 (t, 2H), 3.42 (t, 4H), 2.59-2.38 (t, 24H), 1.55 (q, 24H), 1.36-1.20 (m, 250H), 0.87 (t, 35H); ¹³C NMR (CDCl₃, 125 MHz) δ (ppm) = 164.82, 145.61, 141.35, 140.76, 140.51, 137.17, 134.96, 134.83, 134.36, 133.89, 131.12, 130.85, 119.99, 118.73, 118.43, 118.05, 117.17, 33.59, 30.92, 30.69, 30.33, 30.25, 30.19, 28.74, 28.67, 28.47, 28.37, 26.26, 26.09, 21.68, 13.95,

13.08; FT-IR (KBr) ν_{\max} = 716, 910, 1019, 1257, 1356, 1473, 1544, 1645, 2849, 2920, 3289, 3440 cm^{-1} ; MALDI-TOF-MS (m/z) = 2394.16 (Found) (calculated mass = 2394.20).



Synthesis of OTV3: The experimental procedure used for the preparation of **OTV3** was adopted for the synthesis of **OTV2**. Yield = 28%, mp. 145-147 °C, ^1H NMR (CDCl_3 , 500 MHz) δ (ppm)= 7.82-7.77 (J = 15 Hz, d, 2H), 7.09-7.03 (J = 18 Hz, d, 10H), 6.98-6.92 (J = 18 Hz, d, 2H), 6.10-6.05 (J = 15 Hz, d, 2H), 5.37 (t, 2H), 3.36 (t, 4H), 2.52-2.10 (t, 12H), 1.53 (q, 12H), 1.33-1.15 (m, 386H), 0.83 (t, 51H); ^{13}C NMR (CDCl_3 , 125 MHz) δ (ppm)= 165.83, 146.62, 142.36, 141.85, 141.67, 138.23, 136.02, 135.53, 135.19, 134.70, 132.13, 121.05, 119.92, 119.50, 118.94, 118.14, 117.04, 99.97, 95.60, 92.76, 34.59, 31.93, 31.70, 31.28, 29.74, 29.68, 29.48, 29.38, 27.12, 22.68, 14.95, 14.08; FT-IR (KBr) ν_{\max} = 716, 773, 924, 1019, 1257, 1457, 1544, 1645, 2855, 2920, 3289, 3418 cm^{-1} ; MALDI-TOF-MS (m/z) = 3283.07 (Found) (calculated mass = 3283.80).



3.5.2. Description of Experimental Techniques

Electronic absorption spectra were recorded on a Shimadzu UV-3101 PC NIR scanning spectrophotometer. Temperature dependent studies were carried out either in a 0.1 cm or 1 cm quartz cuvette with a thermistor directly attached to the wall of the cuvette holder. Gelation studies of **OTV1-3** were performed as reported in Chapter 2. Gels were prepared in glass vials of 0.5 cm diameter using the required amount of the gelator in 1 mL of hexane, decane, dodecane etc. followed by heating and then cooling to room temperature. Semi transparent gels with orange, purple and dark colors were obtained. The gel melting temperatures were determined by the dropping ball method.

Transmission Electron Microscopy (TEM): TEM measurements were carried out using FEI (TECNAI G² 30 S-TWIN) with an accelerating voltage of 100 kV. Samples were prepared by drop casting of decane solutions of **OTV1-3** on to carbon coated copper grids at the required concentrations at ambient conditions. The solvent was removed under vacuum. TEM images were obtained without staining.

Scanning Electron Microscopy (SEM): SEM studies were carried out on a JEOL 5600 LV scanning electron microscope with an accelerating voltage of 10 kV, or a Hitachi S 2008 at an accelerating voltage of 15 kV. The SEM samples were prepared by transferring the solutions of **OTVs** onto a copper grid. The samples were allowed to dry under vacuum conditions.

Atomic Force Microscopy (AFM): Atomic Force Microscopy images were recorded under ambient conditions using a NTEGRA (NT-MDT) operating with a tapping mode regime. Micro-fabricated TiN cantilever tips (NSG10) with a resonance frequency of 299 kHz and a spring constant of 20-80 Nm⁻¹ were used. AFM section analysis was done offline. Samples for the imaging were prepared by drop casting the **OTV1-3** solution on

freshly cleaved mica, highly ordered pyrolytic graphite (HOPG) or silicon wafer substrates at the required concentrations at ambient conditions.

Current Sensing (Conductive) Atomic Force Microscopy (C-AFM): We have used the tapping mode to image the **OTV** samples with a resonance frequency of 224 kHz and a spring constant of 6-22 Nm⁻¹. Micro-fabricated diamond coating was doped with nitrogen cantilever tips (DCP11) and employed an operator-activated external circuit to switch to contact mode for point contact electrical characterization of the selected positions. After completion of the measurement, we have deactivated the external circuit to return to the tapping mode feedback. This procedure prevents damage to the **OTV** fibres and the metal coated tips by avoiding the frictional wear associated with the contact mode imaging. Samples for the imaging and electrical properties were prepared by drop casting the **OTV1-3** solution on HOPG at the required concentrations at ambient conditions. Conductance was measured on the bundled fibres at different positions before and after exposing to iodine vapors at different intervals. The value of the conductivity (σ) was calculated from the equation

$$\sigma = d/(A_t R) \text{ S/cm}$$

where σ is the conductivity, and d is the film thickness (~ 50-60 nm). A_t is the area of the C-AFM probe in contact with the surface. ' A_t ' was computed as πr^2 , assuming that the contact radius between tip and sample is 70 nm. R is the resistance of the sample, estimated from the inverse slope of the I - V curve.

Four-Probe dc resistance measurements: For conductivity measurements, xerogels were prepared on glass slides from the **OTV1-3** samples. Then xerogels were put on the base plate of the four probe arrangement. The probes were placed on the flat surface of the film. Current was passed through the two outer electrodes, and the floating potential was measured across the inner pair. In this measurement, a known current was applied and the potential across the probes was determined. This experiment was repeated three

times and the average resistance values were taken. The value of the resistivity (ρ) was calculated from the equation

$$\rho = (V / I) \times \pi t / \ln 2$$

where t = thickness of the film. (Thickness of the film was measured by ellipsometric technique. For **OTV1**, $t = 18 \mu\text{m}$, **OTV2**, $t = 27 \mu\text{m}$, and **OTV3**, $t = 18 \mu\text{m}$ respectively).

The conductivity (σ) was calculated from the equation, $\sigma = 1 / \rho_{\text{actual}}$ (S/cm).

Interaction of p-Type Gelators with n-Type Semiconductors: Co-assembly, Morphology and Charge Carrier Properties

4.1. Abstract

Detailed studies on the co-assembly, morphology, substrate interaction, and charge-carrier mobilities of the p-type thienylenevinylene gelators (TVI-4) with the n-type perylene bisimide (PBI) semiconductor have been carried out. AFM and TEM investigations of the co-assembly on mica and silicon wafer surfaces revealed that the co-assembly leads to a distinct morphology which is different from the individual self-assemblies. This observation rules out macroscopic phase separation between the two components. Charge generation of the co-assemblies were measured using Kelvin probe force microscopy (KPFM) and FP-TRMC. KPFM analysis revealed that the surface potential exhibits more negative values for the self-assembled nanowires on silicon wafer when compared to those formed on mica surface. Mobility data showed the enhancement of uni-directional charge carrier transport in self-assembled films when compared to those obtained from isotropic solution. X-ray studies on films indicated the occurrence of phase separation of the self-sorted aggregates on the nanometer scale.

4.2. Introduction

Electronic devices made of organic materials, in particular photovoltaic devices, are intensively studied during the past several years owing to their cheap processing costs, application to large areas, and compatibility with flexible substrates [Goetzberger *et al.* 2003; Hoppe *et al.* 2004; Spangaard *et al.* 2004; Li *et al.* 2006]. In organic solar cells, charge separation of the strongly bound electron-hole pairs, the so called excitons is enabled at a donor-acceptor (DA) interface or heterojunction upon illumination, where they dissociate and then drift towards the respective electrodes [Hoppe *et al.* 2004; Li *et al.* 2006]. In all organic photovoltaic cells, the active material consists of π -conjugated electron donors and electron acceptors. The nature of the intermolecular interaction between electron donors and electron acceptors influences the charge transfer for which the packing of the molecules play an important role. The active-layer morphology should strike a balance between the intermolecular interaction between and within the electron donors and the electron acceptors [Bredas *et al.* 2009; Cheng *et al.* 2009; Heremans *et al.* 2009; Helgesen *et al.* 2010]. Molecular architecture plays a key role in achieving this balance [Ma *et al.* 2005; Benanti *et al.* 2006; Yang *et al.* 2007; Kim *et al.* 2008]. In general, when electron rich conjugated molecules are mixed with electron-poor conjugated molecules, two types of assemblies, a mixed stack motif or the segregated stack motif are expected (Figure 4.1). Since n-type semiconductors are electron-deficient (acceptor), and p-type semiconductors are electron-rich (donor), there is a natural tendency for these molecules to mix each other through charge transfer and aromatic stacking interactions. The mixed stack is a common motif, whereas the segregated stack is a rare motif in condensed-phase structures [Hunter *et al.* 1990; Hunter *et al.* 2001].

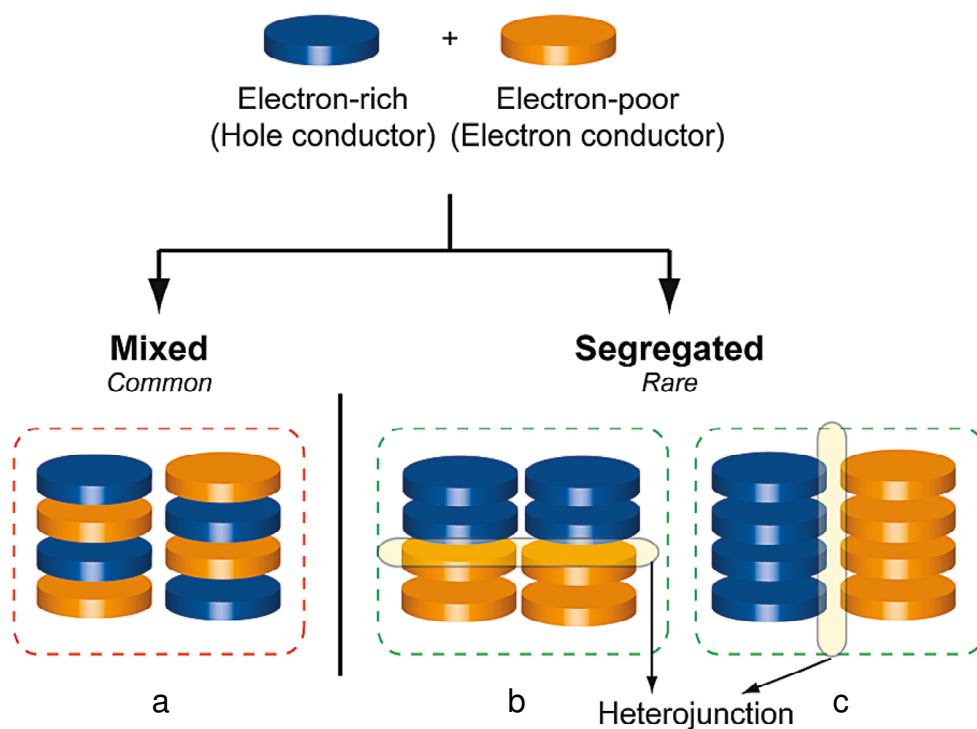


Figure 4.1. Illustration of mixed packing and segregated arrangements of electron-rich conjugated molecules (blue, hole conductor, donor) and electron-poor conjugated molecules (orange, electron conductor, acceptor). Although the illustration shows planar electron-poor compounds, the mixing also happens with nonplanar, fullerene-based compounds.

Meijer and co-workers have reported the self-sorting behavior of p-type and n-type supramolecular fibre structures where oligo(*p*-phenylenevinylene) (**1**) and perylene derivatives (**2**) were used as p-type and n-type materials respectively (Figure 4.2) [Herrickhuyzen *et al.* 2004]. UV-vis absorption spectra and AFM images revealed an ordered network of fibre formation in methyl cyclohexane (MCH) (Figure 4.2a and 4.2b). However, irregular packing of donor/acceptor was observed in toluene. Bulk heterojunction solar cells of these mixed films showed poor performance, which is probably due to the lateral orientation of the stacks on the surface. Therefore, for improving the device characteristics, it seems essential to vertically align the supramolecular stacks in thin films.

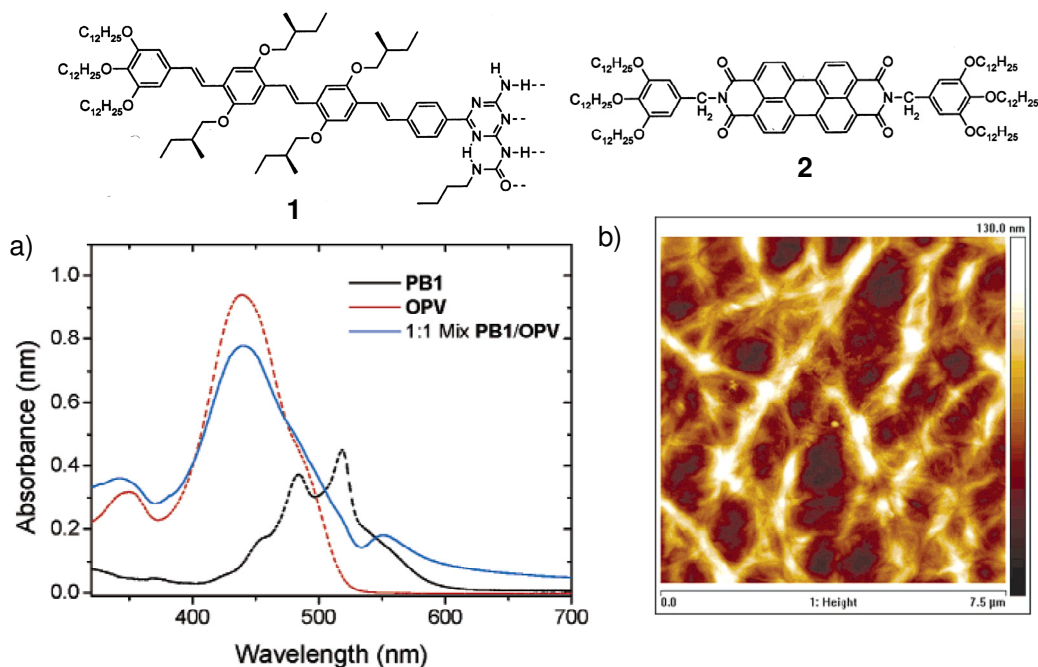
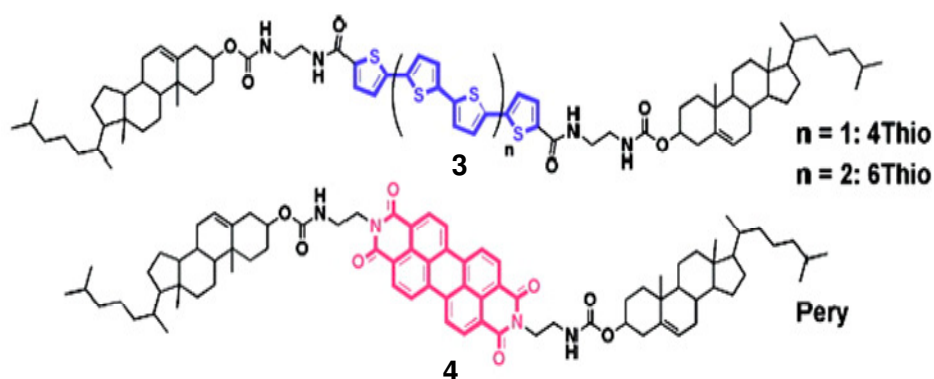


Figure 4.2. a) UV-vis spectral data of **1** and **2** in MCH at room temperature of separate and mixed samples at concentrations of 1×10^{-5} M. b) Tapping mode AFM image of spin-coated films from MCH of a 1:1 mixture of **1** and **2** of a glass/ITO/PEDOT:PSS/OPV:PB1/Al device.

Shinkai and co-workers have reported the self-sorting organogel formation by two different π -conjugated molecules **3** and **4** (Scheme 4.1) [Sugiyasu *et al.* 2008]. This system is composed of precise π -stacking structures entangled at p-n heterojunction points. Solution-processible material facilitates the preparation of the cast film that shows photoelectrical conversion by visible light irradiation.



Scheme 4.1. Chemical Structures of the self-sorting gelators **3** (4Thio) and **4** (6Pery).

The self-sorting gelation process was monitored by variable temperature UV-vis and CD spectral studies. These studies indicate that **3** and **4** self-assemble independently (self-sorting) and do not interfere in each other's aggregation-dissociation processes. SEM images of these gels revealed the formation of fibrous aggregates of around 20 nm diameters (Figure 4.3a-c). This is a simple and convenient technique offering more complicated and advanced design of organic devices.

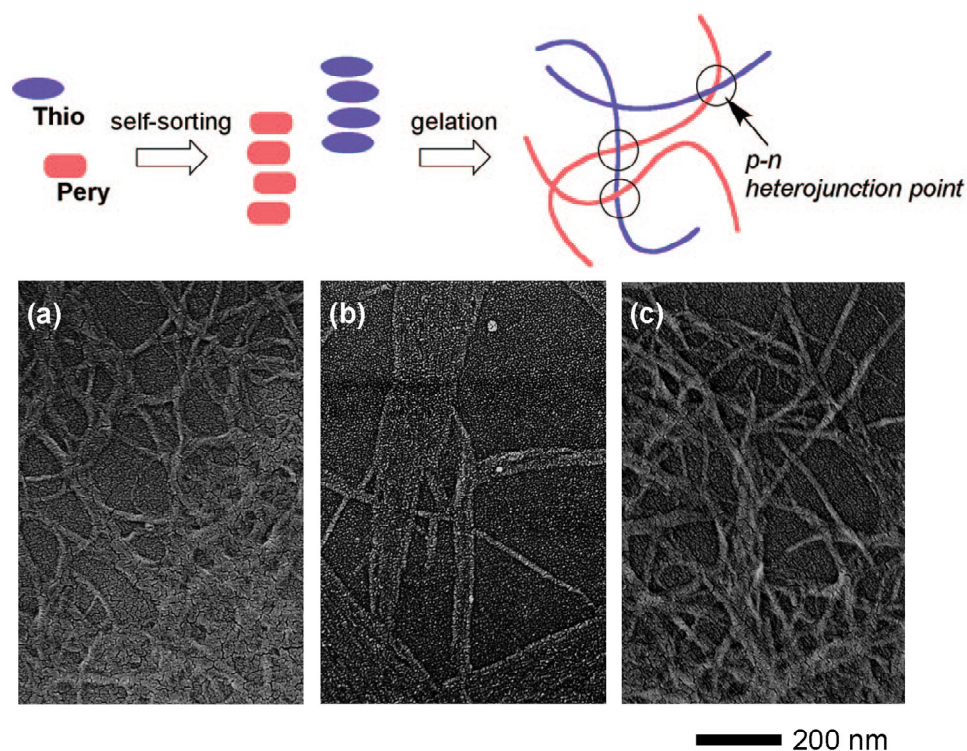


Figure 4.3. Schematic representation of the self-sorting organogel formation yielding p-n heterojunction points and the SEM images of the gels of **3** (a), **4** (b) and the self-sorted **3/4** gel (c).

Xue *et al.* have reported the higher photocurrent generation from 1D self-assemblies of a complex of **5** and C₆₀COOH [Xue *et al.* 2010]. Compound **5** (Figure 4.4) was found to be an excellent gelator for organic solvents, such as dichloromethane, benzene, o-dichlorobenzene, and DMSO/water. Microscopic analysis revealed that hybrid gel can self-assemble into nanofibres in which C₆₀COOH and **5** are packed into 1-D superstructures which are interdigitated each other (Figure 4.4a and b). Such an

ordered microstructure ensures efficient charge-carrier transport so that large photocurrents can be achieved.

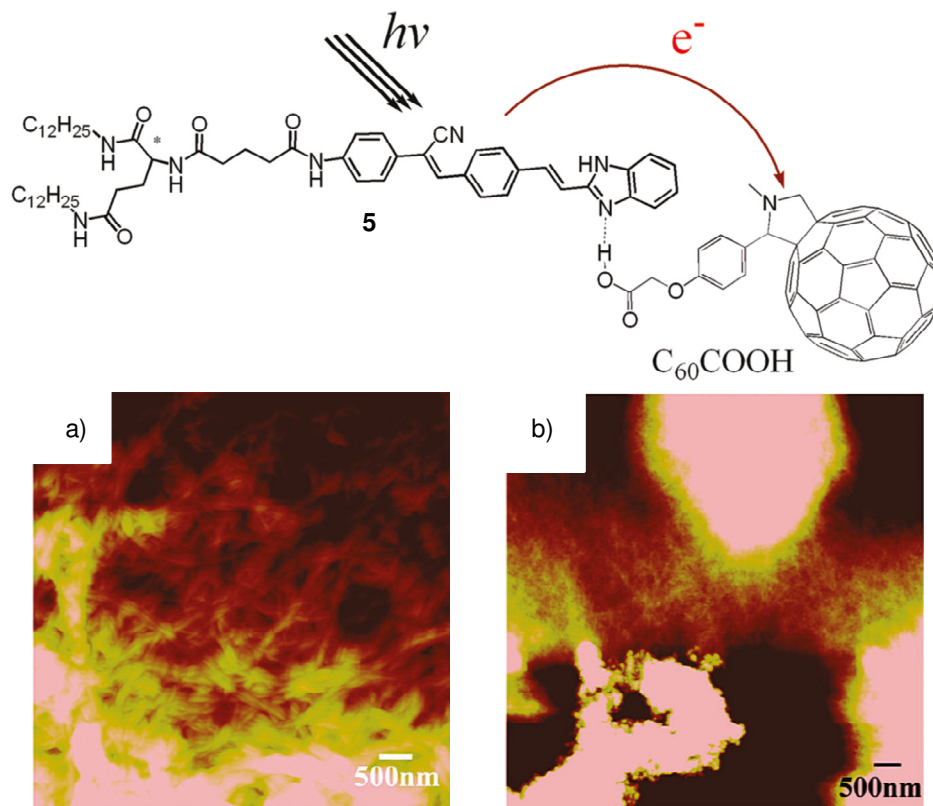


Figure 4.4. Schematic representation of the photoinduced electron transfer from **5** to $C_{60}COOH$. AFM images of a) **5** and b) **5** and $C_{60}COOH$ (1:1 wt ratio).

Recently, Zhang and co-workers have reported the photocurrent generation from gel medium consisting of ex-TTF (**6**) and Fullerene (Figure 4.5) [Yang *et al.* 2010]. Compound **6** formed gel in several organic solvents such as toluene, DMSO and ethanol. Upon addition of C_{60} , enhancement in the gelation ability of **6** was observed. 1H NMR and absorption spectral studies indicated that the intermolecular interaction between the ex-TTF unit in **6** and C_{60} may be responsible for this phenomenon. Further studies imply that the assembly structures in the gel phases in the absence and presence of C_{60} may be different and is shown schematically in Figure 4.5. Gelation-induced CD signals were observed for the gels with either **6** or the mixture of **6** and C_{60} . Additionally, organogels

prepared from **6** and PCBM were used to modify ITO electrode. A stable and rapid photocurrent was generated after exposure of the modified ITO electrode to light. This may provide an alternative way to fabricate photovoltaic cell with high energy conversion efficiency.

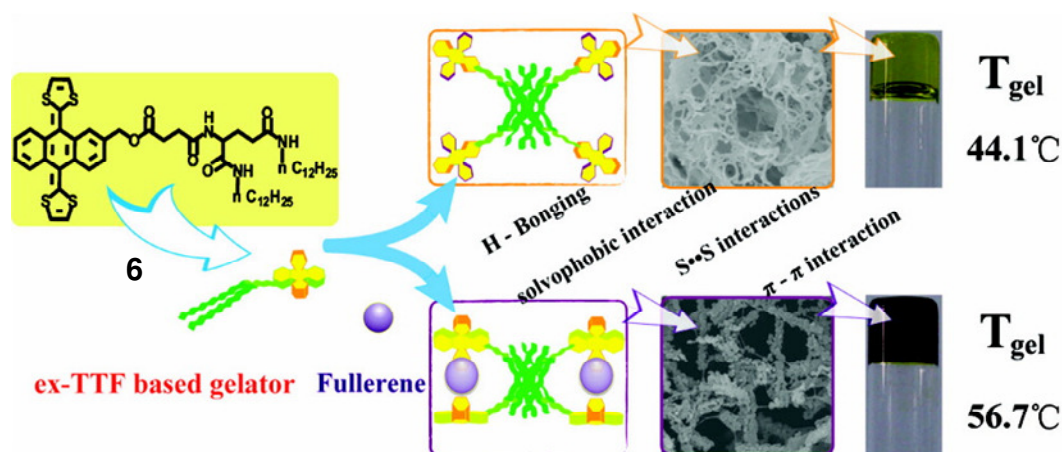


Figure 4.5. Schematic representation of the possible molecular assembly mechanism for **6** in the gel phases in the absence and presence of C₆₀.

Even though there are reports on the self-sorting of donor and acceptor molecules during gel formation, achieving a controlled self-assembly of the self-sorted 1D aggregates as shown in Figure 4.1c remains a challenge. Donor-acceptor self-assembly as shown in Figure 4.1b or 4.1c could be achieved only by logically suppressing alternate donor-acceptor interaction. This could be possible by inducing spontaneous self-assembly of one of the components through H-bonding or similar interactions and the aggregation of the other by weak interactions such as π -stacking. Subsequently, such 1D assemblies should interact laterally to form hierarchical assemblies leading to supramolecular architectures of aligned 1D donor and acceptors. Such an assembly is molecularly phase separated, however macroscopically continuous. The charge separation in such a system is expected to be efficient when compared to random donor-acceptor assemblies. In this chapter, we describe the attempt to prepare such donor-

acceptor self-assembly using thienylenevinylene (**TV**) based molecular gelators which are electron donors and a nongelling perylene bisimide (**PBI**) acceptor which is an electron acceptor (Chart 4.1). Details of the interaction between these molecules, gelation properties, morphological features and charge carrier mobilities are described.

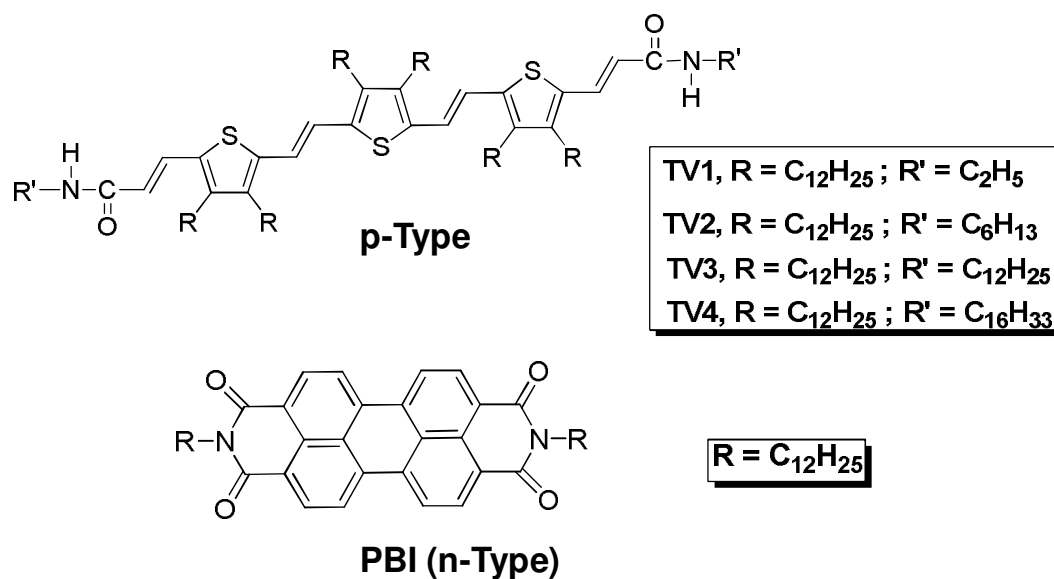
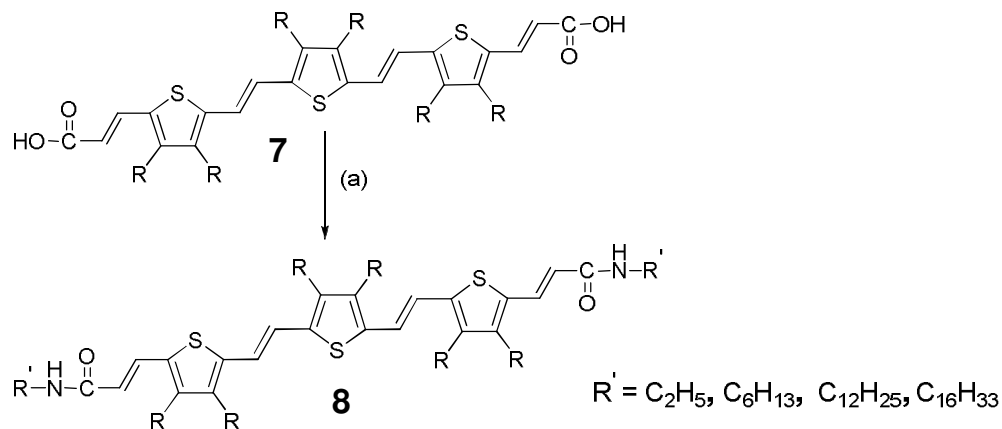


Chart 4.1

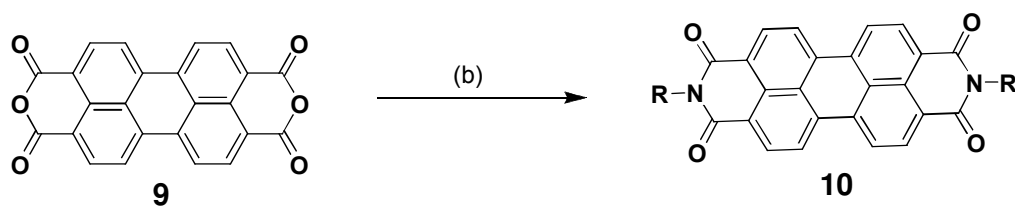
4.3. Results and Discussion

4.3.1. Synthesis of TV1-4 and PBI

TV1-4 prepared from (E)-3-(5-((E)-2-(5-((E)-2-(3,4-didodecyl-5-((E)-3-hydroxybuta-1,3-dienyl)thiophen-2-yl)vinyl)-3,4-didodecylthiophen-2-yl)vinyl)-3,4-didodecylthiophen-2-yl)acrylic acid (**7**) by treating with ethylamine, hexylamine, dodecylamine and hexadecylamine in the presence of HATU to give the products as shown in Scheme 4.2. **PBI** was synthesized from perylene (3,4,9,10) tetracarboxylic dianhydride (PTCDA) (**9**) by reacting with dodecylamine (Scheme 4.3).



Scheme 4.2. Synthesis of **TV1-4**. Reagents and conditions: (a) $\text{R}' \text{NH}_2$, HATU, DIPEA, 20h, 30 °C.



Scheme 4.3. Synthesis of **PBI**. Reagents and conditions: (b) $\text{C}_{12}\text{H}_{25}\text{NH}_2$, t-BuOH, 20 h, 120 °C, 82 %.

4.3.2. Photophysical Properties

Absorption and emission spectral analysis is a useful technique to study the interaction between donor and acceptor systems. UV-vis absorption spectral properties of **TV1** is described in Chapter 2. **TV2-4** also showed similar behavior in chloroform and decane. They exhibited absorption maximum around 501 nm in chloroform which is blue shifted to 464 nm indicating H-type aggregation (Figure 4.6a). The absorption spectrum of **PBI** in chloroform showed sharp bands at 458, 491, and 526 nm. However, in decane, the spectrum showed shoulder band at around 580 nm (Figure 4.6b). A 1:1 mixture of the **TV4** with **PBI** in chloroform exhibited the individual spectral properties indicating that there is no ground state interaction between them. However, in decane, they showed aggregation tendency as indicated by the shift in the spectra (Figure 4.6c). Interestingly,

the nature of the spectrum indicate a combination of the spectra of the individual self-assemblies of **TV4** and **PBI** without the formation of any new band indicating that they do not co-assemble. Aggregation behavior of **TV4**, **PBI** and **TV4/PBI** (1:1 M ratio) mixture were studied by temperature dependent absorption spectral changes (Figure 4.7a-c). **TV4** showed a red-shift of the absorption maximum with increase in temperature indicating the breakage of the H-aggregates to the monomer. On the other hand, **PBI** showed weak change during the heating to 70 °C indicating strong π -stacking. Increasing the temperature of the **TV4/PBI** mixture exhibited a red shift of the absorption maximum. However, the shoulder band at 580 nm showed weak change leaving significant residual absorption. From this observation, it is inferred that in the **TV4/PBI** mixture only **TV4** aggregates are breaking and the **PBI** aggregates may not be breaking as observed in the individual cases.

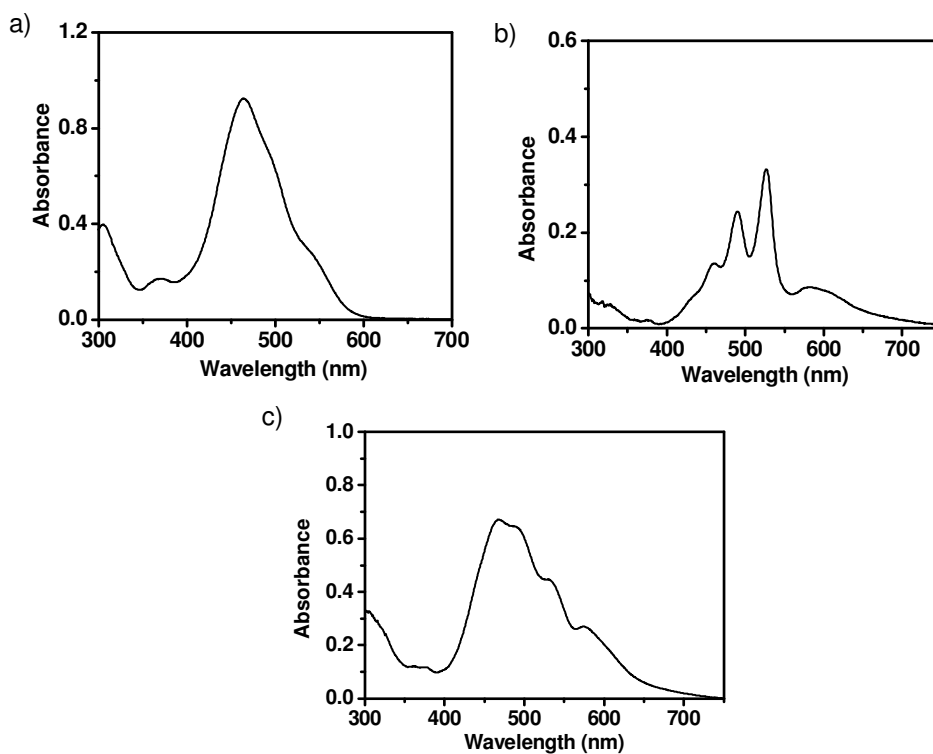


Figure 4.6. Absorption spectra of a) **TV4**, b) **PBI** and c) **TV4/PBI** (1:1 M ratio) in decane ($c = 1 \times 10^{-4}$ M).

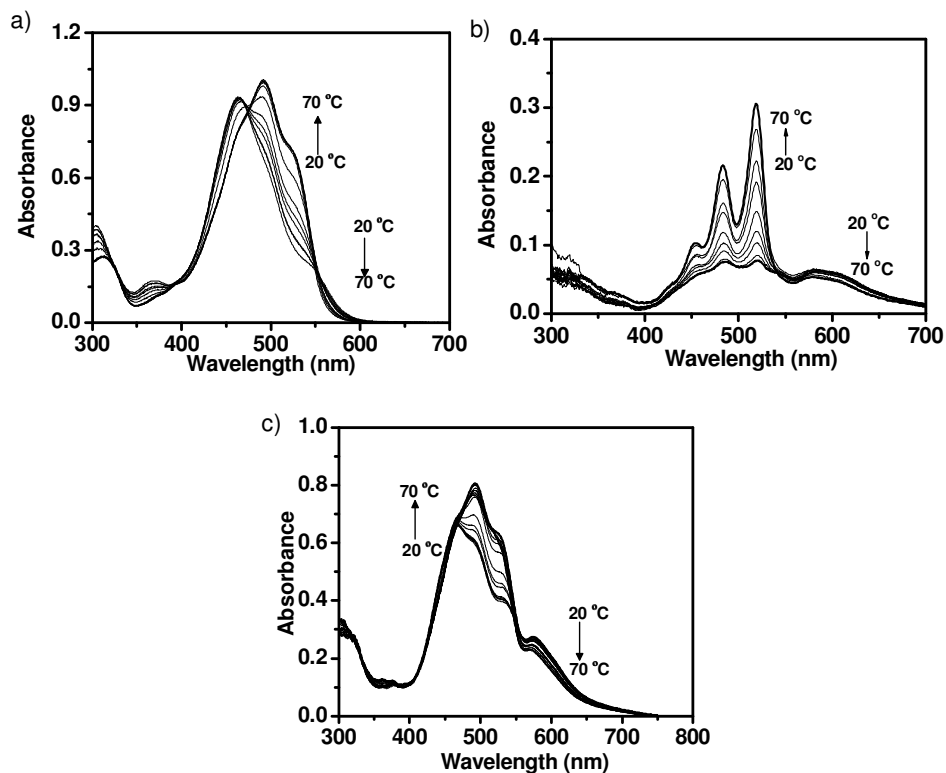


Figure 4.7. Temperature dependent absorption studies of a) **TV4**, b) **PBI** and c) **TV4/PBI** (1:1 M ratio) in decane in the range from 20-70 °C.

Thermal stability of **TV4**, **TV4/PBI** (1:1 M) aggregates were determined from the temperature dependent absorption spectral changes. Figure 4.8 represents the fraction of aggregates versus temperature, which revealed that thermal stability of co-assembled aggregates increases when compared to individual assemblies of **TV4** alone.

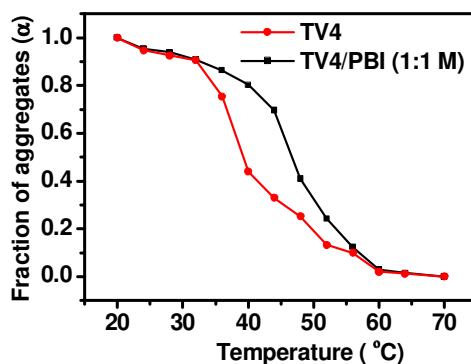


Figure 4.8. Plot of fraction of aggregation (α) versus temperature monitored at 520 nm for **TV4** and **TV4/PBI** (1:1 M).

4.3.3. Gelation Studies

Gelation property of **TV1** is described in Chapter 2. Strong gels were obtained in solvents such as hexane, decane etc. Similarly, **TV2-4** also formed stable gels in nonpolar solvents. The critical gelator concentration to form a stable gel of **TV1** in decane is 0.98 mM whereas that of **TV2**, **TV3**, and **TV4** is 0.87, 0.69 and 0.48 mM, respectively and hence **TV4** belongs to the class of super gelators. The gelation properties of these molecules are presented in Table 4.1.

Table 4.1. Gelation Studies of **TV1-4** in polar and non-polar solvents

SI. No.	Solvent	Nature of gel	CGC			
			TV1 (mM)	TV2 (mM)	TV3 (mM)	TV4 (mM)
1.	Decane	G	0.98	0.87	0.69	0.48
2.	Cyclohexane	G	1.22	1.09	0.90	0.59
3.	Hexane	G	1.61	1.46	1.34	0.97
4.	Benzene	G	4.63	3.88	3.37	2.71
5.	Toluene	G	5.29	4.66	4.28	3.84
6.	Chloroform	S	-	-	-	-
7.	Methanol	NS	-	-	-	-

G = gel, S = Soluble, and NS = Not soluble.

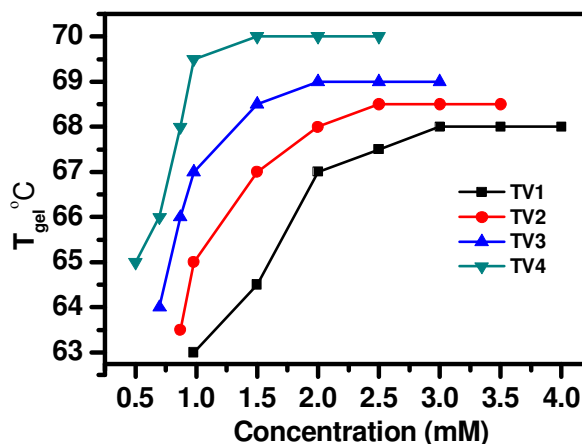


Figure 4.9. Plot of T_{gel} versus concentration for **TV1-4**.

The gel stabilities were determined from the plots of the gel melting temperature (T_{gel}) at different concentration of the gelator (Figure 4.9). Figure 4.9a shows increase of T_{gel} with increase in the alkyl chain length. Hence **TV4** form strong gels at a much lower concentration of 1.5 mM whereas for **TV1**, a concentration of 3 mM was required.

4.3.4. Morphological Studies

Interaction of **TV1-4** with **PBI** was studied using AFM and TEM analyses. For AFM analysis, films of **TV1-4** were prepared from decane solutions ($c = 1 \times 10^{-5}$ M) and drop casted on freshly cleaved mica and silicon wafer surfaces. AFM image of **TV1** showed the formation of unidirectionally oriented 1D fibres whereas for **TV4**, parallel oriented cross-patterned rods having several junction zones were formed. The average height of these rods are 3-5 nm with diameter in the range of 50-150 nm (Figure 4.10a and d). **TV2** and **TV3** also showed parallel and anti-parallel fibre formation with average size 50-200 nm (Figure 4.10b and c). However, these fibres are not properly oriented as in the case of **TV1** and **TV4**. From the AFM images, it is obvious that the morphology of **TV1-4** gelators are significantly different from that of the other π -gelators. AFM images of **TV1-4** are clear indication of epitaxy controlled self-assembly as described in Chapter 3. AFM images also suggest that increasing the alkyl chain length of the molecule play a significant role in the epitaxial self-assembly. However, upon increasing the concentration of the solution from 1×10^{-5} M to 5×10^{-5} M, **TV1-4** showed considerable variation in the morphology (Figure 4.11a-d). For example, in the case of **TV3** the less patterned arrangement at 1×10^{-5} M concentration changed to a more organized pattern of short fibres at 5×10^{-5} M concentration. However, an opposite trend is observed in the case of **TV4**.

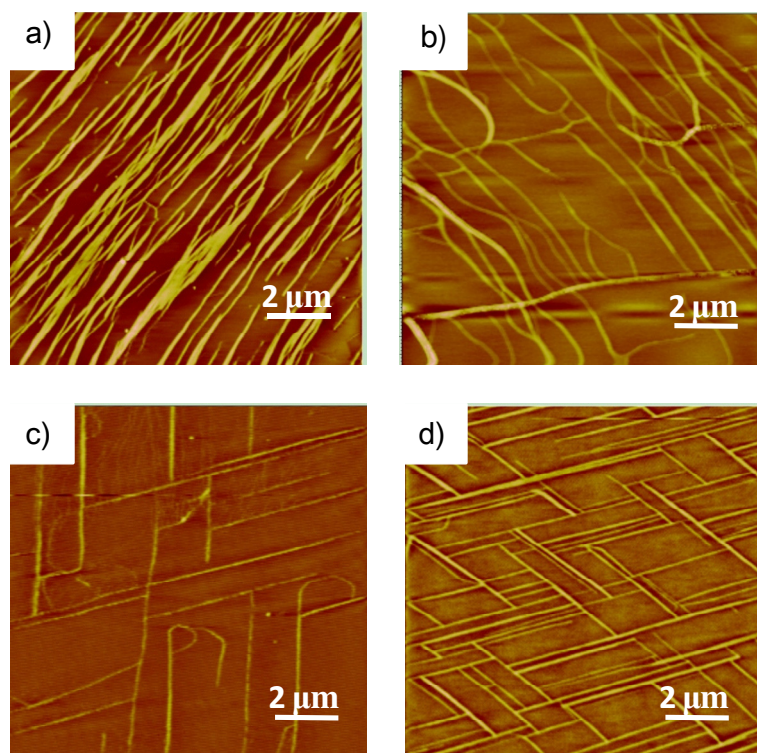


Figure 4.10. AFM images of a) TV1, b) TV2, c) TV3 and d) TV4 from decane drop casted on freshly cleaved mica surface at room temperature ($c = 1 \times 10^{-5}$ M).

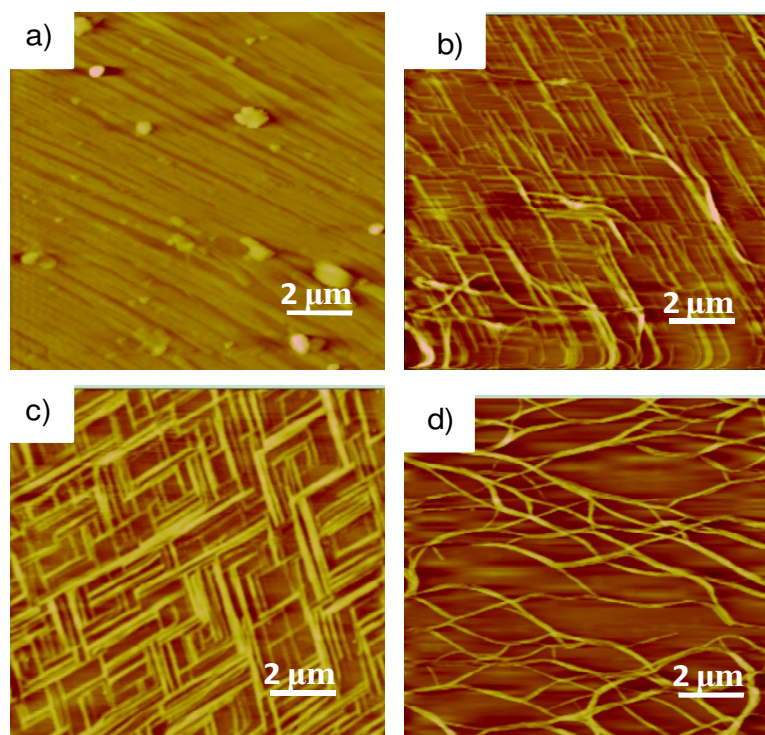


Figure 4.11. AFM images of a) TV1, b) TV2, c) TV3 and d) TV4 from decane drop casted on freshly cleaved mica surface at room temperature ($c = 5 \times 10^{-5}$ M).

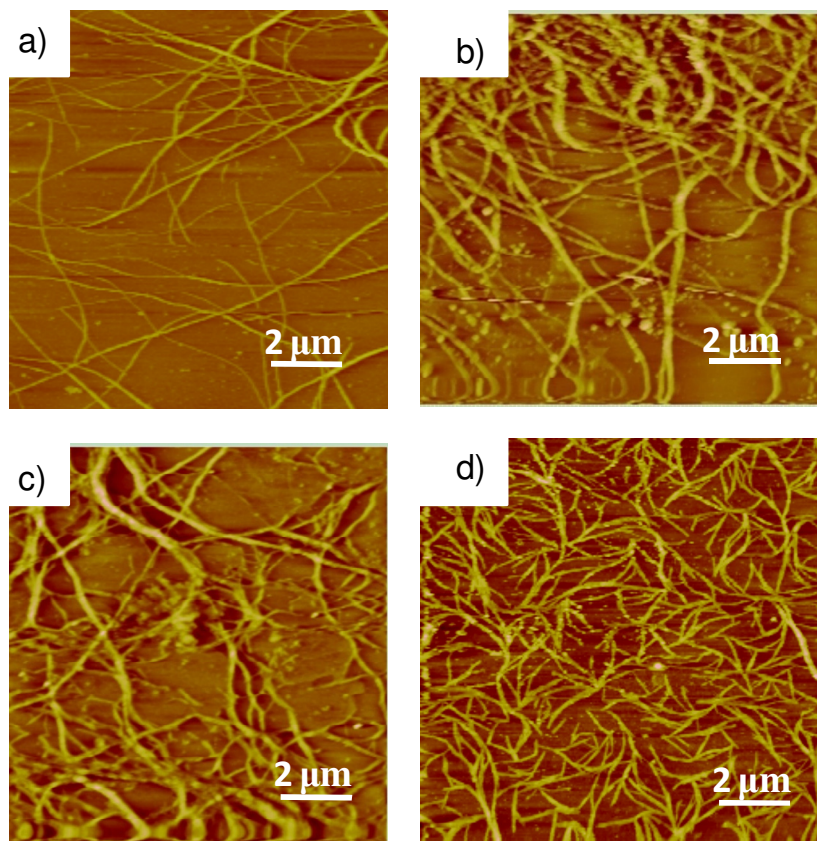


Figure 4.12. AFM images of a) TV1, b) TV2, c) TV3 and d) TV4 from decane drop casted on silicon wafer surface at room temperature ($c = 5 \times 10^{-5}$ M).

TV1-4 showed the formation of flexible thin nanowires on silicon wafer with average diameter of 50-200 nm and several micrometers in length (Figure 4.12a-d). In these cases, no pattern formation is observed, instead entangled fibres were formed. A comparison of the morphological features of AFM images on mica and silicon wafer reveals the fact that mica substrate plays considerable role in the substrate-molecule interactions. It is also obvious that the substrate-molecule interaction varies with the length of the alkyl chains in the amide group. TEM images of solutions prepared from decane (5×10^{-5} M) showed entangled long fibres as shown in Figure 4.13. TEM images revealed the formation of very thin elementary fibrils which bundle to form large fibers of 50-300 nm in diameter and several micrometers in length.

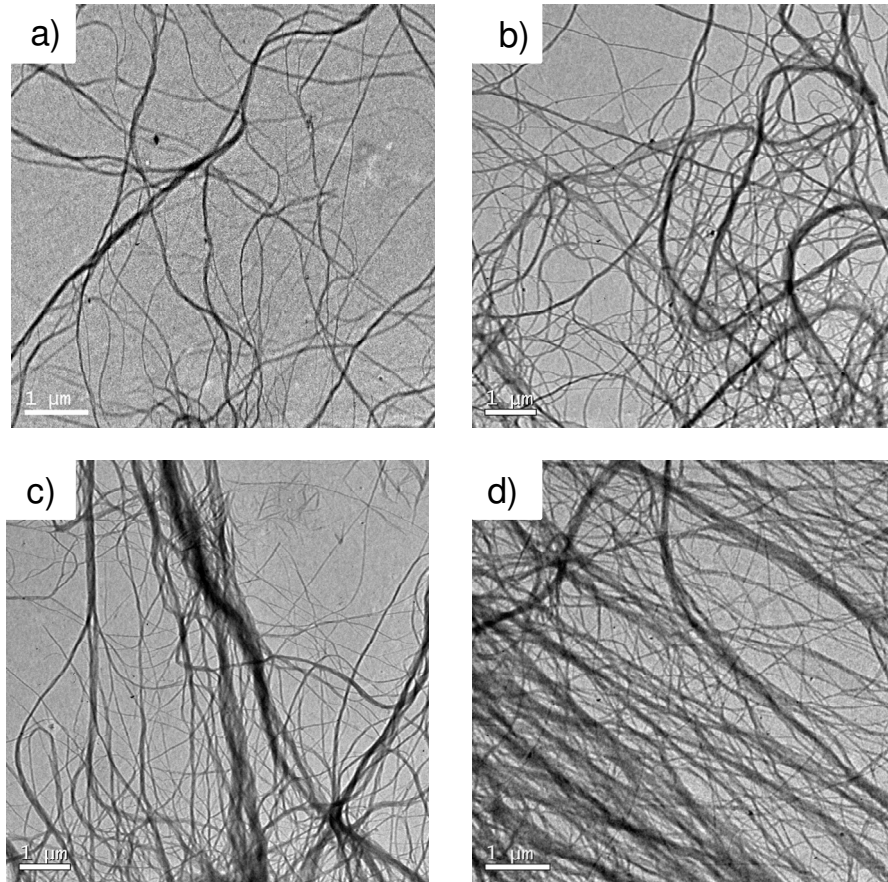


Figure 4.13. TEM images of a) TV1, b)TV2, c) TV3 and d) TV4 from decane drop casted on copper coated grid ($c = 5 \times 10^{-5}$ M).

TEM images of **PBI** showed the formation of thin tapes with an average of 0.5-1 μm in width and several micrometers in length as shown in Figure 4.14a. AFM images of **PBI** exhibited short fibre-like assemblies having a width of 300-400 nm, average height in the range of 10-70 nm, and a 1-3 μm in length on freshly cleaved mica surface (Figure 4.14b). However, on silicon wafer, AFM images showed tape-like structures with 0.5-1 micrometers in width and several micrometers in length as observed in TEM image (Figure 4.14b).

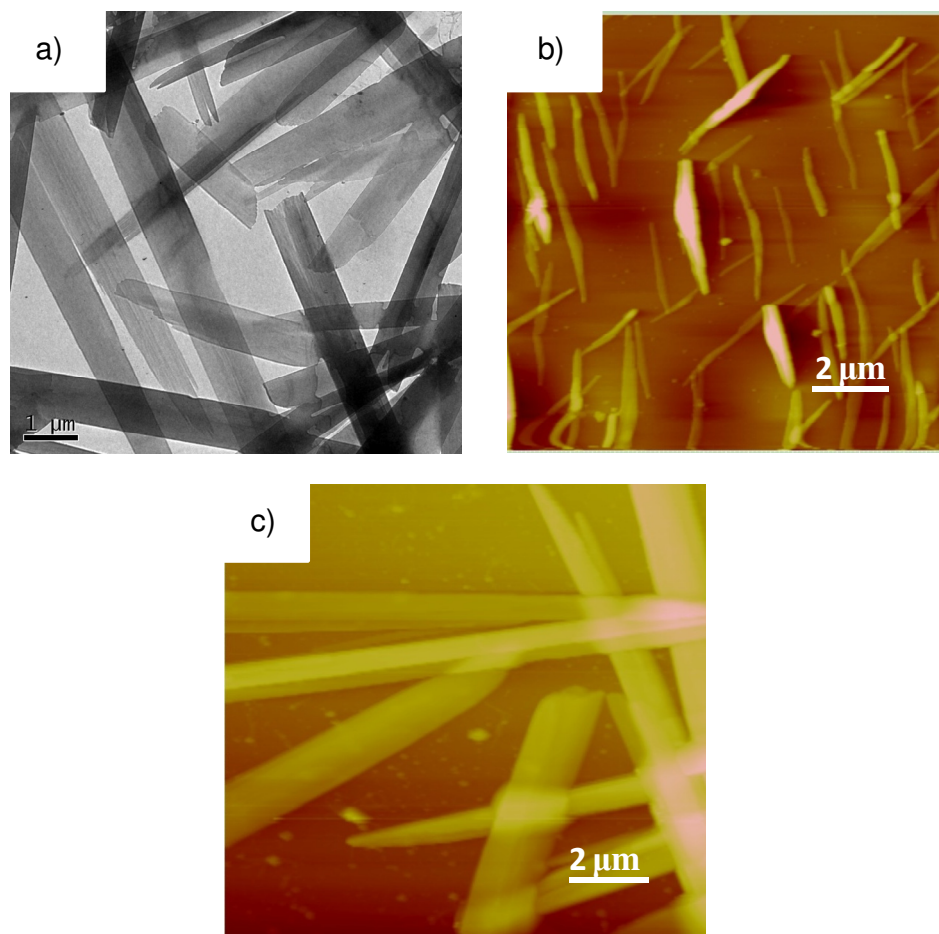


Figure 4.14. a) TEM image of **PBI** on copper coated grid. AFM images of **PBI** drop casted b) on freshly cleaved mica and c) on silicon wafer ($c = 1 \times 10^{-4}$ M).

Interestingly, mixture of **TV1-4/PBI** showed morphological features which are different from those of the individual assemblies of **TV1-4** and **PBI**. AFM images of **TV1-4/PBI** (1:1 M ratio) showed aligned tapes of several micrometers in length on freshly cleaved mica surface (Figure 4.15a-d). These tapes exhibited average diameter of 50-300 nm and height of 5-60 nm. However, on silicon wafer, the mixture showed thicker fibres of 0.3-0.7 μm diameter and several micrometers in length (Figure 4.16a-d). In mica surfaces and silicon wafer, the morphological features are significantly different from those of the individual **PBI** and **TV1-4** assemblies.

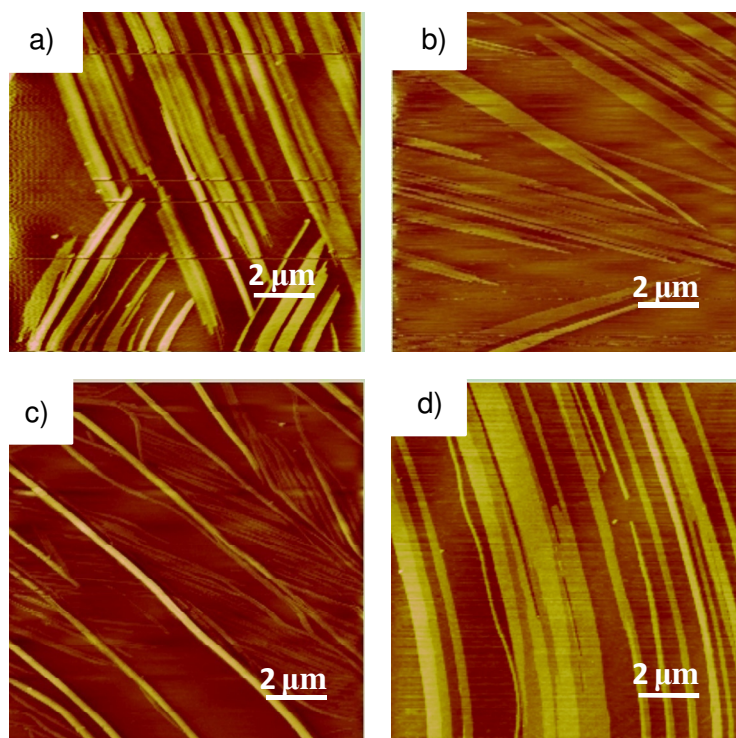


Figure 4.15. AFM images of a) TV1/PBI, b) TV2/PBI, c) TV3/PBI and d) TV4 /PBI (1:1 M) from decane drop casted on freshly cleaved mica ($c = 5 \times 10^{-5}$ M).

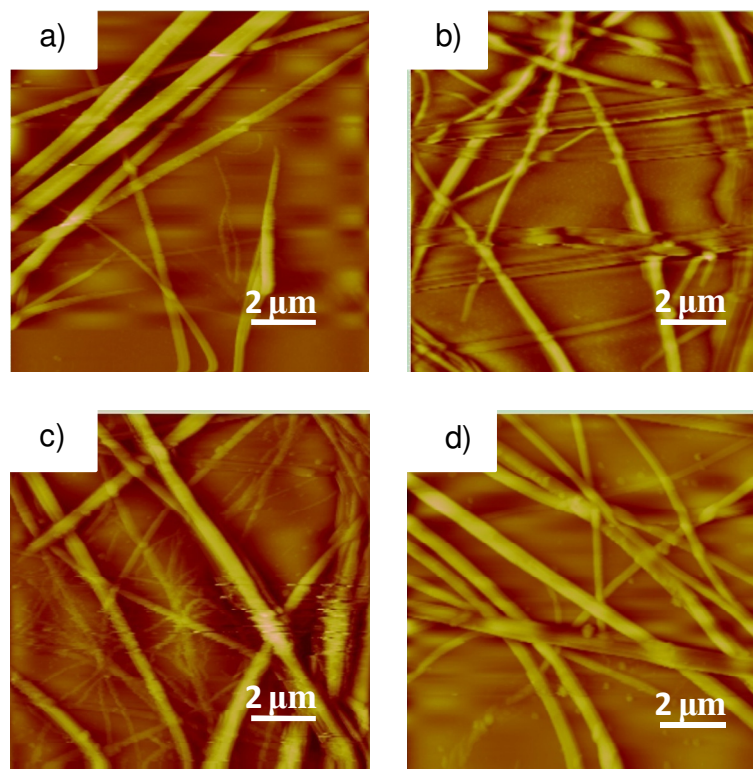


Figure 4.16. AFM images of a) TV1/PBI, b) TV2/PBI, c) TV3/PBI and d) TV4 /PBI (1:1 M) from decane drop casted on silicon wafer ($c = 5 \times 10^{-5}$ M).

TEM images of **TV1-4/PBI** (1:1 M) revealed the formation of elongated rods with dimensions ranging from a 0.3-0.7 μm in diameter and several micrometers in length (Figure 4.17). Thin and large rods could be seen which indicate that the large rods are formed by the lateral joining of thinner fibres. AFM images on silicon wafer and TEM images showed almost identical morphological features.

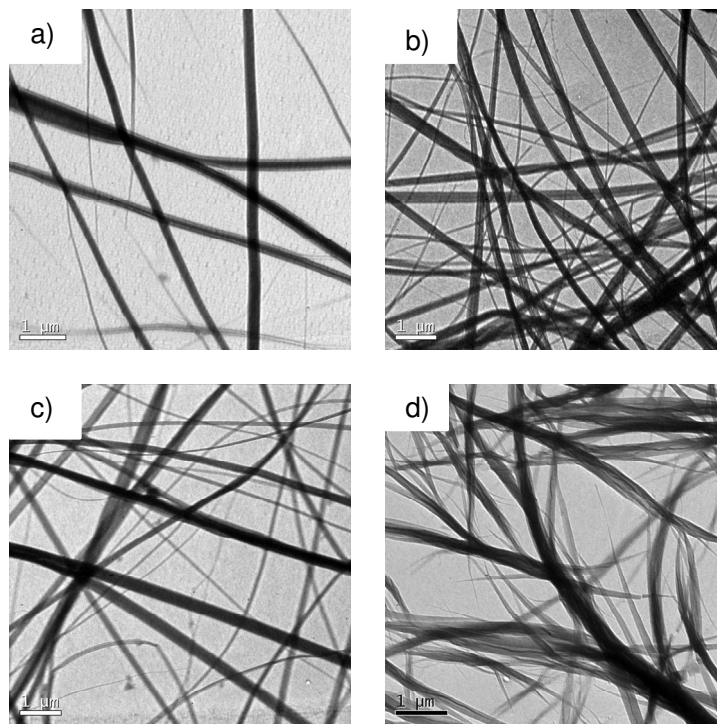


Figure 4.17. TEM images of a) **TV1/PBI**, b) **TV2/PBI**, c) **TV3/PBI** and d) **TV4 /PBI** (1:1 M) from decane drop casted on freshly cleaved mica ($c = 5 \times 10^{-5}$ M).

4.3.5. Kelvin Probe Force Microscopy Investigation

In order to have more insight into the electronic properties of the co-assembly, their surface potentials (SP) were measured by Kelvin probe force microscopy. KPFM is a contactless technique that allows the quantitative measurement of the electric surface potential with nanoscale resolution without significantly perturbing the potential of the system under study, enabling an in situ exploration of the operation of electronic devices. The SP of a sample can be considered as the work function of the sample by taking into

account, effects due to the surface polarizability as well as band bending [Martin *et al.* 1988; Palermo *et al.* 2006; Liscio *et al.* 2010].

AFM and KPFM images of a thin layer of **TV1-4**, **PBI** and **TV1-4/PBI** (1:1 M ratio) on freshly cleaved mica and silicon wafer substrates were recorded [Liscio *et al.* 2008; Dabirian *et al.* 2009]. For these studies, films were prepared by drop casting from decane solution. KPFM analysis of **TV1-4** exhibits surface potential approximately in the range of 20 ± 5 mV where thickness of the fibre is 10 nm. Figure 4.18 represents AFM and KPFM images of **TV4** on mica surface. The corresponding section analysis is also shown in Figure 4.18c and 4.18d. The surface potential of **TV4** is obtained from KPFM analysis and the value is 10 ± 2 mV. These results were obtained from interconnected fibres with few micrometers in length on mica surface. Conversely, **PBI** films on mica, exhibit short fibre-like assemblies having a width of 300-400 nm, and 1-3 μm in length. The corresponding SP found was found to be -15 ± 10 mV (Figure 4.19a-d) [Liscio *et al.* 2006; Liscio *et al.* 2008; Dabirian *et al.* 2009].

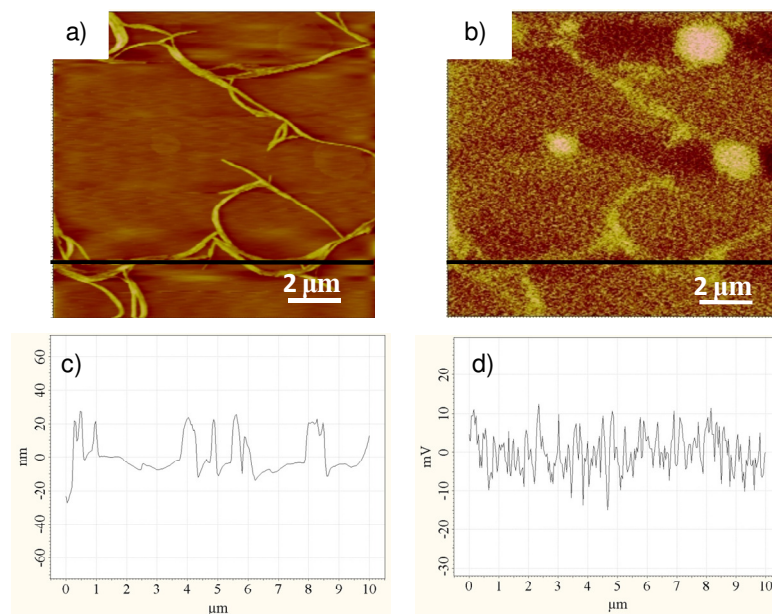


Figure 4.18. AFM/KPFM images of **TV4** from toluene drop casted on mica at room temperature ($c = 1 \times 10^{-4}$ M). a) Topography and b) KPFM image. The corresponding section analyses are shown in c and d.

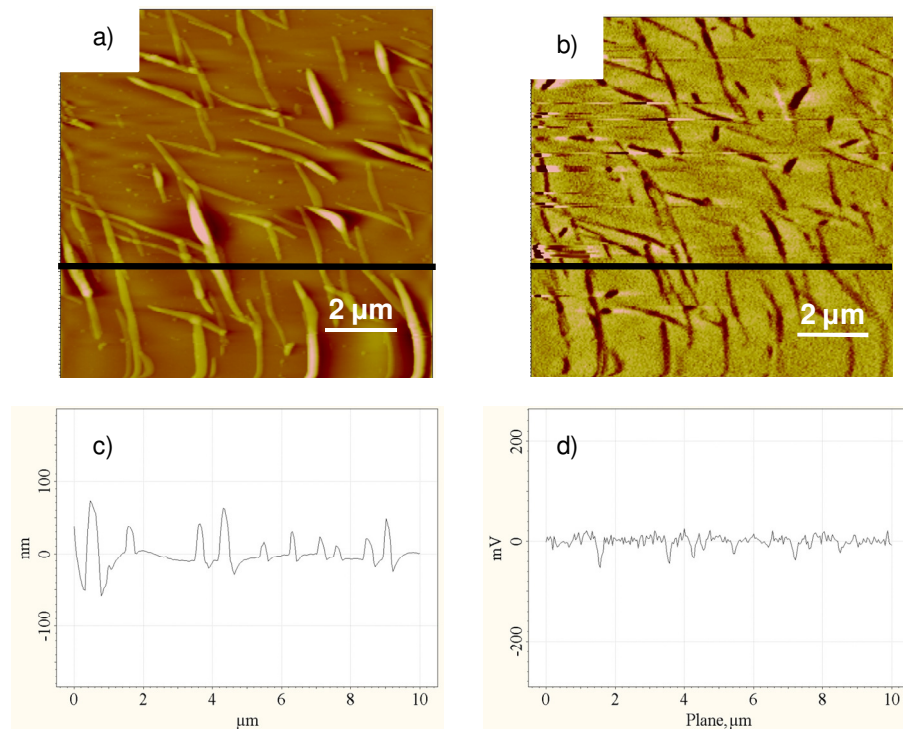


Figure 4.19. AFM/KPFM images of **PBI** from toluene drop casted on mica at room temperature ($c = 1 \times 10^{-4}$ M). a) Topography and b) KPFM image. The corresponding section analyses are shown in c and d.

KPFM image of **TV4/PBI** (1:1 M ratio) on mica is shown in Figure 4.20b. The corresponding AFM image is shown in Figure 4.20a. Figure 4.20b represents the SP variations in the nanowires obtained from different positions (I, II and III). The SP value of nanowire at position I is found to be 15 ± 5 mV which is close to the SP value of **TV4**. The surface potential of the nanowire at position II is measured as -20 ± 5 mV which is close to the value of **PBI** (Figure 4.18b and 4.19b). Surprisingly, some of the nanowires at position III exhibit -40 ± 5 mV, which shows more negative shift when compared to individual assemblies of **PBI** (Figure 4.19b). These data implies that the **PBI** is in physical contact with the **TV4** aggregates. The driving force for exciton splitting and charge separation derives from the difference in the electron affinity of the electron acceptor (**PBI**) and electron donor (**TV4**) phases. Because of this, significant charging

was observed only for the **PBI** aggregates in contact with the **TV4**. Similarly, KPFM of **TV1-3** with **PBI** were measured and the resultant SP values shown in Table 4.2.

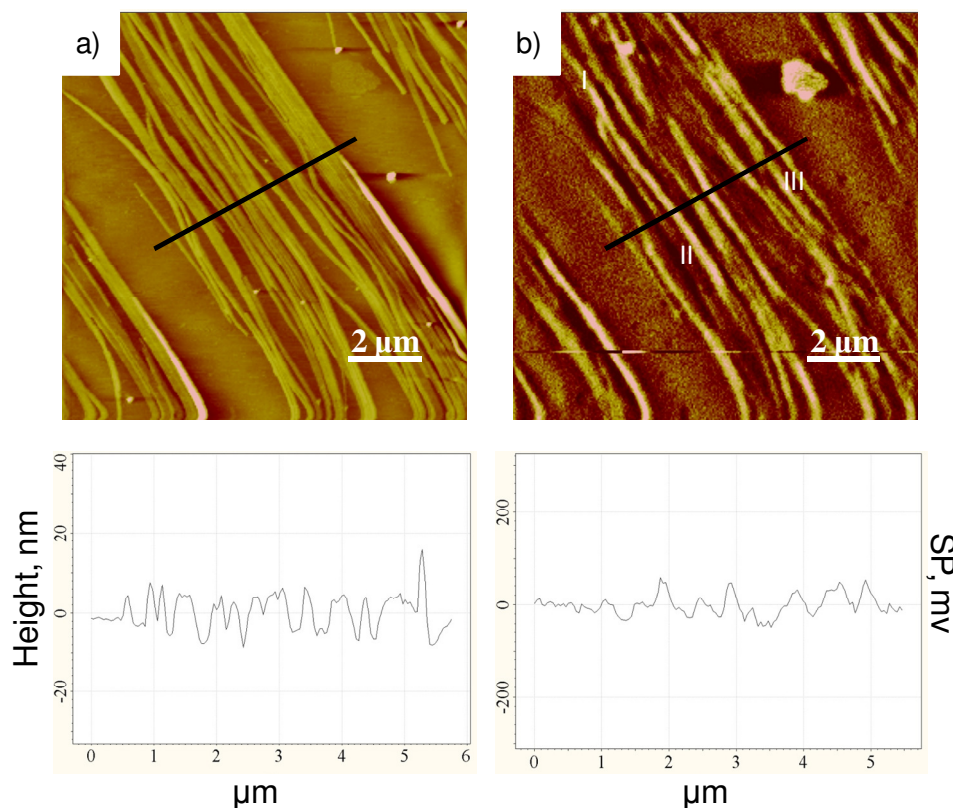


Figure 4.20. a) AFM and b) KPFM images of **TV4 /PBI** (1:1 M) drop casted from decane on mica ($c = 5 \times 10^{-5}$ M) at room temperature. The corresponding section analyses are also shown.

On silicon wafer, **TV4** exhibits a surface potential of 15 ± 5 mV at open air condition as shown in Figure 4.21b. All the calculated SP values were obtained from section analysis. Subsequently, SP of **PBI** was measured and the resultant values are in the range of -40 ± 5 mV (Figure 4.22). Figures 4.23a and 4.23b represent the topography and KPFM image respectively of **TV4/PBI** (1:1 M) which shows elongated fibres with 300-500 nm in diameter and 100-200 nm in height. The corresponding SP value obtained from section analysis is -100 ± 10 mV [Palermo *et al.* 2008]. These SP variations could be mainly due to the substrate-molecule interactions which reduce the strength of molecule-molecule interaction.

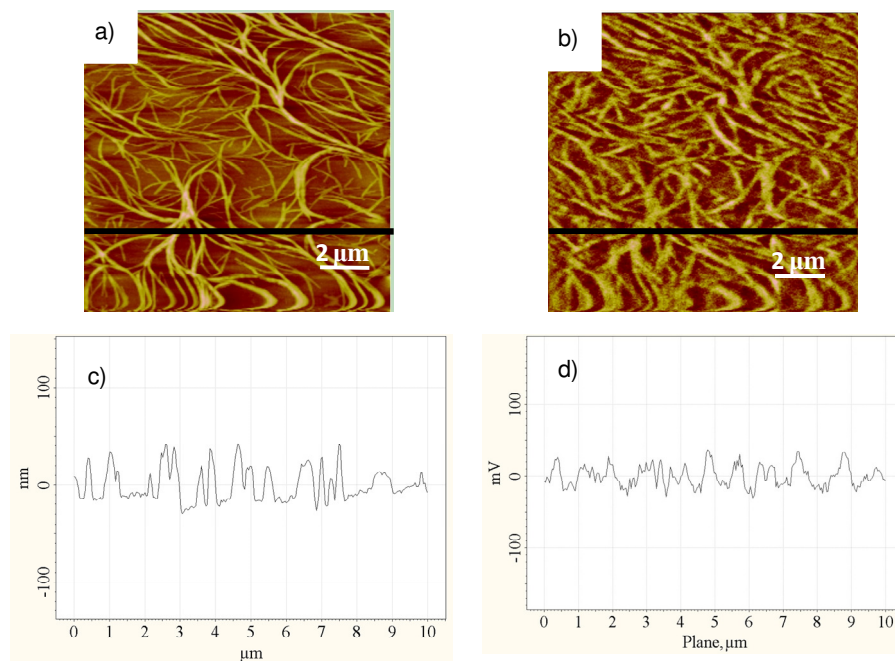


Figure 4.21. AFM/KPFM images of **TV4** from decane drop casted on silicon wafer at room temperature ($c = 5 \times 10^{-5}$ M). a) Topography and b) KPFM image. The corresponding section analyses are shown in c and d.

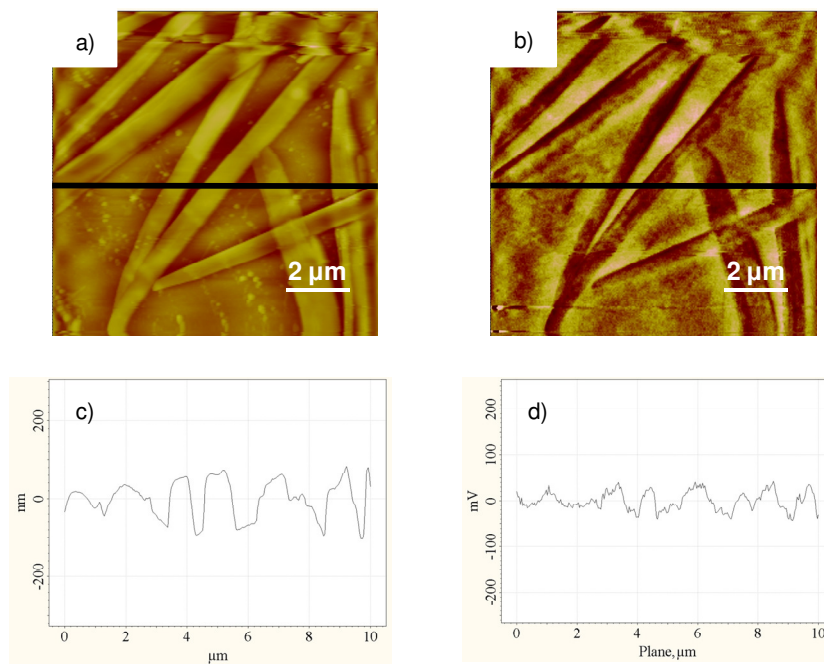


Figure 4.22. AFM/KPFM images of **PBI** from toluene drop casted on silicon wafer at room temperature ($c = 1 \times 10^{-4}$ M). a) Topography and b) KPFM image. The corresponding section analyses are shown in c and d.

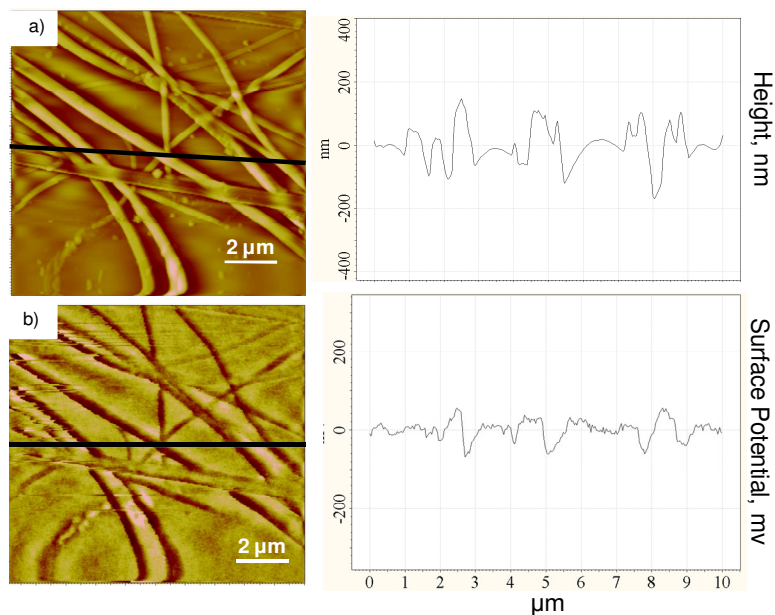


Figure 4.23. a) AFM and b) KPFM images of **TV4 /PBI** (1:1 M) drop casted on silicon wafer from decane ($c = 5 \times 10^{-5}$ M) at room temperature. The corresponding section analyses are also shown.

On silicon wafer, molecule-molecule and inter-fibre interactions are more predominant than molecule-substrate interactions which leads to high surface potential. Subsequently, interaction of **TV1-3** with **PBI** was also studied. The corresponding values are shown in Table 4.2.

Table 4.2. KPFM analysis of donor/acceptor (**PBI**) (1:1 M ratio) on freshly cleaved mica and Silicon wafer surfaces

Donor/Acceptor (PBI) (1:1 M ratio)	Mica SP(mV)	Si wafer SP(mV)
TV1	-20	-55
TV2	-25	-60
TV3	-30	-75
TV4	-45	-110

Surface potential (SP) values are represented in Table 4.2 after subtracting the surface potentials obtained from substrate. Average error for all these measurements, ~ 5 mV for mica and ~ 15 mV for silicon wafer surfaces. SP values of **PBI** on mica and Si wafer values are -10 mV and -40 mV respectively.

4.3.6. X-ray Diffraction Measurements

To have a better understanding of the molecular packing in the co-assembly of **TV1-4/PBI**, X-ray diffraction analysis of **TV1-4**, **PBI**, and **TV1-4/PBI** (1:1 M ratio) xerogel films were performed (Figure 4.24). XRD analysis of **TV4** gel showed intense and sharp reflections with d-spacing of 34.5, 24.1, 20.4, 4.3 and 3.3 Å. The very strong diffraction peak at 34.5 Å in the small angle region is close to the calculated molecular width (34.2 Å) in which the alkyl chains are almost in fully extended conformation. Another intense signal with a d-spacing of 3.3 Å was also observed in the wide angle region corresponding to the π - π stacking distance of **TV4** in the gel state. In addition to these peaks, intense diffraction peak with d-spacing of 4.3 Å was observed in the wide angle region which corresponds to the crystallization of the alkyl chains in the assembly of **TV4**. From these diffraction peaks in the XRD, it can be concluded that **TV4** self-assembles in a lamellar fashion. In the case of **PBI**, distinct diffraction peaks with d-spacing of 24.8, 12.4, 8.3, 6.2, 4.9 and 3.1 Å are observed (Figure 4.24b). The d-spacing of 24.8 Å at small angle region corresponds to the half of the length of two tail-to-tail interdigitated **PBI** molecules. The d-spacing of 3.1 Å corresponds to the cofacial intermolecular stacking, which is consistent with the π - π stacking distance for the planar aromatic molecules. Another intense peak observed at wide angle region with a d-spacing of 4.9 Å arises due to the edge-to-edge distance between the stacked **PBI** planes. The initial intense and sharp diffraction peak at $2\theta = 3.98^\circ$ is characteristic of a columnar type assemblies [Che *et al.* 2010]. Figure 4.24c represents the mixture of **TV4/PBI** (1:1) which showed sharp diffraction peaks at 24.7, 12.3, 8.2, 6.2, 4.9 and 3.3 Å. These d-spacing values correspond to those values obtained from the individual assemblies of **TV4** and **PBI** as shown above. The absence of any predominant new peak in the XRD pattern of co-assemblies reveals that **TV4** and **PBI** are preferentially aggregating in individual mode during the mixing. These observations are in agreement with the UV-vis

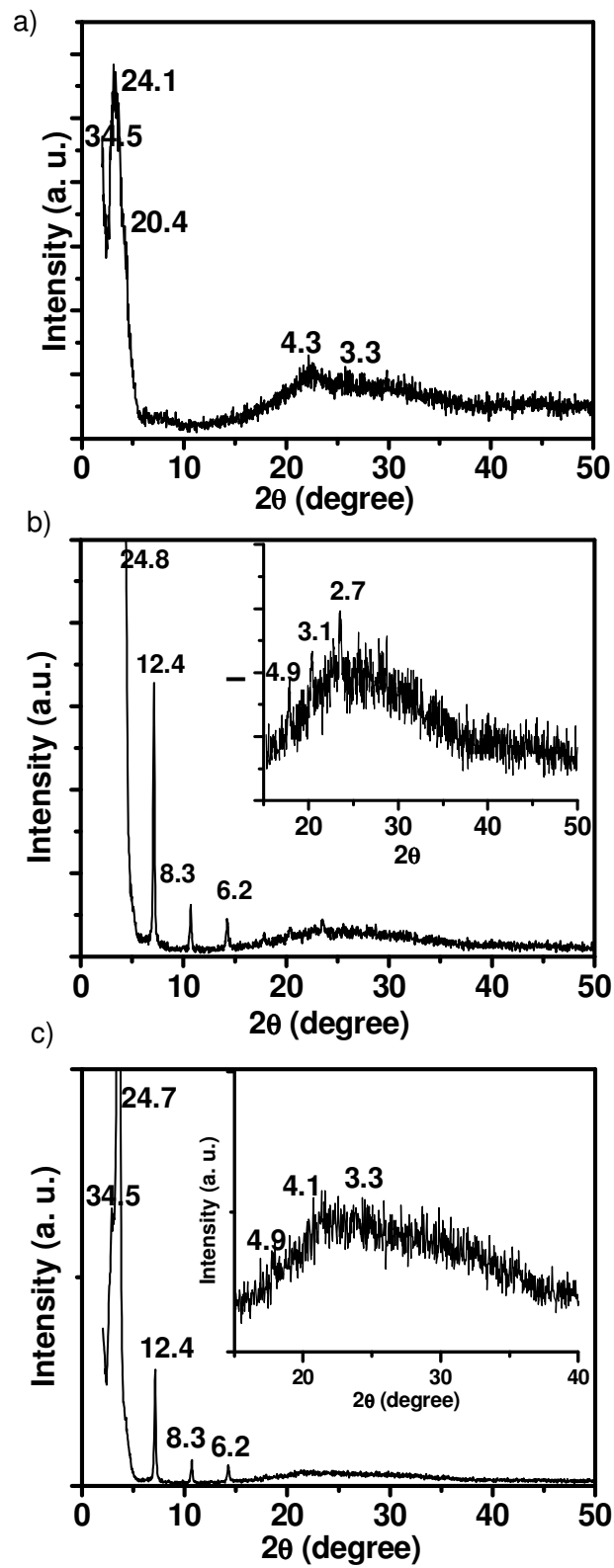


Figure 4.24. X-ray diffraction of a) TV4 (p-type), b) PBI (n-type) and c) TTV/PBI (1:1 M ratio) xerogels on quartz substrate.

studies. The XRD analyses of **TV1-3** and **TV1-3/PBI** showed similar results as in the case of **TV4/PBI**. These data strongly suggest the occurrence of a molecular level self-sorting between the donor and acceptor components in the fibre assemblies.

4.3.7. Mobility Studies: FP-TRMC and TAS Studies

Molecular arrangements of **TV1-4** and **PBI** in co-assemblies can have a significant impact on their charge-carrier mobilities and photoconductivities. We thus investigated the intrinsic charge-carrier mobility of the p-type (**TV1-4**) xerogels by a combination of flash-photolysis time-resolved microwave conductivity and transient absorption spectroscopy upon irradiation by 355 nm light. Charge carriers were generated photolytically by adding *N,N'*-bis(dodecyl)-3,4,9,10-perylenedicarboximide as an electron acceptor. For these studies, a 1 mM CHCl_3 solution of **PBI** was mixed with **TV1-4** solution. The volume of **PBI** solution was changed so that 50, and 100 wt% **PBI** relative to 100 wt% **TV1-4** was incorporated in the mixed solution. The solutions were drop casted on quartz substrate and dried in vacuum oven and measured the conductivity using TRMC.

The data in Figure 4.25 suggest that $\phi\Sigma\mu$ values are progressively increased by the addition of small amount of **PBI**, as a result of efficient electron transfer from **TV4** to **PBI**. In order to facilitate the comparison of the mobility between amorphous and self-assembled films, **TV4/PBI** films were dissolved again in decane- CHCl_3 mixed solvent and the conductivity was measured (Figure 4.25b). The results revealed that the $\phi\Sigma\mu$ values are slightly higher in decane- CHCl_3 mixture than in CHCl_3 films. The minimum charge carrier mobilities ($\Sigma\mu_{\text{min}}$) of **TV4** films drop casted on quartz plates were determined by dividing $\phi\Sigma\mu$ of TRMC by ϕ , where $\phi\Sigma\mu$ quantum efficiency of charge carrier generation) which was estimated from the transient absorption spectra of **PBI** radical anion. The ϕ at the peak of each **PBI** fraction was estimated by TAS from the

absorption of **PBI** radical anion using its reported extinction coefficient, according to the reported procedure.

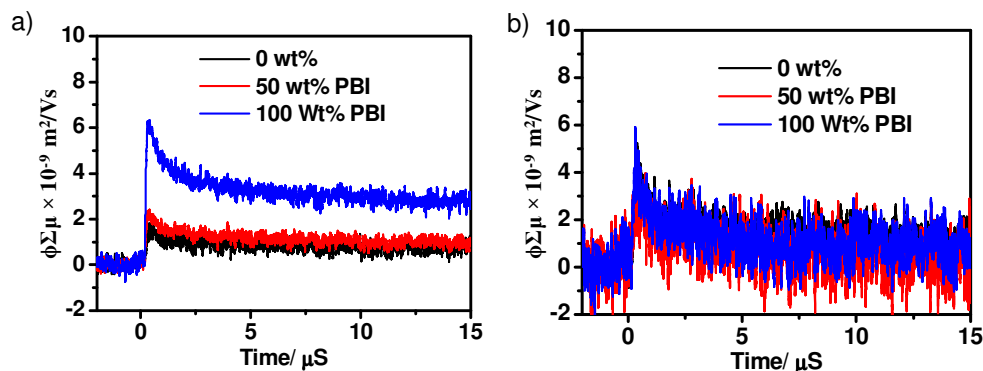


Figure 4.25. FP-TRMC profiles of **TV4** films prepared with **PBI** from a) chloroform and b) *n*-decane/chloroform (1:1 v/v) solutions. The color represents weight fraction of **PBI** relative to 100 wt% **TV4**.

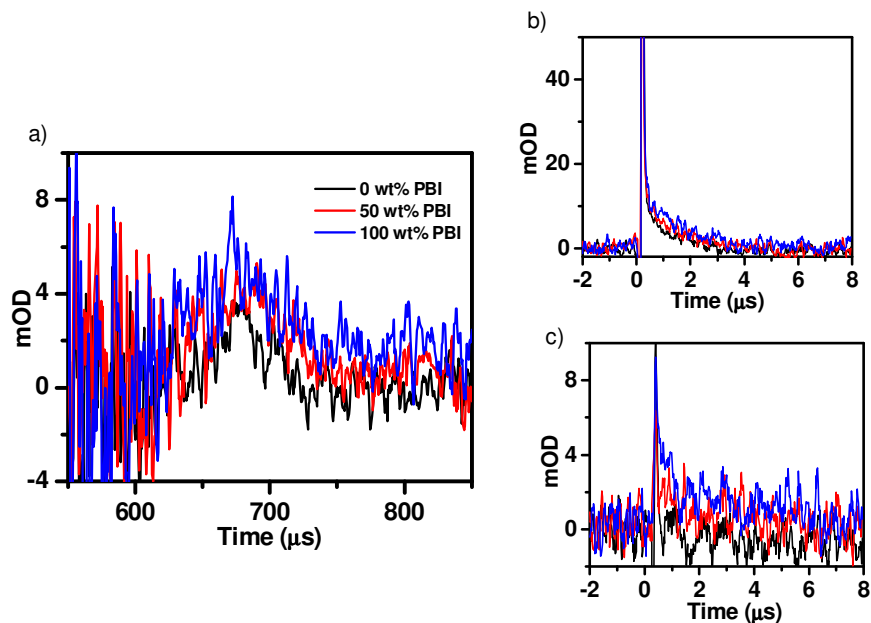


Figure 4.26. a) Transient absorption spectra ($\lambda_{\text{ex}} = 355 \text{ nm}$) of **TV4** films prepared with **PBI** from chloroform solution. The color represents weight fraction of **PBI** relative to 100 wt% **TV4**. Kinetic decay profiles obtained at 670 nm (b) and 800 nm (c).

In Figure 4.26, the observed transient absorption of **TV4** radical cation and **PBI** radical anion are relatively weak. The mobility was estimated indirectly, and it is described by the $\Sigma\mu_{\text{min}}$. As seen in Figure 4.27a, the TA intensities of **TV4** with **PBI**

decreased in *n*-decane/ CHCl_3 xerogel films. This means that the quantum efficiency of the charge carrier generation (ϕ) is decreased because **PBI** may be entrapped in **TV4** assemblies. However, the TRMC transients ($\phi\Sigma\mu$) shown in Figure 4.26b are rather increased in spite of the decrease of ϕ indicating enhanced charge-carrier mobility in the mixed solvent. The absolute value of charge-carrier mobility is not determined in this study, due to the overlap of **TV** radical cation and **PBI** radical anion signals and due to the weak intensity of their TA spectra. It is noteworthy that the minimum charge-carrier mobilities ($\Sigma\mu_{\min}$) of the p-type **TV4** were ca. $0.12 \text{ cm}^2/\text{Vs}$ in the films prepared from CHCl_3 solutions. Once the films were prepared from decane- CHCl_3 , the $\Sigma\mu_{\min}$ of **TV4** was increased to $\sim 0.14 \text{ cm}^2/\text{Vs}$, which is slightly larger than those prepared from CHCl_3 . Subsequently, mobilities of **TV1-3** with **PBI** were measured using the same procedure and the values are shown in Figure 4.29a.

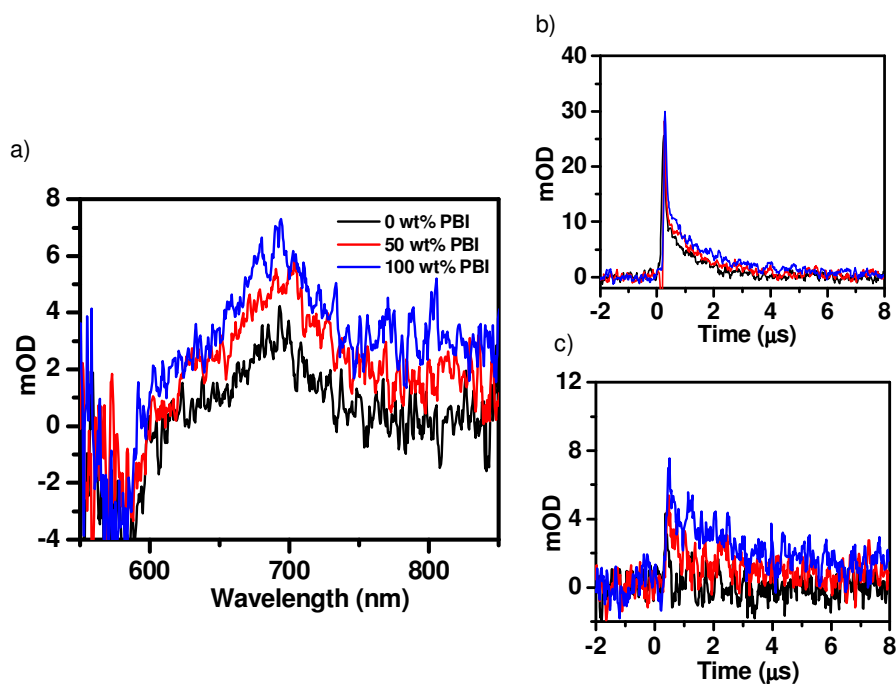


Figure 4.27. a) Transient absorption spectra ($\lambda_{\text{ex}} = 355 \text{ nm}$) of **TV4** films prepared with **PBI** from *n*-decane/chloroform (1:1 v/v) solutions. The color represents different weight fraction of **PBI** relative to 100 wt% **TV4**. Kinetic decay profiles obtained at 670 nm (b) and 800 nm (c).

Furthermore, measurements on the anisotropic conduction of the fibres were performed with amorphous and self-assembled films (Figure 4.28). Figure 4.28a shows transient conductivities ($\Delta\sigma$) observed for the parallel ($\Delta\sigma_{\parallel}$) and perpendicular ($\Delta\sigma_{\perp}$) directions to the electric-field vector of the microwave radiation. The data obtained for the film prepared from chloroform indicates that the donor and the acceptor are in irregular packing resulting in low anisotropy (~ 2). In the case of self-assembled films, transient conductivity for $\Delta\sigma_{\parallel}$ was more predominant and no signal was observed for $\Delta\sigma_{\perp}$ indicating 10 times more anisotropy (Figure 4.28b). The higher value for $\Delta\sigma_{\parallel}$ reveals that majority of the donor and the acceptor molecules are unidirectionally packed along the fibre axis. This study illustrates that the supramolecularly engineered aggregation of **TV4** and **PBI** in co-assembly would enhance the potential utility of these materials in optoelectronic applications.

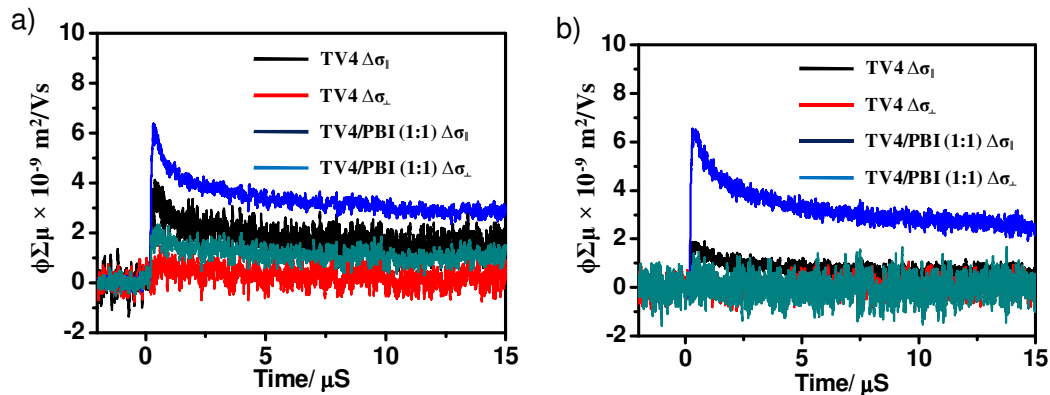


Figure 4.28. Transient profiles of TV4/PBI (1:1 M) observed for parallel ($\Delta\sigma_{\parallel}$) and perpendicular ($\Delta\sigma_{\perp}$) directions to the electric-field vector of the microwave in (a) chloroform and (b) decane-chloroform.

For a comparison, TRMC of **TV1-4** with *N,N'*-bis(2,5-di-*tert*-butylphenyl)-3,4,9,10-perylenedicarboximide (**PDI**) were performed in chloroform and in decane-chloroform (Figure 4.29b). The results show that the $\phi\Sigma\mu$ values are higher for the self-assembled films. A comparison of the charge-carrier mobility data in Figure 4.29a and

4.29b indicates that **PBI** is a better electron acceptor than **PDI**. In order to understand the phase separation of co-assemblies in self-assembled films, bilayer films were prepared as shown schematically in Figure 4.30a. The $\phi\Sigma\mu$ values were almost the same for front and back exposure to 355 nm nanosecond laser (Figure 4.30b), and almost identical to those prepared from decane- CHCl_3 . This observation suggest that the nanofibrils of **TVs** and **PBI** mixtures obtained from decane- CHCl_3 are composed of the self-sorted individual aggregates and these fibrils may be laterally bundled to form large fibers with high charge carrier mobilities.

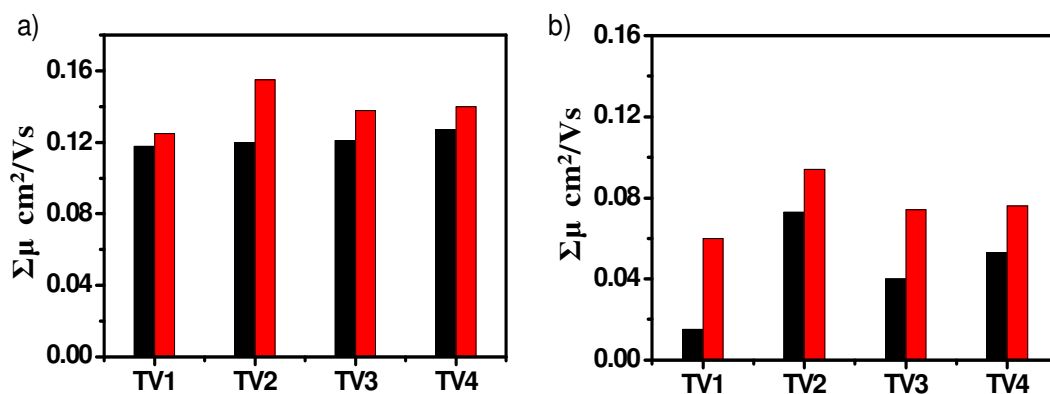


Figure 4.29. Bar diagram represents $\Sigma\mu$ values of a) **TV1-4/PBI** and b) **TV1-4/PDI** from decane-chloroform (1:1 v/v) (red) and chloroform (black) solutions.

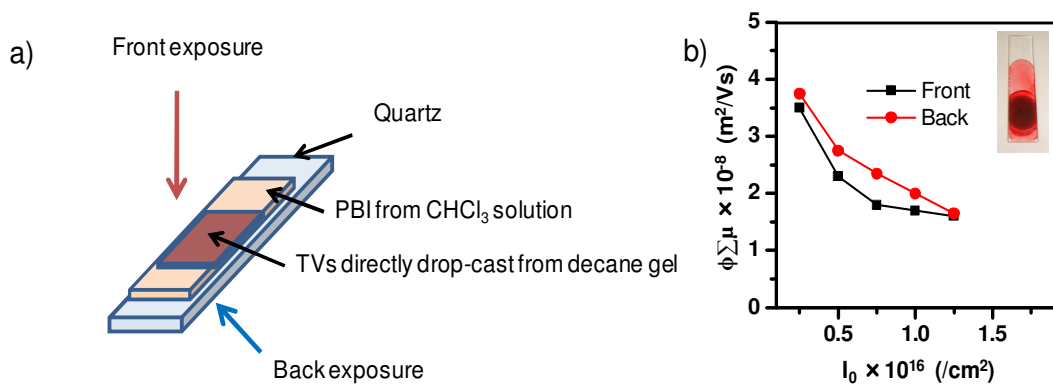


Figure 4.30. a) Schematic representation of bilayer of thienylenevinylenes and perylene bisimide films prepared from chloroform and decane. b) Plot of I_0 (photon density) versus $\phi\Sigma\mu$: Front and back exposure. Inset shows photograph of the **TVs/PBI** film.

4.4. Conclusions

In summary, we have demonstrated supramolecular assemblies of p- and n-type semiconducting organogelators on insulating and semiconducting substrates. When electron-accepting material was assembled with an electron-donating system such as oligo(thienylenevinylene), a continuous path of nanophase-segregated, yet interdigitated electron-accepting and electron-donating nanostructures were formed. **TV1-4** showed solution phase epitaxial growth of fibre on freshly cleaved mica surface. However, thin, flexible nanowire formation was observed on silicon wafer. The unravelled interdependence between intermolecular and molecule-substrate interactions thus provides control over the delicately balanced interactions driving the self-assembly processes. KPFM results highlight that surface potential is very high on silicon wafer when compared to surface potential obtained from co-assemblies on mica surface at open air condition. Mobility data showed the enhancement of uni-directional charge carrier transport in the self-assembled films when compared to those obtained from isotropic solution. These results highlight the role of the arrangements of donor/acceptor assemblies in self-assembled fibres to improve the charge transport properties and the charge separation for optoelectronic devices.

4.5. Experimental Section

4.5.1. Synthesis and Characterization

Unless otherwise stated, all starting materials and reagents were purchased from commercial suppliers and used without further purification. The solvents and the reagents were purified and dried by standard methods prior to use. Details of the instrumental techniques used for characterization of molecules are described in the experimental section (section of 2.5.1.) of Chapter 2. Preparation, yield, melting point, and spectral details of new molecules are given below.

Synthesis of TV2-4: TV2-4 were synthesized from an ice cooled solution of (E)-3-(5-((E)-2-(5-((E)-2-(3,4-didodecyl-5-((E)-3-hydroxybuta-1,3-dienyl)thiophen-2-yl)vinyl)-3,4-didodecylthiophen-2-yl)vinyl)-3,4-didodecylthiophen-2-yl) acrylic acid (0.15 g, 0.103 mmol), in dry chloroform (30 mL), alkylamines (hexylamine, dodecylamine, hexadecylamine) (0.25 mmol) and HATU (0.08 g, 0.192 mmol). Then, *N,N'*-diisopropylethylamine (0.056 g, 0.4 mmol) was added drop wise to the reaction mixture and stirred at room temperature for 12 h. After removal of the solvent, the residue was dissolved in chloroform and washed with water. After extraction, the organic layer was separated and dried over Na₂SO₄. The solvent was evaporated under vacuum. The crude product was purified by column chromatography (basic alumina, hexane/ethyl acetate 8:2) to give a pure red solid compound.

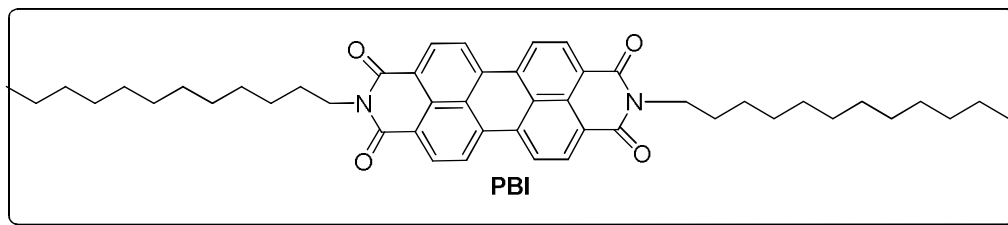
TV2: Yield = 47%, mp = 135-136 °C. ¹H NMR (CDCl₃, 500 MHz); δ (ppm) = 7.80-7.78 (J = 15 Hz, d, 2H), 7.00-6.97 (J = 15.5 Hz, d, 2H), 6.95-6.92 (J = 15.9 Hz, d, 2H), 6.10-6.07 (J = 14.5 Hz, d, 2H), 5.58 (t, 2H), 3.44 (t, 4H), 2.61-2.45 (t, 12H), 1.59 (q, 12H), 1.39-1.31 (m, 131H), 0.89 (t, 24H). ¹³C NMR (CDCl₃, 125 MHz) δ (ppm) = 165.89, 146.63, 142.26, 141.67, 138.01, 135.34, 132.09, 131.97, 120.80, 119.31, 118.26, 39.80, 31.93, 31.71, 31.52, 31.33, 31.21, 29.84, 29.48, 27.25, 26.56, 22.66, 14.03. FT-IR (KBr) ν_{max} = 719, 820, 930, 1019, 1257, 1479, 1545, 1637, 2849, 2920, 3291 cm⁻¹. MALDI-TOF-MS (m/z) = 1616.88 (Found), 1616.37 (Calcd).

TV3: Yield = 45 % mp = 139-140 °C. ¹H NMR (CDCl₃, 500 MHz, TMS) δ (ppm) = 7.81-7.78 (J = 15.0 Hz, d, 2H), 6.98 (d, 2H), 6.96 (d, 2H), 6.10-6.07 (J = 14.5 Hz, d, 2H), 5.46 (t, 2H), 3.37 (t, 4H), 2.58 (t, 12H), 1.59 (q, 12H), 1.26 (m, 120H), 0.89 (t, 18H); ¹³C NMR (CDCl₃, 125 MHz, TMS) δ (ppm) = 164.88, 145.61, 141.25, 140.67, 137.01, 134.35, 131.09, 130.99, 119.83, 118.34, 117.29, 38.81, 30.91, 28.83, 28.73, 28.66, 28.64, 28.55, 28.47, 28.41, 28.36, 25.99, 21.67, 13.09; FT-IR (KBr) ν_{max} = 720,

816, 930, 1019, 1257, 1479, 1544, 1638, 2849, 2920, 3291 cm^{-1} ; MALDI-TOF-MS (m/z) = 1785.19 (Found), 1785.14 (Calcd).

TV4: Yield = 45 %. mp = 139-140 $^{\circ}\text{C}$. ^1H NMR (CDCl_3 , 500 MHz, TMS) δ (ppm) = 7.73-7.70 (J = 15.0 Hz, d, 2H), 6.94-6.91 (J = 15.5 Hz, d, 2H), 6.89-6.86 (J = 15.5 Hz, d, 2H), 6.03-6.00 (J = 15 Hz, d, 2H), 5.41 (t, 2H), 3.31 (t, 4H), 2.55 (t, 12H), 1.59 (q, 14H), 1.26 (m, 182H), 0.81 (t, 24 H); ^{13}C NMR (CDCl_3 , 125 MHz, TMS) δ (ppm) = 165.87, 146.62, 142.28, 141.70, 138.03, 135.38, 132.02, 120.86, 119.38, 118.33, 39.83, 31.94, 31.71, 31.33, 30.91, 29.86, 29.70, 29.50, 29.38, 27.29, 27.02, 22.70, 14.11; FT-IR (KBr) ν_{max} = 719, 818, 925, 1019, 1257, 1479, 1544, 1638, 2849, 2920, 3291 cm^{-1} ; MALDI-TOF-MS (m/z) = 1897.58 (Found), 1897.68 (Calcd).

Synthesis of PBI



Perylene tetracarboxylic dianhydride (PTCDA) (0.1 g, 0.25 mM) and dodecylamine (0.2 mL, 1 mM) were dissolved in *t*-BuOH (20 mL) and then refluxed for 20 h at 120 $^{\circ}\text{C}$. After removal of the solvent, the residue was dissolved in chloroform and washed with water. After extraction, the organic layer was separated and dried over Na_2SO_4 . The solvent was evaporated under vacuum. The crude product was purified by column chromatography (silica gel, chloroform) to give a pure red solid compound. Yield = 90% . ^1H NMR (CDCl_3 , 300 MHz); δ (ppm) = 8.69-8.66 (J = 9 Hz, d, 4H), 8.61-8.58 (J = 9 Hz, d, 4H), 4.20 (t, 4H), 1.76 (q, 4H), 1.25 (m, 41H), 0.87 (t, 6H); FT-IR (KBr) ν_{max} = 630, 746, 808, 862, 1089, 1253, 1344, 1438, 1591, 1651, 1696, 2846, 2922, 2963 cm^{-1} ; FAB-MS (m/z) = 728.2 (Found), 726.9 (Calcd).

4.5.2. Description of Experimental Techniques

Transmission Electron Microscopy (TEM): TEM measurements were carried out using FEI (TECNAI G² 30 S-TWIN) with an accelerating voltage of 100 kV. Samples were prepared by drop casting of decane solutions of **TV1-4**, **PBI** and **TV1-4/PBI** (1:1) on to carbon coated copper grids at the required concentrations at ambient conditions. The solvent was removed under vacuum. TEM images were obtained without staining.

Atomic Force Microscopy (AFM): Atomic Force Microscopy images were recorded under ambient conditions using a NTEGRA (NT-MDT) operating with a tapping mode regime. Micro-fabricated TiN cantilever tips (NSG10) with a resonance frequency of 299 kHz and a spring constant of 20-80 Nm⁻¹ were used. AFM section analysis was done offline. Samples for the imaging were prepared by drop casting the **TV1-4**, **PBI** and **TV1-4/PBI** (1:1 M ratio) solution on freshly cleaved mica and Si wafer at the required concentrations at ambient conditions.

Kelvin Probe Force Microscopy (KPFM): AFM/KPFM images of **TV1-4**, **PBI** and **TV1-4/PBI** (1:1 M ratio) blends were recorded under ambient conditions using a NTEGRA (NT-MDT) operating with a tapping mode regime. Micro-fabricated Pt cantilever tips (NSG03) with a resonance frequency of 80 kHz < ω < 100 kHz and a spring constant of 0.35-6.06 Nm⁻¹ were used. To acquire “simultaneous” AFM and KPFM images, a topographic line scan was first obtained by AFM operating in tapping mode, and then the same line was rescanned in lift mode with the tip raised to a lift height of ~10 nm. KPFM provides a local measure of the SP differences between the conductive tip and the sample under investigation. The SP is defined as $(WF_{\text{tip}} - WF_{\text{sample}} - \Delta_{\text{pol}})/q$, where WF_{tip} and WF_{sample} are the work functions of the tip and sample, respectively, Δ_{pol} is the polarization induced by the tip, and q is the magnitude of the elementary charge. In the KPFM, a bias voltage $V_{\text{tip}} = V_{\text{DC}} + V_{\text{AC}} \sin \omega t$, where ω is the resonant frequency of the cantilever and V_{DC} and V_{AC} are continuous and alternate bias,

respectively, was applied directly to the tip, and the sample was held at the ground potential.

Flash-Photolysis Time Resolved Microwave Conductivity (FP-TRMC): The details of the FP-TRMC and TAS were reported in the Chapter 2. All the experiments were carried out at room temperature. **PBI** and **PDI** were used as acceptors. The chloroform solutions of **TV1-4** and **PBI** and **PDI** were mixed according to the fraction of each weight, giving the mixed solutions of 0-100 wt% **PBI** relative to 100 wt% **TV1-4**. The solutions were drop-casted on a quartz plate and dried in vacuum at 40 °C. After the TRMC and TAS, the films were treated by *n*-decane/chloroform mixed solvent (1:1 v/v) and dried in vacuum at 100 °C. TRMC and TAS of these films were performed again. The TAS showed the absorption of **PBI** radical anion and **TV1-4** radical cation at visible to near-infrared (ca. 600-850 nm).

References

- Abdallah, D. J.; Weiss, R. G. Organogels and low molecular mass organic gelators. *Adv. Mater.* **12**, **2000**, 1237.
- Ajayaghosh, A.; George, S. J.; Schenning, A. P. H. J. Hydrogen-bonded assemblies of dyes and extended π -conjugated systems. *Top. Curr. Chem.* **258**, **2005**, 83.
- Ajayaghosh, A.; Praveen, V. K. π -Organogels of self-assembled *p*-phenylenevinylenes: Soft materials with distinct size, shape, and functions. *Acc. Chem. Res.* **40**, **2007**, 644.
- Akutagawa, T.; Kakiuchi, K.; Hasegawa, T.; Noro, S.-i.; Nakamura, T.; Hasegawa, H.; Mashiko, S.; Becher, J. Molecularly assembled nanostructures of a redox-active organogelator. *Angew. Chem. Int. Ed.* **44**, **2005**, 7283.
- Akutagawa, T.; Ohta, T.; Hasegawa, T.; Nakamura, T.; Christensen, C. A.; Becher, J. Formation of oriented molecular nanowires on mica surface. *Proc. Nat. Acad. Sci.* **99**, **2002**, 5028.
- Allard, S.; Forster, M.; Souharce, B.; Thiem, H.; Scherf, U. Organic semiconductors for solution-processable field-effect transistors (OFETs). *Angew. Chem., Int. Ed.* **47**, **2008**, 4070.
- Arias, A. C.; MacKenzie, J. D.; McCulloch, I.; Rivnay, J.; Salleo, A. Materials and applications for large area electronics: Solution-based approaches. *Chem. Rev.* **110**, **2010**, 3.
- Ariga, K.; Hill, J. P.; Lee, M. V.; Vinu, A.; Charvet, R.; Acharya, S. Challenges and breakthroughs in recent research on self-assembly. *Sci. Technol. Adv. Mater.* **9**, **2008**, 014109.
- Aviram, A. Molecules for memory, logic, and amplification. *J. Am. Chem. Soc.* **110**, **1988**, 5687.

- Azumi, R.; Götz, G.; Debaerdemaeker, T.; Bäuerle, P. Coincidence of the molecular organization of β -substituted oligothiophenes in two-dimensional layers and three-dimensional crystals. *Chem. Eur. J.* **6**, **2000**, 735.
- Benanti, T. L.; Venkataraman, D. Organic solar cells: An overview focusing on active layer morphology. *Photosynth. Res.* **87**, **2006**, 73.
- Blom, P. W. M.; Mihailetschi, V. D.; Koster, L. J. A.; Markov, D. E. Device physics of polymer:fullerene bulk heterojunction solar cells. *Adv. Mater.* **19**, **2007**, 1551.
- Borghesi, A.; Besana, D.; Sassella, A. Epitaxial growth of quaterthiophene thin films by organic molecular beam deposition. *Vacuum.* **61**, **2001**, 193.
- Bottari, G.; Olea, D.; -Navarro, C. G.; Zamora, F.; -Herrero, J. G.; Torres, T. Highly conductive supramolecular nanostructures of a covalently linked phthalocyanine-C₆₀ fullerene conjugate. *Angew. Chem. Int. Ed.* **47**, **2008**, 2026.
- Bredas, J. L.; Norton, J. E.; Cornil, J.; Coropceanu, V. Molecular understanding of organic solar cells: The challenges. *Acc. Chem. Res.* **42**, **2009**, 1691.
- Campione, M.; Sassella, A.; Moret, M.; Papagni, A.; Trabattoni, S.; Resel, R.; Lengyel, O.; Marcon, V.; Raos, G. Organic-organic epitaxy of incommensurate systems: Quaterthiophene on potassium hydrogen phthalate single crystals. *J. Am. Chem. Soc.* **128**, **2006**, 13378.
- Carrasco-Orozco, M.; Tsoi, W. C.; O'Neill, M.; Aldred, M. P.; Vlachos, P.; Kelly, S. M. New photovoltaic concept: Liquid-crystal solar cells using a nematic gel template. *Adv. Mater.* **18**, **2006**, 1754.
- Charvet, R.; Acharya, S.; Hill, J. P.; Akada, M.; Liao, M.; Seki, S.; Honsho, Y.; Saeki, A.; Ariga, K. Block-copolymer-nanowires with nanosized domain

- segregation and high charge mobilities as stacked p/n heterojunction arrays for repeatable photocurrent switching. *J. Am. Chem. Soc.* **131**, **2009**, 18030.
- Cheng, Y. J.; Yang, S. H.; Hsu, C. S. Synthesis of conjugated polymers for organic solar cell applications. *Chem. Rev.* **109**, **2009**, 5868.
- Che, Y.; Yang, X.; Liu, G.; Yu, C.; Ji, H.; Zuo, J.; Zhao, J.; Zang, L. Ultrathin n-type organic nanoribbons with high photoconductivity and application in optoelectronic vapor sensing of explosives. *J. Am. Chem. Soc.* **132**, **2010**, 5743.
- Chen, H.-Y.; Hour, J.; Zhang, S.; Liang, Y.; Yang, G.; Yang, Y.; Yu, L.; Li, G. Polymer solar cells with enhanced open-circuit voltage and efficiency. *Nat. Photon.* **3**, **2009**, 649.
- Cho, S.; Coates, N.; Moon, J. S.; Park, S. H.; Roy, A.; Beaupre, S.; Moses, D.; Leclerc, M.; Lee, K.; Heeger, A. J. Bulk heterojunction solar cells with internal quantum efficiency approaching 100%. *Nat. Photon.* **3**, **2009**, 297.
- Chung, J. W.; Yang, H.; Singh, B.; Moon, H.; An, B.; Leed, S. Y.; Park, S. Y. Single-crystalline organic nanowires with large mobility and strong fluorescence emission: A conductive-AFM and space-charge-limited-current study. *Chem. Commun.* **2009**, 5920.
- Cicoira, F.; Miwa, J. A.; Melucci, M.; Barbarella, G.; Rosei, F. Ordered assembly of α -quinoxithiophene on a copper oxide nanotemplate. *Small* **2**, **2006**, 1366.
- Coakley, K. M.; McGehee, M. D. Conjugated polymer photovoltaic cells. *Chem. Mater.* **16**, **2004**, 4533.
- Dabirian, R.; Palermo, V.; Liscio, A.; Schwartz, E.; Otten, M. B. J.; Finlayson, C. E.; Treossi, E.; Friend, R. H.; Calestani, G.; Müllen, K.; Nolte, R. J. M.; Rowan, A. E.; Samorì, P. The relationship between nanoscale architecture and charge

- transport in conjugated nanocrystals bridged by multichromophoric polymers. *J. Am. Chem. Soc.* **131**, **2009**, 7055.
- Danila, I.; Riobé, F.; Puigmartí-Luis, J.; Pérez del Pino, Á.; Wallis, J. D.; Amabilino, D. B.; Avarvarig, N. Supramolecular electroactive organogel and conducting nanofibers with C₃-symmetrical architectures. *J. Mater. Chem.* **19**, **2009**, 4495.
- De Boer, R. W. I.; Stassen, A. F.; Craciun, M. F.; Mulder, C. L.; Molinari, A.; Rogge, S.; Morpurgo, A. F. Ambipolar Cu- and Fe-phthalocyanine single-crystal field-effect transistors. *Appl. Phys. Lett.* **86**, **2005**, 262109.
- De Loos, M.; Van Esch, J.; Stokroos, I.; Kellogg, R. M.; Feringa, B. L. Remarkable stabilization of self-assembled organogels by polymerization. *J. Am. Chem. Soc.* **119**, **1997**, 12675.
- Diegelmann, S. R.; Gorham, J. M.; Tovar, J. D. One-dimensional optoelectronic nanostructures derived from the aqueous self-Assembly of π -conjugated oligopeptides. *J. Am. Chem. Soc.* **130**, **2008**, 13840.
- Dienel, T.; Loppacher, C.; Mannsfeld, S. C. B.; Forker, R.; Fritz, T. Growth-mode-induced narrowing of optical spectra of an organic adlayer. *Adv. Mater.* **20**, **2008**, 959.
- Diring, S., Camerel, F., Donnio, B., Dintzer, T., Toffanin, S., Capelli, R., Muccini, M. & Ziessel, R. Luminescent ethynyl-pyrene liquid crystals and gels for optoelectronic devices. *J. Am. Chem. Soc.* **131**, **2009**, 18177.
- Durkut, M.; Mas-Torrent, M.; Hadley, P.; Jonkheijm, P.; Schenning, A. P. H. J.; Meijer, E. W.; George, S.; Ajayaghosh, A. Electrical transport measurements on self-assembled organic molecular wires. *J. Chem. Phys.* **124**, **2006**, 154704.
- Feng, X.; Marcon, V.; Pisula, W.; Hansen, M. R.; Kirkpatrick, J.; Grozema, F.; Andrienko, D.; Kremer, K.; Müllen, K. Towards high charge-carrier

- mobilities by rational design of the shape and periphery of discotics. *Nat. Mater.* **8**, **2009**, 421.
- Forrest, S. R. The path to ubiquitous and low-cost organic electronic appliances on plastic. *Nature.* **428**, **2004**, 911.
- Forrest, S. R. Ultrathin organic films grown by organic molecular beam deposition and related techniques, *Chem Rev.* **97**, **1997**, 1793.
- Fujita, N.; Sakamoto, Y.; Shirakawa, M.; Ojima, M.; Fujii, A.; Ozaki, M.; Shinkai, S. Polydiacetylene nanofibers created in low-molecular-weight gels by post modification: Control of blue and red phases by the odd-even effect in alkyl chains. *J. Am. Chem. Soc.* **129**, **2007**, 4134.
- George, M.; Weiss, R. G. Low molecular-mass gelators with diyne functional groups and their unpolymerized and polymerized gel assemblies. *Chem. Mater.* **15**, **2003**, 2879.
- George, M.; Weiss, R. G. Molecular organogels. Soft matter comprised of low-molecular-mass organic gelators and organic liquids. *Acc. Chem. Soc.* **39**, **2006**, 489.
- George, S. J.; Ajayaghosh, A. Self-assembled nanotapes of oligo(*p*-phenylene vinylene)s: Sol-gel-controlled optical properties in fluorescent *p*-electronic gels. *Chem. Eur. J.* **11**, **2005**, 3217.
- Goetzberger, A.; Hebling, C.; Schock, H. W. Photovoltaic materials, history, status and outlook. *Mater. Sci. Eng., R* **40**, **2003**, 1.
- Gomar-Nadal, E.; Puigmartí-Luis, J.; Amabilino, D. B.; Assembly of functional molecular nanostructures on surfaces. *Chem. Soc. Rev.* **37**, **2008**, 490.
- Gosztola, D.; Niemczyk, M. P.; Svec, W.; Lukas, A. S.; Wasielewski, M. R. Excited doublet states of electrochemically generated aromatic imide and diimide radical anions. *J. Phys. Chem. A* **104**, **2000**, 6545.

- Grévin, B.; Demadrille, R.; Linares, M.; Lazzaroni, R.; Leclère, P. Probing the local conformation within π -conjugated one-dimensional supramolecular stacks using frequency modulation atomic force microscopy. *Adv. Mater.* **21**, **2009**, 4124.
- Grimsdale, A. C.; Müllen, K. The chemistry of organic nanomaterials. *Angew. Chem. Int. Ed.* **44**, **2005**, 5592.
- Gronowitz, S. Thiophene and its derivatives. In *The Chemistry of Heterocyclic Compounds*; Weissberger, A., Taylor, E. C., Eds.; John Wiley & Sons: New York, **44**, **1985**, 1.
- Helgesen, M.; Sondergaard, R.; Krebs, F. C. Advanced materials and processes for polymer solar cell devices. *J. Mater. Chem.* **20**, **2010**, 36.
- Heremans, P.; Cheyns, D.; Rand, B. P. Strategies for increasing the efficiency of heterojunction organic solar cells: Material selection and device architecture. *Acc. Chem. Res.* **42**, **2009**, 1740.
- Herrickhuyzen, J. v.; Syamakumari, A.; Schenning, A. P. H. J.; Meijer, E. W. Synthesis of n-type perylene bisimide derivatives and their orthogonal self-assembly with p-type oligo(p-phenylene vinylene)s. *J. Am. Chem. Soc.* **126**, **2004**, 10021.
- Hill, J. P.; Jin, W.; Kosaka, A.; Fukushima, T.; Ichihara, H.; Shimomura, T.; Ito, K.; Hashizume, T.; Ishii, N.; Aida, T. Self-assembled hexa-*peri*-hexabenzocoronene graphitic nanotube. *Science*. **304**, **2004**, 1481.
- Hoeben, F. J. M.; Jonkheijm, P.; Meijer, E. W.; Schenning, A. P. H. J. About supramolecular assemblies of π -conjugated systems. *Chem. Rev.* **105**, **2005**, 1491.
- Hong, J.-P.; Um, M.-C.; Nam, S.-R.; Hong, J.-I.; Lee, S. Organic single-nanofiber transistors from organogels. *Chem. Commun.* **2009**, 310.

- Honna, Y.; Isomura, E.; Enozawa, H.; Hasegawa, M.; Takase, M.; Nishinaga, T.; Iyoda, M. Synthesis of bitetrathiafulvalenes with FeCl₃-mediated homo-coupling of tetrathiafulvalenyl magnesium bromide and formation of nanostructures from bi tetrathiafulvalenes having long alkylthio chains. *Tetrahedron Lett.* **51**, **2010**, 679.
- Hoppe, H.; Sariciftci, N. S. Organic solar cells: An overview. *J. Mater. Res.* **19**, **2004**, 1924.
- Hunter, C. A.; Lawson, K. R.; Perkins, J.; Urch, C. J. Aromatic interactions. *J. Chem. Soc., Perkin Trans. 2*, **2001**, 651.
- Hunter, C. A.; Sanders, J. K. M. The Nature of π - π Interactions. *J. Am. Chem. Soc.* **112**, **1990**, 5525.
- Ikkala, O.; ten Brinke, G. Hierarchical self-assembly in polymeric complexes: Towards functional materials. *Chem. Commun.* **2004**, 2131.
- Ishi-i, T.; Jung, J. H.; Shinkai, S. Intermolecular porphyrin-fullerene interaction can reinforce the organogel structure of a porphyrin-appended cholesterol derivative. *J. Mater. Chem.* **10**, **2000**, 2238.
- Ito, S.; Herwig, P. T.; Bolhme, T.; Rabe, J. P.; Rettig, W.; Müllen, K. Bis(hexa-peri-hexabenzocorononyl): A "superbiphenyl". *J. Am. Chem. Soc.* **2000**, **122**, 7698.
- Iyoda, M.; Hasegawa, M.; Enozawa, H. Self-assembly and nanostructure formation of multi-functional organic π -donors. *Chem. Lett.* **36**, **2007**, 1402.
- Jang, K.; Ranasinghe, A. D.; Heske, C.; Lee, D.-C. Organogels from functionalized T-shaped π -conjugated bisphenazines. *Langmuir.* **26**, **2008**, 13630.
- Jestín, I.; Frère, P.; Blanchard, P.; Roncali, J. Extended thienylenevinylene oligomers as highly efficient molecular wires. *Angew. Chem. Int. Ed.* **30**, **1998**, 942.
- Jestín, I.; Frère, P.; Mercier, N.; Levillain, E.; Stievenard, D.; Roncali, J. Synthesis and characterization of the electronic and electrochemical properties of

- thienylenevinylene oligomers with multianometer dimensions. *J. Am. Chem. Soc.* **120**, **1998**, 8150.
- Jørgensen, M.; Bechgaard, K. Synthesis and structural characterization of a bis-arborol-tetrathiafulvalene gel: Toward a self-assembling "molecular" wire. *J. Org. Chem.* **59**, **1994**, 5877.
- Kaake, L. G.; Barbara, P. F.; Zhu, X.-Y. Intrinsic charge trapping in organic and polymeric semiconductors: A physical chemistry perspective. *J. Phys. Chem. Lett.* **1**, **2010**, 628.
- Kaiser, T. E.; Wang, H.; Stepanenko, V.; Würthner, F. Supramolecular construction of fluorescent J-aggregates based on hydrogen-bonded perylene dyes. *Angew. Chem. Int. Ed.* **46**, **2007**, 5541.
- Kato, T. Self-assembly of phase-segregated liquid crystal structures. *Science* **295**, **2002**, 2414.
- Katz, H. E.; Bao, Z.; Gilat, S. L. Synthetic chemistry for ultrapure, processable, and high-mobility organic transistor semiconductors. *Acc. Chem. Res.* **34**, **2001**, 359.
- Kawano, S. -i.; Fujita, N.; Shinkai, S. Quater-, quinque-, and sexithiophene organogelators: Unique thermochromism and heating-free sol-gel phase transition. *Chem. Eur. J.* **11**, **2005**, 4735.
- Kelley, T.W.; Granstrom, E. L.; Frisbie, C. D. Conducting probe atomic force microscopy: A characterization tool for molecular electronics. *Adv. Mater.* **11**, **1999**, 261.
- Kim, Y.; Anthopoulos, T. D.; Stavrinou, P. N.; Bradley, D. D. C.; Nelson, J. Morphology evolution via self-organization and lateral and vertical diffusion in polymer:fullerene solar cell blends. *Nat. Mater.* **7**, **2008**, 150.

- Kiriy, N.; Bocharova, V.; Kiriy, A.; Stamm, M.; Krebs, F. C.; Adler, H.-J. Designing thiophene-based azomethine oligomers with tailored properties: Self-assembly and charge carrier mobility. *Chem. Mater.* **16**, **2004**, 4765.
- Kitahara, T.; Shirakawa, M.; Kawano, S.-i.; Beginn, U.; Fujita, N.; Shinkai, S. Creation of a mixed-valence state from one-dimensionally aligned TTF utilizing the self-assembling nature of a low molecular-weight gel. *J. Am. Chem. Soc.* **127**, **2005**, 14980.
- Kitamura, T.; Nakaso, S.; Mizoshita, N.; Tochigi, Y.; Shimomura, T.; Moriyama, M.; Ito, K.; Kato, T. Electroactive supramolecular self-assembled fibers comprised of doped tetrathiafulvalene-based gelators. *J. Am. Chem. Soc.* **127**, **2005**, 14769.
- Koller, G.; Berkebile, S.; Krenn, J. R.; Tzvetkov, G.; Hlawacek, G.; Lengyel, O.; Netzer, F. P.; Teichert, C.; Resel, R.; Ramsey, M. G. Oriented sexiphenyl single crystal nanoneedles on TiO₂ (110). *Adv. Mater.* **16**, **2004**, 2159.
- Krieg, E.; Shirman, E.; Weissman, H.; Shimoni, E.; Wolf, S. G.; Pinkas, I.; Rybtchinski, B. Supramolecular gel based on a perylene diimide dye: Multiple stimuli responsiveness, robustness, and photofunction. *J. Am. Chem. Soc.* **131**, **2009**, 14365.
- Kumar, R. J.; MacDonald, J. M.; Singh, T. B.; Waddington, L. J.; Holmes, A. B. Hierarchical self-assembly of semiconductor functionalized peptide α -helices and optoelectronic properties. *J. Am. Chem. Soc.* **133**, **2011**, 8564.
- Lau, Y. K. A.; Chernak, D. J.; Bierman, M. J.; Jin, S. Epitaxial growth of hierarchical PbS nanowires. *J. Mater. Chem.* **19**, **2009**, 934.
- Leclère, P.; Surin, M.; Viville, P.; Lazzaroni, R.; Kilbinger, A. F. M.; Henze, O.; Feast, W. J.; Cavallini, M.; Biscarini, F.; Schenning, A. P. H. J.; Meijer, E. W.

- About oligothiophene self-assembly: From aggregation in solution to solid-state nanostructures. *Chem. Mater.* **16**, **2004**, 4452.
- Lee, D.-C.; McGrath, K. K.; Jang, K. Nanofibers of asymmetrically substituted bisphenazine through organogelation and their acid sensing properties. *Chem. Commun.* **2008**, 3636.
- Lehn, J.-M. *Supramolecular Chemistry, Concepts and Perspectives*; VCH: Weinheim, Germany, **1995**.
- Lehn, J. -M. Supramolecular chemistry-scope and perspectives molecules, supermolecules, and molecular devices. *Angew. Chem. Int. Ed.* **27**, **1988**, 89.
- Lehn, J. -M. Toward self-organization and complex matter. *Science* **295**, **2002**, 2400.
- Li, B.; Wang, L. D.; Kang, B. N.; Wang, P.; Qiu, Y. Review of recent progress in solid-state dye-sensitized solar cells. *Sol. Energy Mater. Sol. Cells* **90**, **2006**, 549.
- Li, R.; Hu, W.; Liu, Y.; Zhu, D. Micro- and nanocrystals of organic semiconductors. *Acc. Chem. Res.* **43**, **2010**, 529.
- Li, X.-Q.; Stepanenko, V.; Chen, Z.; Prins, P.; Siebbeles, L. D. A.; Würthner, F. Functional organogels from highly efficient organogelator based on perylene bisimide semiconductor. *Chem. Commun.* **2006**, 3871.
- Li, X.-Q.; Zhang, X.; Ghosh, S.; Würthner, F. Highly fluorescent lyotropic mesophases and organogels based on J-aggregates of core-twisted perylene bisimide dyes. *Chem. Eur. J.* **2008**, **14**, 8074.
- Liang, Y.; Xu, Z.; Xia, J.; Tsai, S.-T.; Wu, Y.; Li, G.; Ray, C.; Yu, L. For the bright future; bulk heterojunction polymer solar cells with power conversion efficiency of 7.4%. *Adv. Mater.* **22**, **2010**, E135.
- Liscio, A.; De Luca, G.; Nolde, F.; Palermo, V.; Müllen, K.; Samorì, P. Photovoltaic charge generation visualized at the nanoscale: A proof of principle. *J. Am. Chem. Soc.* **130**, **2008**, 780.

- Liscio, A.; Palermo, V.; Gentilini, D.; Nolde, F.; Müllen, K.; Samorì, P. Quantitative measurement of the local surface potential of π -conjugated nanostructures: A kelvin probe force microscopy study. *Adv. Funct. Mater.* **16**, **2006**, 1407.
- Liscio, A.; Palermo, V.; Samorì, P. Probing local surface potential of quasi-one-dimensional systems: A KPFM study of P3HT nanofibers. *Adv. Funct. Mater.* **18**, **2008**, 907.
- Liscio, A.; Palermo, V.; Samorì, P. Nanoscale quantitative measurement of the potential of charged nanostructures by electrostatic and kelvin probe force microscopy: Unraveling electronic processes in complex materials. *Acc. Chem. Res.* **43**, **2010**, 541.
- Liu, S.; Wang, W. M.; Briseno, A. L.; Mannsfeld, S. C. B.; Bao, Z. Controlled deposition of crystalline organic semiconductors for field-effect-transistor applications. *Adv. Mater.* **21**, **2009**, 1217.
- Loiacono, M. J.; Granstrom, E. L.; Frisbie, C. D. Investigation of charge transport in thin, doped sexithiophene crystals by conducting probe atomic force microscopy. *J. Phys. Chem. B* **102**, **1998**, 1679.
- Ma, W.; Yang, C.; Gong, X.; Lee, K.; Heeger, A. J. Thermally stable, efficient polymer solar cells with nanoscale control of the interpenetrating network morphology. *Adv. Funct. Mater.* **15**, **2005**, 1617.
- Martin, Y.; Abraham, D. W.; Wickramasinghe, H. K. High-resolution capacitance measurement and potentiometry by force microscopy. *Appl. Phys. Lett.* **52**, **1988**, 1103.
- Masuda, M.; Hanada, T.; Okada, Y.; Yase, K.; Shimizu, T. Polymerization in nanometer-sized fibers: Molecular packing order and polymerizability. *Macromolecules.* **33**, **2000**, 9233.

- McGrath, K. K.; Jang, K.; Robins, K. A.; Lee, D.-C. Substituent effect on the electronic properties and morphologies of self-assembling bisphenazine derivatives. *Chem. Eur. J.* **15**, **2009**, 4070.
- Mena-Osteritz, E.; Meyer, A.; Langeveld-Voss, B. M. W.; Janssen, R. A. J.; Meijer, E. W.; Bäuerle, P. Two-dimensional crystals of poly(3-Alkyl-thiophene)s: Direct visualization of polymer folds in submolecular resolution. *Angew. Chem. Int. Ed.* **39**, **2000**, 2679.
- Messmore, B. W.; Hulvat, J. F.; Sone, E. D.; Stupp, S. I. Synthesis, self-assembly, and characterization of supramolecular polymers from electroactive dendron rodcoil molecules. *J. Am. Chem. Soc.* **126**, **2004**, 14452.
- Mishra, A.; Ma, C.-Q.; Bäuerle, P. Functional oligothiophenes: Molecular design for multidimensional nanoarchitectures and their Applications. *Chem. Rev.* **109**, **2009**, 1141.
- Molla, M. R.; Ghosh, S. Structural variations on self-assembly and macroscopic properties of 1,4,5,8-naphthalene-diimide chromophores. *Chem. Mater.* **23**, **2011**, 95.
- Mukhopadhyay, P.; Iwashita, Y.; Shirakawa, M.; Kawano, S.-i.; Fujita, N.; Shinkai, S. Spontaneous colorimetric sensing of the positional isomers of dihydroxynaphthalene in a 1D organogel matrix. *Angew. Chem. Int. Ed.* **45**, **2006**, 1592.
- Murata, K.; Aoki, M.; Suzuki, T.; Harada, T.; Kawabata, H.; Komori, T.; Ohseto, F.; Ueda, K.; Shinkai, S. Thermal and light control of the sol-gel phase transition in cholesterol-based organic gels. Novel helical aggregation modes as detected by circular dichroism and electron microscopic observation. *J. Am. Chem. Soc.* **116**, **1994**, 6664.

- Negishi, N.; Ie, Y.; Taniguchi, M.; Kawai, T.; Tada, H.; Kaneda, T.; Aso, Y. Synthesis of dendritic oligothiophenes and their self-association properties by intermolecular π - π interactions. *Org. Lett.* **9**, **2007**, 829.
- Nogueira, A. F.; Longo, C.; De Paoli, M. A. Polymers in dye sensitized solar cells: Overview and perspectives. *Chem. Rev.* **248**, **2004**, 1455.
- Otsubo, T.; Aso, Y.; Takimiya, K. Functional oligothiophenes as advanced molecular electronic materials. *J. Mater. Chem.* **12**, **2002**, 2565.
- Palermo, V.; Palma, M.; Samorì, P. Electronic characterization of organic thin films by kelvin probe force microscopy. *Adv. Mater.* **18**, **2006**, 145.
- Palermo, V.; Otten, M. B. J.; Liscio, A.; Schwartz, E.; de Witte, P. A. J.; Castriciano, M. A.; Wienk, M. M.; Nolde, F.; De Luca, G.; Cornelissen, J. J. L. M.; Janssen, R. A. J.; Müllen, K.; Rowan, A. E.; Nolte, R. J. M.; Samorì, P. The relationship between nanoscale architecture and function in photovoltaic multichromophoric arrays as visualized by kelvin probe force microscopy. *J. Am. Chem. Soc.* **130**, **2008**, 14605.
- Palmer, L. C.; Stupp, S. I. Molecular self-assembly into one-dimensional nanostructures. *Acc. Chem. Res.* **41**, **2008**, 1674.
- Peet, J.; Heeger, A. J.; Bazan, G. C. "Plastic" solar cells: Self-assembly of bulk heterojunction nanomaterials by spontaneous phase separation. *Acc. Chem. Res.* **42**, **2009**, 1700.
- Pratihari, P.; Ghosh, S.; Stepanenko, V.; Patwardhan, S.; Grozema, F. C.; Siebbeles, L. D. A.; Würthner, F. Self-assembly and semiconductivity of an oligothiophene supergelator. *Beilstein J. Org. Chem.* **6**, **2010**, 1070.

- Puigmartí-Luis, J.; Laukhin, V.; Pérez del Pino, Á.; Vidal-Gancedo, J.; Rovira, C.; Laukhina, E.; Amabilino, D. B. Supramolecular conducting nanowires from organogels. *Angew. Chem. Int. Ed.* **46**, **2007**, 238.
- Puigmartí-Luis, J.; Pérez del Pino, Á.; Laukhina, E.; Esquena, J.; Laukhin, V.; Rovira, C.; Vidal-Gancedo, J.; Kanaras, A. G.; Nichols, R. J.; Brust, M.; Amabilino, D. B. Shaping supramolecular nanofibers with nanoparticles forming complementary hydrogen bonds. *Angew. Chem. Int. Ed.* **47**, **2008**, 1861.
- Puigmartí-Luis, J.; Pérez del Pino, Á.; Laukhin, V.; Feldborg, L. N.; Rovira, C.; Laukhina, E.; Amabilino, D. B. Solvent effect on the morphology and function of novel gel-derived molecular materials. *J. Mater. Chem.* **20**, **2010**, 466.
- Rep, D. B. A.; Roelfsema, R.; van Esch, J. H.; Schoonbeek, F. S.; Kellogg, R. M.; Feringa, B. L.; Palstra, T. T. M.; Klapwijk, T. M. Self-assembly of low-dimensional arrays of thiophene oligomers from solution on solid substrates. *Adv. Mater.* **12**, **2000**, 563.
- Resel, R. Crystallographic studies on hexaphenyl thin films - a review, *Thin Solid Films.* **433**, **2003**, 1.
- Riede, M.; Mueller, T.; Tress, W.; Schueppel, R.; Leo, K. Small-molecule solar cells - status and perspectives. *Nanotechnology* **19**, **2008**, 424001.
- Roncali, J. Oligothiolenylenevinylenes as a new class of multianometer linear π -conjugated systems for micro- and nanoelectronics. *Acc. Chem. Res.* **33**, **2000**, 147.
- Roncali, J. Synthetic principles for bandgap control in linear π -conjugated systems. *Chem. Rev.* **97**, **1997**, 173.

- Saeki, A.; Ohsaki, S.-i.; Seki, S.; Tagawa, S. Electrodeless determination of charge carrier mobility in poly(3-hexylthiophene) films incorporating perylene diimide as photoconductivity sensitizer and spectroscopic probe. *J. Phys. Chem. C* **112**, **2008**, 16643.
- Saiani, A.; Guenet, J. M. On the helical form in syndiotactic poly(methylmethacrylate) thermoreversible gels as revealed by small-angle neutron scattering. *Macromolecules*. **30**, **1997**, 966.
- Samorí, P.; Francke, V.; Müllen, K.; Rabe, J. P. Self-assembly of a conjugated polymer: From molecular rods to a nanoribbon architecture with molecular dimensions. *Chem. Eur. J.* **5**, **1999**, 2312.
- Sangeetha, N. M.; Maitra, U. Supramolecular gels: Functions and uses. *Chem. Soc. Rev.* **2005**, **34**, 821.
- Sassella, A.; Campione, M.; Raimondo, L.; Tavazzi, S.; Borghesi, A.; Goletti, C.; Bussetti, G.; Chiaradia, P. Epitaxial growth of organic heterostructures: Morphology, structure, and growth mode. *Surface Science*. **601**, **2007**, 2571.
- Sawamura, M.; Kawai, K.; Matsuo, Y.; Kanie, K.; Kato, T.; Nakamura, E. Stacking of conical molecules with a fullerene apex into polar columns in crystals and liquid crystals. *Nature* **419**, **2002**, 702.
- Scharber, M. C.; Mühlbacher, D.; Koppe, M.; Denk, P.; Waldauf, C.; Heeger, a. J.; Brabec, C. J. Design rules for donors in bulk-heterojunction solar cells; towards 10% energy-conversion efficiency. *Adv. Mater.* **18**, **2006**, 789.
- Schenning, A. P. H. J.; Meijer, E. W. Supramolecular electronics; nanowires from self-assembled π -conjugated systems. *Chem. Commun.* **2005**, 3245.
- Schoonbeek, F. S.; van Esch, J. H.; Wegewijs, B.; Rep, D. B. A.; de Haas, M. P.; Klapwijk, T. M.; Kellogg, R. M.; Feringa, B. L. Efficient intermolecular

- charge transport in self-assembled fibers of mono- and bithiophene bisurea compounds. *Angew. Chem. Int. Ed.* **38**, **1999**, 1393.
- Service, R. F. Can chemists assemble a future for molecular electronics. *Science* **295**, **2002**, 2398.
- Shao, H.; Seifert, J.; Romano, N. C.; Gao, M.; Helmus, J. J.; Jaroniec, C. P.; Modarelli, D. A.; Parquette, J. R. Amphiphilic self-assembly of an n-type nanotube. *Angew. Chem. Int. Ed.* **49**, **2010**, 7688.
- Shimizu, T.; Masuda, M.; Minamikawa, H. Supramolecular nanotube architectures based on amphiphilic molecules. *Chem. Rev.* **105**, **2005**, 1401.
- Shinkai, S.; Murata, K. Cholesterol-based functional tectons as versatile building-blocks for liquid crystals, organic gels and monolayers. *J. Mater. Chem.* **8**, **1998**, 485.
- Shirakawa, M.; Fujita, N.; Shinkai, S. [60]Fullerene-motivated organogel formation in a porphyrin derivative bearing programmed hydrogen-bonding sites. *J. Am. Chem. Soc.* **2003**, *125*, 9902.
- Silverstein, R. M.; Bassler, G. C.; Morrill, T. C. Spectrometric identification of organic compounds. John Wiley & Sons. **1983**.
- Sly, J.; Kasák, P.; Gomar-Nadal, E.; Rovira, C.; Górriz, L.; Thordarson, P.; Amabilino, D. B.; Rowan, A. E.; Nolte, R. J. M. Chiral molecular tapes from novel tetra(thiafulvalene-crownether)-substituted phthalocyanine building blocks. *Chem. Commun.* **2005**, 1255.
- Spanggaard, H.; Krebs, F. C. A. brief history of the development of organic and polymeric photovoltaics. *Sol. Energy Mater. Sol. Cells* **83**, **2004**, 125.
- Stone, D. A.; Hsua, L.; Stupp, S. I. Self-assembling quinquethiophene-oligopeptide hydrogelators. *Soft matter*. **5**, **2009**, 1990.

- Stone, D. A.; Tayi, A. S.; Goldberger, J. E.; Palmera, L. C.; Stupp, S. I. Self-assembly and conductivity of hydrogen-bonded oligothiophene nanofiber networks. *Chem. Commun.* **2011**, 3871.
- Sugiyasu, K.; Fujita, N.; Shinkai, S. Visible-light-harvesting organogel composed of cholesterol-based perylene derivatives. *Angew. Chem. Int. Ed.* **43**, **2004**, 1229.
- Sugiyasu, K.; Kawano, S.-i.; Fujita, N.; Shinkai, S. Self-sorting organogels with p-n heterojunction points. *Chem. Mater.* **20**, **2008**, 2863.
- Suzuki, T.; Shinkai, S.; Sada, K. Supramolecular crosslinked linear poly(trimethylene iminium trifluorosulfonimide) polymer gels sensitive to light and thermal stimuli. *Adv. Mater.* **18**, **2006**, 1043.
- Takami, K.; Mizuno, J.; Akai-kasaya, M.; Saito, A.; Aono, M.; Kuwahara, Y. Conductivity measurement of polydiacetylene thin films by double-tip scanning tunneling microscopy. *J. Phys. Chem. B* **108**, **2004**, 16353.
- Tamaoki, N.; Shimada, S.; Okada, Y.; Belaisaoui, K.; Kruk, G.; Yase, K.; Matsuda, H. Polymerization of a diacetylene dicholesteryl ester having two urethanes in organic gel states. *Langmuir.* **16**, **2000**, 7545.
- Tang, C. W. Two-layer organic photovoltaic cell. *Appl. Phys. Lett.* **48**, **1986**, 183.
- Terao, J.; Tanaka, Y.; Tsuda, S.; Kambe N.; Taniguchi, M.; Kawai, T.; Saeki, A.; Seki, S. Insulated molecular wire with highly conductive π -conjugated polymer core. *J. Am. Chem. Soc.* **131**, **2009**, 18046.
- Terech, P.; Weiss, R. G. Low molecular mass gelators of organic liquids and the properties of their gels. *Chem. Rev.* **97**, **1997**, 3133.
- Thompson, B. C.; Frechet, J. M. J. Polymer-fullerene composite solar cells. *Angew. Chem. Int. Ed.* **47**, **2008**, 58.

- Tsao, H. N.; Müllen, K. Improving polymer transistor performance *via* morphology control. *Chem. Soc. Rev.* **39**, **2010**, 2372.
- Tsai, W. -W.; Tevis, I. D.; Tayi, A. S.; Cui, H.; Stupp, S. I. Semiconducting nanowires from hairpin-shaped self-assembling sexithiophenes. *J. Phys. Chem. B* **114**, **2010**, 14778.
- van Esch, J.; De Feyter, S.; Kellogg, R. M.; De Schryver, F.; Feringa, B. L. Self-assembly of bisurea compounds in organic solvents and on solid substrates. *Chem. Eur. J.* **3**, **1997**, 1238.
- van Esch, J. H.; Feringa, B. L. New functional materials based on self-assembling organogels: From serendipity towards design. *Angew. Chem. Int. Ed.* **39**, **2000**, 2263.
- Wang, C.; Zhang, D.; Zhu, D. A. Low-molecular-mass gelator with an electroactive tetrathiafulvalene group: Tuning the gel formation by charge-transfer interaction and oxidation. *J. Am. Chem. Soc.* **127**, **2005**, 16372.
- Wang, H. B.; Zhu, F.; Yang, J. L.; Geng, Y. H.; Yan, D. H. Weak epitaxy growth affording high-mobility thin films of disk-like organic semiconductors. *Adv. Mater.* **19**, **2007**, 2168.
- Wang, X.-J.; Xing, L.-B.; Cao, W.-N.; Li, X.-B.; Chen, B.; Tung, C.-H.; Wu, L.-Z. Organogelators based on TTF supramolecular assemblies: Synthesis, characterization, and conductive property. *Langmuir.* **27**, **2011**, 774.
- Wicklein, A.; Ghosh, S.; Sommer, M.; Würthner, F.; Thelakkat, M. Self-assembly of semiconductor organogelator nanowires for photoinduced charge separation. *ACS Nano.* **3**, **2009**, 1107.
- Würthner, F. Perylene bisimide dyes as versatile building blocks for functional supramolecular architectures. *Chem. Commun.* **2004**, 1564.

- Würthner, F.; Bauer, C.; Stepanenko, V.; Yagai, S. A black perylene bisimide super gelator with an unexpected J-type absorption band. *Adv. Mater.* **20**, **2008**, 1695.
- Würthner, F.; Chen, Z. J.; Hoeben, F. J. M.; Osswald, P.; You, C. C.; Jonkheijm, P.; von Herrikhuyzen, J.; Schenning, A.; vander Schoot, P.; Meijer, E.W.; Beckers, E. H. A.; Meskers, S. C. J.; Janssen, R. A. J. Supramolecular p-n-heterojunctions by co-self-organization of oligo(*p*-phenylenevinylene) and perylene bisimide dyes. *J. Am. Chem. Soc.* **126**, **2004**, 10611.
- Würthner, F.; Hanke, B.; Lysetska, M.; Lambright, G.; Harms, G. S. Gelation of a highly fluorescent urea-functionalized perylene bisimide dye. *Org. Lett.* **7**, **2005**, 967.
- Xin, H.; Kim, F. S.; Jenekhe, S. A. Highly efficient solar cells based on poly(3-butylthiophene) nanowires. *J. Am. Chem. Soc.* **130**, **2008**, 5424.
- Xue, P.; Lu, R.; Zhao, L.; Xu, D.; Zhang, X.; Li, K.; Song, Z.; Yang, X.; Takafuji, M.; Ihara, H. Hybrid self-assembly of a π gelator and fullerene derivative with photoinduced electron transfer for photocurrent generation. *Langmuir* **26**, **2010**, 6669.
- Yagai, S.; Kinoshita, T.; Kikkawa, Y.; Karatsu, T.; Kitamura, A.; Honsho, Y.; Seki, S. Interconvertible oligothiophene nanorods and nanotapes with high charge-carrier mobilities. *Chem. Eur. J.* **15**, **2009**, 9320.
- Yagai, S.; Seki, T.; Murayama, H.; Wakikawa, Y.; Ikoma, T.; Kikkawa, Y.; Karatsu, T.; Kitamura, A.; Honsho, Y.; Seki, S. Structural and electronic properties of extremely long perylene bisimide nanofibers formed through a stoichiometrically mismatched, hydrogen-bonded complexation. *Small*. **6**, **2010**, 2731.

- Yagai, S.; Nakano, Y.; Seki, S.; Asano, A.; Okubo, T.; Isoshima, T.; Karatsu, T.; Kitamura, A.; Kikkawa, Y. Supramolecular engineered aggregation of a dipolar dye: Vesicular and ribbon like architectures. *Angew. Chem. Int. Ed.* **49**, **2010**, 1592.
- Yamamoto, Y.; Fukushima, T.; Jin, W.; Kosaka, A.; Hara, T.; Nakamura, T.; Saeki, A.; Seki, S.; Tagawa, S.; Aida, T. A glass hook allows fishing of hexa-*peri*-hexabenzocoronene graphitic nanotubes: Fabrication of a macroscopic fiber with anisotropic electrical conduction. *Adv. Mater.* **18**, **2006**, 1297.
- Yamamoto, Y.; Fukushima, T.; Saeki, A.; Seki, S.; Tagawa, S.; Ishii, N.; Aida, T. Molecular engineering of coaxial donor-acceptor heterojunction by coassembly of two different hexabenzocoronenes: Graphitic nanotubes with enhanced photoconducting properties. *J. Am. Chem. Soc.* **129**, **2007**, 9276.
- Yamamoto, Y.; Zhanga, G.; Jina, W.; Fukushima, T.; Ishiid, N.; Saeki, A.; Seki, S.; Tagawa, S.; Minarif, T.; Tsukagoshif, K.; Aida, T. Ambipolar-transporting coaxial nanotubes with a tailored molecular graphene–fullerene heterojunction. *Proc Natl Acad Sci USA.* **106**, **2009**, 21051.
- Yanagi, H.; Araki, Y.; Ohara, T.; Hotta, S.; Ichikawa, M.; Taniguchi, Y. Comparative carrier transport characteristics in organic field-effect transistors with vapor-deposited thin films and epitaxially grown crystals of biphenyl-capped thiophene oligomers. *Adv. Funct. Mater.* **13**, **2003**, 767.
- Yang, X.; Zhang, G.; Zhang, D.; Zhu, D. A new ex-TTF-based organogelator: Formation of organogels and tuning with fullerene. *Langmuir* **26**, **2010**, 11720.
- Yang, X.; Loos, J. Toward high-performance polymer solar cells: The importance of morphology control. *Macromolecules* **40**, **2007**, 1353.

- Yoshio, M.; Shoji, Y.; Tochigi, Y.; Nishikawa, Y.; Kato, T. Electric field-assisted alignment of self-assembled fibers composed of hydrogen-bonded molecules having laterally fluorinated mesogens. *J. Am. Chem. Soc.* **131**, **2009**, 6763.
- Yum, J. H.; Chen, P.; Gratzel, M.; Nazeeruddin, M. K. Recent developments in solid-state dye-sensitized solar cells. *ChemSusChem*. **1**, **2008**, 699.
- Zhang, L.; Che, Y.; Moore, J. S. One-Dimensional self-Assembly of planar π -conjugated molecules: Adaptable building blocks for organic nanodevices. *Acc. Chem. Res.* **41**, **2008**, 1596.
- Zeis, R.; Siegrist, T.; Kloc, C. Single-crystal field-effect transistors based on copper phthalocyanine. *Appl. Phys. Lett.* **86**, **2005**, 022103.

List of Publications

1. Self-Assembly of Thienylenevinylene Molecular Wires to Semiconducting Gels with Doped Metallic Conductivity
Seelam Prasanthkumar, Anesh Gopal and Ayyappanpillai Ajayaghosh, *J. Am. Chem. Soc.* **2010**, *132*, 13206-13207
2. Solution Phase Epitaxial Self-Assembly and Highly Charge-Carrier Mobility Nanofibers of Semiconducting Molecular Gelators
Seelam Prasanthkumar, Akinori Saeki, Shu Seki, and Ayyappanpillai Ajayaghosh, *J. Am. Chem. Soc.* **2010**, *132*, 8866-8867
3. Self-Assembly of Oligo(para-phenylenevinylene)s through Arene-Perfluorene Interactions: π - Gels with Longitudinally Controlled Fiber Growth and Supramolecular Exciplex – Mediated Enhanced Emission
Sukumaran S. Babu, Vakayil K. Praveen, **Seelam Prasanthkumar**, and Ayyappanpillai Ajayaghosh, *Chem. Eur. J.* 2008, *14*, 9577-9584
4. Self-assembled Gelators for Organic Electronics
Sukumaran S. Babu, **Seelam Prasanthkumar**, and Ayyappanpillai Ajayaghosh, *Angew. Chem. Int. Ed. mini review.* **2011** (Accepted)
5. Nanoscopic Phase Segregation and Charge Generation of p/n Heterojunction Organogelators on Insulating and Conducting Surfaces
Seelam Prasanthkumar and Ayyappanpillai Ajayaghosh (To be communicated)
6. Soft Epitaxial Growth Approach Towards Highly Conducting Supramolecular Nanofibers
Seelam Prasanthkumar, Akinori Saeki, Shu Seki and Ayyappanpillai Ajayaghosh (To be communicated)
7. Electrical Transport Measurements of Oligo(thienylenevinylene) Derived Organogelators
Seelam Prasanthkumar and Ayyappanpillai Ajayaghosh (To be communicated)

Posters Presented at Conferences

1. Synthesis, Self-assembly and Optical Properties of Oligo(thienylenevinylene) Based Electrically Conducting Organogelators
Seelam Prasanthkumar and A. Ajayaghosh
a poster presented at the *Chemical Research Society of India-RSC Symposium*, ICT(CSIR), Hyderabad, India, **2010**
2. Oligo(thienylenevinylene) Based Electrically Conducting Organogelators
Seelam Prasanthkumar and A. Ajayaghosh
a poster presented at *VIth JNC Research Conference on Chemistry of Materials*, Cochin, Kerala, India, **2010**
3. Oligo(thienylenevinylene) Based Conducting Molecular Wires
Seelam Prasanthkumar and A. Ajayaghosh
a Oral presentation at *VIth JNC Research Conference on Chemistry of Materials*, Cochin, Kerala, India, **2010**
4. Solution Epitaxial Assembly and Highly Conducting Organogelators
Seelam Prasanthkumar and A. Ajayaghosh
a poster presented at the *Research Council Meeting on Materials*, NIIST(CSIR), Trivandrum, Kerala, India, **2011**
5. Conducting Organogels: Design, Synthesis and Self-assembly of oligo(thienylenevinylene) Derived Molecular Wires
Seelam Prasanthkumar, C. Vijayakumar, A. Saeki, S. Seki and A. Ajayaghosh
a Oral presentation at *JENESYS mini-symposium*, IMS, Japan, **2011**